

University of Southampton Research Repository ePrints Soton

Copyright © and Moral Rights for this thesis are retained by the author and/or other copyright owners. A copy can be downloaded for personal non-commercial research or study, without prior permission or charge. This thesis cannot be reproduced or quoted extensively from without first obtaining permission in writing from the copyright holder/s. The content must not be changed in any way or sold commercially in any format or medium without the formal permission of the copyright holders.

When referring to this work, full bibliographic details including the author, title, awarding institution and date of the thesis must be given e.g.

AUTHOR (year of submission) "Full thesis title", University of Southampton, name of the University School or Department, PhD Thesis, pagination

University of Southampton
Faculty of Natural and Environmental Sciences
Department of Chemistry

PLANAR INTEGRATED OPTICAL BRAGG GRATING
GAS SENSORS

By

DOMINIC JAMES WALES

Thesis for the degree of Doctor of Philosophy

October 2013

Declaration of Authorship

I, Dominic James Wales, declare that the thesis entitled “Planar Integrated Optical Bragg Grating Gas Sensors” and the work presented in the thesis are both my own, and have been generated by me as the result of my own original research.

I confirm that:

- this work was done wholly or mainly while in candidature for a research degree at this University;
- where any part of the thesis has previously been submitted for a degree or any other qualification at this University or any other institution, this has been clearly stated;
- where I have consulted the published work of others, this is always clearly attributed;
- where I have quoted from the work of others, the source is always given. With the exception of such quotations, this thesis is entirely my own work;
- I have acknowledged all main sources of help
- where the thesis is based on work done by myself jointly with others, I have made clear exactly what was done by other and what I have contributed myself;

Part of this work has been published in the following publication (as indicated in the relevant chapter):

- D.J. Wales, R.M. Parker, J.C. Gates, M.C. Grossel, P.G.R. Smith, “An investigation into relative humidity measurement using an aluminosilicate sol–gel thin film as the active layer in an integrated optical Bragg grating refractometer”, *Sensor and Actuators B: Chem.*, 2013, **188**, 857-866

In addition, this work has been presented at 8 national and international conference, with a full bibliography given in **Chapter 9**.

Signed:.....

Date: **30** **September** **2013**

Acknowledgments

There are many people to whom I wish to thank due to the help and inspiration they have given me, over the course of my PhD.

Firstly, I would like to thank my supervisors, Dr. Martin Grossel (Department of Chemistry), Dr. James Gates (Optoelectronics Research Centre) and Prof. Peter Smith (Optoelectronics Research Centre). Throughout my PhD, with their combined guidance, I have been given the freedom to seek out my own solutions and set my own tasks and goals, but I also have always been able to approach them for advice and support. The collective strengths that they have brought to this interdisciplinary project have enabled it to flourish.

As this PhD project has been multidisciplinary I have had the pleasure of working in two research groups. Therefore, I wish to extend my thanks to all the past and present members of the two research groups, in particular Bingjia (Gavin) Yan and Hassan Gneid and my past project students! Also in particular I would like to thank Dr. Richard Parker who completed his PhD in a similar multidisciplinary project during the course of my PhD. Without his support and friendship the work presented here would not have been possible. Richard, through his advice and sharing of experienced tips and tricks made the challenge of entering the field of photonics a far less daunting experience.

I would also especially like to thank the following characterisation support staff in both the Department of Chemistry and the Optoelectronics Research Centre for their assistance and guidance: Dr. Neil Wells (NMR, Chemistry), Dr. John Langley (MS, Chemistry), Mrs Julie Herniman (MS, Chemistry), Dr. Mark Light (X-ray, Chemistry) and Mr Neil Sessions (SEM & Cleanroom, Optoelectronics Research Centre). I would also like to thank all the other support staff in both departments who, through their hard work, ensure everything runs smoothly.

Most importantly, I would like to extend my gratitude to my parents, Paul and Denise and my sister Victoria for their unwavering support and understanding that

has encouraged me through the high and lows of my PhD studies. In addition, I would like to thank my friends Colin and Alex King, Michael Gates and Andrew Clarke for their support, friendly advice and friendship which has kept me going through the lows and highs of my PhD. Finally, I would like to thank Liisa Niitsoo for her amazing support, friendship and love. Kallis Liisa, ma armastan sind väga palju. (P.S. Aitäh for sending awesome presents from Australia!)

UNIVERSITY OF SOUTHAMPTON

ABSTRACT

FACULTY OF NATURAL AND ENVIRONMENTAL SCIENCES

DEPARTMENT OF CHEMISTRY

DOCTOR OF PHILOSOPHY

PLANAR INTEGRATED OPTICAL BRAGG GRATING GAS SENSORS

By Dominic James Wales

This thesis reports the development and modification of direct ultraviolet (UV) written planar integrated optical Bragg grating refractometers for detection of gases and vapours.

The technique of direct UV writing utilises the localised refractive index increase within a UV-photosensitive silica layer, when the layer is exposed to a tightly focussed UV beam, to fabricate a wide range of optical waveguides and optical components. One such component, the Bragg grating, is used as an optical sensor for changes in refractive index.

This thesis reports on the development of practical planar integrated optical Bragg grating gas sensors. This has been achieved through the use of two approaches. The first approach was to increase the number of gas molecules that can interact with the evanescent wave through the use of films of material that extended normally to the surface of the sensor device. Upon functionalisation of a planar Bragg grating sensor device with sol-gel thin films, a response between relative humidity and Bragg wavelength shift was revealed. Functionalisation of the Bragg grating sensor device with a polysiloxane polymer imparted sensitivity to solvent vapours. A quantitative structure-activity relationship (QSAR) approach was used to develop a linear regression model, between Bragg wavelength shift and solvent properties, which had good predicting power.

The second approach was to utilise the associated change in refractive index of a material, when the material changed colour upon exposure to a gas, to create a measurable Bragg wavelength shift. This method was successfully achieved upon interrogation of a Bragg

grating sensor device, which had been modified with an encapsulated pH sensitive organic dye upon exposure to hydrogen chloride fumes.

Contents

Declaration of Authorship.....	1
1. Introduction	13
1.1 Introduction	13
1.2 Integrated Optics	13
1.3 Applications of optical integrated circuits	15
1.3.1 Telecommunications	15
1.3.2 Sensors	16
1.4 Aim of Research.....	19
1.5 Thesis overview.....	19
2. Planar Integrated Optical Bragg Grating Sensors: Theory	25
2.1 Introduction	25
2.2 Integrated Optics and Optical Waveguides:	25
2.2.1 Physical Concepts:.....	26
2.2.2 Planar Slab Optical Waveguides:	29
2.2.3 Maxwell's Equations	32
2.2.4: Effective Index	40
2.2.5: Effective Guide Thickness	41
2.2.6 Strip Waveguides.....	48
2.3 Bragg grating theory	54
2.3.1: Optical Bragg gratings.....	55
2.3.2: Effective index modulation	56
2.3.3: Bragg grating structures	58
2.3.4: Birefringence	60
2.4: Summary.....	61
3 Planar Bragg grating sensor fabrication	63
3.1 Introduction	63
3.2 Silica-on-silicon substrate platform	64

3.2.1	Growth of the thermal oxide underclad layer	65
3.2.2	Flame hydrolysis deposition	65
3.3	UV photosensitivity.....	70
3.3.1	Photosensitivity of germanium-doped silica.....	70
3.3.2	Hydrogenation.....	74
3.4	The Direct UV-writing process	77
3.4.1	Competing Techniques to Direct UV Writing	79
3.5	Direct UV Grating Writing	82
3.5.1	Direct UV grating writing free space optical set-up	84
3.5.2	Direct UV grating writing of Bragg gratings in the telecoms C band ..	85
3.5.3	Duty cycle	86
3.5.4	Grating engineering	88
3.6	Bragg grating device characterisation and packaging.....	90
3.6.1	Polarisation and stability.....	93
3.7	Summary	94
4	Evanescent Wave Gas Sensors	99
4.1	Introduction	99
4.2	Optical fibre evanescent wave gas sensors	100
4.2.1	Optical fibre evanescent wave relative humidity sensors	102
4.2.2	Optical fibre evanescent wave hydrocarbon and VOC sensors	103
4.2.3	Optical fibre evanescent wave sensors for acidic and basic gases.....	104
4.2.4	Advantages and disadvantages of evanescent wave optical fibre sensors	105
4.3	Surface Plasmon Resonance (SPR) sensors ²³	105
4.3.1	Plasmons ²⁹	105
4.3.2	Surface plasmons	106
4.3.3	Utilising surface plasmons for sensing	108
4.3.3	Waveguide surface plasmon resonance sensors	110
4.3.4	Surface plasmon resonance relative humidity sensors.....	111
4.3.5	Surface plasmon resonance sensors for hydrocarbons and volatile organic compounds.....	111
4.3.6	Surface plasmon resonance sensors for acidic/basic gases.....	111

4.3.7	Advantages and disadvantages of surface plasmon resonance sensors	112
4.4	Mach-Zehnder interferometer (MZI) sensors	112
4.4.1	Integrated optical Mach-Zehnder interferometers	113
4.4.2	Integrated optical Mach-Zehnder interferometer for relative humidity	114
4.4.3	Integrated optical Mach-Zehnder interferometer for hydrocarbons and volatile organic compounds.....	114
4.4.4	Integrated optical Mach-Zehnder interferometer for basic gases	114
4.4.5	Advantages and disadvantages of Mach-Zehnder interferometers	114
4.5	Grating Couplers	115
4.5.1	Integrated optical Bragg grating sensors.....	117
4.5.2	Advantages and disadvantages of integrated Bragg grating sensors ..	118
4.6	Summary	119
5	Increasing Sensitivity: The Evanescent Wave Interaction Volume.....	127
5.1	Introduction	127
5.2	Increasing sensitivity to gases	127
5.2.1	Unfunctionalised Bragg Grating sensors	127
5.2.2	Surface modification	131
5.2.3	Sol-gels	135
5.2.4	Polymer over layers	137
6.	Mesoporous thin films and relative humidity sensing.....	141
6.1	Introduction	141
6.2	Development of the sol-gel sensing thin film	142
6.2.1	Undoped silica sol-gel (1).....	142
6.2.2	Undoped methyl-functionalised silica sol-gel (2)	144
6.2.3	Undoped MTMS silica solid (3).....	149
6.2.4	Undoped mesoporous silica sol-gel thin film (4)	151
6.2.5	Determination of the porous nature of thin films of (4)	155
6.3	Development of a Bragg grating sensor relative humidity sensor	159
6.3.1	Planar Integrated Bragg grating sensor modified with a thin film of (4) as a relative humidity (%RH) sensor	159
6.3.2	Planar Integrated Bragg grating sensor modified with a thin film of (6) as a relative humidity (%RH) sensor	168

6.4	Conclusion.....	181
7.	Sensing of solvent vapours using a polysiloxane thin film as the active sensing element	185
7.1	Introduction	185
7.2	Development of the siloxane polymer	186
7.2.1	Synthesis of poly(methylhydro)-co-poly(methyloctyl)siloxane (8):.....	186
7.2.2:	Synthesis and characterisation of poly(methylhydro) – co – poly(methyloctyl) siloxane	188
7.2.3	Physical characterisation of poly(methylhydro)-co-poly(methyloctyl)siloxane (8):	191
7.3	Refractometric sensing of organic vapours	193
7.3.1	Organic vapour sensing experimental set-up and procedure :.....	193
7.3.2:	Solvent vapour sensing results:	195
7.3.3:	QSAR approach to enable prediction of Bragg wavelength shifts:.....	209
7.4	Conclusions and Further Work	219
8	Utilising the relation between n and κ to achieve refractometric sensing ..	225
8.1	Introduction	225
8.2	Fabrication of a pH chromic thin film.....	225
8.3	Investigation into the pH chromic behaviour of (9).....	227
8.3.1	Visible spectroscopy study	227
8.3.2	Refractometric sensing at 1550 nm.....	230
8.4	Mathematical modelling of refractive indices.....	234
8.4.1	Fitting of Lorentzian functions to absorbance features.....	234
8.4.2	Fitting of Voigt functions to absorbance features.....	237
8.5	Refractometric sensing at 780 nm	240
8.5.1	‘Moist’ ammonia fume refractometric sensing at 780 nm.....	240
8.5.2	‘Moist’ hydrogen chloride fume refractometric sensing at 780 nm ...	241
8.6	Colour change refractometric sensing of volatile organic compounds (VOCs) at 1550 nm	247
8.6.1	Lutetium bisphthalocyanine.....	247
8.6.2	VOC sensing experiments at 1550 nm.....	251

8.7	Conclusions and Further Work	259
9	Conclusions.....	263
9.1	Conclusions	263
9.2	Further work.....	267
9.3	Final comments	275
9.4	Dissemination of Research.....	276
10.	Experimental.....	279
10.1	Introduction	279
10.2	General Experimental.....	279
10.3	Chemical Synthesis	282
10.3.1	Undoped silica sol-gel (1).....	282
10.3.2	Undoped methyl-functionalised silica sol-gel (2)	284
10.3.3	Undoped MTMS silica solid (3).....	285
10.3.4	Undoped mesoporous silica sol-gel thin film (4)	287
10.3.5	Methylene blue doped mesoporous silica sol-gel thin film (5)	288
10.3.6	Undoped mesoporous aluminosilicate sol-gel thin film (6)	289
10.3.7	<i>cis</i> -Dichlorobis(triphenylphosphine)platinum(II) (7).....	290
10.3.8	Poly(methylhydro) – <i>co</i> – poly(methyloctyl)siloxane (8)	291
10.3.9	Neutral red-doped mesoporous silica sol-gel thin film (9).....	293
10.3.10	Lutetium(III) bis-phthalocyanine (10).....	293
10.4	Optical Experiments.....	295
10.4.1	Fabrication of 6” silica on silicon wafers via the Flame Hydrolysis Deposition (FHD) technique	295
10.4.2	Hydrogen loading to increase photosensitivity	295
10.4.3	Simultaneous Direct UV-writing of waveguides and Bragg gratings	295
10.4.4	Pigtailing.....	296
10.4.5	Characterisation of a Bragg grating device	296
10.4.6	Water vapour sensing in a gas flow system.....	297
10.4.7	Sensing of organic solvent vapour in a flow system at 1550 nm using a Bragg grating device modified with a film of (8)	298

10.4.8 UV-Visible spectrometric measurement of the absorbance changes of (9) when exposed to acidic and basic gases	300
10.4.9 Experimental investigation of refractometric sensing at 1550 nm of ammonia gas in a static ‘dunk’ system using a 1550 nm Bragg grating sensor device modified with (9)	301
10.4.10 Experimental investigation of refractometric sensing at 1550 nm of ammonia gas in a flow system using a 1550 nm Bragg grating sensor device modified with (9)	302
10.4.11 Experimental investigation of refractometric sensing at 780 nm of either ammonia gas or hydrogen chloride (HCl) vapour in a static ‘dunk’ system using a 1550 nm Bragg grating sensor device modified with (9)	303
10.4.12 Sensing of organic solvent vapour in a flow system at 1550 nm using a Bragg grating device modified with a thin film of (10)	304
Appendix 1: Utilising the relation between absorption & refraction to sense gases	
307	
A1.1 Introduction	307
A1.2 The complex relative dielectric constant ¹	307
A1.2.1 Refraction.....	307
A1.2.2 Absorption ¹	308
A1.2.3 Complex refractive index ¹	310
A1.2.4 Microscopic classical dipole oscillator model ¹	314
A1.3 The Kramers-Kronig Relations	326
A1.4 Utilising the relationship between n and κ to sense gases.....	327

1. Introduction

1.1 Introduction

A sensor is defined as a device that responds to a physical input of interest, and converts the input into a recordable, electrical or optical output that can be interpreted by a machine or a human observer ¹.

Sensors can be found in many everyday objects, for example in cars, planes and household white goods. In addition, the non-military, open world market for sensors systems was estimated to be worth \$490 billion in 2010 ².

Sensing of gases is required within a diverse set of fields, including industry, environmental monitoring and homeland security, and traditionally is achieved by use of electronic sensors. However, optical sensors (sensors that are operated with light instead of electricity) demonstrate many benefits over electronic sensors, including remote interrogation of large sensor arrays via standard optical fibre and telecoms equipment, and do not present a spark risk in flammable environments ³.

One type of optical sensor is the integrated optical sensor. Integrated optics focuses the miniaturisation and integration of multiple photonic functions within a single smart device. Integrated optics lends itself to the field of optical sensing as it allows for the development and fabrication of smaller, more powerful, safer and more cost-effective sensor devices.

1.2 Integrated Optics

The term “integrated optics” was coined in 1969 by Miller ⁴. The term encapsulates all methods and exploratory work towards the use of “laser beam circuitry” to fabricate improved or novel optical devices ⁵. These optical devices can contain several optical guided-wave functions all combined on one common substrate; integrated yet

miniaturized and compact ⁵. Miller's description of "laser beam circuitry" refers to what are now known as optical integrated circuits (OICs). OICs can be considered to be analogous to electrical integrated circuits; however the electrical copper tracks/interconnects are replaced with optical waveguides ⁶. Optical waveguides are different to copper tracks in that light propagates along the length of the waveguide rather than electrical charge. Since Miller's paper in 1969, the optical component market has grown significantly; it is predicted that between 2012 and 2018 the optical component market will grow by 8% and be worth \$10.5bn ⁷. In addition, the production, and use, of integrated devices has become increasingly popular ⁸.

Many parallels can be drawn between the disciplines of integrated optics and integrated electronics. However, the field of integrated optics is still at a relatively early stage compared to the field of integrated electronics ⁸. Unlike the field of integrated electronics, where single crystal silicon is the dominant material used as the substrate for the circuit, integrated optical circuits have been fabricated from a variety of materials ⁹. These materials include silica-on-silicon or silicon-on-insulator substrates, organic polymers and semiconductor materials such as silicon or gallium arsenide ⁹. The choice of substrate is dependent on what function is to be integrated; each material has inherent advantages and disadvantages for each application. Once a suitable material has been chosen, photolithography (the most commonly used technique) is used to pattern the substrates for further definition of the waveguides and optical components by additional etching or material deposition steps ¹⁰.

Optical integrated circuits can be comprised of a large variety of optical components; this is in contrast to integrated electronics where the primary component is the transistor. The photonic components within the OICs are usually miniaturised versions of bench-top components used in conventional free-space optics; this can afford higher performance than with discrete optical components. The diverse range of optical components that have been realised in OICs includes power splitters ¹¹, optical amplifiers ¹², optical modulators and filters ^{13,14} and on-chip lasers and detectors ^{15,16}. In addition, increased functionality can be achieved by combination of integrated optical circuits with integrated electronic circuits; a bridge between the two fields ¹⁷. However, as stated above, due to the inherent advantages and disadvantages of the variety of different materials and fabrication techniques that are utilised, it can be challenging to realise complex OICs on a single chip.

1.3 Applications of optical integrated circuits

The drive to develop and grow the field of integrated optics has primarily come from the telecommunication industry, where the demand from consumers for increased network bandwidth is increasing. This is due to the explosion in the popularity of web-based video services such as *YouTube* and television catch-up services such as the BBC's *iPlayer* ⁶.

To cope with the increased demand, telecommunication networks are being enhanced. This has been achieved by installing more optical fibres and by replacing electronic telecommunication systems with optical systems, such as the introduction of optical fibre to the home. By switching to an optical network, benefits in terms of reduced power consumption, improved economy and speed will be achieved ¹⁸. To achieve this goal, network switches must be switched from all electrical or electrical-optical hybrid to all optical integrated devices ¹⁸; thus the drive to develop and grow the field of integrated optics.

1.3.1 Telecommunications

Transmission of optical signals in optical telecommunications network is achieved, in the most part, through the use of optical fibres. Typically the optical fibres are made from silica and demonstrate the property of low optical loss at certain wavelengths. This allows for the transmission of information over 1000's of km. To utilise the spectral regions of inherent low optical power loss in silica, specific telecommunication wavelength 'window bands' were defined. One such 'window band' is the C-band. This 'window band' is in the near-infrared region of the electromagnetic spectrum and is between 1530 nm and 1565 nm; located at a minimum between regions where Rayleigh scattering and absorption occur.

However, despite use of the telecommunication 'window bands', such as the C-band, the infrared signal is still attenuated as it travels along the optical fibre over the distances required for transatlantic data communication. This issue was remedied with the invention of the erbium doped fibre amplifier (EDFA). An EDFA allows for broadband amplification in the C-band, thus increasing the range of optical signal transmission via optical fibre networks. In addition, the use of EDFAs removes the complex and inefficient signal conversion and electronic amplification equipment previously used to overcome this issue.

Furthermore, the capacity of optical fibre networks has been increased by introduction of a new ‘window band’ by removal of the water absorption peak at ~ 1400 nm ¹⁹. In addition, optical network capacity can also be increased, as stated above, by the laying of additional optical fibre. However, a significant method used to increase capacity, which has attracted the use of integrated optics, is a method known as Wavelength Division Multiplexing (WDM) ²⁰. In the WDM technique, the transmission ‘window band’ is carved into discrete non-overlapping wavelength channels; preventing overlapping is essential to avoid inter-channel crosstalk. Each wavelength channel allows for the transmission of optical signals at different wavelengths along a single optical fibre, in both directions. This allows for each carrier channel to be individually separated, routed and switched. Crucial components within WDM equipment are the optical multiplexers/demultiplexers ²¹. These components are usually formed from integrated optics ²¹; the desire for higher capacities has driven improvement of WDM systems and thus has driven research into integrated optics.

However, in addition to the improved efficiencies in the telecommunication industry there also have been many secondary applications that have benefited from the attention and investment poured into optical fibre and integrated optical technologies. One such application is the field of optical sensing.

During and between the boom periods of the telecommunication industry there were many types of optical sensor reported in the literature which covered a wide range of stimuli. The stimuli covered ranged from physical properties such as temperature ²² or pressure ²³ through to biological and chemical sensing ²⁴. Optical sensors are of particular interest as they possess advantages over electrical sensors which include immunity to electro-magnetic interference and the absence of spark risk in flammable or explosive environments.

1.3.2 Sensors

As mentioned above, a sensor is defined as a device that responds to a physical input of interest, and converts the input into a recordable, electrical or optical output that can be interpreted by a machine or a human observer ¹. A wide range of sensors for sensing of physical changes or chemical/biological species have been reported in the literature or are available commercially. For good performance, the general properties a sensor should possess, according to Rakočević *et.al* ²⁵, are:

- sensitivity to the measured property,
- a large dynamic range
- ideally a linear transfer function (the relation between input and output)
- low noise
- inertness i.e. does not influence the measurand property,
- insensitivity to any other property likely to be encountered during use.

1.3.2.1 Gas Sensing:

The sensing of gases is required in a vast range of different applications in a variety of scientific, industrial and domestic settings. From biomedical diagnosis, monitoring of industrial processes and waste gas steams to detection of terror threats, gas sensing features in every facet of modern life ²⁶. Gas sensors are also widely used to detect oxygen deficiency or the build-up of toxic gases in confined spaces such as on submarines or in mines for the health and safety of the personnel ²⁷. In addition, the estimated market worth of the gas sensing market is \$3.5 million per annum ²⁷.

Gas sensors, of the type reported in the literature and available commercially, can be broadly categorised into four different types ²⁸:

- electrochemical
- thermometric
- gravimetric
- optical

Electrochemical sensors operate on the transduction of a chemical sensing event into a change in capacitance or resistance. However, as stated above, electrochemical sensors present a spark risk in flammable environments and can suffer from electromagnetic interference. In addition some electronic gas sensors require sporadic heating with ‘on-device’ heating elements to maintain sensitivity by evaporative removal of condensed water vapour ²⁹. These heating elements can be power intensive and also introduce a heated surface which could as an ignition source in flammable environment. Thermometric sensors utilise the change in temperature of the sensor material, either by absorption or evolution of heat, when the internal energy of the sensor material changes (as stated by the first law of thermodynamics) due to a chemical interaction with an analyte ³⁰. In order to the quantify the temperature change, the sensor material is

deposited onto thermal probes, however most of these thermal probes are electrically interrogated and thus present a spark risk³⁰. Gravimetric sensors transduce a change in mass of the sensor material, caused by a chemical sensing event, into a change of frequency, which is usually measured electronically. However, the main disadvantage of gravimetric sensors is the slow dynamic response due to diffusion rate of the analyte into the active sensing material layer³¹. In contrast, optical based sensors are largely suitable for use in hazardous or explosive environments (no inherent spark risk), immunity to electromagnetic or radiation interference and affording the ability to interrogate remotely, large multi-sensor arrays via optical fibre and standard telecommunications equipment³⁰.

The majority of commercial optical chemical sensors are based on free space optics, such as spectrometers³². For gas sensing, open-path sensing systems are routinely employed. These open-path sensing systems are comprised of an optical radiation source, usually a laser, and a physically separate detector. The average concentration of an analyte gas is determined by measuring the amount of attenuation of the beam along the path length, which can be up to 100 m long³³. However, false readings can be caused by scattering losses due to dust or mists of oil. In addition, it is not possible to determine whether a particular concentration value is due to a high concentration over a short path length of the beam, or a lower concentration over a long path length³³.

There has been a considerable research effort to develop optical fibre³⁴, or integrated optical structures for sensing of chemicals^{35,36}. In particular, integrated optics enables sensors to be designed which demonstrate on-chip thermal compensation³⁷, and allows for the combination of multiple optical functions on a single and compact chip for realisation of multi-parameter analysis³⁸. These benefits lend integrated optical sensors towards gas sensor applications; these devices will allow sensing of multiple different gases which will revolutionise point-of-care medical diagnostics and fieldwork applications.

The work presented herein focuses on the development of integrated optical Bragg grating systems, acting as simple refractometers, into working integrated optical gas sensors for volatile organic compound detection and monitoring relative humidity.

1.4 Aim of Research

This work investigates direct UV-written Bragg grating integrated optical devices, for gas sensing applications. Direct UV-writing is a fabrication technique that allows for the simultaneous definition of both the optical waveguides and the Bragg gratings within the optical waveguides. The Bragg gratings are the optical components used for sensing. The theory of optical waveguide and Bragg gratings is discussed in **Chapter 2** and the direct UV-writing technique is described in more detail in **Chapter 3**.

The original aim of this PhD thesis was to develop direct UV-written integrated optical Bragg grating sensor devices for sensing of gases, by bringing together elements of materials chemistry, macrocyclic chemistry, colour chemistry and integrated optics. The aims of this PhD thesis have been achieved through the combination of direct UV-written, integrated optical Bragg grating sensors with material chemistry motifs, such as a mesoporous aluminosilicate sol-gel thin film to fabricate a relative humidity sensor and a polymer thin film to fabricate an organic solvent vapour sensor. Both of these sensors work in gas flow systems which allows for continuous sampling of feedstock gases. These proof-of-concept devices are competitive with rival gas sensing techniques in terms of robustness, sensitivity and practicality, whilst offering specific advantages. In addition, through the combination of a sol-gel thin film and a stimulus-responsive dye, a proof-of-principle integrated optical Bragg grating sensor has been developed that utilised the colour change of the dye, upon a sensing event, to cause a measureable change in refractive index, confirming this approach to gas sensing as viable.

This work has afforded one journal publication and data that have been presented at eight national and international conferences.

1.5 Thesis overview

Following this introduction to integrated optics, the theory of light propagation in optical waveguides along with Bragg grating theory, is discussed in **Chapter 2**. The fundamental physical concepts describing propagation of light through a medium and how this forms the basis of an optical waveguide are described. By expanding on these concepts the different possible geometries of optical waveguides, such as slab and channel waveguides structures, are introduced. In particular, for channel waveguides, an optical mode-solving algorithm, the film mode matching (FMM) method, is described in preparation for a later chapter, wherein commercial FMM algorithm software

(*Fimmwave*) was used to model the guided modes of light in the Bragg grating devices presented in this thesis. **Chapter 2** concludes by introducing and discussing the concept of, and the theory behind optical Bragg gratings.

The methods used to fabricate the integrated optical Bragg grating sensor devices are addressed in **Chapter 3**. Starting with the fabrication of the silica-on-silicon substrate, the theory and history of direct UV writing (including a comparison to other methods of waveguide fabrication) is then discussed. The substrate composition required for direct UV writing, including the introduction of germanium as a UV-photosensitive dopant, is discussed together with the proposed mechanisms for the UV-writing photochemical effect. The design of Bragg grating structures is also discussed and the chapter concludes by detailing optical Bragg grating characterisation and interrogation.

Chapter 4 is an overview of chemical gas sensing using refractive index-based evanescent field sensors such as Mach-Zehnder interferometers (MZI), surface plasmon resonance (SPR, the main competing technique) sensors, and Bragg grating refractometers.

In **Chapter 5**, the use of the 3D sensing volume, normal to the surface of a planar Bragg grating sensor, to increase sensitivity is proposed. The theory describing the sensitivity increase is discussed with theoretical Fimmwave modelling of the optical modes, before an introduction to the materials used to achieve this goal; mesoporous sol-gel thin films and polymer thin films that swell upon exposure to solvent vapours.

Chapter 6 focuses on the development of an integrated optical Bragg grating relative humidity sensor through the use of a mesoporous silica sol-gel thin film. The fabrication and characterisation of the intermediate reaction sol and the silica sol-gel thin film is discussed before the results of relative humidity sensing experiments, performed in a flow system, are analysed. It was then found that hydrolytic degradation of the silica sol-gel thin film active sensing element had occurred, thus an aluminosilicate grafted mesoporous sol-gel thin film was fabricated and the resulting sensing results of this improved sensor are presented. Finally, the performance of the sensor in the ambient ‘static’ laboratory environment and the response time of the sensor are explored.

Chapter 7 focuses on the development of an integrated optical Bragg grating organic solvent vapour sensor, through the use of a polymer thin film. The fabrication and

characterisation of the siloxane polymer is presented before the results of solvent vapour sensing experiments, performed in a flow system, are analysed. A model to describe the Bragg wavelength shift behaviour when the device was exposed to the vapour of different solvents, based on the solvation power of the solvents, is then proposed. The response time of the sensor is also investigated and reported. Finally, using the quantitative structural activity response (QSAR) method, a multiple linear regression model was developed. This model allows for prediction of the Bragg wavelength shift for any solvent for which certain common and easily obtainable properties are known.

In **Chapter 8**, the use of the relationship between the colour of a material and the refractive index of that material for sensing is explored. The physical origin of theory this relationship, known as the Kramers-Kronig relation is discussed, and then it is proposed that a colour change in a material, due to a chemical binding event, will be accompanied by a change of refractive index. This change in refractive index, caused by the colour change, could be measured with the Bragg gratings.

After **Chapter 9**, which presents the overall conclusions and discusses future work, the chemical syntheses, experimental procedures and methods performed in this work are discussed in greater detail in **Chapter 10**, the **Experimental Details** chapter.

Finally in **Appendix 1** the use of the Kramers-Kronig relation as a viable method for refractive index of gases is demonstrated. The fabrication and characterisation of a neutral red doped mesoporous silica sol-gel thin film is described and then the results of the hydrogen chloride vapour sensing experiment at 780 nm are discussed. The aim to achieve refractive index sensing of organic solvent vapours at 1550 nm using a very thin film of a lanthanide *bisphthalocyanine* organometallic sandwich complex as the chemical probe, is then discussed. The synthesis and characterisation of lutetium *bisphthalocyanine* is described in addition to the fabrication of the thin film of the phthalocyanine. Finally the results of organic solvent vapour sensing experiments at 1550 nm are analysed

1. D. P. Jones, in *Biomedical Sensors*, ed. D. P. Jones, Momentum Press, New York, 1st edn., 2010, p. ix.
2. Scottish Enterprise, *Sensing a brighter future*, Glasgow, 2010.
3. B. D. Gupta, *Fiber Optic Sensors: Principles and Applications*, New India Publishing Agency, New Delhi, 1st edn., 2006.
4. S. E. Miller, *Bell Syst. Tech. J.*, 1969, **48**, 2059.
5. H. Kogelnik, *IEEE Transactions on Microwave Theory and Techniques*, 1975, **MTT-23**, 2–16.
6. R. G. Hunsperger, *Integrated Optics: Theory and Technology*, Springer, 6th edn., 2009.
7. Europa Science, *Fibre Systems*, 2013.
8. Information Gateway Inc., *Integrated Optics Suppliers*, Allston, MA, U.S.A., 2002.
9. E. M. Conwell and R. D. Burnham, *Ann. Rev. Mater. Sci.*, 1978, **8**, 135–179.
10. J. V. Magill, in *Optical Fiber Sensor Technology: Volume 4: Chemical and Environmental Sensing*, eds. B. T. V. Grattan and B. G. Meggitt, Kluwer Academic Publishers, 1999, pp. 122–123.
11. H. Takahashi, K. Okamoto, and Y. Ohmori, *IEEE Photonics Technology Letters*, 1993, **5**, 58–60.
12. M. Kull and G. Manneberg, *Journal of Lightwave Technology*, 1989, **7**, 331–335.
13. K. Preston, S. Manipatruni, A. Gondarenko, C. B. Poitras, and M. Lipson, *Optics Express*, 2009, **17**, 5118–5124.
14. Y. Wu, S. Liu, G. Wei, R. Lu, Y. Liu, and Z. Zhong, *Science China Technological Sciences*, 2013, **56**, 563–566.
15. Y. Wang, Y. Wei, Y. Huang, Y. Tu, D. Ng, C. Lee, Y. Zheng, B. Liu, and S.-T. Ho, *Optics express*, 2011, **19**, 2006–13.
16. G. E. Marx, M. Gottlieb, and G. B. Brandt, *IEEE Journal of Solid-State Circuits*, 1977, **SC-12**, 10–13.
17. IBM, 2012.
18. X. Ye, A. Venkatesh, and S. J. B. Yoo, in *OSA/OFC/NFOEC 2011*, Los Angeles, 2011, p. OThQ4.

19. G. Kuyt, P. Pluenis, A. van Bergen, and R. van Laere, in *Broadband Access and Technology*, eds. D. W. Faulkner and A. L. Harmer, IOS Press, 1999, p. 57.
20. B. Mukherjee and H. Zang, in *Optical WDM Networks: Principles and Practice*, eds. K. M. Sivalingam and S. Subramaniam, Springer, Norwell, MA, 2000, p. 6.
21. H. Ishio, J. Minowa, and K. Nosu, *Journal of Lightwave Technology*, 1984, **LT-2**, 448–463.
22. A. Kumar, R. Jindal, R. K. Varshney, and S. K. Sharma, *Optical Fiber Technology*, 2000, **6**, 83–90.
23. W. N. MacPherson, M. J. Gander, J. S. Barton, J. D. C. Jones, C. L. Owen, A. J. Watson, and R. M. Allen, *Measurement Science and Technology*, 2000, **11**, 95–102.
24. X.-D. Wang and O. S. Wolfbeis, *Analytical chemistry*, 2013, **85**, 487–508.
25. G. Rakočević, in *Application and Multidisciplinary Aspects of Wireless Sensor Networks: Concepts, Integration, and Case Studies*, eds. L. Gavrilovska, S. Krco, V. Milutinovic, I. Stojmenovic, and R. Trobec, Springer-Verlag, London, 2010, pp. 14–16.
26. D. J. Wales, R. M. Parker, J. C. Gates, P. G. R. Smith, and M. C. Grossel, in *SET for BRITAIN 2011*, London, 2011, p. 1.
27. T. Shigemore, in *The 14th International Meeting on Chemical Sensors (IMCS 2012)*, Nuremberg, Germany, 2012, pp. 49–51.
28. P. K. Sekhar, E. L. Brosha, R. Mukundan, and F. H. Garzon, *Interface (The Electrochemical Society)*, 2010, 35–40.
29. Z. M. Rittersma, *Sensors and Actuators A: Physical*, 2002, **96**, 196–210.
30. J. Janata, *Principles of Chemical Sensors*, Springer Science + Business Media, New York, 2009.
31. F. Thalmayr and G. Fischerauer, *Sensors and Actuators B: Chemical*, 2010, **144**, 27–36.
32. X. Liu, S. Cheng, H. Liu, S. Hu, D. Zhang, and H. Ning, *Sensors (Basel, Switzerland)*, 2012, **12**, 9635–65.
33. Health and Safety Executive, *The selection and use of flammable gas detectors*, 2004.
34. J. P. Dakin, in *Proc. SPIE 1011, Fiber Optic Sensors III, 173, 1988 Intl Congress on Optical Science and Engineering*, ed. R. T. Kersten, International Society for Optics and Photonics, 1989, pp. 173–182.

35. J. Homola, S. S. Yee, and G. Gauglitz, *Sensors and Actuators B: Chemical*, 1999, **54**, 3–15.
36. G. Eranna, B. C. Joshi, D. P. Runthala, and R. P. Gupta, *Critical Reviews in Solid State and Materials Sciences*, 2004, **29**, 111–188.
37. R. M. Parker, J. C. Gates, M. C. Grossel, and P. G. R. Smith, *Sensors and Actuators B: Chemical*, 2010, **145**, 428–432.
38. L. A. Coldren, S. W. Corzine, and M. L. Masanovic, *Diode Lasers and Photonic Integrated Circuits*, John Wiley & Sons, New Jersey, 2nd Editio., 2012.

2. Planar Integrated Optical Bragg Grating Sensors: Theory

2.1 Introduction

In the previous chapter, the field of gas sensing was outlined, the advantages of optical gas sensors over electrical gas sensors were explained and a short discussion on various types of optical gas sensors was also included. One type of sensor discussed above is the planar integrated optical Bragg grating sensor. This type of sensor was used in the work reported herein and is an example of an integrated optical device. The aim of this chapter is to summarise the theoretical basis and analytical techniques that can be applied towards the understanding and design of planar integrated optical Bragg grating sensors.

2.2 Integrated Optics and Optical Waveguides:

The term “integrated optics” was coined in 1969 by Miller ¹. The term encapsulates all methods and exploratory work towards the use of guided-wave techniques to fabricate improved or novel optical devices ². These optical devices can contain several optical guided-wave functions all combined on one chip, i.e. integration, yet are miniaturized and compact ². Optical guided wave functions combined on a common substrate (chip) form an optical integrated circuit (OIC). OICs can be considered to be analogous to electrical integrated circuits; however the electrical copper tracks/interconnects are replaced with optical waveguides ³. Optical waveguides are different to copper tracks in that light propagates along the length of the waveguide rather than electrical charge. The models used to describe how light propagates along optical waveguides (the most crucial components of OICs), are described below.

2.2.1 Physical Concepts:

Before the theoretical basis of optical integrated circuits is discussed, it is necessary for some essential physical concepts to be defined.

2.2.1.1: Refractive Index

Absolute refractive index, n (a unitless quantity), is defined as the ratio of the phase velocity of light in a vacuum (c , units = ms^{-1}) to the phase velocity of light in a material (v_{mat} , units = ms^{-1}). This is shown in **Eqn. 2.1** below,

$$n = \frac{c}{v_{mat}} = \sqrt{\mu_r \epsilon_r}$$

Eqn.2.1

Where ϵ_r is the relative permittivity and μ_r is the relative permeability of the material. The relative permeability of a material is defined as the ratio of magnetic flux density produced in the material to the magnetic flux density produced in a vacuum when exposed to identical conditions and magnetic field strength ⁴. However, at optical frequencies, for most natural materials $\mu_r = 1$ (unity) ⁵. Therefore, at optical frequencies, refractive index is dependent on the relative permittivity of a material as shown in **Eqn. 2.2** below.

$$n \approx \sqrt{\epsilon_r}$$

Eqn. 2.2

Relative permittivity is defined as the ratio of electrical density produced in a material to the electrical flux density produced in a vacuum, when exposed to identical conditions and electrical field strength ⁶. At optical frequencies, for most materials, the relative permittivity is not unity ($\neq 1$). The electric dipoles (i.e. electrons) are excited by the electric field component of the incident light and also radiate with a specific retardation; this is the physical basis of absolute refractive index ⁵.

Mathematically there is a positive solution and a negative solution to **Eqn. 2.2**. Despite this refractive index is almost exclusively positive. However, through the use of metamaterials, negative refractive indices can be achieved and have allowed for the development of optical cloaking devices ⁷ - the metamaterial ‘bends’ the light around the object so it appears to an observer that the object is not there, and a superlens ⁸ - the metamaterial enabled focussing of light beyond the diffraction limit. Metamaterials are beyond the scope of this work, but for the interested reader there are introductory texts ⁹ and reviews ¹⁰ available, including the paper by Veselago that first described materials that possess negative values of ϵ_r and μ_r ¹¹.

The above description of absolute refractive index is sufficient for colourless transparent materials in the visible region of the electromagnetic (EM) spectrum. It must be noted, that cited values of refractive index in the literature are typically based on measurements at a wavelength of 589.8 nm at a certain temperature, usually 20 °C. However, when dealing with a wider range of optical frequencies and coloured and/or non-transparent materials, it must be noted that refractive index depends on the frequency of the light; this effect is known as dispersion ¹².

2.2.1.2: Dispersion

Dispersion is the term given to the dependence of the phase velocity (the rate at which the phase of a wave propagates) of an EM wave on the frequency of the EM wave, when propagating through a medium. Dispersion also describes the dependence of the group velocity of an EM wave (the rate at which the envelope of the EM wave propagates) on the frequency of the EM wave ¹³.

The most familiar example of dispersion is a prism; the spatial separation of ‘white light’ into components of different wavelengths (different colours) is due to dispersion of the propagating light within the prism.

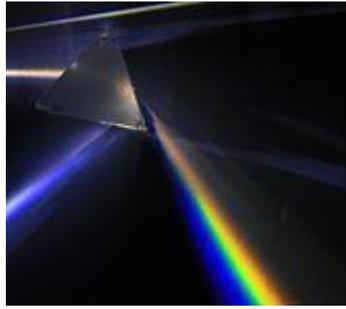


Fig. 2.1: Dispersion of ‘white light’ from a mercury-vapour lamp source, by a flint glass prism. (D-Kuru/Wikimedia Commons, 2009, *Licensed under the Creative Commons Attribution-Share Alike 3.0 Austria License*)

However, a more fundamental effect of dispersion is the degradation of optical signals transmitted over long distances via optical fibre. In this case, group velocity dispersion causes pulses of transmitted light to broaden over time.

There are two types of dispersion, material dispersion and waveguide dispersion. Material dispersion results from the frequency-dependent response of a material to propagating EM waves. Material dispersion gives rise to the desired spatial separation of ‘white light’ into different ‘colours’ in a prism, as described above, but also gives rise to undesired chromatic aberration in lenses. Waveguide dispersion is caused by geometric constraint on the propagating wave imposed by the waveguide; the dispersive phase shifts of an EM wave in a waveguide differ from the dispersive phase shifts an identical EM wave would undergo in a homogeneous material ¹⁴. Both types of dispersion may be present and the combination of material dispersion and waveguide dispersion (not strictly additive) is termed the total dispersion ¹⁵.

There are two types of dispersion, normal and anomalous dispersion. If the refractive index of a material increases, over a certain frequency range, then the material is said to possess ‘normal’ dispersion. If the contrary is true, i.e. the refractive index of a material decrease over a certain frequency range, then the material is said to possess ‘anomalous’ dispersion. However, it must be noted that all natural materials have anomalous dispersion at certain frequencies. The term ‘anomalous’ was coined before the mechanism behind the phenomenon of dispersion had been fully understood and before thorough measurements of the refractive index of natural materials had been made over a wide range of frequencies ¹².

2.2.2 Planar Slab Optical Waveguides:

An optical waveguide can be defined as a spatially inhomogeneous structure that defines the region in which light can propagate in a direction parallel to its axis ¹⁵. The waveguides utilised in the work presented herein were designed to transmit near infrared EM waves in the wavelength region known as the telecoms C band (1530-1560 nm).

The waveguides typically utilised in integrated optics are dielectric waveguides. These waveguides are usually in the form of a strip of material with a refractive index higher than that of the surrounding substrate material; the refractive index difference is on the order of 0.001 – 0.01 ².

The spatial restriction of the propagating light within a waveguide results in the light being incident to the boundary surfaces of the waveguide. When a propagating ray of light is incident to a boundary surface one of two phenomena can occur; reflection or refraction. If a ray of light is travelling within a layer of refractive index n_2 , and is incident to the interface with a layer of refractive index n_1 and where $n_2 > n_1$, then the ray of light can either be refracted within the n_1 layer or reflected from the interface ¹⁶. This depends on the angle θ , between the normal to the interface and the ray of light. The relation between the angles of reflection and refraction is stated by Snell's Law.

$$n_1 \sin \theta_1 = n_2 \sin \theta_2$$

Eqn. 2.3

Where n_1 is the refractive index of one of the layers, n_2 is the refractive index of the other layer, θ_1 is the angle of incidence and θ_2 is the angle of refraction. This concept is further explained in **Fig. 2.2** below.

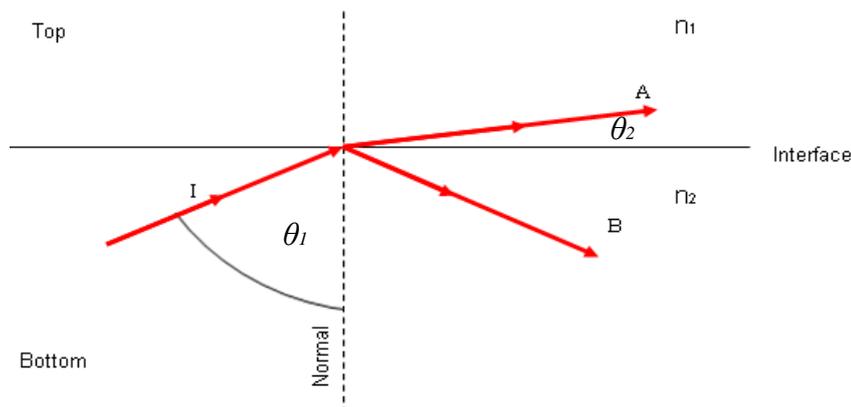


Fig. 2.2: Behaviour of a ray of light travelling in a layer of refractive index = n_2 , incident to the interface with a layer of refractive index = n_1 . If θ_1 is less than the critical angle of the system, θ_c , given by $\theta_c = \sin^{-1}(n_2/n_1)$ then the ray of light is refracted in the lower index layer as shown by A. However, if $\theta_1 > \theta_c$, then the incident ray of light is entirely reflected within the higher index layer as shown by B. θ_2 is the angle of refraction and $\theta_2 > \theta_1$.

If θ_1 , for the incident ray light (I), is less than the critical angle of the system, θ_c defined by **Eqn 2.4** below, then the ray of light is refracted in the n_1 index layer as shown by ray (A) in **Fig. 2.2** above. However, if θ_1 is greater than θ_c then the incident ray of light is entirely reflected within the higher index layer as shown by ray (B).

$$\theta_c = \sin^{-1}(n_2/n_1)$$

Eqn. 2.4

When Snell's Law is satisfied and a ray of light is reflected at the interface then the angle of reflection is equivalent to the angle of incidence relative to the normal.

Extending this to a two-dimensional system, where a layer of refractive index n_f is sandwiched between a top and a bottom layer of lower refractive indices n_t and n_b respectively and where $n_f > n_t$ and $n_f > n_b$, if $\theta > \theta_c$ at both interfaces with the top and bottom layers then total internal reflection (TIR) occurs. The light is therefore trapped within the layer of n_f ; this is an example of a guided mode of light within the structure². In this model, guided modes of light within the layer are represented by plane waves propagating in a 'zigzag' path through the layer as shown in **Fig. 2.3** below.

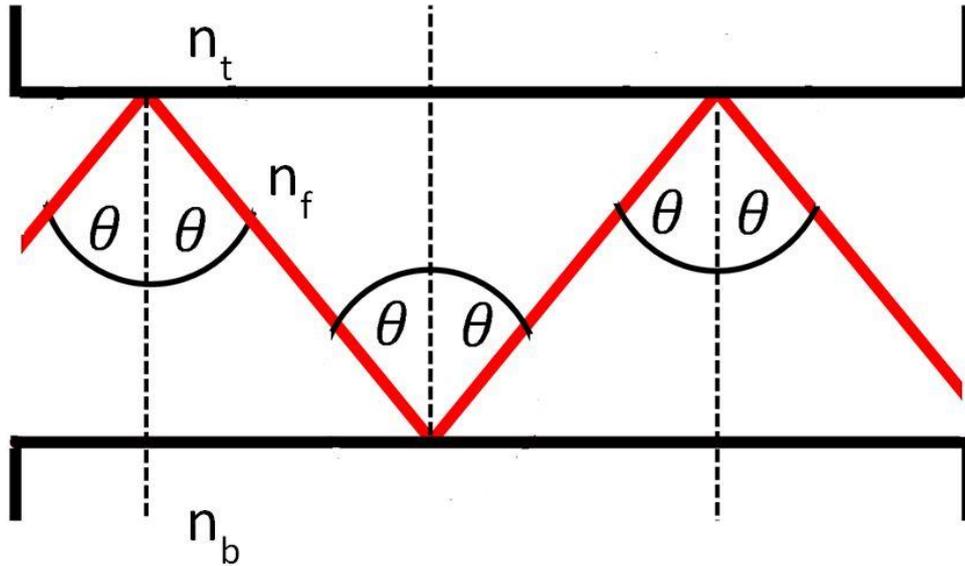


Fig. 2.3: Total internal reflection (TIR) of a ray of light within a layer which possesses a refractive index n_f between two layers: the top layer possesses a refractive index n_t and the bottom layer possesses a refractive index of n_b where $n_f > n_t$ and $n_f > n_b$. At each interface between two layers, the hashed lines represent the normal of the interface at each site of incidence. In each case the angle of incidence = angle of reflection = θ . In this case $\theta > \theta_c$ and thus reflection of the light back into the n_f layer occurs at each site of incidence at an interface resulting in the ‘zigzag’ propagation path of the plane waves of light.

This ‘zigzag’ path can be deconstructed into two wave vectors A_1 and B_1 , which can be further divided into the individual vertical and horizontal vector components¹⁷ as shown in **Fig. 2.4** below.

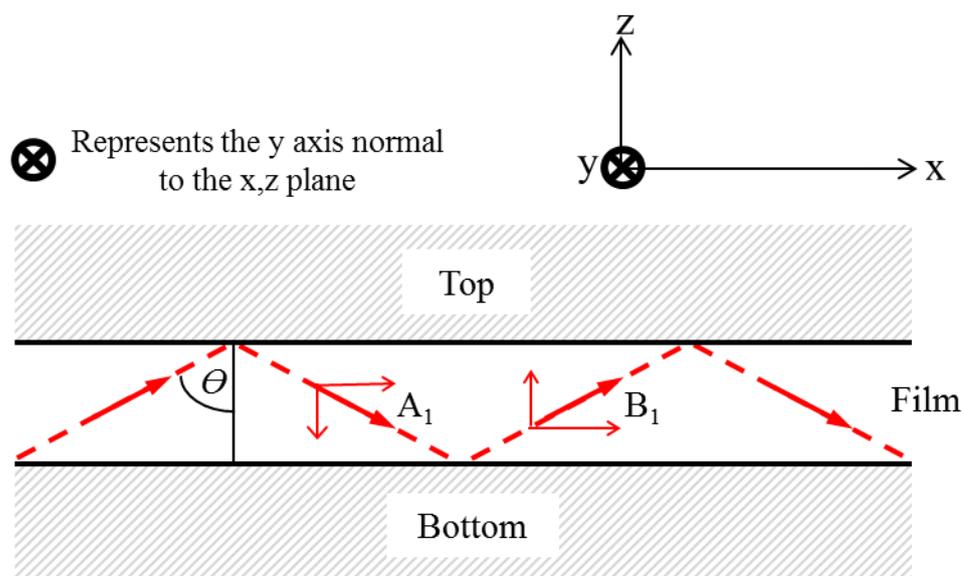


Fig. 2.4: The two wave vectors A_1 and B_1 (red arrows) that represent the ‘zigzag’ motion of the light in the waveguiding film layer. The individual components of the wave vectors are shown by the vertical and horizontal thin red arrows.

The horizontal components of the vectors A_1 and B_1 are equal length; the guided light waves propagate with a constant speed in a direction parallel to the guiding layer. The vertical components of vectors A_1 and B_1 represent the upwards or downwards wave motion respectively. Upon superposition of the upwards and downward waves, a standing wave pattern across the thickness of the waveguiding layer is formed. If θ is changed, the directions of vectors A_1 and B_1 are altered and thus the magnitudes of the horizontal and vertical components also change. Therefore, both the wave velocity parallel to the guiding layer, and the standing wave pattern, change¹⁷.

2.2.3 Maxwell’s Equations

Up to this point in this chapter, the propagation of light within a waveguide has been dealt with classically. However, a photon within a waveguide is analogous to the well-known problem in quantum mechanics of a particle in a box. Just like the discrete wavefunctions (eigenmodes) that are supported within the box, there are a discrete series of wavefunction solutions that exist for the photon in the waveguide. In the case of the particle in a box, the wavefunctions give rise to discrete energy

levels within the box. For the photon in a waveguide, the wavefunctions give rise to a series of discrete effective refractive indices that are supported by the waveguide.

If the sides of the box are finite, then it is possible that the wavefunction of the particle may not be fully confined within the box; the particle may exist outside the box. The probability of finding the particle, at a distance outside the walls of the box, is modelled by an exponential decay function. The same applies to the photon in a waveguide. If the boundaries of the waveguide are finite, then it is also possible that wavefunction of the photon may extend beyond the boundaries of the waveguide. There is a probability of finding the photon outside of the dimensions of the waveguide; this is also modelled by an exponential decay function. If the waveguide is weakly-guiding, then the exponential decay function, describing the probability of finding the photon outside of the waveguide, is referred to as the evanescent wave of the optical wavefunction mode. In addition, if the waveguide is treated as a two dimensional finite potential energy well, then it is apparent that there are different polarisation states of the wavefunctions that are supported. These different polarisations give rise to a pair of discrete modes that are orthogonal.

The mathematical description of these optical modes, in a weakly-guiding waveguide, is given by solving the corresponding Helmholtz equations of the waveguide. The solutions of the Helmholtz equations give rise to the pair of discrete orthogonal modes, which can be labelled as the transverse electric mode and the transverse magnetic mode. It is important to note that these orthogonal polarisation modes in an asymmetric waveguide are exhibited as the property of birefringence; the waveguides utilised in this work were asymmetric.

Firstly, it must be stated that the waveguides used within this work are non-conducting, non-magnetic and have a time-dependence of $e^{i\omega t}$ (where ω is the angular frequency). With these conditions stated, Maxwell's equations, which describe the evolution of the electric field component, $E(t)$ and the magnetic field component, $H(t)$, of the electromagnetic wave over time, t , in the waveguides can be written as follows:

$$\nabla \times E = -i\mu_0\omega H$$

Eqn.2.5

$$\nabla \times H = i\omega\varepsilon_0 E$$

Eqn.2.6

$$\nabla \cdot \varepsilon_0 E = 0$$

Eqn.2.7

$$\nabla \cdot H = 0$$

Eqn.2.8

Where ω is the angular frequency, μ_0 is the permeability of free space and ε_0 is the permittivity of free space.

As an aside, Maxwell's equations describe electromagnetic field theory and are arguably some of the most influential equations in science and technology¹⁸. The four equations, in the order as listed above, are: Faraday's Law, Ampere-Maxwell Law, Gauss' Law for electric fields and Gauss' Law for magnetic fields¹⁸. Derivation of Maxwell's equations are beyond the scope of this work, but a thorough description is given by Fleisch¹⁸.

With application of the mathematical method known as the 'separation of variables', these four partial differential equations can be written as two Helmholtz equations. This is achieved by separating the variables E and H . By taking the curl of **Eqn.2.5**, the Helmholtz equation for the electric field is given by:

$$\nabla_{\Delta}(\nabla_{\Delta} \cdot E) = -i\mu_0\omega\nabla_{\Delta} H$$

Eqn.2.9

By use of a vector identity and **Eqn.2.6** above, this equation (**Eqn.2.9**) can be simplified further to afford,

$$\nabla(\nabla \cdot E) - \nabla^2 E = \varepsilon_0 \mu_0 \omega^2 E$$

Eqn.2.10

Then, if **Eqn.2.7** is rewritten as follows:

$$\nabla(\varepsilon_0 E) = E \cdot (\nabla \varepsilon_0) + \varepsilon_0 \nabla \cdot E = 0$$

then it follows that,

$$\nabla \cdot E = \frac{1}{\varepsilon} E \cdot (\nabla \varepsilon_0)$$

Eqn.2.11

By combining **Eqn.2.11** with **Eqn.2.10** the full vectorial Helmholtz equation for the electric field in the waveguide is afforded.

$$\nabla^2 E + \nabla \left(\frac{1}{\varepsilon_0} \nabla(\varepsilon_0) \cdot E \right) + \varepsilon_0 \mu_0 \omega^2 E = 0$$

Eqn.2.12

In a similar manner the full vectorial Helmholtz equation for the magnetic field can be obtained and is given by:

$$\nabla^2 H + \frac{1}{\varepsilon} \nabla \varepsilon_A (\nabla_{AH}) + \varepsilon_0 \mu_0 \omega^2 \frac{\partial^2 H}{\partial t^2} = 0$$

Eqn.2.13

These full vectorial Helmholtz equations are utilised in numerical modelling software when modelling the optical modes in a waveguide. Numerical modelling software has been used within in this work and is discussed in section **2.2.6.1** below. However, for weakly guiding waveguides, such as the waveguides utilised in this work, these full vectorial Helmholtz equations can be further simplified.

2.2.3.1: Weakly guiding waveguides:

A weakly guiding waveguide is defined as a waveguide which has a core that is of a refractive index that is only $\sim 0.3\%$ greater than the refractive indices of the surrounding cladding layers. For a weakly guiding waveguide the refractive index contrast between the core and cladding layer is small.

If a waveguide is weakly guiding it then leads to the optical mode not being fully confined to the core. As described above, the evanescent waves of the propagating optical mode which extend into the cladding layer. In addition it can be assumed, for a weakly guiding waveguide that $\nabla_{\epsilon} \approx 0$, therefore the Helmholtz equations,

Eqn.2.12 and **Eqn.2.13** can be reduced to,

$$\nabla^2 E + n^2 k^2 E = 0$$

Eqn.2.14

for the electric field and,

$$\nabla^2 H + n^2 k^2 H = 0$$

Eqn.2.15

for the magnetic field, where n is the refractive index and k is known as the wavevector. For an electromagnetic wave, the wavevector is in the direction of the propagating electromagnetic wave and has a magnitude equal to the wave number, which is given by,

$$k = \frac{2\pi}{\lambda}$$

Eqn.2.16

However, the full solutions for the transverse electric mode and the transverse magnetic mode are achieved through further use of Maxwell's equations. From **Eqn.2.5** and **Eqn.2.6** the following six equations can be derived:

$$i\beta E_y = -\omega\mu_0 H_x$$

Eqn.2.17

$$\frac{\partial E_y}{\partial x} = i\omega\mu_0 H_z$$

Eqn.2.18

$$-i\beta H_x - \frac{\partial H_z}{\partial x} = i\omega\epsilon_0 \epsilon E_y$$

Eqn.2.19

$$i\beta H_y = i\omega\epsilon_0 \epsilon E_x$$

Eqn.2.20

$$\frac{\partial H_y}{\partial x} = i\omega\epsilon_0 \epsilon E_z$$

Eqn.2.21

$$-i\beta E_x - \frac{\partial E_z}{\partial x} = i\omega\mu_0 H_y$$

Eqn.2.22

Where x , y and z are the components of the vector field in the x , y and z dimensions respectively, and are relative to a slab waveguide with light propagating along the x -axis. The axes are as defined in **Fig.2.4** above. β is the propagation constant of the propagating mode that is supported within the waveguide and is defined mathematically in **Eqn.2.23** below.

Upon visual inspection of the six equations above, it is clear that **Eqn.2.17** – **Eqn.2.19** (inclusive) are the subject of the variables E_y , H_x and H_z . On the other hand, it can be stated that **Eqn.2.20** – **Eqn.2.22** (inclusive) are the subject of the variables H_y , E_x and E_z . Therefore, it can be stated that there are two independent sets of solutions to Maxwell's equations for a weakly guiding waveguide. The first set, **Eqn.2.17** – **Eqn.2.19** (inclusive), correspond to non-vanishing values of E_y , H_x and H_z . The solutions from this set of equations refer to the Transverse Electric (TE)

modes; the electric vector field component (E_y) is in the x-y plane of the waveguide. In contrast, the second set of equations, **Eqn.2.20 – Eqn.2.22** (inclusive), correspond to non-vanishing values of H_y , E_x and E_z . The solutions from this set of equations refer to the Transverse Magnetic (TM) modes; the magnetic vector field component (H_y) is in the x-y plane of the waveguide.

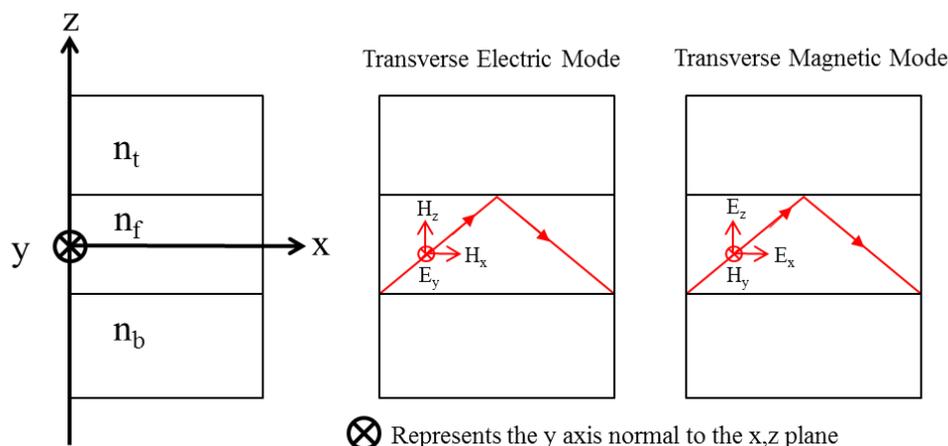


Fig.2.5: The EM field components that comprise the Transverse Electric (TE) mode (centre diagram) and the EM field components that comprise the Transverse Magnetic (TM) mode (right-hand diagram).

For TE modes, the electric field oscillates in the x-y plane and for TM modes the magnetic field oscillates in the x-y plane, as shown in **Fig.2.5** above. For these equations to hold true, the TE and TM modes, must be continuous and smooth at the boundary between the core and the cladding.

As stated above, the waveguides used in this work are asymmetric waveguides due to the absence of a top cladding layer. For a well-guided optical mode in an asymmetric waveguide, the electric field is mostly confined to the core, but the evanescent tail of the electric field decays exponentially into the region above the core layer.

The associated vector field components of the TE and TM modes in the z direction can be described as propagating like $e^{-j\beta z}$, with a propagation constant (β) related to the angle swept out between the incident ray and the normal to the boundary surface, θ (the 'zigzag' angle) by,

$$\beta = kn_f \sin\theta$$

Eqn. 2.23

where,

$$k = 2\pi/\lambda = \omega/c$$

Eqn 2.24

and where λ is the free-space wavelength of the EM wave, ω is the angular frequency of the light and c is the velocity of light in a vacuum. Combining the critical angle of the system and **Eqn. 2.23** gives bounds for β which are represented by,

$$kn_b < \beta < kn_f$$

Eqn 2.25

The value of β varies with ω and for each plane layer waveguide system this relationship can be shown diagrammatically on a ω - β plot.

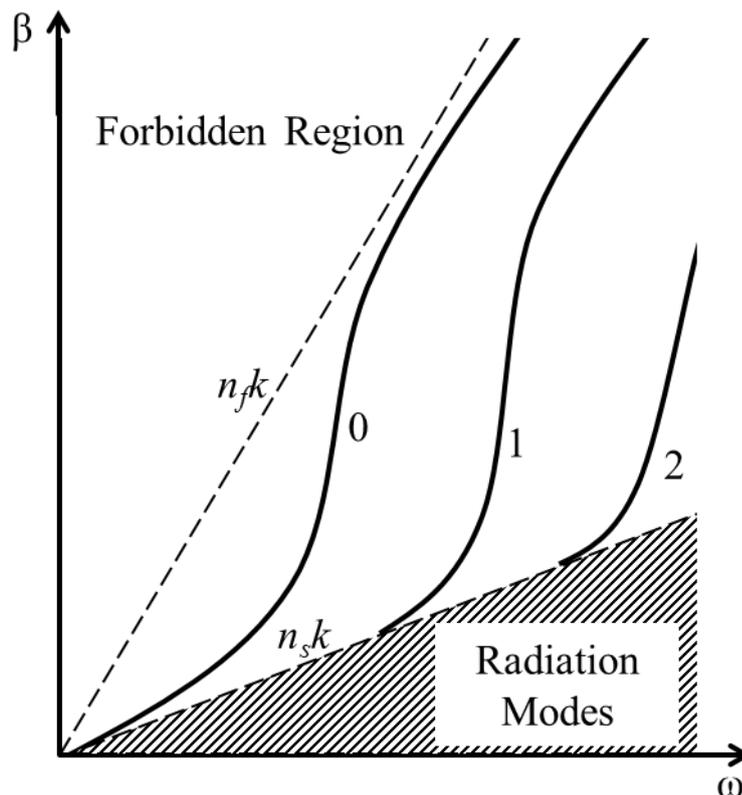


Fig. 2.6: An example of a ω - β diagram for a dielectric plane waveguide. In this example there are three discrete guided modes labelled 0, 1 & 2 respectively. Redrawn from the paper of Kogelnik ².

As is evident, the ω - β plot indicates how β varies with frequency ω (or relative film thickness) and also shows the spectrum of discrete guided modes possible for the particular system. In addition, a continuous spectrum of radiation modes is also shown. The upper bound $n_f k$ is approached at glancing angles of incidence (θ) and the lower bound $n_s k$ is reached when $\theta = \theta_c$; at the critical angle ².

2.2.4: Effective Index

Propagation of an optical signal in dispersive media is usually described by two quantities, the group velocity and the phase velocity. Corresponding to these velocities are the group index and phase (refractive) index respectively. For a plane wave in a dielectric waveguide, the group velocity, v_g is defined as,

$$v_g = \frac{d\omega}{d\beta} = \frac{c}{M}$$

Eqn.2.26

where ω and β are as defined previously and M is the group index of the guide index. For the phase velocity, v_p , there is a similar relationship,

$$v_p = \frac{\omega}{\beta} = \frac{c}{(n_f \sin\theta)} = \frac{c}{N}$$

Eqn.2.27

where again the terms of the equation are as defined above and N is the effective guide index. When discussing the dielectric waveguides used in the work presented herein, the effective guide index N is an important concept. It can be further defined as,

$$N = \beta/k = n_f \sin\theta$$

Eqn. 2.28

The values of the effective guide index, N , are bound by n_b and n_f ,

$$n_b < N < n_f$$

Eqn. 2.29

As mentioned above, the effective guide index is an important concept for the work presented herein, thus it is explained in further detail later on in this chapter and throughout this thesis.

2.2.5: Effective Guide Thickness

Due to the penetration of the evanescent waves into the top and bottom layers, the waveguide appears to have a thickness which is greater than the physical thickness of the waveguide. This is known as the effective guide thickness. The effective guide thickness is a crucial parameter to consider when designing optical planar integrated Bragg grating gas sensors. By maximising the effective guide thickness, a larger extent of the evanescent wave interacts with the gas molecules or active sensing layer, thus increasing the sensitivity. The following section outlines the theory, using the zigzag ray model approach, required to calculate the effective guide thickness.

2.2.5.1: Failure of the Simple Zigzag Ray Model

The zigzag-ray model is a useful tool to understand guided-wave structures. From this model, many characteristics of a propagating optical mode in a guided-wave structure, such as the propagation constant β , the critical angle θ_c and the phase velocity, can be deduced. However, as stated by both Kogelnik and Burke, a more thorough model to describe the propagation of light in a planar waveguide is required when considering the exchange or flow of energy². As defined above, the zigzag-ray model implies that energy is propagated in the guide (x-axis) direction with a group velocity, \tilde{v}_g given by,

$$\tilde{v}_g = \frac{c}{m_f} \sin\theta = \frac{cN}{(m_f n_f)}$$

Eqn.2.30

Where m_f is the group index of the film layer and the other terms have been previously defined in this chapter. This results in the concept of slower and slower group velocities for smaller values of θ (i.e. steeper zigzags). At the critical angle, θ_c , the group velocity would be given by

$$\tilde{v}_{g\theta c} = \frac{cn_f}{m_f n_f}$$

Eqn.2.31

On the other hand, for modes near the critical angle, it is known that most of the energy is in the bottom layer and the modes have expected group velocities of c/m_b , where m_b is the group index of the bottom layer. This is an example of the failure of the simple zigzag ray model to predict the correct group velocities, which can be routinely calculated from the dispersion relation of the waveguide¹⁹. This failure results from the over-simplified treatment of reflection of light from the waveguide boundary surfaces in the zigzag-ray model. To overcome these failures, the time delay and ray shifts, that occur upon total reflection of light from the waveguide boundary surfaces, need to be taken into account¹⁹.

To enable determination of the ray shift and the time delay that occur upon total reflection, an examination of what happens at the film boundary needs to be performed as shown in **Fig.2.7** below.

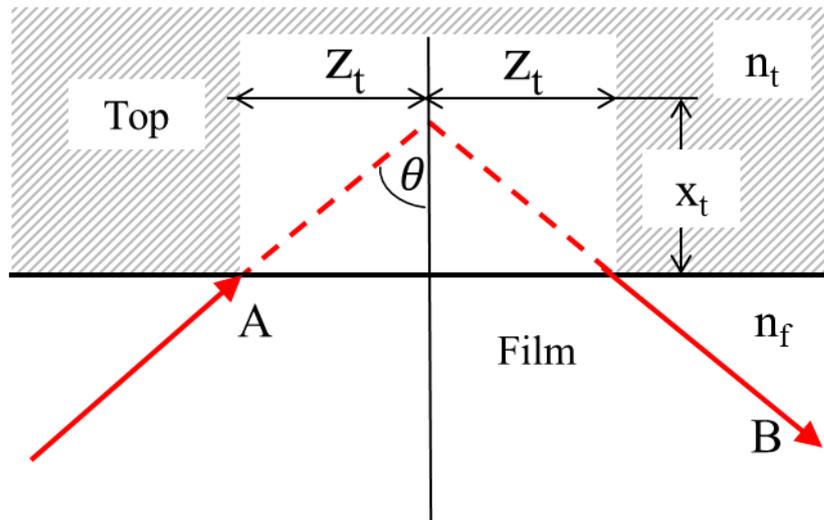


Fig.2.7: Reflection of a ray at a film boundary surface. The reflected ray is shifted by $2z_t$ and penetrates into the top layer to a depth of x_t .

As shown in **Fig.2.7** above, there is an plane wave, A of field $Ae^{j(\omega t - \beta x)}$, that is incident to the film-top boundary interface and a reflected plane wave, B of field $Be^{j(\omega t - \beta x)}$ at the film-top boundary interface, where j is the imaginary unit, t is time and the other terms are as defined above. The complex amplitudes of both plane waves are related by what is known as the reflection law,

$$B = A \cdot e^{2j\Phi}$$

Eqn.2.32

where Φ is the phase shift. Formulas for Φ are well known and are given in the literature¹⁹. However, it is important to note that $\Phi(\omega, \beta)$, i.e. Φ is a function of the two independent variables ω and β . This is significant when time-like and space-like wave packets are considered, instead of the plane monochromatic waves ('rays') in the zigzag-ray model. Therefore, a ray now represents the axis of a space-like wave packet e.g. a beam with a Gaussian cross section.

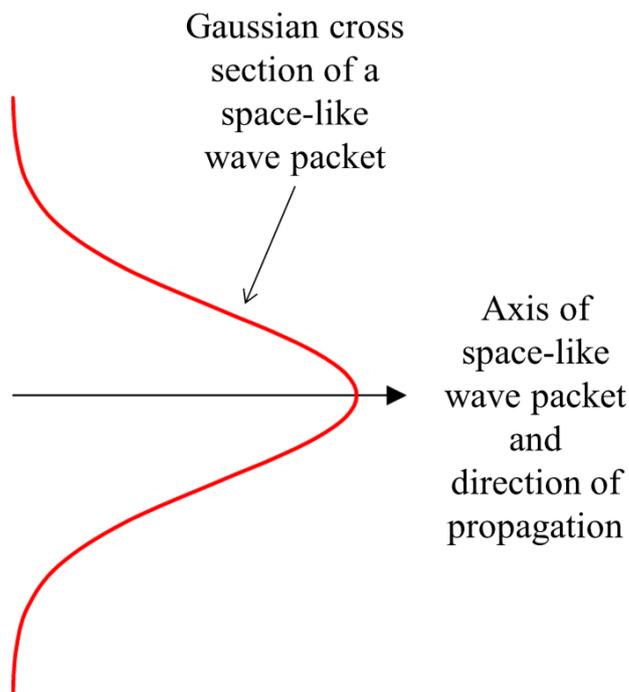


Fig.2.8: A space-like wave packet with a Gaussian cross section about the ray axis.

As shown in **Fig.2.7** above the reflected ray B , is shifted relative to the incident ray A . This shift is known as the Goos-Hänchen effect. Pillon *et. al.* give a more complete definition: a Goos-Hänchen shift as a small displacement of a light beam that occurs during total reflection from the interface separating two infinite half-spaces, where the refractive index of one of the half-spaces is higher than the other²⁰. By defining the lateral ray shift for the example given in **Fig.2.7** above as $2z_t$, Kogelnik and Weber demonstrated that the shift of the reflected wave packet at the top interface is related to the derivative of the phase shift, ϕ_t for the top interface¹⁹, as shown in **Eqn. 2.14** below,

$$z_t = \frac{d\phi_t}{d\beta}$$

Eqn.2.33

Similarly, for a time-like wave packets (e.g. a pulse), then it is expected that the delay is associated with a frequency-dependent phase shift and thus if the pulse delay is defined (for the given example in **Fig.2.7** above) as $2\tau_t$ then Kogelnik and Weber demonstrated that,

$$\tau_t = -\frac{d\phi}{d\omega}$$

Eqn.2.34

Taking these wave-packet considerations into account, a new zigzag-ray model that includes the lateral ray-shifts and time delays at both film boundaries can be devised as shown in **Fig. 2.9** below.

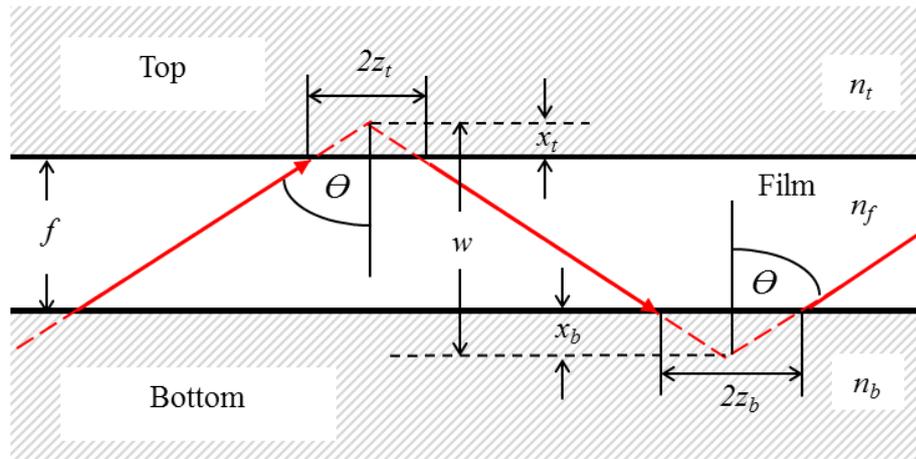


Fig. 2.9: Ray picture for the ‘zigzag’ wave motion of light in a planar slab waveguide where f is the physical thickness of the planar slab waveguide, $2z_t$ and $2z_b$ are the Goos-Hänchen ray shifts for the top and bottom layers respectively, x_t and x_b are the penetration depths for the top and bottom layers respectively, θ is the angle of incidence, n_t , n_f and n_b are the refractive indices of the top, film and bottom layers respectively and w is the effective guide thickness. Goos-Hänchen shifts are shown by the regions where the hashed ray lines (red) penetrate into the top and bottom layers.

The incident ray undergoes a Goos-Hänchen shift of $2z_t$ at the film-top layer interface and penetrates to a depth of x_t , whilst the ray undergoes a Goos-Hänchen shift of $2z_b$ at the film-bottom layer interface and penetrates to a depth of x_b . Therefore, the lateral shifts for the TE mode at both interfaces can be defined as

$$z_t = \frac{d\phi_t}{d\beta} = \frac{1}{\gamma_t} \tan\theta$$

$$z_b = \frac{d\phi_b}{d\beta} = \frac{1}{\gamma_b} \tan\theta$$

Eqn. 2.35

Where γ_t and γ_b are the decays constants for both the top and bottom layers respectively. These decay constants are associated with the Goos-Hänchen shifts by the evanescent waves that were introduced previous in this chapter. The evanescent waves, and the energy carried by these waves are closely related to the Goos-Hänchen shifts¹⁹. These evanescent waves are described in more detail above in section 2.2.3.

The expressions for the decay constants for the bottom and top layers, γ_b & γ_t respectively are,

$$\gamma_b^2 = k^2(N^2 - n_b^2)$$

$$\gamma_t^2 = k^2(N^2 - n_t^2)$$

Eqn. 2.36

For a TE mode the penetration depths of the ray into the top and bottom layers, x_t and x_b respectively can be calculated² by

$$x_t = \frac{1}{\gamma_t}$$

$$x_b = \frac{1}{\gamma_b}$$

Eqn.2.37

For the TM modes there are similar expressions, except for a reduction factor, q which is given by

$$q = \left(\frac{N}{n_b}\right)^2 + \left(\frac{N}{n_f}\right)^2 - 1$$

Eqn.2.38

The top and bottom ray shifts for the TM mode are given by,

$$z_t = \frac{1}{\gamma_t q} \tan \theta$$

&

$$z_b = \frac{1}{\gamma_b q} \tan \theta$$

Eqn.2.39

respectively.

The related ray penetration values are given by,

$$x_t = \frac{1}{\gamma_t q}$$

&

$$x_b = \frac{1}{\gamma_b q}$$

Eqn.2.40

Finally, for completeness, the time delays for the TM modes in the top layer and bottom layer, τ_t & τ_b respectively, are given by,

$$\tau_t = \frac{\beta}{\omega\gamma_t q} \tan \theta = \frac{\beta}{\omega} z_t = \frac{N}{c} z_t$$

&

$$\tau_b = \frac{\beta}{\omega\gamma_b q} \tan \theta = \frac{\beta}{\omega} z_b = \frac{N}{c} z_b$$

Eqn.2.41

Due to the ray penetration into the top and bottom layers, the waveguide appears to have a thickness which is greater than the actual waveguide thickness. This is known as the effective guide thickness, w and is given by,

$$w = f + \frac{1}{\gamma_t} + \frac{1}{\gamma_b}$$

Eqn.2.42

where f is the physical thickness of the waveguide and the decay constants are defined in Eqn.. A normalised guide thickness, W , can be calculated using the following equation,

$$W = kw \sqrt{(n_f^2 - n_b^2)}$$

Eqn.2.43

where all the terms are as defined above.

2.2.6 Strip Waveguides

Planar slab waveguides, of the type described above, provide no confinement of the light in the plane of the guiding film layer. The waveguides utilised in this work do provide confinement of the light in the plane of the guiding film layer. These types of waveguides are known as strip waveguides. An extension to the waveguide model given above is therefore needed to describe how light propagates in these strip waveguides. There are three main types of strip waveguides; buried, ridge and diffuse (see **Fig.2.10** below). The waveguides used in the work presented herein are diffuse waveguides.

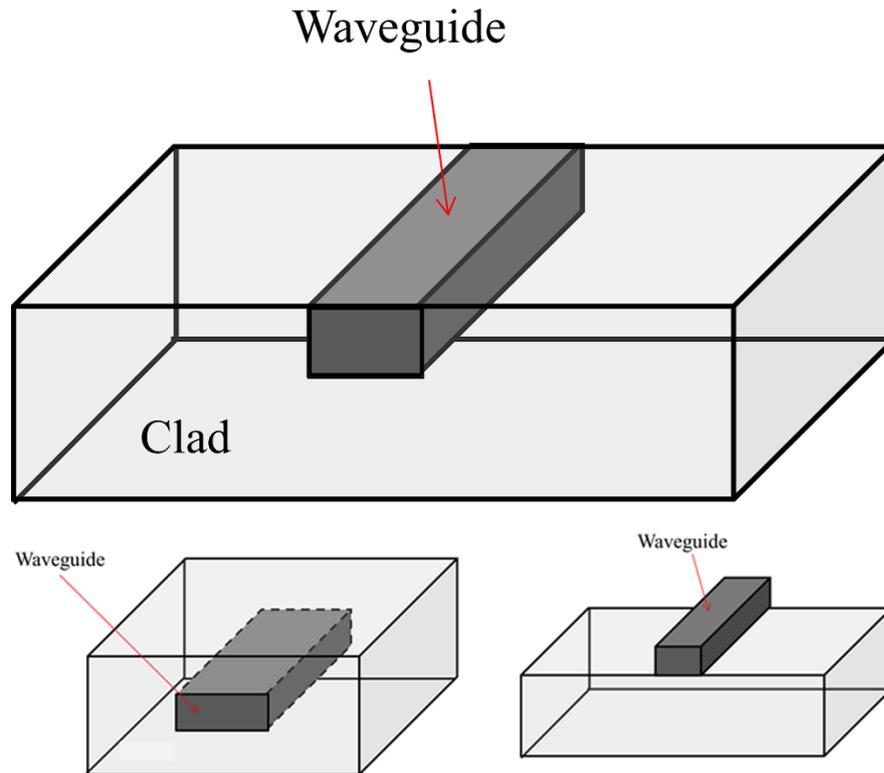


Fig.2.10: A diffuse waveguide (top), a buried waveguide (bottom left) and a ridge waveguide (bottom right).

No exact analytic solutions for optical modes in strip waveguides exist. However, numerical approximate solutions have been given for embedded rectangular dielectric waveguides (in an uniform surround)^{21,22}. In addition, Marcatili *et. al.* has also given approximate solutions for many types of strip waveguides^{23,24}.

The effective index method is another technique for analysing two-dimensional optical waveguide structures²⁵. The assumption of the effective index method is that the refractive index of the waveguide can be split into separate x and y dependencies. Under this assumption the simple planar optical waveguide analysis highlighted above is performed for the x and y dimensions separately. First the waveguide structure is split into a series of one-dimensional planar waveguide structures. Then the effective indices in the x dimension are calculated, as if the system was an individual planar waveguide, as illustrated for a buried waveguide structure in **Fig.2.11** below. Once the effective indices are calculated in the x-dimension, then these effective indices are used to build another one-dimensional structure in the y-dimension from which an overall effective index approximation can be made.

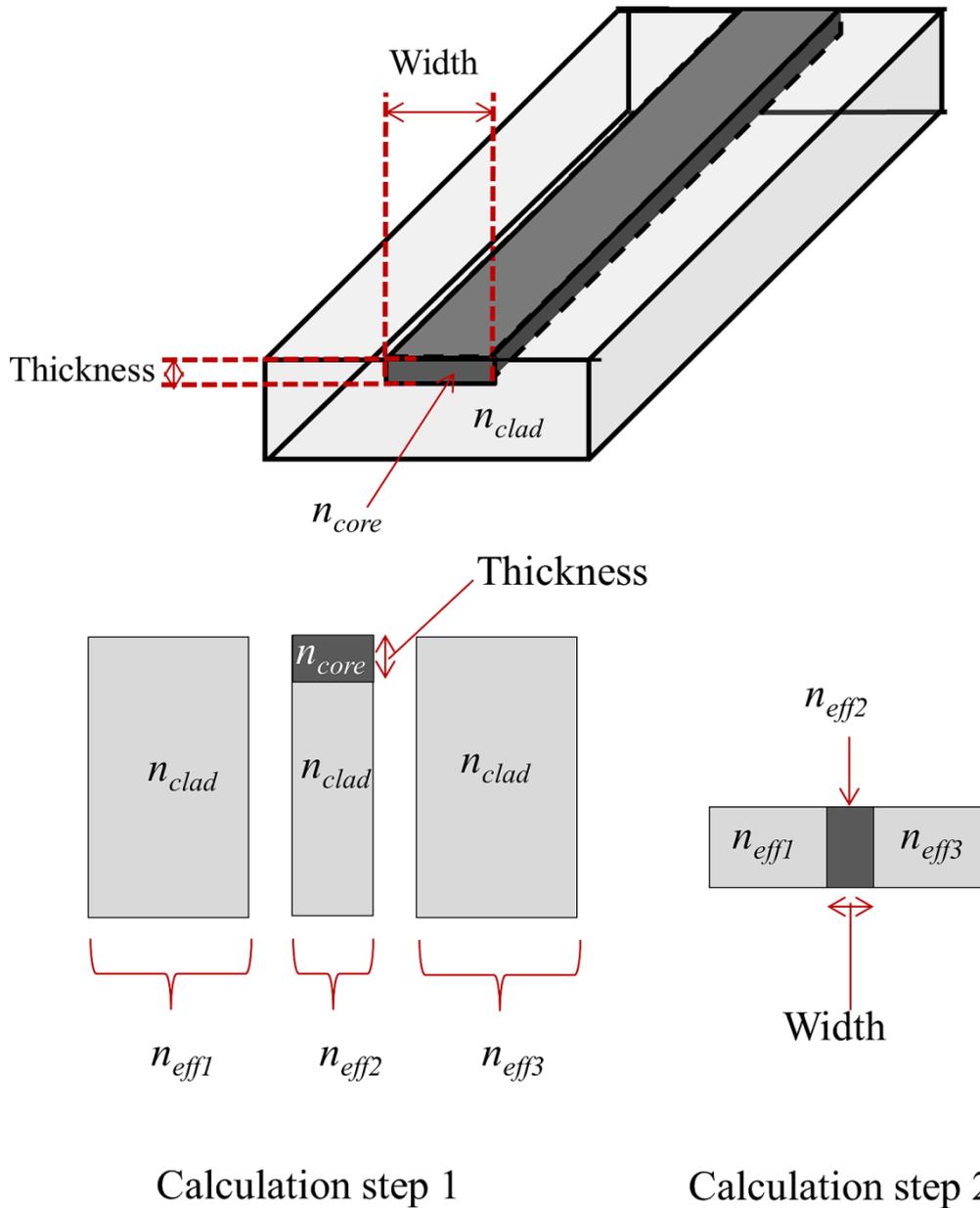


Fig.2.11: The calculation method utilised in the Effective Index Method.

2.2.6.1 Numerical Mode Solving

The effective index method and the other approximations, are idealised solutions that are only accurate for very simple waveguide geometries. Real world, functional waveguides are typically more complicated geometries; for these waveguides the full vectorial Helmholtz equations need to be solved to obtain modal solutions. In these cases, where there are no simple analytical solutions, numerical solutions are sought. Indeed, numerical mode solving tools have become common place in academia and industry due to the abundance of inexpensive computing power. An additional reason is the exponential growth in the sophistication of modern computers; most

mode solving algorithms can now be executed on a desktop computer. This means that the traditional issue of the dependence between the accuracy of a numerical mode solution and the required computational processing (speed) and memory is no longer a factor for major consideration.

Numerical calculations are used in the three main areas of photonic waveguide modelling; beam propagation, network simulation and mode solving. In the work presented herein, waveguide modelling was performed using numerical mode solving techniques to calculate the effective indices of exposed channel waveguides.

The majority of numerical mode-solving techniques are performed by subdivision of the space into smaller section; this allows for easier calculation, rather than solving the whole problem in one go. An extensive list of mode solving techniques that utilise the subdivision method for solving the full vectorial Helmholtz equations are given by Chari & Salon²⁶ and Hammond & Sykulski²⁷. There are several numerical methods that are used to find the eigenmodal solutions of waveguides, including the Beam Propagation Method (BPM), Finite Difference Method (FDM), Finite Element Method (FEM) and the Film Mode Matching (FMM) technique. The optical modes in this work were solved using a commercial mode solving software package called Fimmwave; this software is based on the FMM technique.

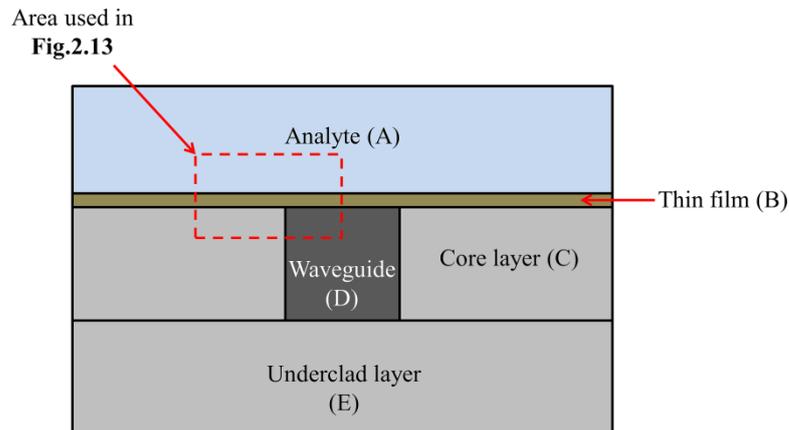


Fig.2.12: Cross-section schematic of the type of exposed waveguide sensor used within this work. The thin film (B) represents the type of thin films used in this work for sensing and is an arbitrary thickness. (D) represents the waveguide. The highlighted box (hashed red line) represents the area used in **Fig.2.13** below for the diagrammatic representations of the different numerical mode solving techniques.

The beam propagation method (BPM) was developed by Feit and Fleck²⁸. In this scheme the propagating waves are modelled, in the spectral regime, as a spectrum of plane waves²⁹. Any inhomogeneity of the media is taken into account by applying a phase correction (the spatial regime) at the end of each propagation step and by taking the Fourier transform, the spatial and spectral regimes are linked²⁹. However, this technique is insufficient when dealing with weakly-guiding waveguides; only scalar wave equations can be solved using this approach when dealing with low index contrasts²⁹.

The finite difference method (FDM) is a powerful technique which has been extensively used for modelling propagating optical modes in longitudinally invariant waveguides, i.e. the refractive index does not vary along the length of the waveguides³⁰. In this method, the partial derivatives of the Helmholtz equations are replaced with what are known as finite difference equations. To achieve this, a cross section of the waveguide structure is taken, as shown in **Fig.2.13** below, and a grid structure of nodes is set-up within the cross section. Each cell within the grid, that contains a node, is a constant refractive index and changes in refractive index are only permitted at the boundaries of each cell³⁰. The partial differential equations at each node are then approximated by taking the finite differences between a node and the four closest neighbouring nodes by using either scalar, semi-vectorial or full vectorial formalisms²⁵. This grid network nodal based approach means that FDM is comparatively easier to program and calculate compared to other numerical modelling techniques. However, this approach is also a disadvantage; the rigid grid network does not allow for adaptive subdivision of the waveguide space²⁵.

The finite element method (FEM) has emerged as a powerful tool for calculating optical mode propagation in waveguides due to its applicability to waveguides with arbitrary refractive index profiles, arbitrarily shaped waveguides and to waveguides which are composed of anisotropic or non-linear materials³¹. In this technique the cross-sectional domain of the waveguide is separated into 'elements' as shown in **Fig.2.13** below. Within each element there is a node and the elements can take on any shape, however the elements are usually triangular²⁵. The field in each element is approximated and then the total field solution for the waveguide is evaluated by a linear summation of the fields in each element²⁵. However, a major limitation of this technique is the inability to accurately calculate optical modes which are propagating

in a manner close to the cut-off of the elemental grid. This can be overcome by extending elements beyond the waveguide and into the surrounding material, however, the number of elements required for this increases rapidly, thus becomes increasingly more computationally taxing.

As mentioned above, propagating optical modes were calculated through use of commercial mode solving software. The software used was *Fimmwave*, and it is based on an improved formulation of the film mode matching (FMM) method which was derived by Sudbø³². It has been demonstrated by Sudbø that the FMM method can yield more accurate optical mode modelling results than a full FEM calculation and also have requirements on computational power and programming that are an order of magnitude smaller than for the FEM technique³².

In the FMM method, the waveguide area of interest is divided into strips which are created from areas of the waveguide that have equivalent and uniform refractive indices. The waveguide, which is considered to be comprised of a N^{th} number of layers ($n = 1, 2, \dots, N$) is split into a sandwich-like structure of an M^{th} number of slices ($m = 1, 2, \dots, M$), as shown in **Fig.2.13** below. Of course, if symmetry is present within the waveguide structure, then this enables the number of calculations to be reduced²⁵. Once the waveguide has been divided into slices, the optical modes which have the same propagation constant are collected and the distribution of the fields are matched at the interface between each slice by adjustment of the modal amplitudes in each film. Only certain propagation constant values allow for a set of non-zero film mode amplitudes, that also have matching distributions at each slice interface to be found; each of these sets that are found represent a waveguide mode³².

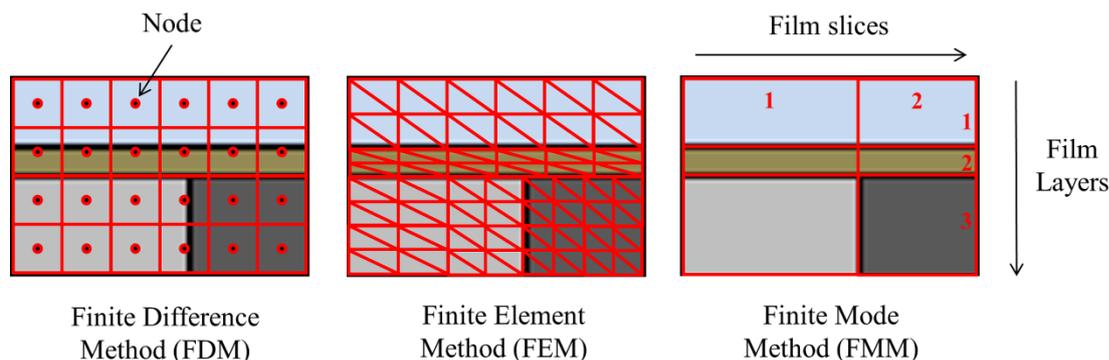


Fig.2.12: Diagrammatic comparison of the three common computational mode solving methods, finite difference method (FDM), finite element method (FEM) and the film mode method (FMM) for the area of planar waveguide defined in **Fig.2.12** above. Note: A finer mesh of elements is defined around and on the actual waveguide in the FEM method.

2.3 Bragg grating theory

Planar waveguides can be modified to facilitate particular optical functions. One way to modify planar waveguides is to insert an optical component known as a Bragg grating. Bragg gratings are used in the work presented herein to detect changes in refractive index and thus detect/sense changes in the surrounding environment.

The interaction of waves with periodic materials is a well-studied phenomenon. A classic example is the diffraction of neutrons or x-rays by a crystalline lattice. This diffraction is known as Bragg diffraction. Bragg diffraction occurs when particle waves (e.g. neutrons) or electromagnetic radiation waves (e.g. x-rays) are incident to a crystalline lattice and the wavelength of the incident wave is comparable to the spacing between the crystallographic planes within the lattice. The incident waves are scattered in a specular manner by the atoms within the crystallographic planes and thus can be considered to be scattered from crystallographic planes separated by the interplanar distance, d . The scattered waves subsequently either interfere constructively or destructively. Where constructive interference occurs the scattered waves are in phase; the path length of wave is equal to an integer multiple, n , of the wavelength, λ . The difference in path length between two waves that have undergone constructive interference, is described mathematically by $2d \sin \theta$, where θ is the scattering angle. From this Bragg's law can be derived, as given by **Eqn.2.44** below.

$$n\lambda = 2d \sin \theta$$

Eqn.2.44

Bragg's law describes the condition for constructive interference of scattered waves from successive crystallographic planes of a crystalline lattice.

In the case of optical Bragg gratings, the only difference is that the incident light waves are confined to the transverse plane, therefore the interactions are in one dimension.

2.3.1: Optical Bragg gratings

A Bragg grating is a section of periodic modulation of the effective index of a waveguide which can be considered as an optical wavelength filter. This periodic modulation of the effective index can be visualised as a periodic fringe pattern containing fringes of high effective index and fringes of low effective index as shown in **Fig.2.14** below.

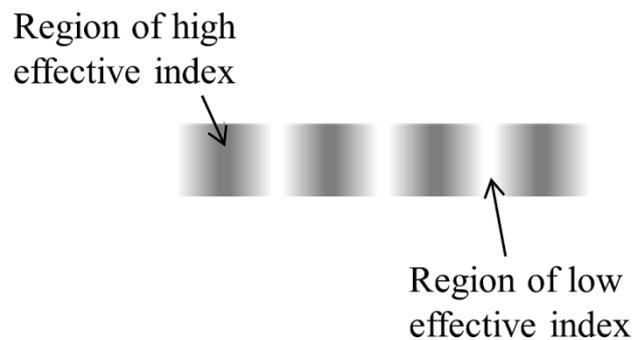


Fig.2.14: Schematic of regions of high effective index and low effective index.

Optical Bragg gratings can be one of two types; long-period gratings or short-period gratings. For both types of optical Bragg grating, the period describes the distance between a fringe of high or low effective index and the sequential fringe of the same effective index, i.e. high or low. Long-period gratings typically have periods on the sub-millimetre length scale and work by coupling forward propagating light, of a certain wavelength, into forward coupling cladding modes. The wavelength is dependent on the period of the Bragg grating. The power of the forward coupling modes is typically lost through absorption and scattering losses. This results in a dip, at the coupled wavelength, in the resulting transmission spectrum. In contrast, short-period Bragg gratings have a period on the sub-micrometre length scale. This shorter

period results in mode coupling between counter propagating modes of a certain wavelength, thus there is a reflection peak at the coupled wavelength in the reflection spectrum and a dip at the coupled wavelength in the transmission spectrum. This is depicted in **Fig.2.15** below:

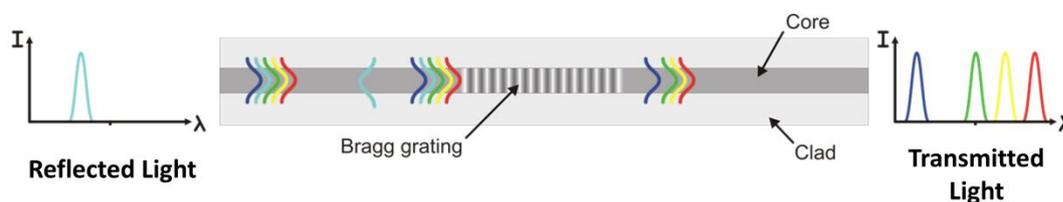


Fig.2.15: Pictorial description of a short-period Bragg grating showing different wavelengths of light (represented by the dark blue through to red curves) propagating from left to right along the waveguide and interacting with the Bragg grating. The short period Bragg grating results in one wavelength to be reflected (cyan curve) and transmission of the other wavelengths (dark blue, green, yellow and red curves).

The Bragg gratings used in this work are short-period Bragg gratings.

2.3.2: Effective index modulation

The modulation of the effective index can be achieved by variation of either the physical dimensions of the waveguide or the refractive index of the waveguide. At each fringe of high or low refractive index, a particular wavelength of the propagating light is reflected. The repeated modulation pattern of high and low refractive index results in multiple reflections along the length of the Bragg grating. The particular wavelength of light that is reflected, known as the Bragg wavelength, is dependent on the period of the refractive index modulation. In addition, the relative phase, of each reflected wave of light, is dependent on the period. For a the Bragg wavelength all of the back reflected light signals are in phase and thus undergo constructive interference. Light reflected at other wavelengths undergoes destructive interference and thus these wavelengths are transmitted through the Bragg grating.

Describing this phenomenon mathematically, it can be stated that the periodic structure of refractive index modulation has a wavevector component, k_G (**Fig.2.16**).

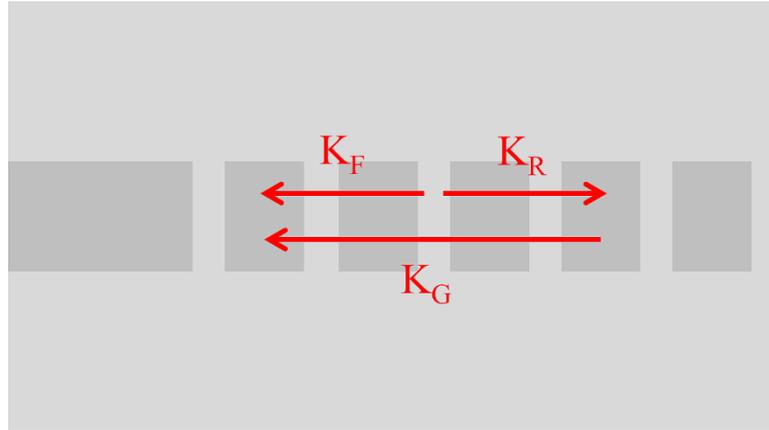


Fig.2.16: The forward propagating wavevector, k_F , reflected counter-propagating wavevector, k_R and overall Bragg grating wavevector, k_G .

If this wavevector component is equal to the sum of the forward-propagating wavevector, k_F and the reflected counter-propagated wavevector, k_R , then the Bragg condition is satisfied, as defined by:

$$k_R = k_F + k_G$$

$$\Rightarrow n \sin(\theta_C) = n \sin(\theta_F) + m \frac{\lambda}{\Lambda}$$

Eqn.2.44

where m is the diffraction order of the grating and is defined, along with θ_C & θ_F in **Fig.2.17** below.

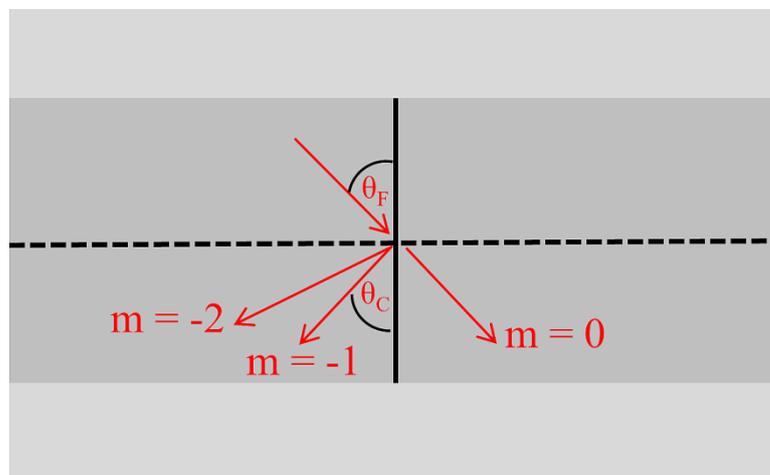


Fig.2.17: Definition of the diffractions orders of an optical Bragg grating.

Taking the case of first order diffraction, where $m = -1$ and a forward-propagating mode is coupled into an equal but counter-propagating mode, the Bragg condition simplifies to $k_R = k_F$. Thus, **Eqn.2.44** can be rewritten as,

$$-n_{eff} = n_{eff} - \frac{\lambda}{\Lambda}$$

$$\Rightarrow \lambda = 2n_{eff}\Lambda$$

Eqn.2.45

where Λ is the period of the Bragg grating and the wavelength that satisfies the Bragg condition, defined in **Eqn.2.45**, is λ , the Bragg wavelength. The Bragg wavelength will be implied by the symbol λ_B from now on throughout the rest of this work. As is obvious from **Eqn.2.45**, changing either the period of the grating and/or the effective index will change the value of the Bragg wavelength.

The Bragg grating refractometric sensors used in this work utilise the Bragg relation, given by **Eqn.2.45**, for indirect measurement of changes in the refractive index environment local to an exposed Bragg grating. Changes in the local refractive index cause a change in n_{eff} and thus cause a corresponding change in λ_B , the Bragg wavelength, that can be measured.

The initial effective index, n_{eff} , of a direct UV-written Bragg grating, of the type within the sensors utilised in this work, is defined by the photosensitivity enhancement of the core layer; a germanosilicate glass. This is achieved by altering the period of the Bragg grating, as discussed in **Chapter 3**.

2.3.3: Bragg grating structures

As described above, the periodic structure of an ideal Bragg grating can be considered to be uniform and as having a well-defined beginning and endpoint. However, real Bragg gratings will deviate from the ideal uniformly periodic structure either through the design of the Bragg grating, how the grating was fabricated, or actuation. If the refractive index of a Bragg grating varies slowly over the length of the grating, then the Bragg grating is labelled as a chirped Bragg grating. On the

other hand, if the fringe intensity changes with position along the length of the Bragg grating, then the Bragg grating is labelled as an apodised Bragg grating; this is demonstrated in **Fig.2.18** below. In addition, by specific modulation of the refractive index, phase-shifts can be introduced into a Bragg grating. This results in sharp spectral dips³³.

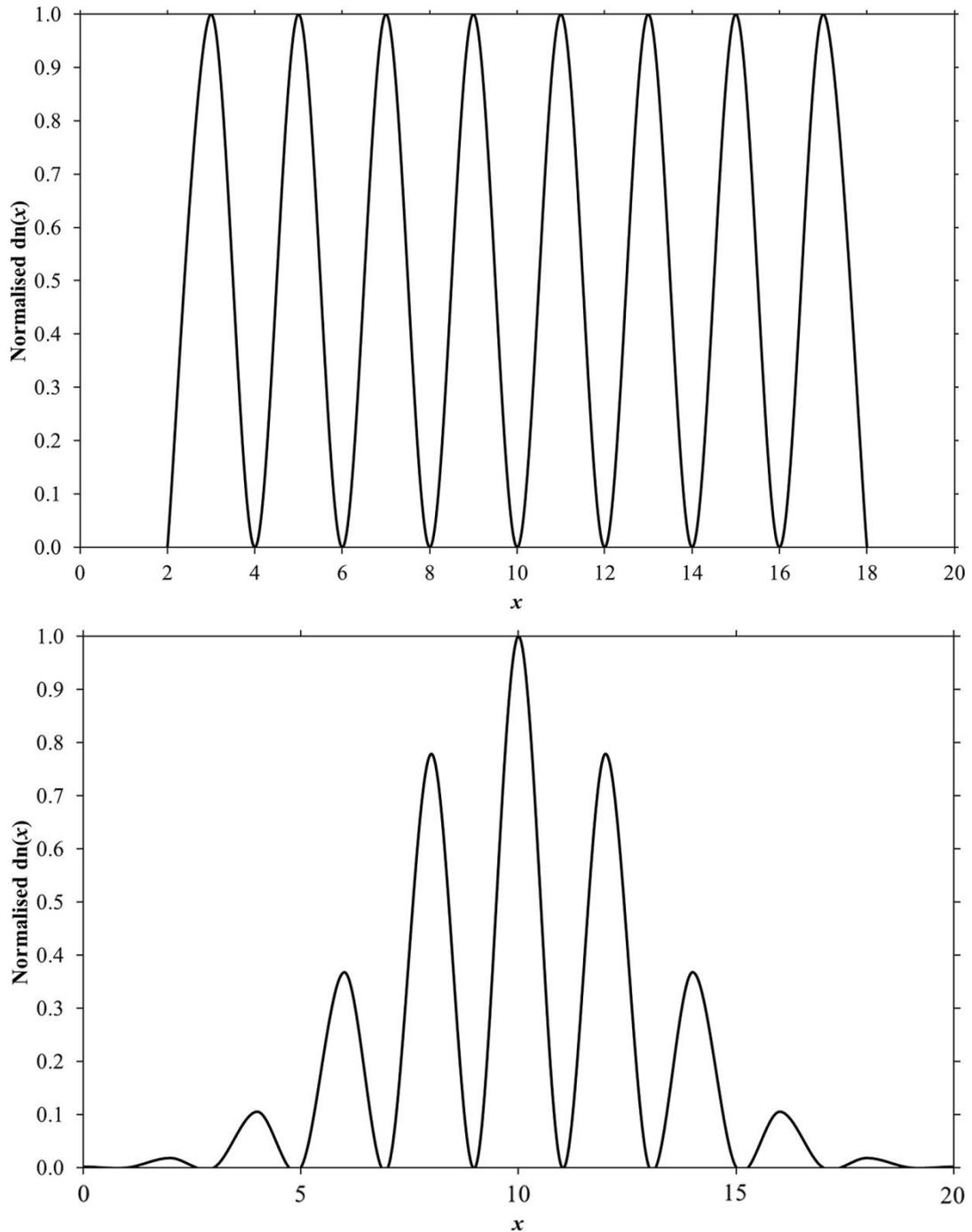


Fig.2.18: The refractive index profile of a uniform and a Gaussian apodised Bragg grating.

By taking the Fourier transform of the spatial structure of a Bragg grating, an approximation of the spectral response of the grating is obtained. For example, an uniform Bragg grating has, what is known as, a ‘top hat’ form (shown in **Fig.2.18** above) and this transforms into a ‘sinc’ function. Similarly the form of a Gaussian apodised grating is transformed into a Gaussian function, as shown in **Fig.2.19** below. A more thorough analysis of the spectral form of Bragg gratings is achieved through the use of co-directional coupled mode theory³⁴.

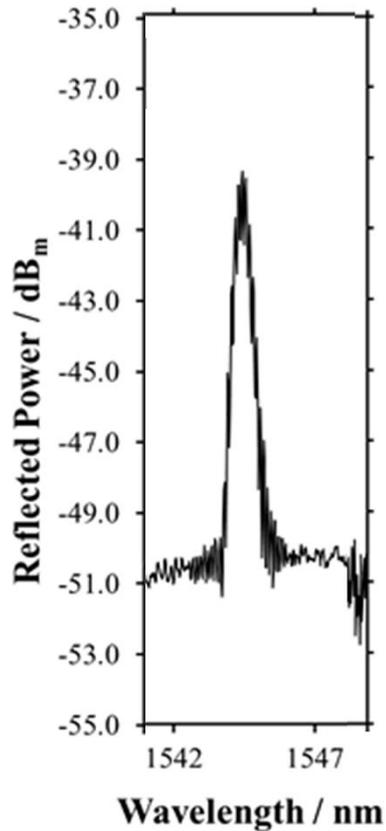


Fig.2.19: The reflectance spectrum of a Gaussian apodised Bragg grating demonstrating high side-lobe suppression.

2.3.4: Birefringence

For an ideal symmetric waveguide, the orthogonal TE and TM modes will experience the same effective index profile along the length of the waveguide. However, as explained above, the waveguides used in this work are inherently asymmetric and thus the TE and TM modes experience different effective indices. Typically this birefringence is small, but if the input light is unpolarised then broadening of the reflection Bragg peak occurs due to both TE and TM modes being supported in the waveguide. This makes it necessary to select a single polarisation

and this is achieved by independent guiding of polarised light either perpendicular or parallel to the plane of the waveguide; then only the TE mode or only the TM mode is supported in the waveguide.

2.4: Summary

The key concept of refractive index, and how it applies to the propagation of light in waveguides and Bragg gratings, has been introduced. The theory of light propagation, in waveguides and Bragg gratings, has been developed from Maxwell's equations, and for a symmetric ideal waveguide, the analytical solutions for the TE and TM polarisation modes have been stated. However, the waveguides used within this work are unsymmetrical, in terms of the refractive index profile, and thus numerical mode solving techniques are required to solve for these optical modes. Finally, the principle behind Bragg gratings and the engineering of Bragg gratings to produce refractometric gas sensors discussed.

In **Chapter 3** the fabrication of the layered structure of the waveguides by flame hydrolysis deposition (FHD) will be explored, in addition to the theory behind the direct UV-writing of waveguides and Bragg gratings in the layered structure of the sensor chip.

1. S. E. Miller, *Bell Syst. Tech. J.*, 1969, **48**, 2059.
2. H. Kogelnik, *IEEE Transactions on Microwave Theory and Techniques*, 1975, **MTT-23**, 2–16.
3. R. G. Hunsperger, *Integrated Optics: Theory and Technology*, Springer, 6th edn., 2009.
4. U. A. Bakshi and V. U. Bakshi, *Basics Of Electrical Engineering*, Technical Publications Pune, 1st edn., 2008.
5. S. Linden, C. Enkrich, G. Dolling, M. W. Klein, J. Zhou, T. Koschny, C. M. Soukoulis, S. Burger, F. Schmidt, and M. Wegener, *IEEE Journal of Selected Topics in Quantum Electronics*, 2006, **12**, 1097–1105.
6. R. T. Thompson, in *Electronic Materials Handbook: Volume 1 Packaging*, ed. M. L. Mingos, ASM International, 1st edn., 1989, pp. 670–675.
7. W. Cai, U. K. Chettiar, A. V. Kildishev, and V. M. Shalaev, *Nature Photonics*, 2007, **1**, 224–227.

8. F. Mesa, M. J. Freire, R. Marques, and J. D. Baena, *Phys. Rev. B*, 2005, **72**, 235117.
9. R. W. Ziolkowski and N. Engheta, in *Metamaterials: Physics and Engineering Explorations*, eds. N. Engheta and R. W. Ziolkowski, John Wiley & Sons, 2006, pp. 5–37.
10. Y. Liu and X. Zhang, *Chemical Society Reviews*, 2011, **40**, 2494–507.
11. V. G. Veselago, *Soviet Physics Uspekhi*, 1968, **10**, 509–514.
12. M. Fox, *Optical Properties of Solids*, Oxford University Press, 1st edn., 2001.
13. R. M. Parker, University of Southampton, 2009.
14. R. Paschotta, *RP Photonics Encyclopedia*, 2013.
15. R. Paschotta, *RP Photonics Encyclopedia*, 2013.
16. R. A. Serway, C. Vuille, and J. S. Faughn, *College Physics*, Brookes/Cole Cengage Learning, 8th edn., 2008.
17. P. K. Tien, *Applied optics*, 1971, **10**, 2395–2413.
18. D. Fleisch, *A Student's Guide to Maxwell's Equations*, Cambridge University Press, 1st Editio., 2008.
19. H. Kogelnik and H. P. Weber, *J. Opt. Soc. Am.*, 1974, **64**, 174–185.
20. F. Pillon, H. Gilles, S. Girard, M. Laroche, R. Kaiser, and A. Gazibegovic, *J. Opt. Soc. Am. B*, 2005, **22**, 1290–1299.
21. W. Schlosser and H.-G. Unger, in *Advances in Microwaves*, ed. L. Young, Academic Press Inc. (London) Ltd., London, 1st edn., 1966, pp. 319–388.
22. J. E. Goell, *Bell Syst. Tech. J.*, 1969, **48**, 2133.
23. E. A. J. Marcatili, *Bell Syst. Tech. J.*, 1969, **48**, 2071–2102.
24. E. A. J. Marcatili, *Bell Syst. Tech. J.*, 1974, **53**, 645–674.
25. R. M. Parker, University of Southampton, 2010.
26. M. V. K. Chari and S. J. Salon, *Numerical Methods in Electromagnetism*, Academic Press Inc., New York, 2000.
27. P. Hammond and J. K. Sykulski, *Engineering Electromagnetism: Physical Process and Computation*, Oxford University Press, Oxford, 1999.
28. M. D. Feit and J. A. Fleck, *Applied optics*, 1978, **17**, 3990–8.

29. W. Huang, C. Xu, S.-T. Chu, and S. K. Chaudhuri, *Journal of Lightwave Technology*, 1992, **10**, 295–305.
30. M. S. Stern, *Progress in Electromagnetics Research*, 1995, **10**, 123–186.
31. B. M. A. Rahman, *Progress in Electromagnetics Research*, 1995, **10**, 187–216.
32. A. S. Sudbo, *Pure and Applied Optics: Journal of the European Optical Society Part A*, 1993, **2**, 211–233.
33. C. Sima, J. C. Gates, H. L. Rogers, P. L. Mennea, C. Holmes, M. N. Zervas, and P. G. R. Smith, *Optics letters*, 2013, **38**, 727–9.
34. A.-P. Zhang, B. Guan, X.-M. Tao, and H. Tam, *IEEE Photonics Technology Letters*, 2002, **14**, 489–491.

3 Planar Bragg grating sensor fabrication

3.1 Introduction

Fabrication of functional optical components on the sub-micron scale often requires the use of complex techniques and stringent clean-room conditions ¹. After the inception of integrated optics by Miller ², micro-electronics fabrication techniques have been commonly employed for fabrication of integrated optical components ³; the use of well-established micro-electronic fabrication techniques is cost effective ⁴. The result is that many integrated optical devices have been developed that are based on the silicon wafer substrate platform or the silica-on-silicon substrate platform, both of which are commonly used in micro-electronics ⁵. An added benefit of this approach is that integration of both integrated electronic and integrated optics components on one chip is possible.

Once the substrate platform has been chosen, silica-on-silicon or silicon wafer, the integrated optical circuits are commonly fabricated by deposition, photolithography and etching techniques. However, whilst these techniques are suited to large scale mass production of integrated electronics, the cost and time involved with production of precision lithography masks and the requirement for clean-room conditions results in these techniques being less suited to prototyping and small-scale fabrication ⁴.

The optical sensor devices utilised in this work were fabricated with an alternative optical circuit definition technique, known as direct UV-writing. This technique does not require clean-room conditions, nor photolithography and is suitable for definition of waveguides in silica-on-silicon substrates. The technique is based on the localised

increase of refractive index in a photosensitive germanium-doped silica-on-silicon glass layer caused by exposure to a tightly focussed UV beam.

This chapter will focus on the fabrication of the germanium-doped silica-on-silicon waveguide substrates and the direct UV-writing of the waveguides and the Bragg gratings into the photosensitive layer. Throughout, alternative techniques will be compared and contrasted.

3.2 Silica-on-silicon substrate platform

The ‘topless’ waveguides described above in **Chapter 2** can be constructed by deposition of a layer of high refractive index material (waveguide core layer) on top of a layer of material with a lower refractive index. This results in trapping of light within the waveguide core layer due to total refractive reflection. This structure can be realised by deposition of two layers of silica onto a silicon substrate, where the topmost layer of silica, the waveguide core layer, is doped with germanium, boron or phosphorous to raise the refractive index and thus allow the guiding of light within it. The typical waveguide structure is shown below in **Fig.3.1**.

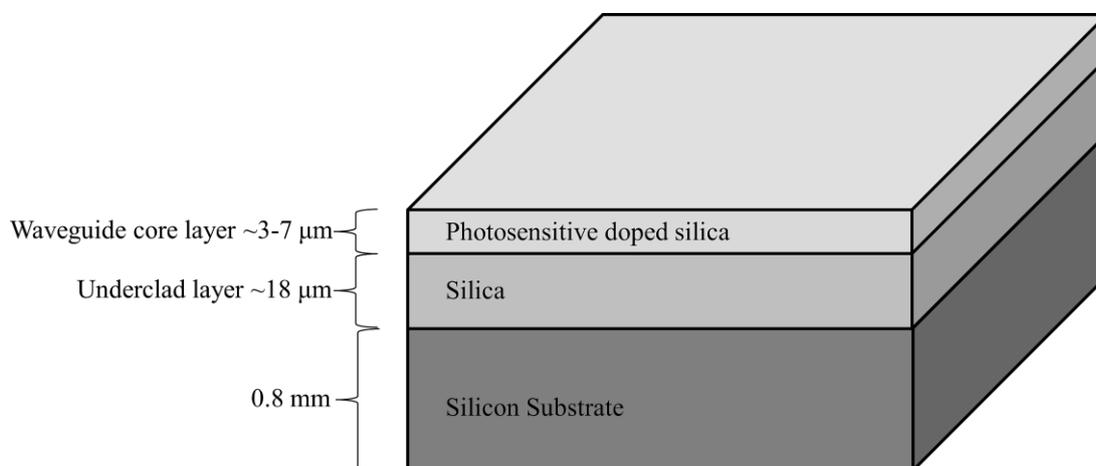


Fig.3.1: Layer structure of the waveguides used in this work, highlighting the doped silica waveguide core layer and the silicon substrate. NOT TO SCALE.

The underclad layer, typically 14 – 20 μm thick, is the thermal oxide layer (silica) of the silicon substrate. The waveguide core layer is then deposited on top of the underclad layer. The thickness of the waveguide core layer is typically 3 – 7 μm thick; this enables transverse single mode operation at telecoms wavelengths within a UV-written waveguide. There is also a requirement on the thickness of the underclad, which must be thicker than the magnitude of penetration depth of the

evanescent wave of a first-order guided mode within the waveguide core layer. This is essential so as to avoid interaction of the evanescent wave of the guided optical mode with the high index silicon substrate. Finally, above the waveguide core layer, is the ambient chemical environment.

3.2.1 Growth of the thermal oxide underclad layer

First the thermal oxide underclad layer is grown upon a standard silicon wafer. The underclad layer aids the adhesion of the subsequent waveguide core layer and also prevents the evanescent wave of the guide mode interacting with the high index silicon substrate. The underclad layer is grown using a similar method that is commonly used in industry ¹. The silicon wafers are heated in an oxygen and water vapour rich environment at >1000 °C and at several atmospheres ¹. The silicon surface in contact with the steam is oxidised and a silica layer is formed. Prolonged exposure to these conditions results in the interface between the silicon and the silica moving further into the bulk of the silicon; steam and oxygen penetrate through the silica over layer and oxidise the native silicon underneath ¹. To create the required underclad thickness, the silicon wafers need to be exposed to these oxidising conditions for several weeks; the rate of diffusion of the steam and oxygen through the forming silica over layer increases as the silica over layer increases in thickness. It must be noted that this technique is not a deposition technique as the native silicon is being consumed and reacting to form silica.

Once an underclad layer of thermal oxide silica of the appropriate thickness has been grown the waveguide core layer is then deposited on top using a technique known as flame hydrolysis deposition (FHD). Flame hydrolysis deposition is a derivative technique of chemical vapour deposition (CVD) and is outlined below ⁶. In addition the advantages and disadvantages of FHD compared to the main competing technique of plasma enhanced chemical vapour deposition (PECVD) are discussed.

3.2.2 Flame hydrolysis deposition

Flame hydrolysis deposition (FHD) is a commonly used technique for the deposition of silica and doped silica upon silicon wafers ^{7,8}. The FHD process allows for the deposition of silica films that exhibit low inherent optical losses and low stress at high deposition rates ⁹. A pictorial diagram of the FHD process is shown below in **Fig.3.2**.

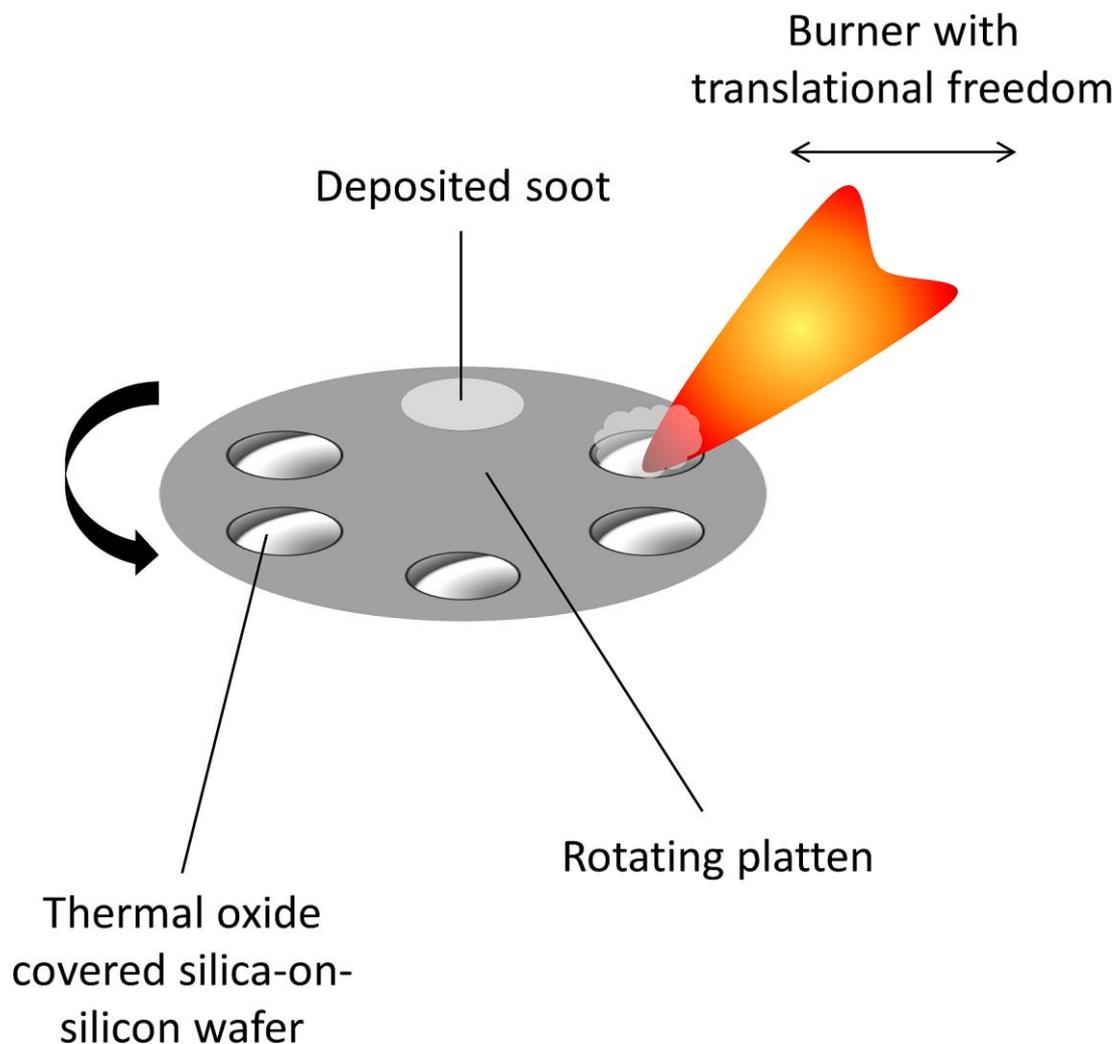
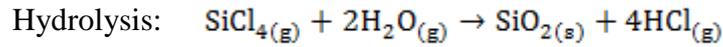
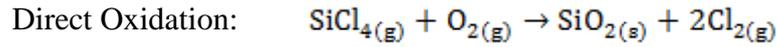
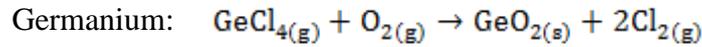


Fig.3.2: Pictorial representation of the flame hydrolysis deposition technique which is used to deposit the core waveguide layer.

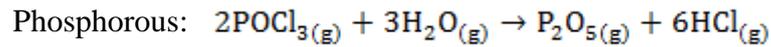
The first step of the process is the deposition of the doped glass soot layer upon the thermal oxide underclad layer of the substrate. This is achieved by the direct oxidation and/or hydrolysis of vaporised halide precursors in a hydrogen-oxygen flame. For the deposition of silica, the precursor is silicon tetrachloride (SiCl_4). Silicon tetrachloride undergoes direct oxidation to form silica and chlorine gas within the centre of the flame, where temperatures reach $\sim 2000\text{ }^\circ\text{C}$ and hydrolysis in areas of the flame where the temperature has fallen below $\sim 1200\text{ }^\circ\text{C}$. Under hydrolysis conditions silica and hydrochloric acid gas are formed. The direct oxidation and hydrolysis reactions are outlined below:



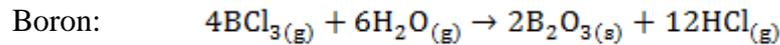
To achieve deposition of the doped waveguide core layer, other precursors are vaporised and simultaneously introduced into the hydrogen-oxygen flame. For doping with phosphorous, boron and germanium the precursors are germanium chloride (GeCl_4), phosphorous oxychloride (POCl_3) or phosphorous trichloride (PCl_3) and boron chloride (BCl_3) respectively. The oxidation reactions in each case are shown below:



where GeO_2 is germanium dioxide, otherwise referred to as germania.



where P_2O_5 is phosphorous pentoxide.



where B_2O_3 is boron trioxide.

By successive passes of the hydrogen-oxygen burner flame over the silica-on-silicon wafer on the rotating platen, several layers of doped silica soot are deposited. The presence of phosphorous and boron species in the silica alter the refractive index at telecoms wavelengths; phosphorous increases the index whereas boron decreases the index. By altering the concentration of each vaporised precursor in the flame, careful control of the refractive index of the waveguide core layer is possible. In addition phosphorous pentoxide is added to the deposited silica as it is known to reduce the melting point of the silica, which enables the thermal annealing consolidation step to be conducted at a temperature which does not compromise the integrity of the thermal oxide underclad layer. The presence of germanium species in the waveguide core layer introduces photosensitivity to UV light. This photosensitivity is exploited in the UV-writing waveguide fabrication method which is described in section 3.3 below.

3.2.2.1: Plasma Enhanced Chemical Vapour Deposition

The main competing technique to FHD is plasma enhanced chemical vapour deposition (PECVD) wherein plasma is utilised to initiate reaction of precursor chemicals in the vapour state, resulting in the formation of and subsequent deposition of products in the solid state onto a substrate. PECVD was the deposition technique utilised to deposit silica layers in work by Svalgaard, wherein direct UV-written waveguides in planar silica-on-silicon waveguides were demonstrated for the first time^{10,11}.

The PECVD method has been used to deposit layers of dielectric material, at temperatures <300 °C, since the 1960's¹². Chemical species in the gaseous or vapour state, diluted with a carrier gas, are delivered into the PECVD chamber (**Fig.3.3** below). For example the precursor for silica is tetraethyl orthosilicate (TEOS) and nitrous oxide is the carrier gas. In the chamber a high voltage radio-frequency electric field exists. Upon collision with the accelerated electrons, the precursor species are ionised and form a plasma. This energetic plasma reacts with the surface of the substrate to be coated and the sides of the chamber resulting in the adsorption of the charged plasma species. Further reactions on the surface between adsorbed charged species results in the chemical bonding of the species with the surface, ultimately leading to the formation of layers of the target dielectric material on the substrate¹³.

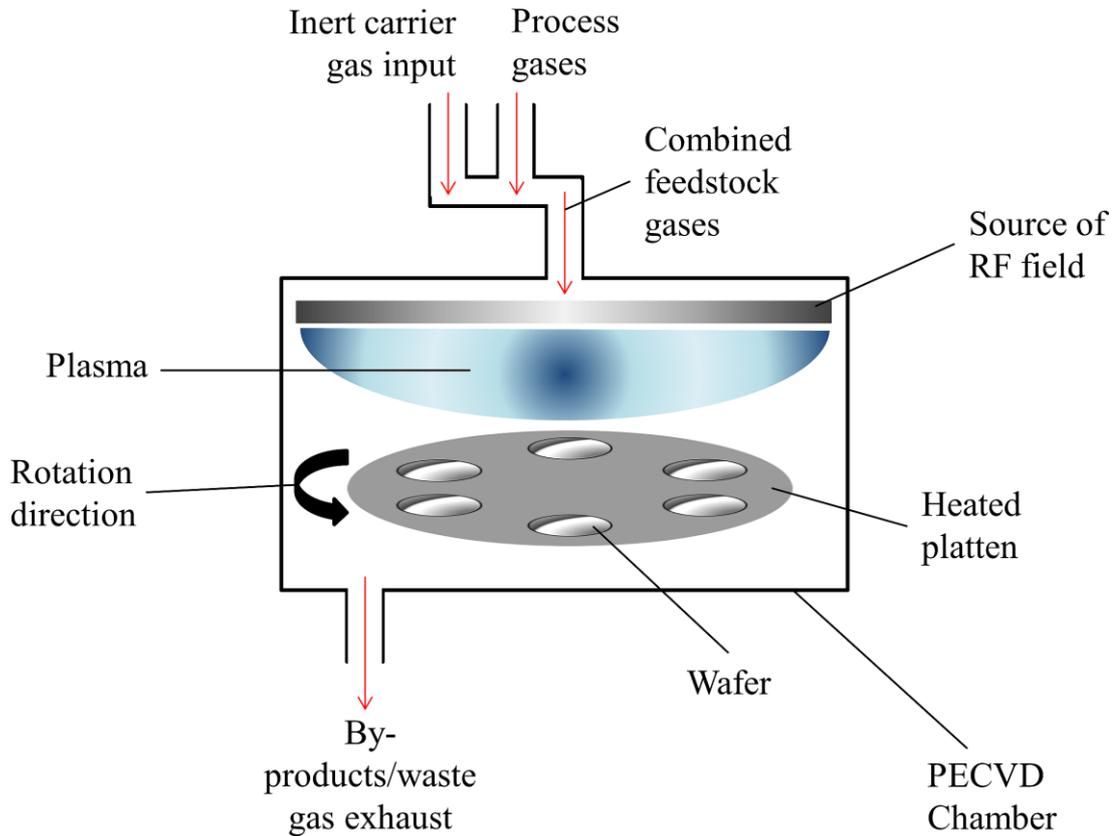


Fig.3.3: Schematic of the PECVD process, the competing technique to FHD.

One disadvantage of PECVD compared to FHD, is that PECVD deposited silica typically contains inclusions of free or bonded hydrogen and nitrogen (from the nitrous oxide precursor). These inclusions, which can be hydroxyl (-OH), hydride (-H) or amine (-NH) groups, can result in high optical losses at telecoms wavelengths¹⁴. High temperature annealing of the deposited layer (several hours, >1000 °C) results in reduction of these optical losses but this thermal treatment negates many of the benefits of the initial low temperature deposition conditions. However, through alternative process controls, and the exclusion of nitrogen containing precursors, optical losses can be reduced significantly without the need for the thermal annealing treatment step¹⁵.

In contrast, one advantage of PECVD, is that unlike FHD, the precursors do not need to be halides which allows for a much greater selection of dopants and precursors. However, the major disadvantage of PECVD compared to FHD is that there are limitations on the maximum deposition thickness which results in a viable layer, in a single PECVD run. For example, it has been found that blistering of germanium doped silica deposited layers of ~ 5 μm thickness occurs if the layer is deposited in a

single PECVD run ¹. On the other hand, layers up to 10's microns thick can be deposited in a single FHD run ¹. As stated above the thickness of the waveguide core layer can be anywhere between 3 – 7 μm , thus two PECVD cycles may be required using to achieve deposition of a thicker waveguide core layer; this makes the PECVD technique more labour intensive and expensive than FHD.

3.3 UV photosensitivity

As stated above, during the fabrication of the sensor devices used in this work, the waveguide core layer is doped with germanium to induce UV photosensitivity. The induced UV photosensitivity enables definition of the optical waveguides and Bragg gratings in the waveguide core layer, by a technique known as direct UV-writing. This technique is based on the localised increase of refractive index in the photosensitive germanium-doped silica glass layer caused by exposure to a tightly focussed UV laser beam. The exposure to UV beam leads to physical changes in the structure of the germanium-doped silica, which in turn causes the localised change in refractive index.

3.3.1 Photosensitivity of germanium-doped silica

Refractive index changes in bulk germanium-doped silica, otherwise known as germanosilica, due to exposure to laser light, were first reported by Hill *et.al.* ^{16,17}. In that work, launching of 488 nm light, from an argon ion laser, into optical fibres, which were heavily doped with germanium led to a time dependent phenomenon of decreasing transmitted optical power with an accompanying increase in reflected optical power. It was found that over one metre of the germanosilica fibre the launched laser light would eventually become reflected due to the establishment of a standing wave structure within the core of the fibre. Points of high intensity along the standing wave induced refractive index changes on the order of $\sim 10^{-6}$ in a periodic manner, due to the periodic structure of the standing wave. This periodic variation in refractive index along the length of the fibre was ultimately a Bragg grating structure and over minute timescales 100% Bragg reflection could be achieved due to the self-enhancing nature of the process. However, despite creating Bragg grating structures in germanosilica fibres, these systems reported by Hill *et.al* were not technically useful due to operation at wavelengths outside of the main telecoms wavelength range. In addition the index modulation in the Bragg grating

structure was relatively weak and thus to achieve sufficient reflected optical power long grating lengths were required, rendering these fibres impractical for localised sensing applications. Before this technique could be utilised to create practical Bragg gratings, these disadvantages had to be overcome.

The issue of weak index contrast was overcome through interpretation of the work by Lam and Garside¹⁸. Lam and Garside reported that the magnitude of the photoinduced refractive index change was dependent on the square of the power of the laser source; this implied that the optical process occurring in the germanosilica was a two-photon process. Work by Hand *et.al.* and Meltz *et.al.* elucidated that the exposure of germanosilica to UV light resulted in photobleaching of absorption defects and refractive index changes (if the UV light is in the 240 – 250 nm wavelength region), respectively^{19,20}. Therefore, it was proposed that to achieve strong refractive index contrast, 244 nm light could be used instead of 488 nm. Exposure of germanosilica to light within the wavelength region 240 – 250 nm can result in refractive index changes of the order $\sim 10^{-3}$.

3.3.1.1 Photomechanism and defects in germanosilica

The presence of defects in crystalline and amorphous solid is entropically driven. As such, defects in both pure amorphous silica and germanosilica occur. These defects involve deviation away from the ideal structure of silica and germania centres within the bulk structure. Such defects may occur due to oxygen deficiency within the forming silica layer. Such defects are known as oxygen deficient centres (ODCs). One type of ODC is the neutral oxygen vacancy (NOV) where two silicon atoms are bonded directly together without the bridging oxygen; the usual structure of silica contains the bridging oxygen atom. The ideal silica centre and the NOV ODC are shown below in **Fig.3.4**.

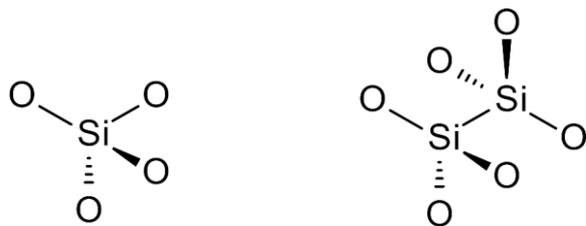


Fig.3.4: (Left) the ideal tetrahedral structure of silica, a silicon atom bonded to four oxygen atoms. (Right) the structure of a neutral oxygen vacancy (NOV), where two silicon atoms are directly bonded without a bridging oxygen atom. In both cases, a bold wedge bond represents a bond coming out of the plane of the page toward the reader and a wedge bond represents a bond going into the plane of the page away from the reader.

Due to germanium having the same valency as silicon, both Ge and Si are in Group 4 of the periodic table under C, germanium can substitute silicon atoms within the silica lattice without significant deviation away from the ideal bulk silica structure. The substituted germanium atoms are found to exist in two forms, the Ge(1) centre or a Ge(2) centre. A Ge(1) centre is where the germanium atom is bonded to four silica atoms via bridging oxygen atoms (c.f. the ideal tetrahedral structure of silica in **Fig.3.4** above) and a Ge(2) centre is where the germanium atom is bonded to three silicon atoms and another germanium atom via bridging oxygen atoms. Oxygen deficiency in the forming germanosilica layer can result in NOV defects that feature both Ge(1) and Ge(2) centres, wherein silicon-germanium direct bonding or germanium-germanium direct bonding occurs respectively; an example of a Ge(1) NOV defect is shown in **Fig.3.5** below. In addition, another defect type typical to germanium in germanosilica is the Ge^{2+} defect, where Ge^{2+} is a bi-valent species.

The Ge(1) and Ge(2) centre NOVs and the Ge^{2+} defect absorb between 240 – 245 nm, thus it is understood that these defects contribute to the UV photosensitivity of germanosilica²⁰. Upon exposure to UV light in the wavelength region 240 nm – 250 nm electrons on the atoms are excited which can lead to the release of bonding electrons and subsequent bond breaking. For example the breaking of the bond between the Si and Ge atom in a Ge(1) NOV leads to the formation of another germanium centered defect known as a GeE' defect and a liberated electron. The released electron can then undergo two processes: diffusion through the lattice of the bulk material or recombination with the GeE' centre resulting in luminescence. However, if the electron does diffuse through the bulk lattice it can then react with a

Ge(1) or a Ge(2) centre to form paramagnetic Ge(1) \cdot and Ge(2) \cdot defects respectively. These processes are described pictorially in **Fig.3.5** below.

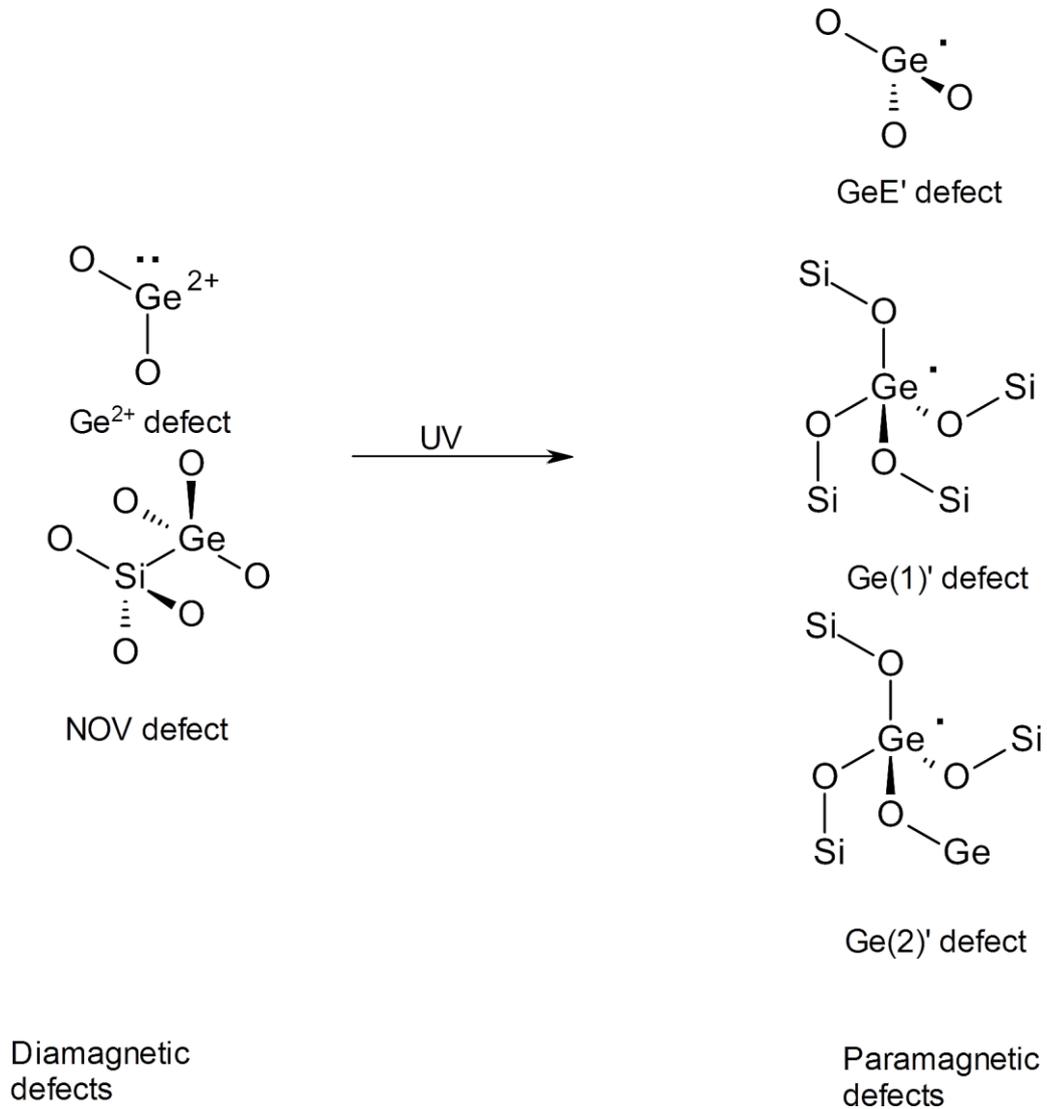


Fig.3.5: The defects in germanosilica that are understood to be responsible for the phenomenon of UV photosensitivity in germanosilica. The diamagnetic defects (left) absorb in the UV 240 nm – 250 nm region to produce the paramagnetic GeE' defect and a liberated electron. The liberated electron can go on to combine with a Ge(1) or a Ge(2) centre to form a Ge(1) \cdot or a Ge(2) \cdot centre, both paramagnetic species.

The change from diamagnetic defects to paramagnetic defects is accepted as the main cause of the photoinduced refractive index change. However, theoretical modelling of the change from diamagnetic defects to paramagnetic defects, predicts a refractive index change that is an order of magnitude less than the experimentally measured values. It is therefore proposed that other mechanisms, which cause the changes in the refractive index are also occurring ¹, such as thermal effects or change

in the stresses within the layer²¹⁻²³. One explanation is that densification of the exposed material also occurs and thus contributes to the change in refractive index. It is known that densification occurs in a germanosilica planar layer upon exposure to UV light and that the densification leads to variations in the stresses within a germanosilica layer and changes to the refractive index of the exposed material²¹.

Photosensitivity of germanosilica and the refractive index changes upon exposure to UV light can be described as quasi-permanent. This is because both generally have long lifetimes. However, thermal treatment at temperatures lower than the temperature needed to achieve reflowing of the glass, can remove the induced index change. For example, thermal treatment at 800 °C for 30 minutes can erase the induced localised refractive index changes⁴; the dissociative bond energy of a Ge – O bond is ~15% smaller than a Si – O bond²⁴.

3.3.2 Hydrogenation

As stated above, direct stimulation of germanosilica to a focussed beam of UV light in the wavelength region 240 – 250 nm can result in localised changes in refractive index on the order of $\sim 10^{-3}$. However, any further attempts to increase the resulting refractive index change caused by exposure to UV light by increasing the concentration of germanium leads to undesirable excessive optical losses within the layer⁴.

An alternative method to increase the refractive index change upon UV exposure is by loading the germanosilica layer with hydrogen gas. Lemaire et.al. demonstrated that permanent refractive index changes of $\sim 10^{-2}$ could be achieved with exposing a germanosilica fibre, that had been previously stored in a high pressure (>120 bar) atmosphere of hydrogen gas, to UV light²⁵. It was proposed that hydrogen had diffused into the germanosilica²⁵.

There are two mechanisms proposed in the literature to explain photosensitivity enhancement afforded by hydrogenation. The first mechanism involves the thermo- or photo-induced reactions of hydrogen with GeO₂ sites in the matrix resulting in breaking of a germanium-oxygen bond, the formation of a Si-OH group and an oxygen deficient centre²⁶. The second mechanism involves hydrogen acting as a photobleaching catalyst.

However, despite the greater refractive index changes gained with hydrogen doping before UV exposure, the increase in hydroxyl groups formed at defects sites increases absorption losses in the telecoms wavelength region²⁷. However, this can be overcome by using deuterium instead of hydrogen gas. Deuterium also increases photosensitivity with the germanosilica layer, but instead of hydroxide (-OH) groups being formed, deutroxide (-OD) are formed. The advantage of this is that the resonant frequency of the O-D bond is lower than the resonant frequency of the O-H bond, due to deuterium having double the mass of hydrogen. Therefore, the -OD absorptions, which are at higher wavelengths than the -OH absorptions, are not in the telecoms window. Thus the source of optical power losses within the telecom window is removed, but the benefit of increase photosensitivity remains²⁸.

3.3.2.1 Hydrogen out-diffusion

At room temperature and pressure the hydrogen loaded within the glass layer will readily out-diffuse, thus reducing the photosensitivity enhancement effect over time, until all of the hydrogen has out-diffused and the photosensitivity has returned to the pre-hydrogen loading state. Significant reduction in the photosensitivity enhancement can occur over ~ 30 minutes, therefore it is imperative to reduce the rate of out-diffusion rate by lowering the thermal energy of the system.

The rate of diffusion can be quantified by a parameter known as the diffusivity. Diffusivity, D , is defined as the rate at which substances that are diffusing, traverse between opposite faces of a unit cube with a unit concentration difference between them²⁹. This concept is expressed mathematically in **Eqn.3.1** below:

$$D = D_0 e^{-\left(\frac{E}{RT}\right)}$$

Eqn.3.1

Where D_0 is a pre-exponential factor, E is the diffusion activation energy, R is the real gas constant ($8.318 \text{ JK}^{-1}\text{mol}^{-1}$) and T is the absolute temperature of the system. Values of E can be determined experimentally; a value of $\sim 40 \text{ kJmol}^{-1}$ is typical³⁰. It has been demonstrated by Svalgaard *et.al.* that the time available for UV writing, τ_{UV} , is given by³¹:

$$\tau_{UV} = -\ln(\alpha)\tau_0 e^{\frac{E}{R}\left[\frac{1}{T} - \frac{1}{T_0}\right]}$$

Eqn.3.2

Where α is the concentration of hydrogen in the glass and τ_0 is the decay time at temperature T_0 .

The relationship between τ_{UV} and ambient temperature was demonstrated graphically by Svalgaard.

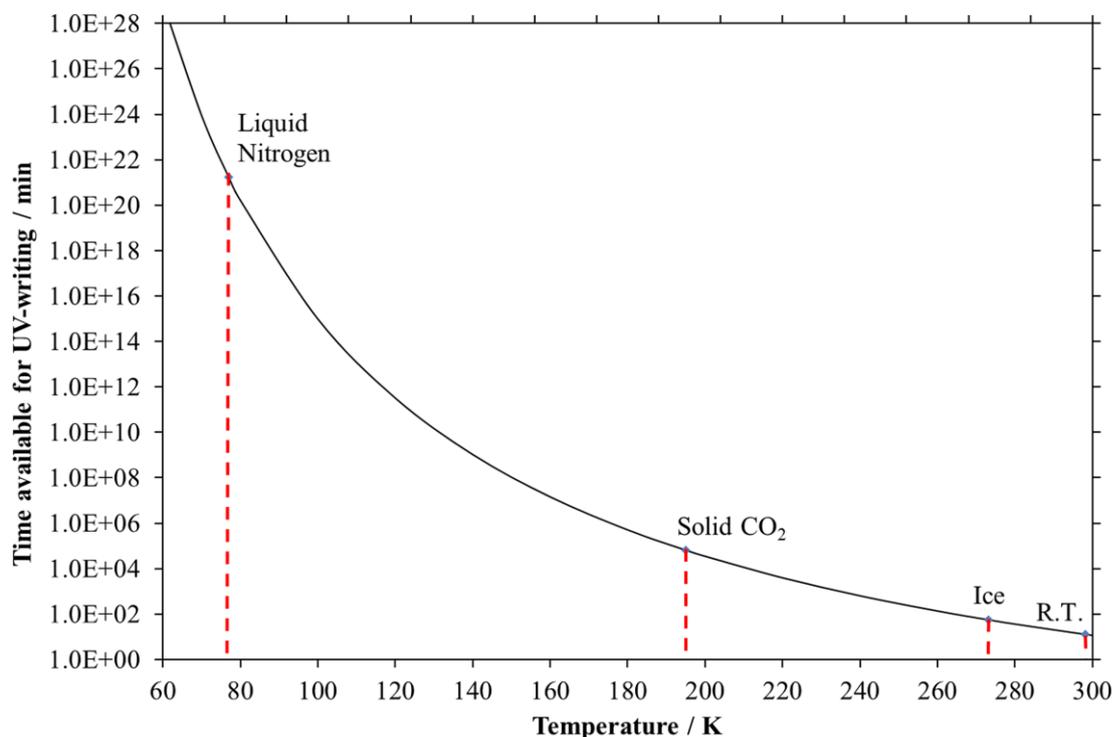


Fig.3.6: The dependence of temperature on the time available for UV-writing due to hydrogen out-diffusion. The higher the value of T , the quicker the hydrogen out-diffuses and thus shorter the time period available for UV-writing.

As indicated in **Fig.3.6** above, the time available for direct UV writing can be increased, and thus the rate of hydrogen out-diffusion can be greatly reduced, by storing the hydrogen loaded Bragg device in liquid nitrogen (77 K) or dry ice (195 K) until the time of direct UV-writing. Storage at these reduced temperatures (relative to room temperature R.T., 298 K) increases the time in which the device can be direct UV-written with the enhanced photosensitivity from ~20 mins, if exposed to room temperature directly after hydrogen loading, to a period of days.

3.4 The Direct UV-writing process

As mentioned above, the direct UV-writing process is based on the localised refractive index increase of a UV photosensitive glass layer when exposed to a tightly focussed UV-laser beam. The method is used to define, or ‘write’ the lines of higher refractive index which act as the waveguides in the Bragg grating devices used in this work.

The direct UV-writing method was first demonstrated as a suitable technique for the definition of waveguides in 1974 by Chandros *et.al.*, who defined optical waveguides in polymeric layers ³². However, the use of the direct UV-writing technique for definition of waveguides in silica-on-silicon wafers was initiated and developed by Svalgaard ¹¹ and now the technique has become a well-established method of fabricating integrated optical circuits in silica-on-silicon wafers ³³.

As discussed above, the Bragg grating devices used in this work are known as ‘topless’ device; the waveguide core layer, doped with germanium, is the topmost layer. If a UV laser is focussed into this UV photosensitive layer, then a localised refractive index change occurs. If the sample is translated relative to the beam spot, using a set of high precision translation stages, then two-dimensional refractive index structures can be achieved. The advantages of this technique to other waveguide definition techniques, which will be discussed below, are that neither clean-room conditions, nor photolithography is required.

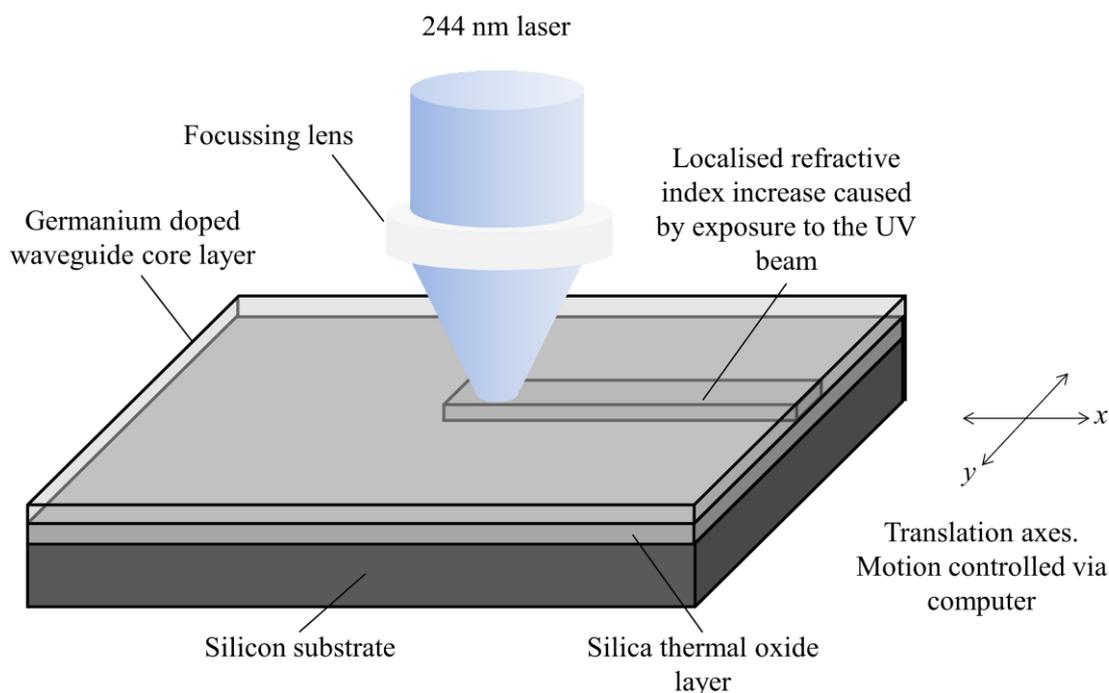


Fig.3.7: Schematic of direct UV-writing of a channel waveguide into the photosensitive waveguide core layer using a focussed 244 nm laser. NOT TO SCALE.

The optical circuits utilised in this work were defined using 244.0 nm UV radiation that was frequency doubled 488.0 nm radiation from an argon ion (Ar^+) laser. The radiation at 244.0 nm lies within the main absorption bands of germanosilica. The highest output power from an Ar^+ laser is at 514.5 nm, however the frequency doubled radiation is at 257.25 nm, which is outside the main absorptions of germanosilica¹⁰. Therefore despite lower output power, the 244.0 nm UV radiation from frequency doubled 488.0 nm radiation is used.

The magnitude of the localised refractive index contrast, that is photoinduced into the germanosilica by the UV radiation, is dependent on the total number of photons that are incident on a given spot of the waveguide core layer at an instant in time. In turn, the total number of incident photons depends on the power of the incident 244 nm radiation, the tightness of the focus of the beam and the translation speed of the device under the beam spot. The refractive index contrast of the UV-written structures can be as high as 2×10^{-2} , but is typically 5×10^{-3} or lower. To regulate the resulting refractive index change, the degree of exposure to the UV radiation is quantified by the fluence parameter, F , which is defined in **Eqn.3.3** below:

$$F = \frac{I_{UV} d}{v}$$

Eqn.3.3

Where F is the fluence (kJ cm^{-2}) is a measure of the energy delivered to the sample and is dependent on the power of the UV radiation, which is given by the product of the average power density of the UV writing beam spot, I_{UV} (kW cm^{-2}) and the diameter of the writing spot, d (cm, a typical value of the $1/e^2$ width of the spot is $\sim 7 \mu\text{m}$), and the speed at which the sample is translated under the spot, v (cm s^{-1}). By controlling the fluence, the refractive index contrast of the resultant UV-written structures is typically 5×10^{-3} or lower, but refractive index contrast as high as 2×10^{-2} can be achieved. In addition, the minimum feature size that can be defined is dependent on the focussed spot size and the resolution and precision of the translation stages.

Overall the direct UV-writing technique offers a facile route towards rapid prototyping of optical waveguides and complete optical circuitry. Direct UV-writing is very well suited to the production of integrated optical devices in small to medium volumes where design flexibility, low initial investment (no need for fabrication of photolithographic masks etc.) and rapid development are required. However, the writing time of complex or large devices can be significantly longer due to the one beamspot writing approach; each different waveguide/optical circuit segment must be written individually and sequentially. Therefore, for medium to high volume production, the direct UV-writing approach is unfavourable and the technique of photolithography, wherein simultaneous definition of multiple optical features on multiple devices is achievable, becomes attractive. Because all of the Bragg grating devices used in this work were prototype devices, direct UV-writing was the waveguide definition technique used. However, for completeness, some other competing techniques are described briefly below.

3.4.1 Competing Techniques to Direct UV Writing

The relatively new technique of direct UV-writing competes against well-established waveguide fabrication technologies such as photolithography and etching that were adapted from the microelectronics industry. In addition, another direct laser writing

technique known as femtosecond (fs) laser writing is also emerging as a competing technique.

3.4.1.1: Photolithography and etching

Photolithography is a technique that has been, and still is, extensively used in the microelectronics industry for the definition of microelectronic circuits. Recently, photolithography has been used as fabrication technique for optical waveguides and integrated optical circuits³⁴.

To fabricate optical waveguides and integrated optical circuits, first a higher index doped silica layer is deposited onto a thermal oxide-coated silicon wafer by either PECVD or FHD. Then a photoresponsive polymer, that undergoes crosslinking when exposed to UV radiation, known as photoresist, is then spin deposited onto the surface of the high index silica layer. A lithography mask of the desired optical circuit design is made and then used to selectively expose the photoresist layer to UV radiation, thus transferring the desired optical circuit design onto the surface. The unexposed photoresist is then washed with solvent to leave the desired design. This developed photolithographic design is then etched using wet/dry etch techniques thus resulting in the definition of the optical circuit structure. Invariably, an additional deposition of silica is then performed so as to provide a protective cladding layer. These steps are outlined diagrammatically in **Fig.3.8** below.

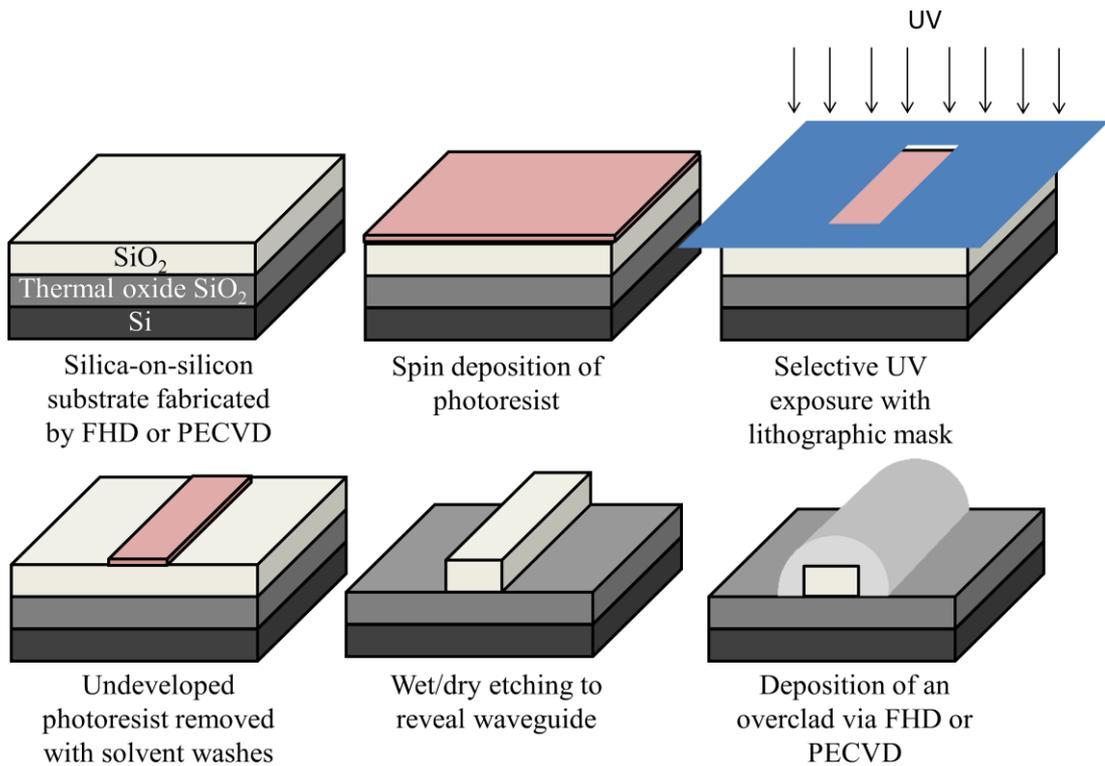


Fig.3.8: Schematic of the photolithographic process for fabrication of waveguides. ‘SiO₂’ represents a doped silica glass with a higher refractive index than the ‘Thermal Oxide SiO₂’ layer.

Photolithography allows for the fabrication of multiple devices in parallel and thus is a cost efficient method for mass production. However, as mentioned above, for prototyping and small-scale production runs (100’s to 1000’s of devices) the technique is prohibitive in terms of time taken and financial costs due to the need for a new photoresist mask to be designed and fabricated every time an alteration to the photoresist circuit pattern is required. Current photolithographical capabilities allow for waveguides of the order of 100’s of nanometres to be defined and etched, but the resolution of any defined feature is limited by the quality of the UV exposure, the lithographic mask and the etching procedure³⁵.

3.4.1.2 Direct femtosecond writing

The technique of direct femtosecond writing utilises a femtosecond pulse near-infrared laser (fs laser) to define waveguides and was demonstrated by Davis³⁶. The fs laser is focussed into a glass substrate and waveguides are defined by translating the sample relative to the laser beam. The high energy density at the point of focus

causes localised densification of the glass, which results in localised increases in refractive index as large as 4×10^{-2} . Bragg gratings can also be realised by actively modulating the exposure³⁷.

Whilst the direct femtosecond writing technique is similar to the direct UV-writing technique, in that a laser is focussed into a glass to induce localised refractive index changes, it is different in that non-linear effects in the material are used, instead of photosensitivity, to achieve writing. An advantage of this is it is possible to write three-dimensional optical circuits instead of in just two dimensions³⁸. However, there are major disadvantages to the direct femtosecond laser writing. The laser required for the fabrication is far more expensive and less stable. In addition, the technique generally has a slow rate of writing and the resulting waveguides can demonstrate high propagation losses³⁹.

3.5 Direct UV Grating Writing

Direct UV grating writing (DGW), developed at the Optoelectronics Research Centre, is a derivative of the direct UV-writing system described above. This well-established technique allows for simultaneous definition of waveguides and Bragg gratings⁴⁰, thus enabling fabrication of a broad range of optical devices containing customisable Bragg gratings and channel waveguides^{41,42}.

Direct UV grating writing is similar to direct UV writing in that a UV laser is used to induce localised refractive index changes in the photosensitive waveguide core layer. However, the DGW method is different in that the single UV laser beam, used in direct UV writing, is split into two focussed beams that form an interference pattern within the waveguide core layer. Compared to other techniques used for fabrication of Bragg gratings in waveguides, the DGW technique offers two main advantages. Firstly, the Bragg gratings are not overwritten on top of pre-existing waveguides, an issue in fibre Bragg grating systems, and secondly this method provides a facile route to different period Bragg gratings through control of the laser modulation, without the need to alter the alignment of the system.

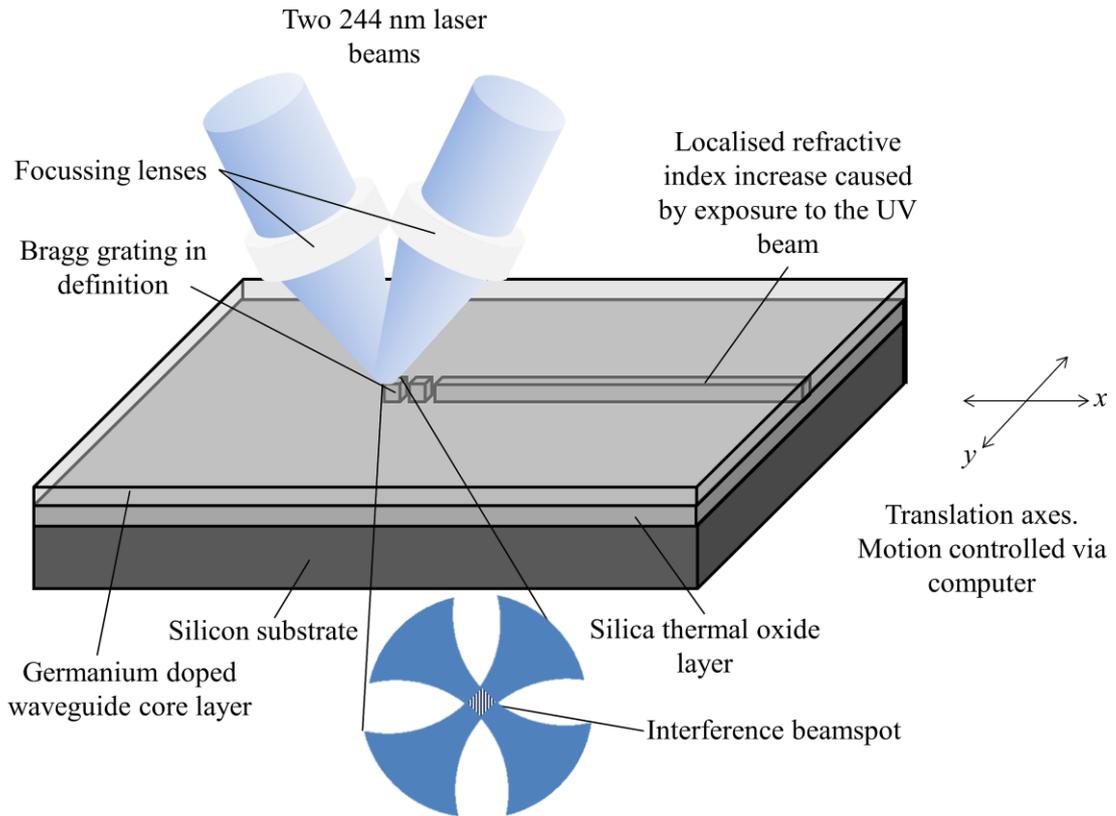


Fig.3.9: Schematic of the definition of a channel waveguide containing a Bragg grating using the direct UV grating writing technique, highlighting the two focussed UV 244 nm laser beams and the inherent interference pattern at the interference beamspot. NOT TO SCALE.

The two coherent and focussed beams produce an interference pattern with the waveguide core layer, the period of which is defined by the angle between the two beams. Through use of high-precision air-bearing stages the silica-on-silicon substrate is translated under the combined beam spot of the two focussed beams resulting in a localised refractive index increase, thus forming a channel waveguide. Bragg gratings are defined simultaneously with the channel waveguides by modulation of the writing beam such that the interference pattern stamps periodically upon itself. The simultaneous approach to UV writing of channel waveguides and Bragg gratings means that the waveguide and the Bragg gratings result from the same index change mechanism and thus the contrast of the Bragg gratings can be controlled without altering the strength of the waveguide. In addition, the DGW technique is highly flexible in that a wide range of Bragg grating periods can be realised with the same setup of the system; ideal for rapid prototyping of Bragg grating bases integrated optical devices.

3.5.1 Direct UV grating writing free space optical set-up

The free space optical set up of the direct UV grating writing system is shown below in **Fig.3.10**. The optical set-up consists of a continuous wave argon-ion laser operating in the frequency doubled 488 nm regime, i.e. 244 nm at an output power of ~80 mW. The laser beam from the argon-ion laser is directed into an acousto-optic modulator (AOM) that modulates the amplitude of the beam, resulting in the power of the laser being reduced to ~40 – 50 mW. The AOM is used to modulate the intensity of the laser beam for writing of Bragg gratings. The laser beam then passes through a free-space optical set-up containing mirror until the propagating beam is above the translation stage. At this point the beam passes through a beam splitter to produce the two identical UV laser beams, which are then focussed into a spot of ~4 μm using a pair of identical lenses (numerical aperture = 0.18 and focal length of 40 mm) on the waveguide core layer to produce the interference pattern. The focussed beam spot contains approximately 7 periods.

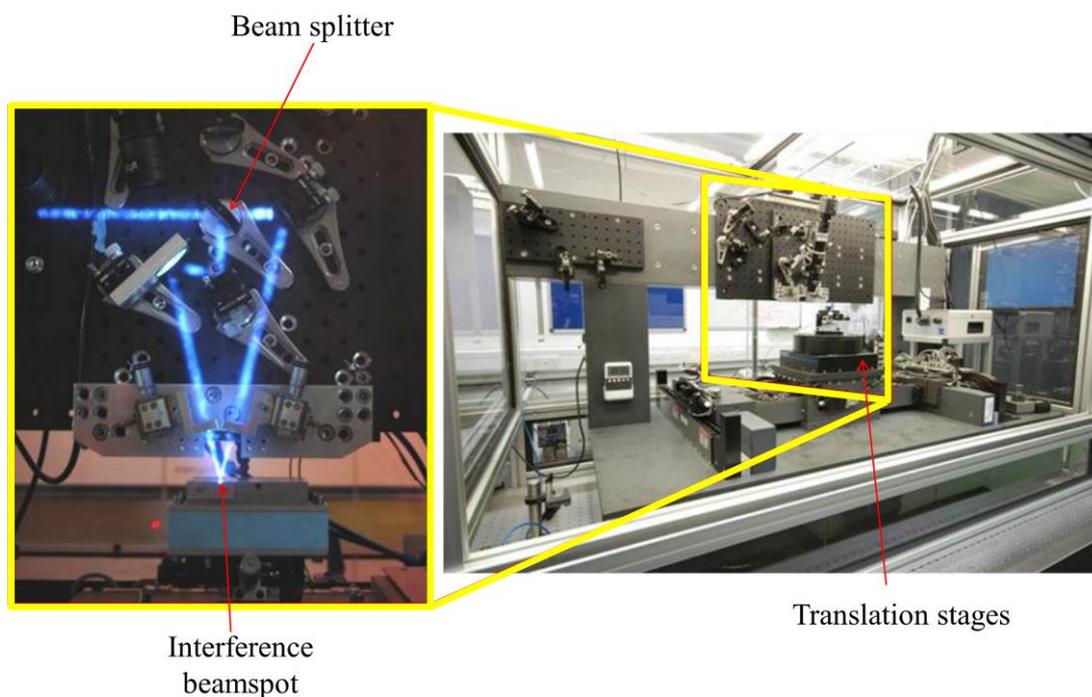


Fig.3.10: Photograph of the free space optical set-up of the direct UV grating writing system. Original photographs courtesy of Dr James Gates⁴³.

A high degree of positional accuracy in the stages is required to enable precise writing into the photosensitive waveguide core. This is achieved through use of computer-controlled air-bearing translation stages which have ~10 nm positional accuracy. The translation of the stages in the x,y & z axes is controlled by G-code, a

standard CNC (computer numerically controlled) software tool, thus the writing process is fully automated. The combination of the translation of the sample under the interference beam spot and the modulation of the intensity of the laser beam with the AOM, enables the writing of Bragg gratings.

3.5.2 Direct UV grating writing of Bragg gratings in the telecoms C band

To achieve definition of Bragg gratings that operate in the telecoms C band (1530 – 1565 nm), the angle of the two beams must be set so as to achieve the required periodicity. For Bragg gratings in the telecoms C band, if the effective index of a guided mode in a UV-written waveguide is taken to be ~ 1.445 then by rearrangement of the Bragg condition (**Eqn.3.4** below, as defined in **Chapter 2**) in terms of the period, Λ , then required period is ~ 540 nm.

$$\lambda = 2n_{eff}\Lambda$$

Eqn.3.4

The crossing angle between the two beams, θ , is then given by,

$$\theta = 2\arcsin\left(\frac{\lambda_{UV}}{2\Lambda}\right)$$

Eqn.3.5

where λ_{UV} is the wavelength of the UV laser. For example, an angle of 26° intersecting the two beams will correspond to a period of 542 nm which will in turn produce a Bragg grating that has a Bragg wavelength of 1566 nm.

It should be noted that the technique of direct UV grating writing is similar to the side exposure dual UV beam fibre technique used to fabricate Bragg grating in optical fibres. However, the spot size of the direct UV grating writing technique (~ 4 μm) is far smaller than the spot size used in the side exposure dual UV beam fibre technique (~ 100 μm). This limits the channel waveguides to a single guided mode and also allows for greater control over Bragg grating fabrication.

However, the basic description of how the direct UV grating writing technique functions given thus far suggests that to write several Bragg gratings with different Bragg wavelengths (thus of different periods), the angle intersecting the two beams

would have to be altered each time. In fact the direct UV grating writing technique has been developed to overcome this limitation, thus enabling the definition of grating periods around the intrinsic grating period value, without the need to alter the angle intersecting the two beams. This allows for multiple Bragg grating with different periods to be written along a single waveguide in a single writing run. This is achieved through detuning of the interference pattern.

Detuning of the interference pattern is achieved by introducing an additional displacement, Δ , subtracted from or added to the inherent period of the interference pattern, Λ , thus resulting in a Bragg grating period of $\Lambda \pm \Delta$. There is a limit to how far the period can be shifted, or detuned; the greater the detuning of the inherent interference period, the weaker the reflectivity of the Bragg grating. However, this technique has enabled the writing of Bragg gratings in all the telecommunication bands (E, S, C, L and U), a spectral window of 1400 nm up to 1700 nm, with the intersecting angle between the beams kept at $\sim 26^\circ$.

Other variables that can be varied across the length of a Bragg grating are the duty cycle, the pitch and the refractive index. Deviation of these variables across the length of a Bragg grating will alter the spectral response of the Bragg grating. These changes are commonly engineered into the Bragg grating during the direct UV grating writing process, but also can be the result of physical changes in the grating or exposure to a chemical.

3.5.3 Duty cycle

To achieve the strongest reflected Bragg spectrum for a written Bragg grating, the refractive index of the Bragg grating needs to be matched to the refractive index of the waveguide leading up to the Bragg grating. If an average refractive index value is taken as the refractive index of the Bragg grating and this is compared to the average index of the waveguide preceding the Bragg grating, it is clear to see that the greater the index contrast between the two interfaces the greater the percentage of unwanted Fresnel reflections. To overcome, this impedance or index matching of the Bragg grating to the waveguide is performed. This achieved by adapting the fluence such that the duty cycle is taken into consideration, where the duty cycle is defined as the

fraction of the distance of a single period for which the laser is on, as shown in Fig.3.11 below.

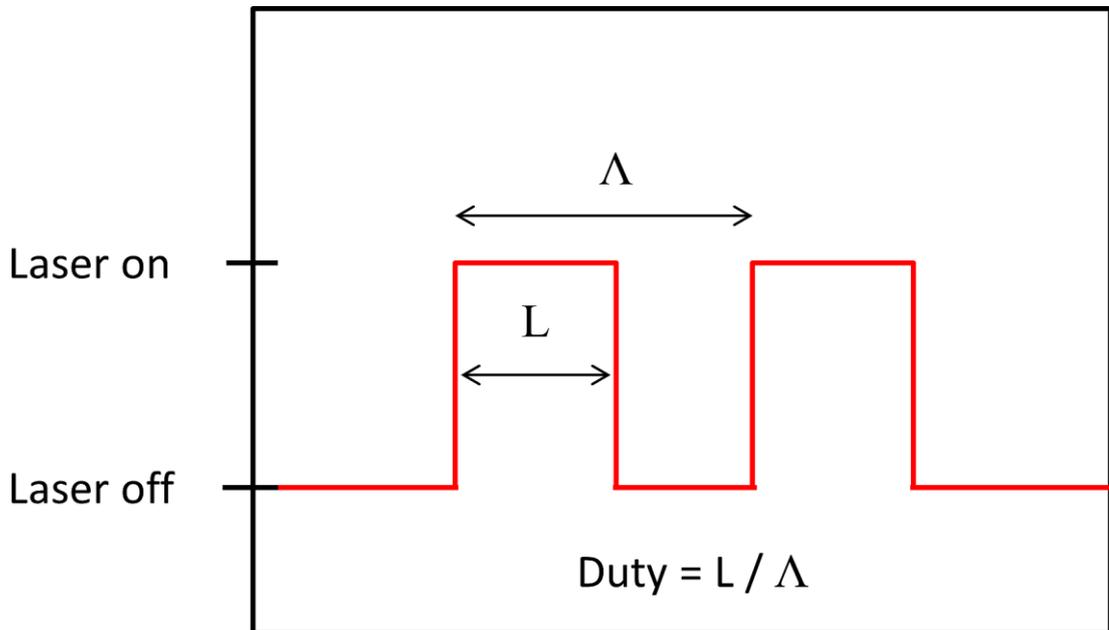


Fig.3.11: Schematic of the laser duty cycle. Note: This schematic refers to the switching on and off of a continuous wave laser and not a pulsed laser.

A duty cycle of zero corresponds to the laser being continuously off during the writing run and thus no index structure is defined in the waveguide core layer. In contrast a duty cycle of one corresponds to the laser being continuously on during the writing run and thus a channel waveguide is defined in the waveguide core layer. The lower the duty cycle, the higher the index contrast for impedance matching to occur⁴⁴. However, if the index contrast is high, then the fluence must also be high and thus with laser power a constant, the time taken to define the structure will be long. However, the time available to write the device with a high degree of photosensitivity enhancement afforded by hydrogen loading is defined by the rate of hydrogen out-diffusion. Thus, there is a maximum achievable refractive index change that is limited by the photosensitivity of the waveguide core layer and thus there exists a value of the duty cycle which results in the highest reflected power from the Bragg grating. Previous investigations have suggested the value of the optimal duty cycle is highly dependent upon the wafer used and on the fluence, but generally is ~ 0.35 ⁴⁴. The Bragg gratings used in this work were defined with a duty cycle of 0.5 at a fluence of 20 kJcm^{-2} .

3.5.4 Grating engineering

As described in **Chapter 2**, the spectral response of a Bragg grating can be approximated by taking the Fourier Transform of the physical shape of the Bragg grating. Uniform Bragg gratings have a physical shape that can be approximated with a ‘top-hat’ function and thus the expected spectral response approximates to a ‘sinc’ function. However, the spectral side lobes of uniform Bragg gratings can be an issue when determining the spectral information of Bragg gratings that are spectrally located close together. The side lobes can be suppressed by a form known as apodisation. There are many types of apodisation ⁴⁵, but the Bragg gratings used in this work were Gaussian apodised. Gaussian apodisation was chosen due to the Fourier Transform of a Gaussian function approximating to a Gaussian response. Thus, a Bragg grating written with the physical structure of a Gaussian function will have an approximately Gaussian spectral form as shown in **Fig.3.12** below.

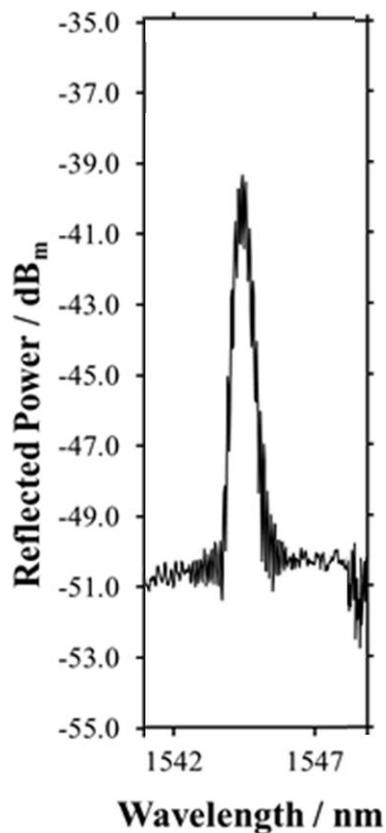


Fig.3.12: The Bragg peak of a Gaussian apodised Bragg grating demonstrating high side-lobe suppression

Over each consecutive period, the average refractive index of a Bragg grating with Gaussian apodisation must remain constant, because otherwise unwanted spectral

fringes can arise due to Fabry-Perot resonances. The Fabry-Perot resonances are formed by light becoming trapped in peripheral sections ^{45,46}. To achieve period-averaging for a Gaussian apodised Bragg grating, the duty cycle and the induced index change are given a Gaussian form profile.

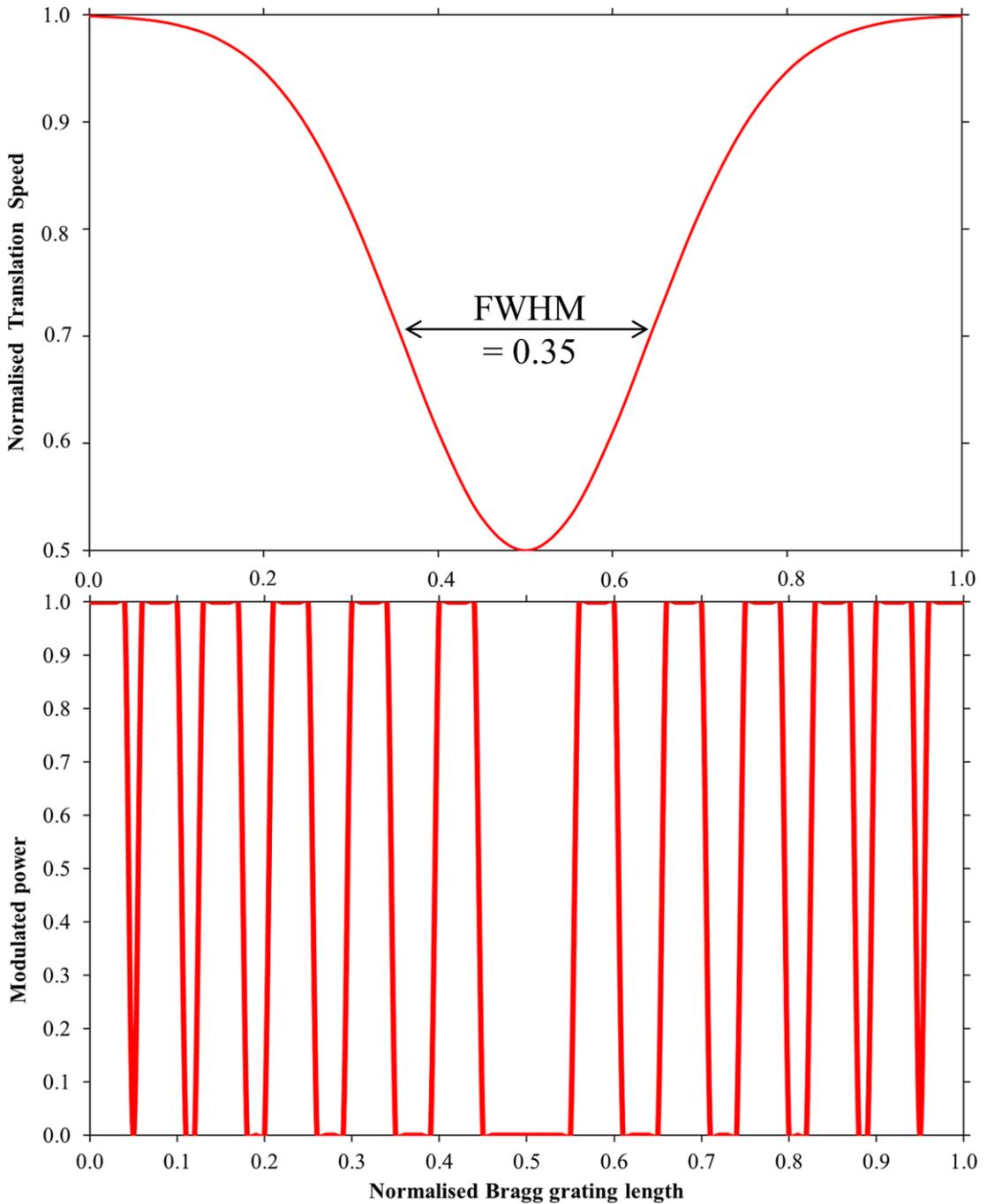


Fig.3.13: Variations in the fluence, achieved by a dynamic translation speeds and dynamic modulated power over the length of the normalised Bragg grating, to achieve a constant period averaged refractive index

For a true grating response that was Gaussian, the length of the Bragg grating would need to be infinite. As the Bragg gratings in the sensors have finite length, this physical limiting of the Gaussian grating structure results in spectral cropping of the Gaussian form; the shorter the structure the greater the deviation from an Gaussian profile form. However, previous experimental work has determined that Gaussian apodised grating with a FWHM set to 35% of the length of the grating, gives significant side-lobe suppression without comprising the strength of the grating or introducing spectral ringing, for a typical length Bragg grating ⁴⁶.

3.6 Bragg grating device characterisation and packaging

Once an optical circuit consisting of waveguides containing Bragg grating, has been written into the waveguide core layer, the spectral response of the waveguides and Bragg gratings are optically interrogated. This interrogation step is used to test the light guiding ability of the waveguides and also to calibrate the properties of the Bragg gratings e.g. the reflectivity and effective index before any modifications to the sensor device are made for sensing applications.

As mentioned in the previous section, hydrogen loading was used to increase the photosensitivity of the germanosilica layer before direct UV-writing. The hydrogen within the glass matrix will readily start to out-diffuse upon exposure to room temperature occurs. Over a period of ~3 hours, a time period in which UV-writing and subsequent characterisation is usually achieved, most of the hydrogen has out-diffused. However, significant differences have been observed between the output Bragg spectrum of a device that been exposed to room temperature conditions for 3 hours and the Bragg spectrum of the same device after exposure to room temperature for >12 hours ⁴⁷. The mechanism of this process is a phenomenon is not fully understood and is beyond the scope of this thesis. Therefore, all devices in this work were stored at ~50 °C for ~12 hours, before characterisation and use, to ensure all hydrogen had out-diffused and the Bragg grating spectrum for the device was stable.

After storage of the device in ~50 °C for at least 12 hours, the device was characterised. This was achieved by aligning one end of an optical fibre to the end of the UV-written waveguide, the other end of the optical fibre being connected to the optical interrogation set-up. The Bragg device is placed on a vacuum chuck and the fibre is brought into contact with one of the end facets. HeNe laser light (633 nm) is

guided through the fibre into the device and the output light from the other end facet of the device is focussed onto a beam stop with a 4x or 10x magnification lens. The Bragg device is manipulated in the x, y and z axes until the output light pattern is a horizontal red line containing dots which shows the presence of waveguides. Once a waveguide is found in this way, the source is then switched to an amplified stimulated emission (ASE) broadband infrared source; the broadband infrared light is launched down the same fibre into the Bragg device. Depending upon the Bragg condition, as described in **Chapter 2**, the infrared light is either coupled back into launch fibre due to reflection from a Bragg grating or it is transmitted out the end of the waveguide (this too can be coupled to another fibre to enable transmission spectrum to be collected). The Bragg device is manipulated further in the x, y and z axes, i.e. the alignment with the fibre is refined, until the output light pattern, imaged with an infrared sensitive CCD camera, is a horizontal white line containing bright dots which shows the presence of waveguides. Once the alignment of the optical fibre to the Bragg device is refined, characterisation is achieved with the following optical set-up.

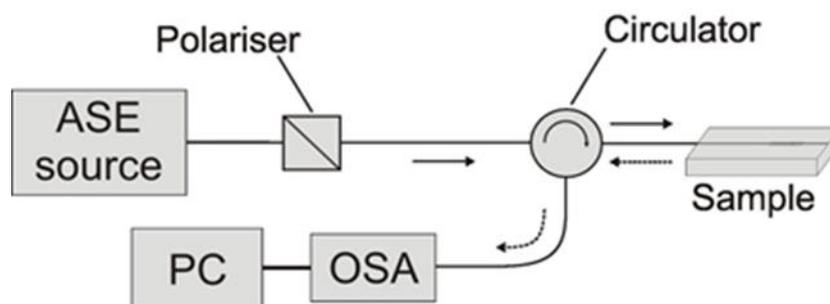


Fig.3.14: Schematic of the optical interrogation set-up used to characterise the Bragg devices in reflection mode. OSA = Optical Spectrum Analyser, ASE Source = Amplified Stimulated Emission Source, Sample = the Bragg grating sensor device.

Through a circulator, the infrared light reflected back from the Bragg gratings is guided through the optical fibres to an optical spectrum analyser (OSA), on which the reflected Bragg grating spectrum is visualised. An optical circulator is a variant of a Faraday Isolator, a component which transmits light in one direction from an input port, but does not transmit light in the opposite direction from the opposite input port⁴⁸. The circulators used in this work typically had three input ports: light in

at port 1 would exit port 2, light in at port 2 would exit port 3 and light in at port 3 would exit at port 1.

At this stage, fine tuning of the alignment is achieved by maximising the signal-to-noise ratio of the Bragg grating peaks. The spectral data is then transferred to a computer running *LabView* software via a general purpose interface bus (GPIB) connection. A purpose built programme in *Labview* utilises an algorithm (originally written by J.C. Gates ⁴³) that fits Gaussian profiles, based on a least squares fitting method, to the Bragg peaks in the reflected Bragg spectrum. The equation of the Gaussian profile that is fitted to the Bragg grating peaks is given below,

$$P = a + b \exp \left[- \left(\frac{\lambda - c}{d} \right)^2 \right]$$

Eqn.3.1

Where P is the reflected power, λ is the wavelength, a is the background intensity, b is the amplitude of the Bragg peak, c is the central Bragg wavelength and d is the bandwidth. The need for a good Gaussian fit is of paramount importance. If the spectral response of the Bragg grating is not a true Gaussian, a good fit of the algorithm with the Bragg peak will not be achieved which will in turn lead to poor resolution of the Bragg peak parameters as shown above in **Eqn.3.1** above. Poor resolution of the central Bragg wavelength will result in poor resolution of changes in refractive index. In addition, weak reflection and/or poor spectral response of a Bragg grating leads to an increased signal to noise ratio and possibly spectral fringes to move across the Bragg peak, further hindering peak fitting.

For long term interrogation of the Bragg grating device, during sensing experiments for example, an optical fibre pigtail can be used instead of just the optical fibre. An optical fibre pigtail is a length of optical fibre where one end is fitted with a fibre connector and the other end facet of the fibre is mounted into a silicon V-groove. The silicon V-groove can be aligned to the device in the exact manner as an optical fibre is aligned, but also enables permanent attachment of the fibre to the Bragg device using optical grade UV-curing epoxy glue. The resulting Bragg grating device is more robust can withstand prolonged constant use and larger temperature differentials. However, exposure to organic solvents is an issue; the solvents are able

to soften and eventually dissolve the epoxy glue. This issue was overcome through use of a silicone rubber sleeve surrounding the joint between the Bragg grating device and the V-groove of the pigtail, without affecting the optical performance of the device.

3.6.1 Polarisation and stability

The differing refractive index profiles along and across the planes of the FHD deposited waveguide core layer result in asymmetry along the length of the UV-written waveguide. This leads to the phenomenon of birefringence between the Transverse Magnetic (TM) and the Transverse Electric (TE) modes, which are orthogonally polarised. The birefringence of the two transverse modes can result in the modes exhibiting different responses to changes in refractive index, thus it is crucial that the TE and TM modes are distinguished and separated.

Separation of the transverse modes is typically achieved through the use of an optical PM polariser and polarising maintaining (PM) components, including a PM pigtail. As shown above in **Fig.3.14**, a PM polariser, with typically a low return loss of > 60 dB, is introduced into the optical characterisation set-up. The PM polariser polarises the light and the output light of the polariser is then aligned either parallel or perpendicular to the axis of a connected PM fibre. This set-up maintains the polarisation of the light from the PM polariser through the PM pigtail and into the planar waveguide, thus ensuring that the light launched into the waveguide is at one polarisation. The input polarisation can be changed between the two orthogonal polarisation states by using either a linear or a 90° rotated fibre connector. The main advantages of this polarisation selection method are that the need to restrict movement of the optical fibre interconnects to maintain the correct polarisation is removed and it also is a reproducible and robust method to select and switch between the orthogonal polarisations.

The direct UV-writing system is capable of producing strong Bragg gratings with good quality Gaussian responses in the reflectance spectrum. This enables good fitting of the Gaussian profile to allow for determination of central Bragg wavelength with potential sub-picometre resolution of the Bragg wavelength achievable. Most 'noise' on a trace of the Bragg wavelength over time exists in the form of wavelength drift due to the high sensitivity Bragg gratings tracking changes in

temperature and strain rather than an uncertainty in the measurement. These effects can be normalised through use of a reference Bragg grating as explained in **Chapter 6**, or through use of a thermocouple. The reference Bragg gratings used in the device reported in this thesis are not functionalised and are uncovered, thus deposition on the sensor surface of particulates or precipitates, while in use, can occur. This can lead to corruption of the Bragg response, thus leading to increases the ‘noise’ on the signal. Therefore, cleaning of the surface of the reference Bragg gratings was performed, when required, before sensing experiments.

3.7 Summary

A silica waveguide core layer is fabricated on a silica-on-silicon substrate using the flame hydrolysis deposition (FHD) technique. The silica waveguide core layer is photosensitive to UV light thus allowing for the use of the direct UV grating writing method for simultaneous definition of waveguides, containing Bragg grating, within it. The direct UV grating writing method is based upon the localised refractive index increase ($\sim 5 \times 10^{-3}$) induced within the photosensitive waveguide core layer due to exposure to a tightly focussed UV laser beam. The UV photosensitivity of the waveguide core layer is introduced by doping with germanium and further enhanced by hydrogenating the sample at a pressure of 120 bar for approximately one week.

The Bragg gratings can be written to operate a variety of wavelengths but mostly are written to operate in the 1400 nm to 1700 nm wavelength region to make use of the abundance of telecoms equipment which operates in this wavelength region. The different wavelength Bragg gratings are achieved by detuning and modulating the inherent interference pattern produced by the overlap of the two focussed and coherent UV laser beams, used in the direct UV grating writing technique.

The reflectance spectrum from the Bragg grating device, in the infrared region, is analysed remotely by commercial telecoms test and measurement equipment via a fibre pigtail, allowing for sub-picometre resolution of the central wavelength of Bragg peaks. Overall the direct UV grating writing method allows for the production of a broad range of optical devices based around combinations of fully customisable Bragg gratings and channel waveguides. This has an advantage over conventional photolithographic and etching techniques, as it allows for rapid prototyping and small scale fabrication at reduced costs.

1. I. J. G. Sparrow, PhD Thesis, University of Southampton, 2005.
2. S. E. Miller, *Bell Syst. Tech. J.*, 1969, **48**, 2059.
3. H. Teichmann, in *Sensors A Comprehensive Survey: Volume 8 Micro- and Nano- Sensor Technology/ Trends in Sensors Markets*, eds. W. Gopel, J. Hesse, and N. Zemel, VCH, Weinheim, 1995, pp. 222–258.
4. R. M. Parker, PhD Thesis, University of Southampton, 2010.
5. T. Caves, *Laser Focus World*, 2001, 219.
6. J. P. Bange, L. S. Patil, and D. K. Gautam, *Progress Electromagn. Res. M*, 2008, **3**, 165–175.
7. J. M. Ruano, V. Benoit, J. S. Aitchison, and J. M. Cooper, *Anal. Chem.*, 2000, **72**, 1093–1097.
8. R. Kazarinov, in *Papers on Optical Access Networks EFOC & N '93 Eleventh Annual Conference*, The European Institute for Communications and Networks, The Hague, 1993, pp. 22–24.
9. P. Tandon and H. Boek, *J. Non. Cryst. Solids*, 2003, **317**, 275–289.
10. M. Svalgaard, Technical University of Denmark, 1997.
11. M. Svalgaard and M. Kristensen, *Electron. Lett.*, 1997, **33**, 861.
12. S. E. Alexandrov and M. L. Hitchman, in *Chemical Vapour Deposition Precursors, Processes & Applications*, eds. A. C. Jones and M. L. Hitchman, RSC Publishing, 2009, pp. 494–534.
13. D. W. Hess, *Ann. Rev. Mater. Sci.*, 1986, **16**, 163–183.
14. G. Grand, J. P. Jadot, H. Denis, S. Valette, A. Fournier, and A. M. Grouillet, *Electron. Lett.*, 1990, **26**, 35–37.
15. M. V. Bazylenko, M. Gross, P. M. Allen, and P. L. Chu, *IEEE Photonics Technol. Lett.*, 1995, **7**, 774–776.
16. K. O. Hill, Y. Fujii, D. C. Johnson, and B. S. Kawasaki, *Appl. Phys. Lett.*, 1978, **32**, 647–649.
17. B. S. Kawasaki, K. O. Hill, D. C. Johnson, and Y. Fujii, *Opt. Lett.*, 1978, **3**, 66–68.
18. D. K. W. Lam and B. K. Garside, *Appl. Opt.*, 1981, **20**, 440–445.
19. D. P. Hand and P. S. J. Russell, *Opt. Lett.*, 1990, **15**, 102–104.

20. G. Meltz, W. W. Morley, and W. H. Glenn, *Opt. Lett.*, 1989, **14**, 823–825.
21. M. Douay, W. X. Xie, T. Taunay, P. Bernage, P. Niay, P. Cordier, B. Pournellec, L. Dong, H. Bayon, H. Poignant, and E. Delevaque, *J. Light Technol.*, 1997, **15**, 1329–1342.
22. A. Wootton, B. Thomas, and P. Harrowell, *J. Chem. Phys.*, 2001, **115**, 3336–3341.
23. L. Zheng, J. C. Lambropoulos, and A. W. Schmid, *J. Non Cryst. Solids*, 2003, **347**, 144–152.
24. T. L. Cottrell, *The Strengths of Chemical Bonds*, Butterworth, London, 2nd edn., 1958.
25. P. J. Lemaire, in *Optical Fiber Communications Conference*, Optical Society of America, San Diego, California, 1995, vol. 8, p. WN5.
26. D. S. Starodubov, E. M. Dianov, S. A. Vasiliev, A. A. Frolov, O. I. Medvedkov, A. O. Rybaltovski, and V. A. Titova, in *Photonics West '97*, ed. M. P. Andrews, International Society for Optics and Photonics, San Jose, 1997, pp. 111–121.
27. C. Holmes, PhD Thesis, University of Southampton, 2009.
28. M. Kristensen, *Bragg Gratings White Paper*, 2005.
29. J. Crank, *The Mathematics of Diffusion*, Oxford University Press, Oxford, 2nd edn., 1975.
30. P. J. Lemaire, *Opt. Eng.*, 1991, **30**, 780–780.
31. M. Svalgaard, *Electron. Lett.*, 1999, **35**, 1840–1842.
32. E. A. Chandross, *Appl. Phys. Lett.*, 1974, **24**, 72.
33. M. F. R. Adikan, J. C. Gates, A. S. Webb, H. E. Major, C. Holmes, M. A. G. Ramirez, B. D. Snow, D. O. Kundys, C. B. E. Gawith, and P. G. R. Smith, in *13th European Conference on Integrated Optics (ECIO 2007)*, 2007.
34. M. Kawachi, *Opt. Quantum Electron.*, 1990, **22**, 391–416.
35. M. Gnan, H. N. H. Chong, and R. M. De La Rue, in *Proceedings of the 12th European Conference on Integrated Optics FrA1-5*, Grenoble, 2005, pp. 310–313.
36. K. M. Davis, K. Miura, N. Sugimoto, and K. Hirao, *Opt. Lett.*, 1996, **21**, 1729.
37. G. D. Marshall, M. Ams, and M. J. Withford, *Opt. Lett.*, 2006, **31**, 2690.

38. S. Nolte, M. Will, J. Burghoff, and A. Tuennermann, *Appl. Phys. A Mater. Sci. Process.*, 2003, **77**, 109–111.
39. S. M. Eaton and P. R. Herman, in *Femtosecond Laser Machining Photonic and Microfluidic Devices in Transparent Materials*, eds. R. Osellame, G. Cerullo, and R. Ramponi, Springer-Verlag, Heidelberg, 2012, pp. 155–196.
40. G. D. Emmerson, S. P. Watts, C. B. E. Gawith, V. Albanis, M. Ibsen, R. B. Williams, and P. G. R. Smith, *Electron. Lett.*, 2002, **38**, 1531–1532.
41. C. Sima, J. C. Gates, H. L. Rogers, P. L. Mennea, C. Holmes, M. N. Zervas, and P. G. R. Smith, *Opt. Lett.*, 2013, **38**, 727–9.
42. J. C. Gates, S. G. Lynch, P. L. Mennea, P. A. Cooper, S. Ambran, H. L. Rogers, L. G. Carpenter, C. Sima, D. J. Wales, C. Holmes, and P. G. R. Smith, in *Advanced Photonics 2013*, Puerto Rico, 2013.
43. J. C. Gates, University of Southampton.
44. G. Emmerson, PhD Thesis University of Southampton, 2003.
45. T. Erdogan, *J. Light. Technol.*, 1997, **15**, 1277–1294.
46. C. R. Giles, *J. Light. Technol.*, 1997, **15**, 1391–1404.
47. C. Holmes, *On-going work*, University of Southampton 2011.
48. R. Paschotta, *RP Photonics Encycl.*, 2013.

4 Evanescent Wave Gas Sensors

4.1 Introduction

Optical sensing can be broadly defined as the use of light to detect the change in a physical property, or the presence of a chemical/biochemical species over time ¹. Optical sensors demonstrate many benefits over electronic sensors, including remote interrogation of large sensor arrays via standard optical fibre and telecoms equipment, and do not present a spark risk in flammable environments ². One type of the many varied types of optical sensors, are sensors based on integrated optics. Integrated optical sensors demonstrate all the advantages of optical sensors in addition to the advantage of the miniaturisation and integration of multiple photonic functions on a single smart sensor device. Integrated optical sensors typically operate through monitoring of perturbation to an evanescent wave due to the presence of a biological or chemical species ³. The perturbation of the evanescent wave can be monitored through detection of changes in optical absorption, luminescence or refractive index. The sensors demonstrated within this thesis are evanescent wave integrated planar optical Bragg grating refractometric gas sensors; the perturbation of the effective index of the evanescent wave, due to the presence of a gas or vapour, is detected by monitoring changes in the Bragg wavelength. Therefore, to place this work within the context of the past and current evanescent field gas sensor literature, other evanescent wave gas sensor technologies are discussed below. For relevance and brevity only examples of evanescent wave based optical sensors for relative humidity, volatile organic compounds and acidic/basic gases are given for comparison with the planar Bragg grating sensors for relative humidity, volatile organic compounds and acidic/basic gases that are demonstrated in the subsequent results and discussion chapters.

4.2 Optical fibre evanescent wave gas sensors

The field of optical fibre based sensing has burgeoned over the 40 years since inception, when a patent for an optical fibre based ‘Fotonic sensor’ was granted in the U.S.A. ⁴. The rapid growth in the field of optical fibre based sensing can be attributed to several factors ⁵, such as the various waveguiding structures that can be realised in optical fibres and low optical loss. In addition, optical fibres allow for optical measurement of analytes over long distances, at sites inaccessible to conventional spectroscopy techniques. In addition sensing is possible at multiple points along the length of a fibre; this is known as distributed sensing.

There are two broad categories of optical fibre based sensors: extrinsic and intrinsic. Extrinsic optical fibre based sensors involve the transmission of propagating light from an optical fibre into another material, whereupon the light undergoes modulation by the parameter of interest. After modulation, the light is collected into the same, or another optical fibre, and the light propagates to the optical interrogation equipment ⁴. In contrast, intrinsic optical fibre based sensors involve the propagating light remaining in the optical fibre along the entire length of the optical fibre; the parameter of interest modulates the propagating light within the fibre ⁴. An evanescent wave optical fibre based sensor is an example of an intrinsic optical fibre based sensor.

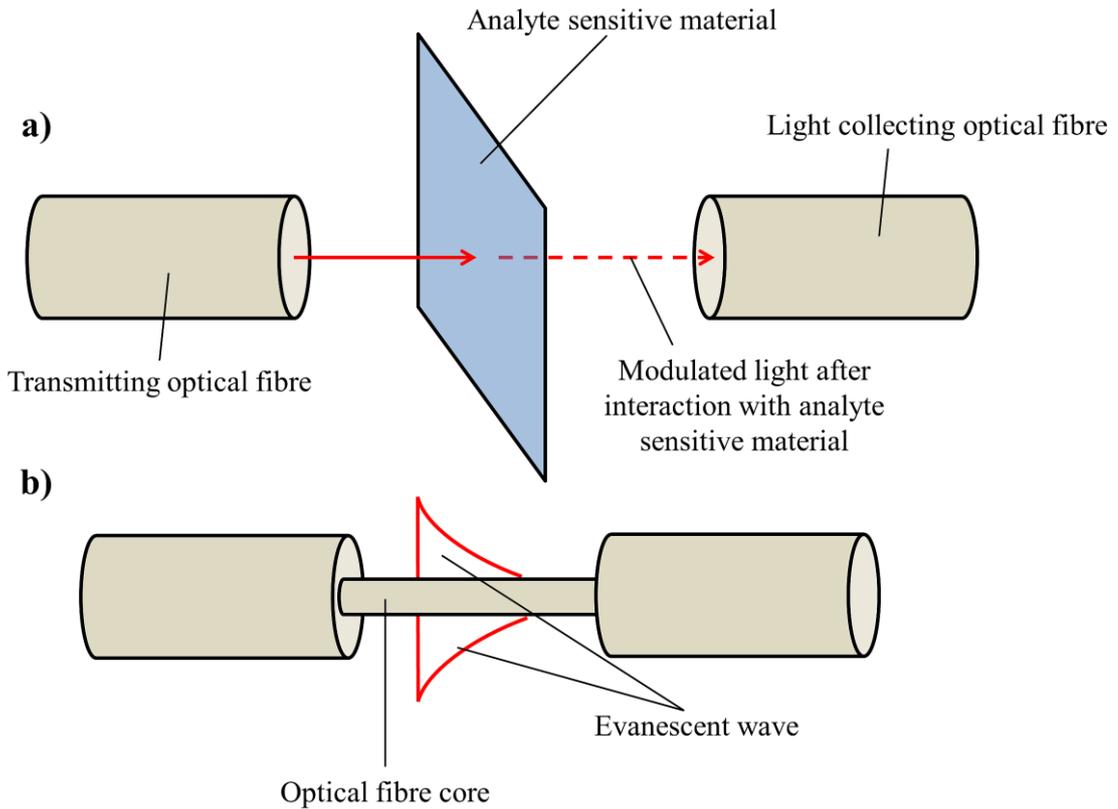


Fig.4.1: (a) Pictorial representation of an extrinsic optical fibre sensor set-up and (b) pictorial representation of an intrinsic optical fibre sensor set-up, in this case an optical fibre evanescent wave sensor. NOT TO SCALE.

Evanescent field optical fibre based sensors operate by transducing the interaction of the evanescent wave of the propagating light within an optical fibre with an external measurand gas into a measurable and quantifiable change in the properties of the transmitted (or reflected) light. This technique is known as fibre-optic evanescent wave spectroscopy (FEWS)⁶. This is typically achieved by stripping away the protective outer cladding of the optical fibre and exposing the core of the fibre to the measurand gas. The core of the fibre can either be left bare⁷ or can be functionalised with a material, the properties of which change upon exposure to the measurand gas⁸. The former approach relies on the measurand gas possessing characteristic absorption at, or near to, the wavelength of the propagating light⁵. The latter approach allows for the functionalisation of the optical fibre with materials that demonstrate selectivity for certain measurand gases against other gases; selectivity is imparted to the sensing system. The interaction of the evanescent wave with either the measurand gas directly, or the coating material that has interacted with the

measurand gas, can cause a change in absorption, effective index or luminescence, which is measured and quantified⁹.

Wolfbeis has written several thorough reviews on fibre optical sensors for biological and chemical analytes, including gases¹⁰⁻¹³. In these reviews the different approaches necessary to achieve sensing of many varied gases and vapours have been outlined. For relevance and brevity, in this thesis, some examples of fibre optic evanescent wave sensors for relative humidity, volatile organic compounds and acidic/basic gases only are given. In addition, it must be noted that there are many examples in the literature of evanescent wave optical fibre gas sensors that contain Bragg gratings and thus Bragg wavelength shifts are measured. However, these will be treated here in this section, but in a later section on grating coupler evanescent wave sensors.

4.2.1 Optical fibre evanescent wave relative humidity sensors

For sensing of relative humidity (%RH), the core layer of an optical layer can be coated with biopolymer materials that swell in the presence of water vapour. The swelling of the material causes a change in the effective index of the evanescent wave and thus modulates the light propagating through the fibre. Mathew *et.al.* utilised films of biopolymeric material, either chitosan or agarose, as the moisture swelling material¹⁴. The sensitivity to change in relative humidity was determined by measuring the attenuation of the transmitted light through the optical fibre segment that was coated with the film of biopolymer. The resulting fibre optic sensors demonstrated good reversibility, low hysteresis and fast response times on the order of seconds¹⁴. However, the agarose film sensor displayed non-linear behaviour at 20 – 40 %RH and due to the experimental set-up the sensitivity to %RH values below 17 %RH was not explored for either sensor¹⁴. In addition, the thermal stability of the biopolymer films must be taken into consideration¹⁵. Gaston *et al.* used a similar approach, but instead of a biopolymer swelling material, polyvinyl alcohol (PVA) was used¹⁶. The side-polished fibre demonstrated a linear variation in transmitted power of ~ 10 dB between 70 – 85 %RH. The authors proposed that when the PVA coating was dry, the film had a higher refractive index than the fibre, thus the propagating guided modes encountered a region with a lossy cladding. However upon exposure to water, the authors proposed that the PVA layer became swollen, which reduced the refractive index of the film and in turn lowered the

optical power losses in the region of the fibre covered by the PVA film¹⁶. However, the sensor displayed non-linear response at some %RH values (50 – 70 %RH) and little to no sensitivity to relative humidity in the 30 – 50 %RH range¹⁶.

4.2.2 Optical fibre evanescent wave hydrocarbon and VOC sensors

The field of the sensing and detection volatile organic compounds (VOCs) with optical fibres sensors has been active for over 25 years¹⁷. Therefore, there are many examples of optical fibre based VOC sensors, which have been thoroughly reviewed^{17,13}.

Hydrocarbons have distinct and characteristic absorptions in the mid-infrared (MIR) region of the electromagnetic spectrum. This allows for bare intrinsic evanescent wave optical fibre based sensors to be operated in the MIR wavelength regime for the detection of gaseous hydrocarbons; the MIR wavelength evanescent wave is strongly absorbed by the gaseous hydrocarbons. However, sensing in the MIR wavelength regime requires the use of MIR-transmitting optical fibres, such as chalcogenide or silver halide optical fibres which are intrinsically more expensive and less readily available, compared to common-place silica optical fibres¹⁸. However, Tai *et.al.* reported a evanescent wave optical fibre sensor for methane that was operated at the 3.392 μm line of a He-Ne laser and used silica optical fibre¹⁹. The 3.392 μm line of a He-Ne laser was chosen as it matches closely with a strong absorption feature of methane. The lowest detectable concentration was 1%, which is lower than the lowest explosive limit of 5%¹⁹. However, the high intrinsic losses at 3.392 μm in silica meant that the sensing fibre had to be limited to a length < 40 cm; unsuitable for remote and distributed sensing¹⁹.

In contrast, Schwotzer *et al* utilised the intrinsic strong electronic absorptions of organic molecules in the UV wavelength region for the sensing of solvent vapours in air¹⁸. A section of the UV-optimised quartz silica fibres was coated with either a film of polydimethylsiloxane or Teflon AF® and exposed to various solvent vapours. When a particular solvent was a good solvent for the polymer film covering, the solvent infiltrated the film and thus came into contact with the evanescent wave. This caused a change in the numerical aperture of the fibre and thus increased the transmission losses¹⁸. The resultant sensor could detect toluene

down to a few ppm in air ¹⁸, but the cost and lower availability of quartz fibre compared to standard silica fibre are prohibitive.

Abdelmalek *et al* demonstrated an evanescent wave fibre optic sensor that was modified with an ormosil sol-gel thin film ²⁰. The organically modified sol-gel thin film contained phenyl groups which favoured aromatic interactions with hydrocarbon solvents and the power of the transmitted light was monitored upon exposure to solvent vapours ²⁰. Good sensitivity to toluene and xylenes was achieved, but the 670 nm interrogation wavelength ²⁰ renders the optical fibre sensor system incompatible with readily available telecoms wavelength test and measurement equipment.

4.2.3 Optical fibre evanescent wave sensors for acidic and basic gases.

The application of optical fibre evanescent wave sensors for acidic and basic gases has also enjoyed attention over the past few decades. Typically optical fibre evanescent wave sensors for acidic and basic gases utilise the colour change of a pH chromic dye that is entrapped within an over layer, to modulate the transmitted or reflected light.

Grady *et al* demonstrated an evanescent wave fibre optic sensor that was modified with a polyvinyl chloride (PVC) film that was functionalised with nitrophenylazophenol calix[4]arene, a pH chromic molecule ²¹. The resultant sensor was used to sense ammonia gas and had a detection limit to ammonia gas of 5 ppm. However, the time taken for the optical signal measurement to return to baseline levels upon removal from an ammonia atmosphere was on the order of 1 h and the sensor device utilised a white light source to measure absorption changes at 500 - 520 nm ²¹. This renders this sensor system incompatible with readily available telecoms wavelength test and measurement equipment.

Scorsone *et al* demonstrated an evanescent wave fibre optic sensor that was modified with a poly(o-methoxyaniline) film for detection of both ammonia and hydrogen chloride gases ²². The fibre was sensitive to 50,000 ppm ammonia and 1000 ppm hydrogen chloride gas, over a broad range of wavelengths in the near-infrared (NIR) wavelength regime and the response time was on the order of 1 min ²². However the major disadvantage was the response of the modified fibre to the levels of ammonia and hydrogen chloride gas given above, was not reversible in ambient air ²².

4.2.4 Advantages and disadvantages of evanescent wave optical fibre sensors

Optical fibre facilitates the miniaturisation of conventional spectroscopy techniques, and introduced new unconventional spectroscopy techniques, such as fibre-optic evanescent wave spectroscopy. This allows for more compact spectroscopy systems that can be used in environments that are impractical for other spectroscopy techniques. In addition distributed spectroscopy and sensing can be realised over large areas. Removal of the cladding exposes the evanescent wave to the local gaseous environment and also enables functionalisation of the core of the fibre with materials that interact more strongly with certain gases over others; specificity can be introduced into the system. However, the main drawback of these sensors is that many of the components found within a conventional spectrometer, such as a white light source and appropriate detectors are still required to interrogate the optical fibre systems.

4.3 Surface Plasmon Resonance (SPR) sensors²³

The potential of surface plasmon resonance (SPR) technology, for monitoring processes and the characterisation of thin films at metal interfaces was recognized by Gordon II *et.al.* in the late seventies^{24,25}. Since then, the field of SPR sensing has enjoyed considerable research attention. In particular SPR research has focussed on optical biosensing, wherein SPR has shown great potential for use in affinity biosensing; real-time analysis of bio-specific interactions on the surface of the sensor without the use of labelled molecules²³. This great potential has led to the commercialisation of SPR sensor technology variants by several companies²⁶ and has led to SPR becoming a leading technology in the field of direct real-time measurement of biomolecular interactions²³. However, SPR has also been successfully used for gas sensing; the use of SPR for the detection of gases was first demonstrated by Nylander in 1982^{27,28}.

4.3.1 Plasmons²⁹

For a wide frequency range, a classical plasma model can be used to explain the optical properties of metals can be explained with a plasma model. This model describes an oscillation of free electron density relative to the positive ions, that are in fixed positions, within a metal. This oscillation of free electron density can be visualised as follows. If a cube of metal is placed in an external electric field, the

direction of which is to the right, then the free electron density will move to the left side. until the field inside the metal is cancelled. This results in the uncovering of the positive ions on the right side of the cube of metal. If the electric field is then switched off, the free electron density moves back to the right; this is driven by inter-electron electrostatic repulsion and electrostatic attraction to the positive ions on the right side. The free electron density will then oscillate back and forth at a frequency known as the plasma frequency until the applied energy is lost through resistance or damping. A plasmon is a quantisation of this type of oscillation of free electron density. If light, incident to a metal, is at a frequency below the plasma frequency of the metal, the light is reflected. This is because the electrons in the metal screen the electric field of the light. However, if light incident to a metal is at a frequency above the plasma frequency of the metal, the light is transmitted. This is because the free electron density cannot respond fast enough. In alkali metals, the plasma frequency is in the ultraviolet frequency regime thus making alkali metals reflective in the visible wavelength range. However, transition metals such as copper and gold, have electronic interband transitions in the visible wavelength region of the electromagnetic spectrum, thus specific wavelengths are absorbed. This gives rise to the distinct colours of these metals.

4.3.2 Surface plasmons

The first documented observation of surface plasmons was made by Wood in 1902 upon illumination of a metallic grating with polychromatic light ³⁰. However, Wood described these results as anomalies ³⁰. It wasn't until 1968 when Otto ³¹ and Kretschmann & Raether ³² published separately descriptions of surface plasmons in materials, that surface plasmons were fully understood. Surface plasmons are plasmons that are confined to a surface and that also interact strongly with incident light, resulting in a polariton, where a polariton is a quasiparticle that results from of the mixing of a photon with an quantised excitation of a material ²⁹. Surface plasmon resonances occur at the interface between two materials which have dielectric constants of opposite signs, such as at the interface between a metal and air ³³. A surface plasmon resonance is a charge-density wave that is associated with an electromagnetic wave which travels parallel to the interface between the two materials and is reflected by total internal reflection ³³. The field vectors of the surface plasmon resonance are maximum at the interface and the intensity decays

evanescently into both materials as a function of distance away from the interface³³. The distribution of the electromagnetic field of the surface plasmon wave is highly asymmetric, with the vast majority of the field is present in the dielectric material.

Incident electron or photons are used to excite surface plasmons in a resonant manner. For this to occur, the impulse of the incident emission source of photons or electrons has to match to the impulse of the plasmon. In the case of incident TM polarised light, this is achieved by passing the light through a block of glass. This increases the wavenumber (and the impulse) of the light, and thus resonance at a given wavelength and angle can be achieved. However, whilst incident TM polarised light with the correct impulse can result in a periodic variation in the surface charge-density, TE polarised light possesses only an electric field component that is parallel to the surface and thus is unable to induce a periodic variation in the surface charge-density that is necessary for the generation of surface plasmons²⁹.

Typical metals that strongly support surface plasmons are silver and gold³⁴, but other metals such as copper, titanium and chromium can also support surface plasmons³⁵. Owing to high losses in the metal within the visible and near-infrared wavelength regimes, the surface plasmon wave experiences high attenuation³⁶. However, a surface plasmon wave propagating along a silver surface is less attenuated, compared to gold, and also exhibits a higher degree of localization of the electromagnetic field in the dielectric.

A typical experimental set-up that is utilised for the generation of surface plasmon resonances is shown below in **Fig.4.2**. In this set-up, a metal film has been deposited onto a glass prism (by evaporative deposition) and the surface of the metal film is illuminated through the glass. An evanescent wave penetrates through the metal film. At a particular illumination wavelength and angle of incidence, the light is coupled to a surface plasmon wave on the bottom side of the metal film and there is absorption.

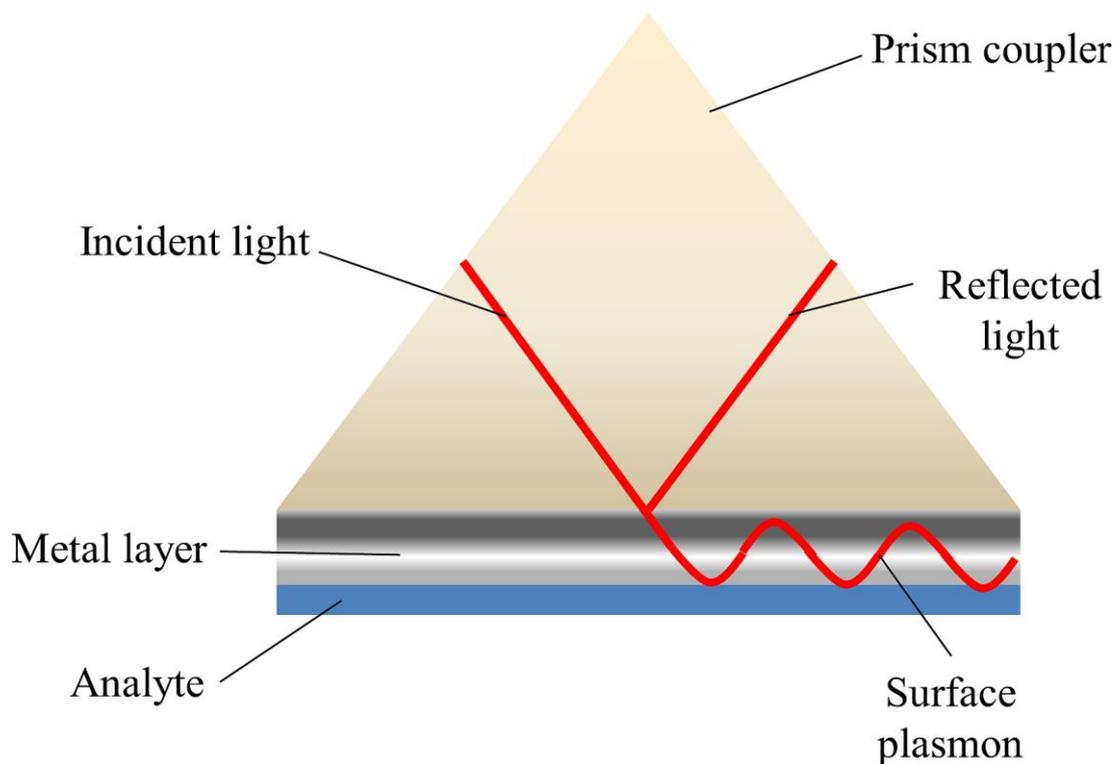


Fig.4.2: A schematic of the typical Kretschmann attenuated total reflectance (ATR) configuration for surface plasmon resonance sensing. This representative diagram is not scientifically exact nor to scale.

4.3.3 Utilising surface plasmons for sensing

The angle of incidence at which a surface plasmon is excited in the interface is highly dependent on the local refractive index near to the interface. At other angles where excitation of a surface plasmon does not occur, reflection of the incident light beams occurs. However, the angle at which excitation of a surface plasmon occurs can change due to changes in the refractive index local to the interface. Therefore, this can be exploited for sensing; if molecular sensing events are occurring within the evanescent wave near the interface the resonance conditions of the surface plasmon will change and thus the angle at which excitation of a surface plasmon occurs will also change. Therefore, SPR reflectivity measurements are used to detect adsorption of molecules such as polymers, DNA or proteins, at the interface. The angle at which reflection minimum occurs, changes in the order of 0.1° during absorption of thin (\sim nm thickness) film. In other cases, changes in the absorption wavelength, i.e. the wavelength of light required to excite a surface plasmon are monitored. This method of detection is also based on changes in the local index of refraction, caused by molecular sensing events, which cause the resonance

conditions of the surface plasmon wave to change. The sensitivity, stability, and resolution of SPR sensors depend upon the properties of both the optical interrogation system and the functionalised transducing metal/dielectric interface. In contrast, the selectivity and response time of the sensor are solely determined by the properties of the functionalised transducing metal/dielectric interface.

Sensor resolution is defined as the minimum change in the parameter of interest that can be resolved by a sensing device³⁷. The resolution of SPR sensors is dependent upon the accuracy with which the monitored SPR parameter (e.g. reflected intensity, angle of incidence or wavelength) can be determined by the specific sensing device. Thus, the resolution is limited by sensor system noise and the subsequent signal to noise ratio. The effect of the light source, thermal noise and noise in the photodetector on the total noise in SPR sensor systems, thus the resolution of SPR sensors has been systematically studied by Kolomenskii *et.al* and Chinowsky *et.al*.^{38,39}

The sensitivity of a SPR sensor is defined as the derivative of the monitored SPR parameter, e.g. the resonant angle, intensity or wavelength, with respect to the parameter of the analyte that is to be determined, e.g. the refractive index of the analyte, the analyte concentration etc.. It was determined by Homola *et. al* that the sensitivity of SPR sensors, where the angle of incidence was the monitored SPR parameter, increased with decreasing operation wavelength⁴⁰. However, in contrast Homola *et.al* determined also that the sensitivity of SPR refractive index sensors, where the wavelength or intensity of reflection was the monitored SPR parameter, increased with increasing wavelength⁴¹. In addition, it has been determined that the use of silver as the SPR-active metal instead of gold for SPR sensors where the wavelength or intensity of reflection is the monitored SPR parameter, increases the sensitivity of the SPR sensor device^{42,41}. The typical sensitivities of different SPR systems to changes in refractive index vary depending on the SPR sensor system used. A range of refractive index changes from 2×10^{-4} to 5×10^{-7} have been achieved⁹.

The operating range is also another important parameter of SPR sensors. The operating range is defined as the range of values of the parameter that is to be determined, which can be measured by the sensor. For example, the operating range

of a SPR sensor based on monitoring of the angular dependence SPR parameter can be limited by the angular range covered by the optical system-angular position detector array. Invariably there is a trade-off between the resolution and the dynamic operating range of SPR sensors.

4.3.3 Waveguide surface plasmon resonance sensors

Surface plasmon resonances can be excited in the metal layer, by the evanescent wave of light that is propagating in a waveguide that is interfaced with the metal layer. The use of optical waveguides to excite the plasmon modes can reduce the footprint of the SPR sensor, relative to ATR SPR sensor system, and improves ruggedness. In addition the sensitivity of waveguide-based SPR sensor devices is approximately equivalent to that of corresponding ATR SPR sensor systems. The excitation of a surface plasmon wave in a metal layer that is interfaced with an optical waveguide structure, is similar to the excitation of a plasmon wave in a Kretschmann ATR coupler, as shown above in **Fig.4.2**. A propagating lightwave is guided in the waveguide and upon encountering the interface region with the thin metal overlayer, the light can evanescently penetrate through the metal layer. If phase matching conditions are met, the light wave can excite a surface plasmon wave at the interface between the metal and analyte as shown pictorially in **Fig.4.3** below. The surface plasmon wave penetrates up to 200 nm into the analyte ⁴³.

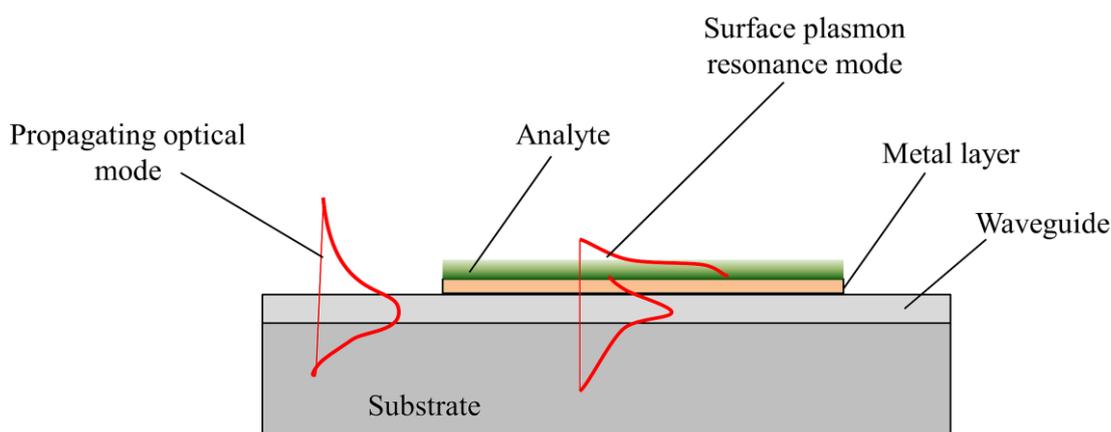


Fig.4.3: Schematic of an optical waveguide based surface plasmon resonance sensor, highlighting the evanescent wave of the surface plasmon resonance mode at the interface between the metal and the analyte.

The incorporation of the SPR sensor technique with integrated optics waveguide show promise for the realisation of multichannel sensing devices on one chip

combined with referencing and multi-component sensor analysis of complex samples. Researchers at the University of Twente pioneering research into integrated optical waveguide SPR sensors in the late eighties⁴⁴. Since then, multiple SPR-sensing devices have been realised in slab and channel single mode integrated optical waveguide devices.⁴⁵⁻⁴⁸ However, a major disadvantage of single-mode integrated optical SPR-sensing devices is that the devices typically exhibit limited operating ranges. There have been many attempts in the literature to tune and improve the operating range of these sensors, with most of the solutions focussing on the application of additional layers^{46,49-51}. However, these approaches to improve the operating range by introduction of additional layers were found to reduce the sensitivity of the SPR sensors. This was due to the reduced extent of the evanescent electromagnetic field that penetrated into the analyte.

4.3.4 Surface plasmon resonance relative humidity sensors

Weiss *et al* demonstrated a surface plasmon based integrated optic relative humidity sensors that utilised a Nafion fluoropolymer as the active transducer layer⁵⁰. The sensor device exhibited a reversible response and the response was linear, but only over the limited relative humidity range of 20 – 50 %RH. In addition, the refractive index sensitivity achieved was only 5×10^{-4} ⁵⁰.

4.3.5 Surface plasmon resonance sensors for hydrocarbons and volatile organic compounds

Aguirre *et al* have demonstrated a SPR sensor that is capable of selective detection of dodecane vapour against a background atmosphere of *n*-butane vapour⁵². The sensor demonstrated good sensitivity down to 100 ppm and good response times. However, the device was not a waveguide surface plasmon resonance sensor thus the experimental set-up footprint was large⁵².

4.3.6 Surface plasmon resonance sensors for acidic/basic gases

Samoylov *et al* have demonstrated a SPR sensor for the sensing of hydrogen chloride gas that is based on the change in conduction of a 2 nm thick layer of polyaniline on the gold metal film⁵³. Detection down to 80 ppm of hydrogen chloride gas was demonstrated, but the response of the sensor was “quasi-reversible”; the sensor device had a very low lifetime.

4.3.7 Advantages and disadvantages of surface plasmon resonance sensors

As mentioned above, surface plasmon resonance sensors possess good sensitivity to refractive index changes local to the interface between the metal and the analyte. Whilst silver enhances the extent of the evanescent field, gold is typically used as the metal layer for SPR sensors. The reasons for this are pragmatic. Gold can be functionalised with chemical and biological agents (to facilitate selective and specific sensing) using the well known thiol - Au based coupling reactions; Au has a strong affinity for S. In addition, a gold surface offers greater stability relative to Ag. The controllable and facile surface functionalisation combined with the relatively short penetration depth of the evanescent wave of the surface plasmon wave, enables the measured changes in the local refractive index to be associated with specific target binding events at the surface; due to the small penetration depth there is little interference from bulk refractive index and environmental changes. Indeed, SPR sensor technology has been well refined and many variations of SPR sensor are commercially available ²⁶. However, there are several disadvantages with SPR sensors. The nature of the evanescent wave sensing regime limits the potential range of measurable refractive indices; indices greater than the waveguide core will couple light out into cladding modes and thus introduce huge losses. Furthermore, referencing of physical effects, such as temperature changes, is necessary, but is not always easily achieved. For temperature referencing, a second SPR sensor is required. This introduces redundancy into the sensor set-up, increases the footprint of the sensor system in addition to increasing the financial cost of the system.

4.4 Mach-Zehnder interferometer (MZI) sensors

A Mach-Zehnder interferometer (MZI), named after the physicists Ludwig Mach and Ludwig Zehnder who designed the device ^{54,55}, is an optical device that can be used to determine the relative phase shift between two collimated beams that have been split from a single coherent light source. MZIs can also be fabricated in an integrated optical format, where the interferometer act as an evanescent wave refractometer. The surface of the integrated optical MZI may be functionalised, thus introducing sensitivity to specific chemical species. Integrated optical MZI sensor devices generally exhibit high sensitivity and are facile to fabricate and in principle a MZI sensor is more sensitive than a waveguide surface plasmon resonance sensor. This is because the MZI sensor does not employ coupling to a lossy waveguide.

4.4.1 Integrated optical Mach-Zehnder interferometers

Using a variety of fabrication techniques, Mach-Zehnder interferometers can be incorporated into integrated optical circuits. In a typical MZI device the input waveguide is split equally into two waveguide arms, before recombining the waveguide arms back into a single waveguide, which goes to the detector. The resulting output, P_{out} , is dependent on the phase difference, $\Delta\phi$, between the two beams that are recombined. The phase difference is used for interrogation in MZI sensors⁵⁶.

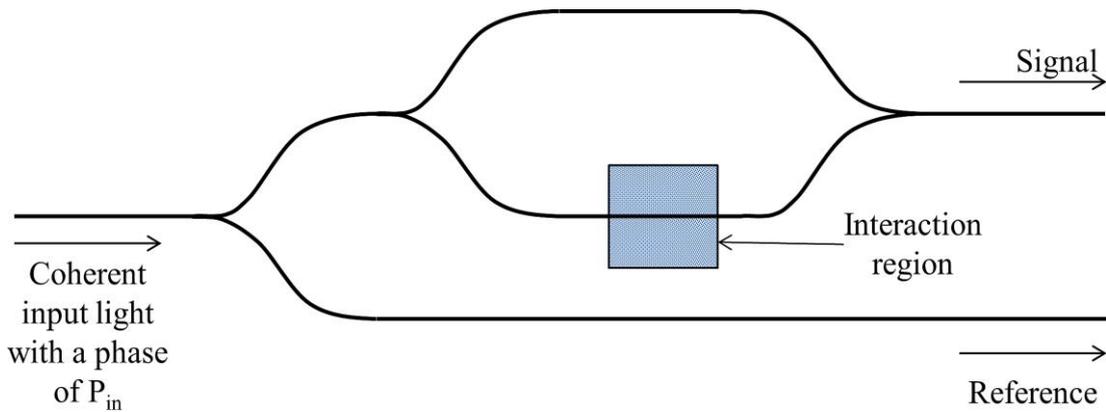


Fig.4.4: Schematic of an experimental Mach-Zehnder integrated optical sensor device, modified from the work of Quigley *et.al*⁵⁷. This device has an addition reference waveguide which allows for compensation for fluctuations in the input power and coupling efficiencies.

If both waveguides in the split waveguide region of the device are buried in the waveguide layer, or are exposed to identical local conditions, then there will be no phase difference between the two beams. Therefore, constructive interference will occur upon recombination of the two beams. However, if one of the two waveguides is exposed to the external environment (as highlighted as the ‘interaction region’ in **Fig.4.4** above) then the evanescent wave within that waveguide will interact with the local chemical environment. Changes in the refractive index of the local chemical environment will result in a difference in the effective path length of the two split waveguides. This leads to a phase shift difference between the output light beams. This phase difference between the unexposed reference waveguide arm and the exposed waveguide arm corresponds to the refractive index difference. Thus the MZI sensor device functions as a refractometer.

4.4.2 Integrated optical Mach-Zehnder interferometer for relative humidity

Lukosz & Stamm demonstrated a MZI relative humidity sensor which utilised a silica/titania waveguide substrate⁵⁸. The sensor device had a fast response time of < 0.1 s and a resolution of 0.1 %RH. However, the device was operated at 633 nm, which is incompatible with standard and readily available telecoms equipment. In addition, the demonstrated dynamic range of the sensor device was very poor; between 63 – 67 %RH.

4.4.3 Integrated optical Mach-Zehnder interferometer for hydrocarbons and volatile organic compounds

An integrated optical Mach-Zehnder interferometer sensor system for measuring gaseous hydrocarbon compounds was demonstrated by Fabricius *et.al*⁵⁹. One of the waveguide arms was covered with a polysiloxane layer that was sensitive to organic solvents. The refractive index of the polysiloxane layer changed continuously upon exposed to solvent vapours and the resulting phase shift of the signal was dependent on the concentration of the gas and the solvent type. The device also demonstrated an extremely short time response. However, the use of a xenon lamp white light source rendering the device incompatible with telecoms standard equipment⁵⁹.

4.4.4 Integrated optical Mach-Zehnder interferometer for basic gases

Fushen *et al* demonstrated an integrated optical Mach-Zehnder interferometer sensor device for ammonia gas, which utilised Langmuir-Blodgett thin films of Zn Metalloporphyrin as the active sensing films⁶⁰. Sensitivity down to 0.7 % v/v ammonia gas was achieved and the sensor device had a reasonable response time in the order of minutes. However, the restoration time was also on the order of minutes and as admitted by the authors themselves, the results presented were only preliminary and further improvements were required⁶⁰.

4.4.5 Advantages and disadvantages of Mach-Zehnder interferometers

Compared to the other techniques discussed in this chapter, Mach-Zehnder interferometers have the highest sensitivity to refractive index change. Similar to SPR, selective sensing of specific analytes can be realised with MZI sensors by functionalisation of the surface. In addition, through use of the reference sidearm waveguide, many physical properties can be referenced and negated. However, the two sidearm waveguides of the splitter section must be in close proximity (with an

area of good thermal conductivity between) for accurate negation and referencing of physical effects, such as temperature⁵⁶. This limits the waveguide design of potential MZI sensors. Guha *et al*⁶¹ have described methods to overcome this limitation through careful and deliberate design of the two waveguide sidearms. However, an intimate knowledge of the waveguide system is required, in addition to very precise fabrication of the waveguides.

The changes in refractive index upon a sensing event are derived from continuous measurements of the relative output power; competing sensing techniques based on wavelength scanning cannot achieve continuous measurement. However, Mach-Zehnder interferometers are inherently susceptible to changes in the optical power from the source. Therefore, suitable power referencing is required to avoid misreading. In addition, the MZI system has an inherent inability to measure refractive index changes directly, thus the output signal must continuously monitored. Any operational pause can result in large uncertainties in the measured refractive index values. Furthermore, changes to the local refractive index must also be on a timescale that is compatible with the interrogation system. Finally, integration and networking of multiple MZI devices is frustrated by the inherent need for direct interrogation of each MZI.

4.5 Grating Couplers

Whereas SPR sensors are based on the interaction of light with metal layers, grating couplers consist of dielectric waveguides, the modal properties of which are dominated by the real part of the complex refractive index of the dielectric waveguide and the analyte. The most typical format of such a device is an optical fibre grating sensor. As described in **Chapter 2** above, grating couplers can be classified as long-period gratings (LPGs) or short-period gratings (Bragg gratings). A Bragg grating is typically 10-100 times shorter than a long-period grating which makes Bragg gratings suitable for near point sensing applications. However, LPGs have also been demonstrated as effective refractive index sensors⁶²⁻⁶⁴.

Gratings can be written, using techniques such as direct UV grating writing or femtosecond writing, into many different substrate geometries, such as the photosensitive core of an optical fibre (**Fig.4.5** below) or the photosensitive silica waveguide core layer of a silica-on-silicon planar substrate.

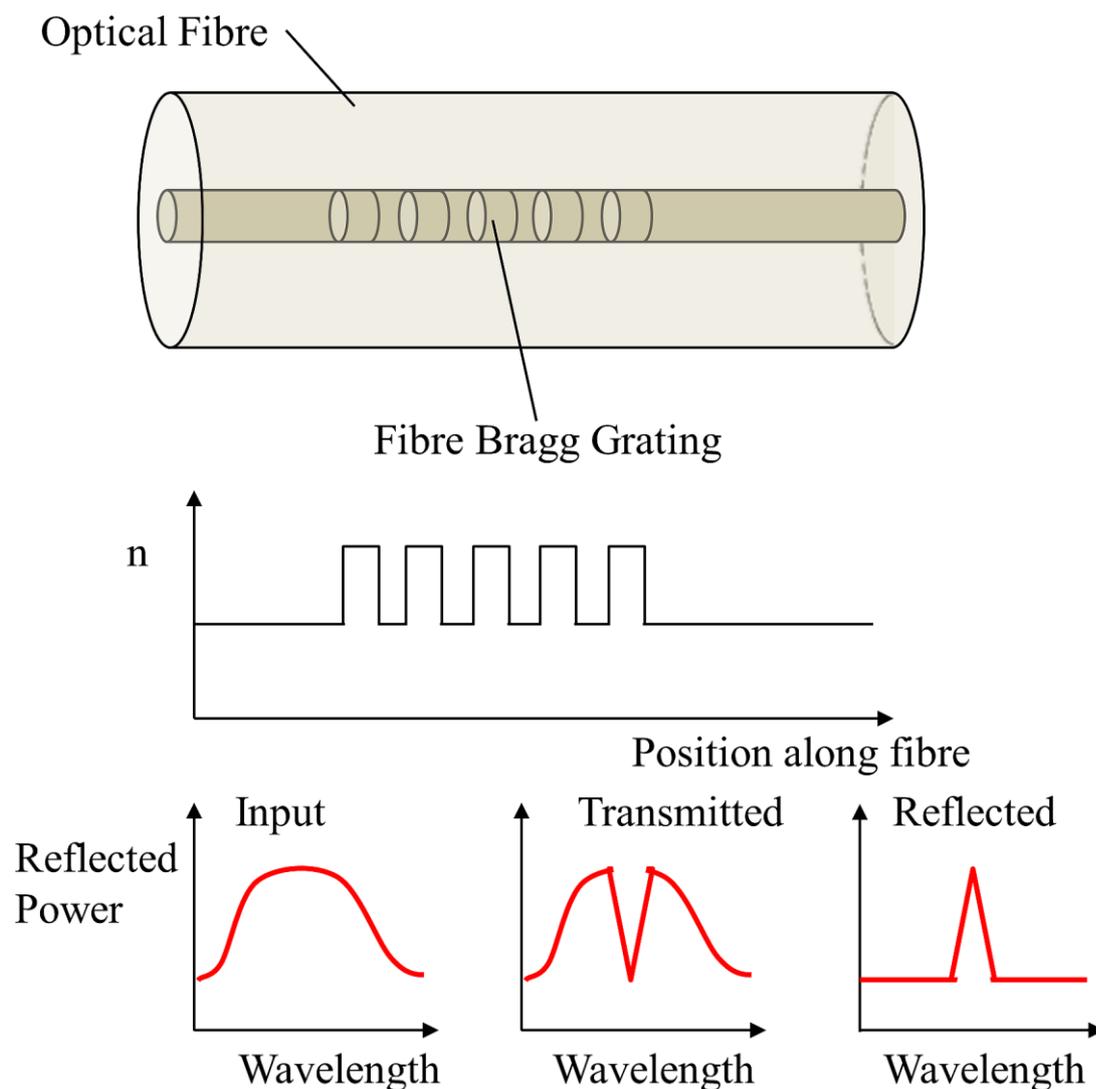


Fig.4.5: A short period fibre Bragg grating

A periodic refractive index structure is introduced into the core of a photosensitive waveguide through exposure of the fibre to UV light. Many different grating structures can be realised. Long-period fibre gratings can couple a forward propagating mode in the core of the fibre into one or more forward propagating cladding modes, whilst a wider reflection spectrum can be achieved with a chirped fibre Bragg grating. A variety of grating structures have been applied in optical sensor systems, but the most commonly used is the fibre Bragg grating.

As discussed in **Chapter 2**, Bragg gratings respond to both changes in temperature and strain. For chemical sensing, these changes need to be excluded or measured in a manner that allows for referencing. One method is to use a reference grating, which

is placed near to the active sensing Bragg grating, but is completely isolated from the chemical environment ⁶⁵.

Fibre Bragg gratings can be used for chemical sensing. This is because the Bragg wavelength of an exposed fibre Bragg grating varies with refractive index change due to the interaction of the evanescent field with the local chemical environment. Fibre Bragg gratings for sensing of relative humidity ⁶⁶, hydrocarbons ⁶⁷ and corrosive gases ⁶⁸ have been demonstrated.

However, due to the constraint of current interrogation techniques, the sensitivity of a fibre Bragg grating, with a typical subpicometre resolution for static Bragg wavelength shift measurement, is in the order of $\Delta n \approx 10^{-5}$; lower than other fibre optic techniques. However, compared to fibre Bragg gratings, long-period gratings have been demonstrated to be more sensitive to refractive index changes; sensitivity of up to 10^{-7} is possible ⁶⁹.

4.5.1 Integrated optical Bragg grating sensors

Compared to the abundance of optical fibre Bragg sensors reported in the literature, there are relatively few examples of Bragg grating sensors in a planar form factor. However, the approaches that have been demonstrated cover a wide variety material platforms such as sol-gels, polymers, lithium niobate, silicon-on-insulator and silica-on-silicon. ⁷⁰⁻⁷⁹. In addition, the fabrication techniques, utilised to make the Bragg grating in the planar form factor have also been highly varied. Therefore, Bragg grating sensing elements based on different waveguide and grating geometries, such as ridge waveguides ⁸⁰, etched corrugated gratings ⁸¹ and UV written waveguides and gratings ^{78,79} have been realised. Such planar Bragg grating devices are appealing for sensing applications for several reasons ²⁶:

- Multiple wavelengths can be used. This enables the possibility of analyte identification through optical dispersion measurements.
- A range of evanescent wave penetration depths can be achieved. This enables the collection of additional information on the structure local to the surface of the sensor;
- Multiple and separate sensing regions can be incorporated onto a single Bragg grating sensor chip. This enables simultaneous testing for multiple

different gases without the need for redundant equipment through duplication or time delays.

- The monolithic silicon chip design is robust, requires no electrical signal input or output, thus the sensor chip does not present a spark risk in flammable or explosive environments, In addition the silica-on-silicon chip design is resistant to a wide range of chemical agents, such as strong acids and bases⁸².

Integrated planar optical Bragg grating sensors are similar to fibre Bragg grating sensors due to the same underlying physics. Therefore, integrated planar optical Bragg grating sensor afford all the same benefits as fibre Bragg grating sensors, such as the ability for real-time and *in-situ* measurement with high sensitivity. However, there are several key differences between integrated planar optical Bragg grating sensor and fibre Bragg grating sensors. The most significant difference is the potential for complex sensor optical circuits and networks one chip that is afforded by planar form factor, but not the fibre form factor. In addition the planar geometry has allowed for the integration of the Bragg gratings with micromachining⁸³ and microfluidics⁸². This enables the development of lab-on-a-chip devices.

The planar integrated optical Bragg grating sensors developed in this work were fabricated in a silica-on-silicon platform using the direct UV grating writing technique. Planar integrated optical Bragg grating sensors of this type have been shown to be able to detect changes in refractive index down to 10^{-6} ⁸⁴.

4.5.2 Advantages and disadvantages of integrated Bragg grating sensors

Despite the lower absolute sensitivity of integrated Bragg grating sensors compared to MZI sensors ($\Delta n \approx 10^{-6}$ versus 10^{-8} respectively), integrated Bragg grating sensors demonstrate the advantageous ability of enabling measurement of the absolute Bragg wavelength. Thus the absolute refractive index of the analyte can be determined. This allows for a high degree of interrogation setup freedom. Continuous interrogation of a single sensor (that can contain multiple Bragg gratings), sampling of a single sensor at set times or even sequential interrogation of multiple independent sensor devices are all possible with integrated planar optical Bragg grating sensors. This would be much more challenging to achieve with a Mach-

Zehnder based system; even integration of multiple sensors on a single integrated MZI device is complex, as highlighted above.

Integrated Bragg grating sensors are most similar to waveguide SPR sensors, but of course the underlying physics for both sensor devices is vastly different. Integrated Bragg grating sensors and waveguide SPR sensor systems both exhibit similar sensitivities to refractive index change ($\Delta n \approx 10^{-6}$), multiple sensors can be integrated into an array and both sensor technologies can be readily chemically functionalised for selective and specific binding/sensing at the sensor surface. However, integrated Bragg sensors possess some advantages over the waveguide SPR sensor technology. Firstly, temperature referencing is facile to achieve with an integrated Bragg grating sensor, by use of a reference grating which is integrated into the same waveguide without any additional fabrication steps required. Secondly, fabrication of an integrated Bragg grating sensor with the direct UV grating writing technique does not require clean-room processing. Thirdly, integrated Bragg grating sensors do not require a metal film to operate whereas waveguide SPR sensors require a metallic surface (typically Au) to support plasmon modes.

Deposition of the thin gold film on a silica waveguide to a certain standard of uniformity, thickness and coverage is not trivial. This is because gold will not robustly bind to silica directly, without the aid of a tethering agent.

In general the evanescent wave of a Bragg grating sensor has a greater penetration depth than the penetration depth of the surface plasmon resonance mode. This may lead to some sensing applications where the deeper penetration of the evanescent wave of the Bragg grating sensor is an advantage over the shallower penetration of the SPR evanescent wave and also *vice versa*.

4.6 Summary

There are many different methods that utilise light to sense specific analytes and/or sense changes in the surrounding environment that are currently and actively being researched, of which the evanescent wave approach has been described. Whilst the methods of device fabrication and the ways of interrogating the sensing environment with an evanescent wave differ greatly, all of the sensors described above have been applied to the sensing of gases and vapours. For analysis systems based upon a

refractometric approach, the refractive index sensitivity limit is typically $10^{-5} - 10^{-7}$, with interferometric system sensors demonstrating the highest sensitivity. Obviously no single sensor system can be labelled as the best evanescent wave optical sensor system as the best solution is always specific to the desired application and other contributing factors and conditions. For example, an integrated optical solution may be more appropriate for highly parallel systems, whereas an optical fibre solution maybe more appropriate in other systems where the ability of direct incorporation into telecoms fibre networks over large areas is required ⁹.

The results demonstrated in the following chapters describe Bragg grating gas sensors that are incorporated into compact planar integrated optical devices. The work has focussed on the development of planar Bragg grating sensors that utilise the interaction between the evanescent wave and functionalised cladding materials for relative humidity, volatile organic compounds and acidic/basic gas sensing. This has been achieved through the use of inorganic material and siloxane polymers, the effective indices of change upon exposure to water vapour and volatile organic compounds. In addition, the use of a pH chromic material which changes colour, and thus an associated change in the refractive index of the material also occurs, upon exposure to hydrogen chloride gas has been demonstrated as a viable refractometric sensor for acidic gases. Ultimately, these approaches will investigate if the gas sensor proposed herein, that is based on a planar integrated optical Bragg grating device, is able to compete with current developments in optical gas sensing.

1. I. Kasik, V. Matejec, M. Chomat, M. Hayer, and D. Berkova, in *Proceedings of the Nato Advanced Study Institute on Optical Chemical Sensors*, eds. F. Baldini, A. N. Chester, J. Homola, and S. Martellucci, Springer, Erice, 2004, pp. 59–77.
2. B. D. Gupta, *Fiber Optic Sensors: Principles and Applications*, New India Publishing Agency, New Delhi, 1st edn., 2006.
3. F. Baldini, A. N. Chester, J. Homola, and S. Martellucci, Eds., *Optical Chemical Sensors*, Springer, Dordrecht, 2006.
4. B. Culshaw and A. Kersey, *J. Light. Technol.*, 2008, **26**, 1064–1078.
5. G. Stewart and B. Culshaw, *Opt. Quantum Electron.*, 1994, **26**, S249–S259.
6. A. Messica, A. Greenstein, and A. Katzir, *Appl. Opt.*, 1996, **35**, 2274–84.
7. U. Willer, D. Scheel, I. Kostjucenko, C. Bohling, W. Schade, and E. Faber, *Spectrochim. Acta. A. Mol. Biomol. Spectrosc.*, 2002, **58**, 2427–32.
8. M. Shadaram, J. J. Martinez, F. Garcia, D. Tavares, A. Symon, N. Godbout, and S. Lacroix, in *Proc. SPIE 2695, Functional Photonic and Fiber Devices*, eds. S. I. Najafi and M. N. Armenise, International Society for Optics and Photonics, San Jose, 1996, pp. 164–168.
9. R. M. Parker, PhD Thesis, University of Southampton, 2010.
10. O. S. Wolfbeis, *Anal. Chem.*, 2002, **74**, 2663–2677.
11. O. S. Wolfbeis, *Anal. Chem.*, 2006, **78**, 3859–74.
12. O. S. Wolfbeis, *Anal. Chem.*, 2008, **80**, 4269–83.
13. X.-D. Wang and O. S. Wolfbeis, *Anal. Chem.*, 2013, **85**, 487–508.
14. J. Mathew, K. J. Thomas, V. P. . Nampoori, and P. Radhakrishnan, *Sensors Transducers J.*, 2007, **84**, 1633–1640.
15. M. A. Diab, A. Z. El-Sonbati, M. M. Al-Halawany, and D. M. D. Bader, *Open J. Polym. Chem.*, 2012, **2**, 14–20.
16. A. Gaston, I. Lozano, F. Perez, F. Auza, and J. Sevilla, *IEEE Sens. J.*, 2003, **3**, 806–811.
17. C. Elosua, I. R. Matias, C. Barriain, and F. J. Arregui, *Sensors*, 2006, **6**, 1440–1465.
18. G. Schwotzer, I. Latka, H. Lehmann, and R. Willsch, *Sensors Actuators B. Chem.*, 1997, **38-39**, 150–153.

19. H. Tai, H. Tanaka, and T. Yoshino, *Opt. Lett.*, 1987, **12**, 437.
20. F. Abdelmalek, J. M. Chovelon, M. Lacroix, and V. Matejec, *Sensors Actuators B. Chem.*, 1999, **56**, 234–242.
21. T. Grady, T. Butler, B. D. Macraith, D. Diamond, and M. Anthony, *Analyst*, 1997, **122**, 803–806.
22. E. Scorsone, S. Christie, K. C. Persaud, and F. Kvasnik, *Sensors Actuators B Chem.*, 2004, **97**, 174–181.
23. J. Homola, S. S. Yee, and G. Gauglitz, *Sensors Actuators B Chem.*, 1999, **54**, 3–15.
24. I. Pockrand, J. D. Swalen, J. G. Gordon II, and M. R. Philpott, *Surf. Sci.*, 1978, **74**, 237–244.
25. J. G. Gordon II and S. Ernst, *Surf. Sci.*, 1980, **101**, 499–506.
26. I. J. G. Sparrow, P. G. R. Smith, G. D. Emmerson, S. P. Watts, and C. Riziotis, *J. Sensors*, 2009, **2009**, 1–13.
27. C. Nylander, B. Liedberg, and T. Lind, *Sensor. Actuator.*, 1982, **3**, 79–88.
28. B. Liedberg, C. Nylander, and I. Lundstrom, *Sensor. Actuator.*, 1983, **4**, 299–304.
29. S. Maier, *Plasmonics: Fundamentals and Applications.*, Springer, New York, 2007.
30. R. W. Wood, *Philos. Mag. Ser. 6*, 1902, **4**, 396–402.
31. A. Otto, *Zeits Phys*, 1968, **216**, 398.
32. E. Kretschmann and H. Raether, *Z. Naturforsch*, 1968, 2135–2136.
33. M. Gargaud, R. Amils, J. Cernicharo, H. J. Cleaves II, W. M. Irvine, D. L. Pinti, and M. Viso, Eds., *Encyclopedia of Astrobiology*, Springer-Verlag, Heidelberg, 2011.
34. J. R. Sambles, G. W. Bradbery, and F. Yang, *Contemp. Phys.*, 1991, **32**, 173–183.
35. M. a Ordal, L. L. Long, R. J. Bell, S. E. Bell, R. R. Bell, R. W. Alexander, and C. a Ward, *Appl. Opt.*, 1983, **22**, 1099–20.
36. J. C. Abanulo, R. D. Harris, a. K. Sheridan, J. S. Wilkinson, and P. N. Bartlett, *Faraday Discuss.*, 2002, **121**, 139–152.

37. T. Kenny, in *Sensor Technology Handbook*, ed. J. S. Wilson, Elsevier, Oxford, 2005, p. 693.
38. A. A. Kolomenskii, P. D. Gershon, and H. A. Schuessler, *Appl. Opt.*, 1997, **36**, 6539–6547.
39. T. M. Chinowsky, L. S. Jung, and S. S. Yee, *Sensors Actuators B. Chem.*, 1989, **54**, 89–97.
40. J. Homola, I. Koudela, and S. S. Yee, *Sensors Actuators B. Chem.*, 1999, **54**, 16–24.
41. J. Homola, *Sensors Actuators B. Chem.*, 1997, **41**, 207–211.
42. E. M. Yeatman, *Biosens. Bioelectron.*, 1996, **11**, 635–649.
43. N. J. Walker, *Science*, 2002, **296**, 557–559.
44. P. V. Lambeck, *Sensors Actuators B. Chem.*, 1992, **8**, 103–116.
45. J. Homola, J. Ctyroky, M. Skalsky, J. Hradilova, and P. Kolarova, *Sensors Actuators B. Chem.*, 1997, **39**, 286–290.
46. C. R. Lavers and J. S. Wilkinson, *Sensors Actuators B. Chem.*, 1994, **22**, 75–81.
47. R. D. Harris and J. S. Wilkinson, *Sensors Actuators B. Chem.*, 1995, **29**, 261–267.
48. C. Mouvet, R. D. Harris, C. Maciag, C. Luff, J. S. Wilkinson, J. Piehler, A. Brecht, A. Gauglitz, R. Abuknesha, and G. Ismail, *Anal. Chim. Acta*, 1997, **338**, 109–117.
49. J. Ctyroky, J. Homola, and M. Skalsky, *Electron. Lett.*, 1997, **33**, 1246–1248.
50. M. N. Weiss, R. Srivastava, and H. Groger, *Electron. Lett.*, 1996, **32**, 842–843.
51. R. Srivastava, M. N. Weiss, H. Groger, P. Lo, and S. F. Luo, *Sensors Actuators A. Phys.*, 1996, **51**, 211–217.
52. N. M. Aguirre, L. M. Pérez, J. A. Colín, and E. Buenrostro-Gonzalez, *Sensors*, 2007, **7**, 1954–1961.
53. A. V. Samoylov, V. M. Mirsky, Q. Hao, C. Swart, Y. M. Shirshov, and O. S. Wolfbeis, *Sensors Actuators B Chem.*, 2005, **106**, 369–372.
54. L. Zehnder, *Zeitschrift fur Instrumentenk.*, 1891, **11**, 275–285.
55. L. Mach, *Zeitschrift fur Instrumentenk.*, 1892, **12**, 89–93.

56. R. G. Heideman and P. V. Lambeck, *Sensors Actuators B. Chem.*, 1999, **61**, 100–127.
57. G. R. Quigley, R. D. Harris, and J. S. Wilkinson, *Appl. Opt.*, 1999, **38**, 6036–6039.
58. W. Lukosz and C. H. Stamm, *Sensors Actuators A. Phys.*, 1991, **25-27**, 185–188.
59. N. Fabricius, G. Gauglitz, and J. Ingenhoff, *Sensors Actuators B Chem.*, 1992, **7**, 672–676.
60. C. Fushen, L. Yunqi, X. Yu, and L. Qu, *Opt. Lett.*, 1996, **21**, 1700–2.
61. B. Guha, A. Gondarenko, and M. Lipson, *Opt. Express*, 2010, **18**, 1879–1887.
62. S. W. James and R. P. Tatam, *Meas. Sci. Technol.*, 2003, **14**, R49–R61.
63. H. J. Patrick, G. M. Williams, A. D. Kersey, J. R. Pedrazzani, and A. M. Vengsarkar, *IEEE Photonics Technol. Lett.*, 1996, **8**, 1223–1225.
64. H. J. Patrick, A. D. Kersey, and F. Bucholtz, *J. Light. Technol.*, 1998, **16**, 1606–1612.
65. M. Song, S. B. Lee, S. S. Choi, and B. Lee, *Opt. Fiber Technol.*, 1997, **3**, 194–196.
66. T. L. Yeo, K. T. V. Grattan, D. Parry, R. Lade, and B. D. Powell, *IEEE Sens. J.*, 2005, **5**, 1082–1089.
67. T. L. Lowder, J. D. Gordon, S. M. Schultz, and R. H. Selfridge, *Opt. Lett.*, 2007, **32**, 2523–5.
68. L. Ai, J.-C. Mau, W.-F. Liu, M.-Y. Fu, and T.-C. Chen, *Microw. Opt. Technol. Lett.*, 2007, **49**, 3063–3066.
69. Y. J. Rao, *Opt. Lasers Eng.*, 1999, **31**, 297–324.
70. S.-L. Tsao and C.-P. Peng, *Microw. Opt. Techn. Lett.*, 2001, **30**, 321–322.
71. F. Ouerghi, W. Belhadj, F. Abdelmalek, M. Mejatty, and H. Bouchriha, *Thin Solid Films*, 2005, **485**, 176–181.
72. C. Wochnowski, M. Abu-El-Qomsan, W. Pieper, K. Meteva, S. Metev, G. Wenke, and F. Vollersten, *Sensors Actuators A. Phys.*, 2005, **120**, 44–52.
73. C. Wochnowski, M. T. Kouamo, W. Pieper, K. Meteva, S. Metev, G. Wenke, and F. Vollersten, *IEEE Sens. J.*, 2006, **6**, 331–339.
74. K. J. Kim and M. C. Oh, *IEEE Photonics Technol. Lett.*, 2008, **20**, 288–290.

75. T. Pustelny, I. Zielonka, C. Tyszkiewicz, P. Karasinski, and B. Pustelny, *Opto-electron. Rev.*, 2006, **14**, 161–166.
76. V. M. N. Passaro, R. Loiacono, G. D’Amico, and F. De Leonardis, *IEEE Sens. J.*, 2008, **8**, 1603–1611.
77. D. Runde, S. Brunken, C. E. Ruter, and D. Kip, *Appl. Phys. B-Lasers O.*, 2007, **86**, 91–95.
78. I. Sparrow, G. Emmerson, C. Gawith, and P. Smith, *Sensors Actuators B Chem.*, 2005, **107**, 856–860.
79. I. J. G. Sparrow, G. D. Emmerson, C. B. E. Gawith, P. G. R. Smith, M. Kaczmarek, and A. Dyadyusha, *Appl. Phys. B-Lasers O.*, 2005, **81**, 1–4.
80. X. Dai, S. J. Mihailov, C. L. Callendar, C. Blanchetiere, and R. B. Walker, *Meas. Sci. Technol.*, 2006, **17**, 1752–1756.
81. A. V. Dotsenko, A. L. Diikov, and T. A. Vartanyan, *Sensors Actuators B Chem.*, 2003, **94**, 116–121.
82. R. M. Parker, J. C. Gates, D. J. Wales, P. G. R. Smith, and M. C. Grossel, *Lab Chip*, 2013, **13**, 377–85.
83. C. Holmes, L. G. Carpenter, J. C. Gates, and P. G. R. Smith, *J. Micromechanics Microengineering*, 2012, **22**, 025017.
84. R. M. Parker, J. C. Gates, M. C. Grossel, and P. G. R. Smith, *Appl. Phys. Lett.*, 2009, **95**, 173306.

5 Increasing Sensitivity: The Evanescent Wave Interaction Volume

5.1 Introduction

The interaction between the evanescent wave, as introduced in **Chapter 2**, and the surrounding chemical environment is the key phenomenon that facilitates refractometric sensing with planar integrated Bragg grating sensors. Under standard temperature and pressure (STP) conditions, liquids are denser than gases. Therefore there are a greater number of interactions between the evanescent wave with molecules in a liquid near to the surface of the sensor, than with molecules in a gas that are near to the surface of the sensor. The resulting change in effective index due to the presence of a liquid is greater than the change in effective index due to the presence of a gas. Therefore, the Bragg wavelength shift caused by the presence of a gas is less than the Bragg wavelength shift caused by the presence of a liquid. To achieve sensitivity to gases that is comparable to the sensitivity to bulk liquids, modification of the sensor surface is required.

In this chapter the need for increasing sensitivity to gases, and the other disadvantages of unfunctionalised sensors, are described in further detail. A technique that has been employed to increase the sensitivity of planar Bragg grating sensors to low concentrations of chemical species in the liquid state is described and the unsuitability of this technique to sensing of gases is discussed. Alternative methods of increasing sensitivity to gases are then proposed, together with a discussion on the imparted selectivity and differentiation of gases that these techniques also afford, in preparation of the gas sensing results presented in **Chapter 6** and **Chapter 7**.

5.2 Increasing sensitivity to gases

5.2.1 Unfunctionalised Bragg Grating sensors

In previous chapters, planar integrated Bragg grating sensor optical theory and fabrication of unfunctionalised bare Bragg grating sensors have been introduced.

Unfunctionalised bare planar integrated optical Bragg grating sensors are inherently sensitive to temperature changes, strain and changes in the local bulk effective index.

As defined in **Chapter 2**, the evanescent wave decays exponentially, normal to the plane of the waveguide. Therefore, in a given instant of the light propagating along the waveguide, the evanescent wave exists with a certain three dimensional volume, normal to the waveguide. A two dimensional pictorial representation of this is shown in **Fig.5.1** below.

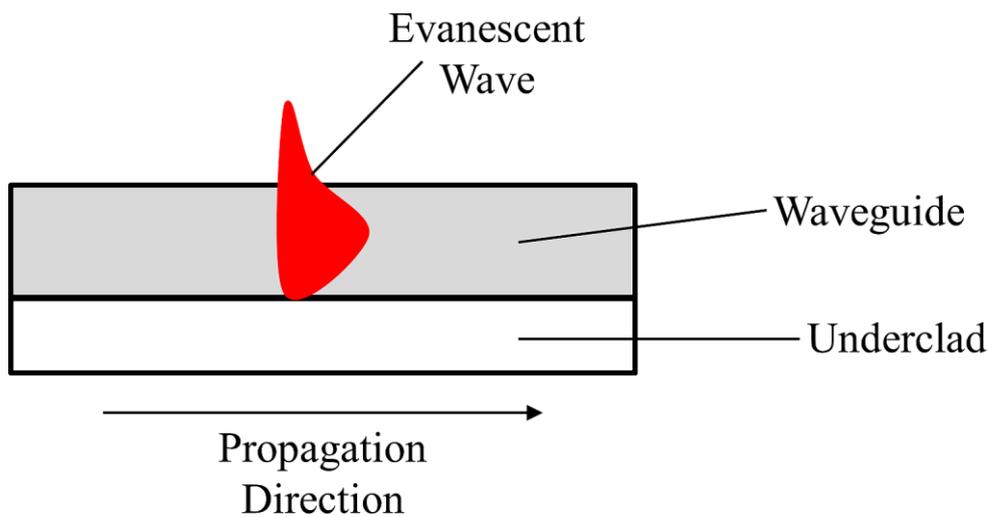


Fig.5.1: Two dimensional schematic of the evanescent wave normal to the waveguide

Under standard temperature and pressure (STP) conditions, liquids are denser than gases. Therefore there are a greater number of interactions between the three dimensional volume of the evanescent wave with molecules in a bulk volume of a liquid, than with molecules in a bulk volume of a gas, as represented in **Fig.5.2** below.

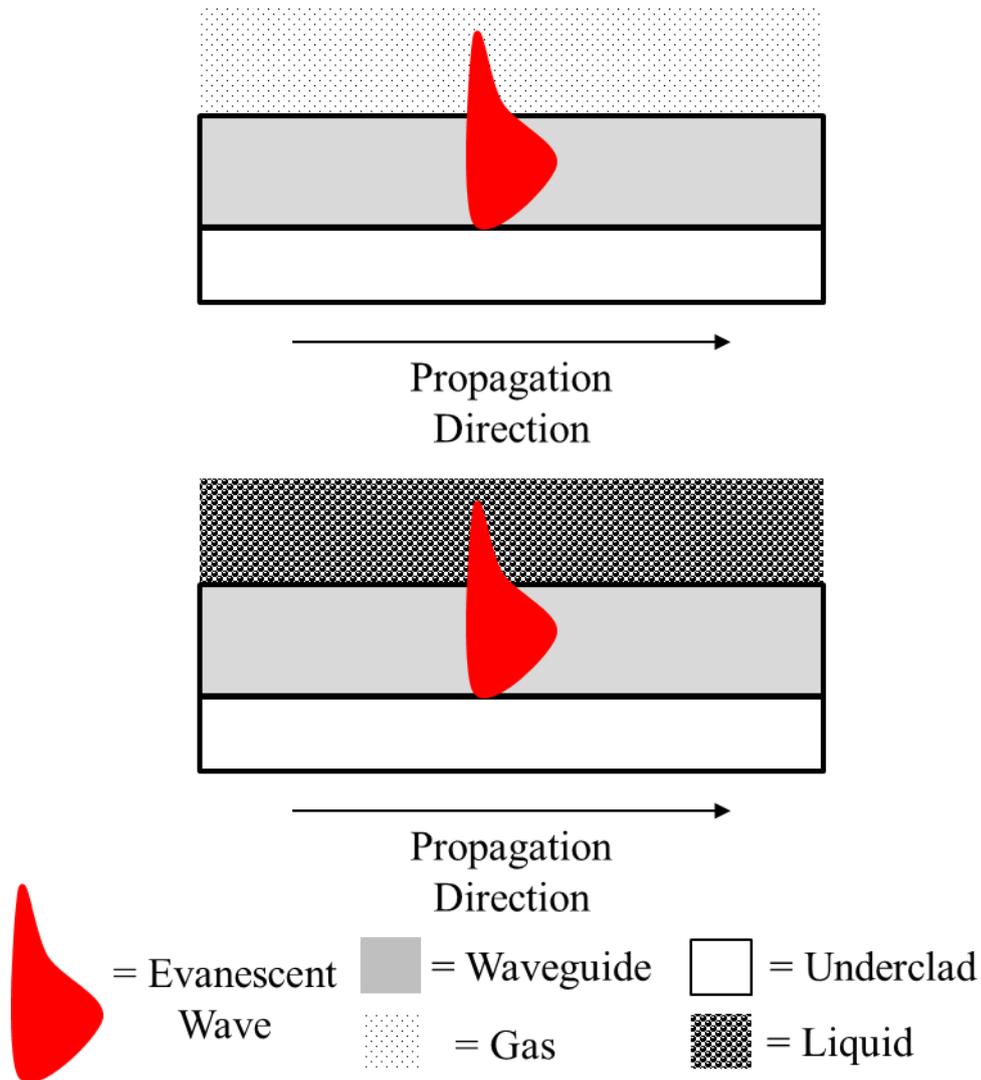


Fig.5.2: Two dimensional pictorial representations of the interaction of the evanescent wave interaction volume, normal to the waveguide, interacting with a gas (top) which is low density, relative to the density of a liquid (bottom).

The resulting change in effective index due to the interaction with a gas present in the evanescent wave volume is therefore less than the change in effective index due to the presence of a liquid. Thus, for an unfunctionalised bare Bragg grating sensor, the Bragg wavelength shift caused by the presence of a gas will be less than the Bragg wavelength shift caused by the presence of a liquid.

Another factor that also contributes to the inherent low sensitivity of unfunctionalised bare Bragg grating sensors is method of the sensing experiment. For example, if the sensor is exposed to a liquid after exposure to air, and then back to air, the magnitude of the Bragg wavelength shift will be greater than the Bragg wavelength shift caused by exposure to different gases. This is explained by

consideration of the refractive index differential between common liquids and gases and also the refractive index differential between different common gases. Some examples of the refractive index of common liquids and gases are shown below in **Table 5.1**.

Liquids		Gases	
Liquid	<i>n</i>	Gas	<i>n</i>
Acetic acid	1.372	Ammonia	1.000 376
Acetone	1.359	Argon	1.000 281
Dichloromethane	1.424	Chlorine	1.000 773
Ethanol	1.362	Helium	1.000 035
Ethyl acetate	1.372	Hydrogen	1.000 132
<i>n</i> -Hexane	1.375	Methane	1.000 444
Isopropanol	1.377	Nitrogen	1.000 298
Methanol	1.329	Oxygen	1.000 271
Water	1.333	Sulphur dioxide	1.000 686

Table 5.1: Highlighting the extensive difference in magnitude between the refractive indices of common liquids and common gases. Data taken from multiple sources in the literature ¹⁻⁴.

As is evident, if a Bragg grating sensor is exposed to a liquid, e.g. dichloromethane, after being exposed to nitrogen, the difference in refractive index (at 589.3 nm, 0 °C) is ~0.4237 and thus the resulting Bragg wavelength shift will be ~90-100 pm. If the Bragg grating sensor is exposed to a gas, e.g. sulphur dioxide, after being stored in nitrogen the difference in refractive index (at 589.3 nm, 0 °C) is $\sim 3.38 \times 10^{-4}$ and the resulting Bragg wavelength shift would be in the order of ~1-2 pm. Even if the unfunctionalised bare Bragg grating sensor was stored in a solvent, such as dichloromethane, and then periodically exposed to different gases, the unfunctionalised sensor would still lack sufficient sensitivity to differentiate between the gases. All of the negative Bragg wavelength shifts would be on the order of ~ 90-100 pm as the refractive indices of common gases tends to ~1 in STP conditions.

Therefore, to achieve sensitivity to analyte gases that is comparable to the sensitivity to bulk liquids, modification of the sensor surface is required.

5.2.2 Surface modification

5.2.2.1 Enhancement of sensitivity in the liquid phase

Modification of the surface of planar integrated optical Bragg gratings sensors, to increase sensitivity in the liquid phase has previously been demonstrated by Parker *et.al.*⁵. In the work of Parker *et.al.*, the top cladding layer was etched away to expose some of the Bragg gratings on the chip to the surrounding chemical environment. Then a thin film of tantalum pentoxide, ~80 nm thick, was deposited onto the etched window. The tantalum pentoxide enhancement layer increased the sensitivity of the sensor to enable the detection of the deposition of sub-nanometre layers as well as the sensitivity to bulk liquids. The increased sensitivity was due to more of the optical mode being “pulled” out of the waveguide because of the high refractive index of tantalum pentoxide ($n \sim 2.1$). With more of the optical mode “pulled” out of the waveguide and into the tantalum pentoxide thin film overlayer, a greater interaction between the evanescent wave and the environment occurred. Therefore, the sensitivity was increased.

However, despite the increase in sensitivity to monolayers and bulk liquids afforded by this method, the sensitivity to gases will only be slightly enhanced. This is because the evanescent wave is mostly confined to the over layer thin film, as confirmed by film mode method modelling of the TE optical modes in an unfunctionalised waveguide and a waveguide functionalised with a thin film (80 nm thick) of $n = 2.1$, representing tantalum pentoxide, as shown in **Fig.5.3** below.

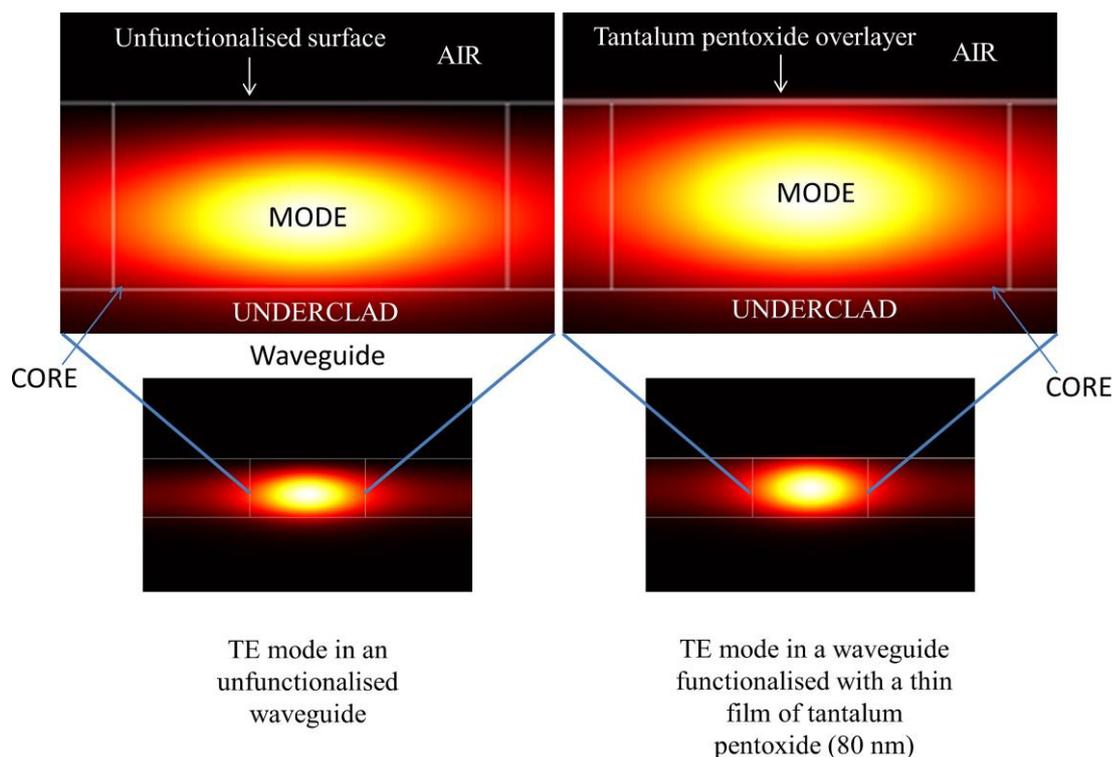


Fig.5.3: TE modes, modelled using *Fimmwave* model solving software (film mode method), in a unfunctionalised bare waveguide (bottom left) and a waveguide functionalised with a 80 nm thin film of tantalum pentoxide (bottom right). The zoomed section of the core in the unfunctionalised waveguide (top left) shows that TE mode is nearly entirely confined within the waveguide. In contrast, the zoomed section of the core in the functionalised waveguide (top right) shows that the mode is partially within the tantalum pentoxide thin film. This is represented by the orange colouration of the thin film and demonstrates the increased sensitivity due to the tantalum pentoxide thin film. The model parameters were as follows

Secondly, despite the addition of the thin film of tantalum pentoxide, the surface area above each Bragg grating is equivalent to the surface area above an unfunctionalised Bragg grating sensor, assuming the tantalum pentoxide thin film is a flat layer. Therefore, in both cases an equivalent number of gas molecules can be thought of as being able to adsorb onto the sensor surface, per unit area.

Therefore, it was proposed that to increase the sensitivity to gases an over layer film with a high surface area would be required to maximise the number of gas molecules that are within the evanescent wave interaction volume.

5.2.2.2 Enhancement of sensitivity in the gas phase

It was proposed that the greater the number of analyte gas molecules within the evanescent wave interaction volume, the greater the change in effective index and

thus the greater the magnitude of the Bragg wavelength shift. This could be achieved through use of a layer of porous material. Porous materials have a very large surface area that allows for a greater density of gas molecules to be within the evanescent wave interaction volume. This concept is represented in **Fig.5.4** below.

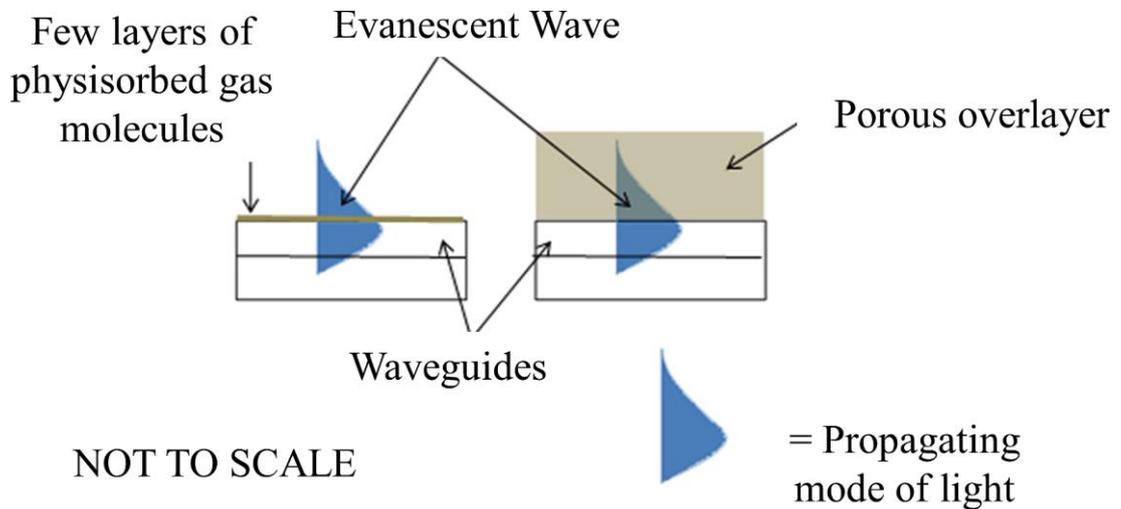


Fig.5.4: Qualitative diagrammatic comparison of (left) the total interaction of the evanescent wave in an unfunctionalised Bragg grating sensor with physisorbed gas molecules on the surface and (right) the total interaction of the evanescent wave in a Bragg grating sensor modified with a porous over layer that is filled with physisorbed gas molecules.

To test this proposed method of increasing the sensitivity, *Fimmwave* modelling was used to compare the TE optical modes in three different types of waveguide. The three types of waveguide were, an unfunctionalised bare waveguide, a waveguide modified with a thin film (80 nm thick) of a material of $n = 2.1$, representing tantalum pentoxide and a waveguide modified with a thicker over layer, 300 nm thick. The particular thick over layer that was modelled represented a known mesoporous layer of alumina, $n = 1.6$, that has been developed in the literature ⁶.

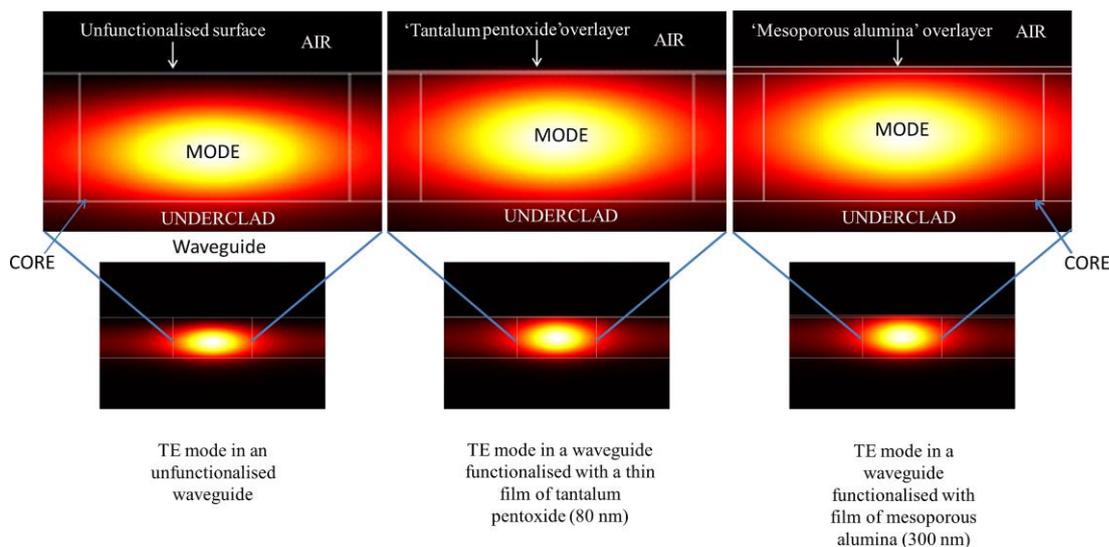


Fig.5.5: TE modes, modelled using *Fimmwave* mode solving software (film mode method), in a unfunctionalised bare waveguide (bottom left) a waveguide functionalised with a 80 nm thin film of refractive index = 2.1 (bottom middle) and a waveguide functionalised with a 300 nm thick overlayer of refractive index = 1.6 (bottom right). The 300 nm thick layer of refractive index = 1.6 represents a mesoporous alumina film and the zoomed region of the core (top right) shows that the TE mode is partially within the alumina film. This is represented by the orange colouration of the film. The porosity of the alumina layer would allow a greater number of gas molecules to interact with the evanescent wave.

The *Fimmwave* modelling results show that the TE optical mode is partially supported within the mesoporous thin film, equivalent to the waveguide functionalised with the 80 nm over layer. However, the surface area of the mesoporous area is much greater than the thin film over layer due to the inherent porosity. Therefore, a greater number of gas molecules will be within the evanescent wave interaction volume when physisorbed onto the internal surfaces within the high surface area porous structure. In comparison, there will be fewer gas molecules physisorbed as multilayers onto the surface of the high refractive index over layer and thus fewer gas molecules in the evanescent wave interaction volume.

As shown above, utilisation of the third-dimension, perpendicular to the surface of the Bragg grating sensor device, increases the number of analyte gas molecules that the evanescent wave encounters. This could be achieved through use of a layer of porous sol-gel on the surface of the sensor. This would increase the sensitivity of the device by increasing the density of analyte gas species within the evanescent wave, compared to a two dimensional functionalised surface. It has been demonstrated in

the literature that the sensitivity of sensors, whereupon analyte molecules interact with the sensing surface, can increase with increasing surface area ⁷. Therefore, the development of engineered sol-gel thin films, to utilise the three-dimensional evanescent wave interaction volume sensing region, became an aim of this work. A brief introduction to sol-gels is given below. Further comprehensive sol-gel theory can be found in the text of Brinker & Scherer ⁸.

5.2.3 Sol-gels

Sol-gels are inorganic porous matrices of solid glass-like materials that possess useful mechanical and optical properties such as transparency in optical and NIR wavelengths ⁹. In addition, sol-gels can exhibit a high degree of porosity with large surface areas and can be processed into a variety of shapes, including thin films ¹⁰.

The most common type of sol-gel described and utilised in the literature are silica sol-gels ⁸. The synthesis of silica sol-gels follows a low-temperature reaction pathway; relative to the traditional method used to fabricate common glass. Silica sol-gels are formed from the gelation and densification of silica sols. A silica sol is a colloidal suspension of silica nanoparticles within a continuous liquid phase. Silica sols are typically synthesised by hydrolysis of tetraalkoxysilanes or organoalkoxysilanes (examples shown in **Fig.5.6** below).

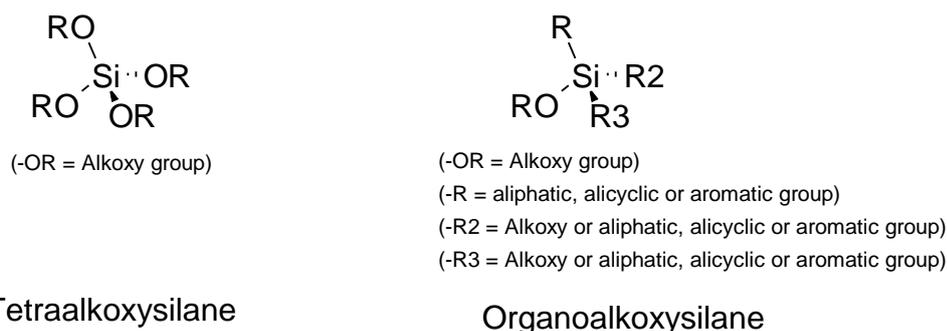


Fig.5.6: Structures of pre-cursor silica species used in the synthesis of silica sols and subsequent fabrication of silica sol-gels.

The general reaction mechanism of silica sol formation, at the functional group level, is outlined below in **Fig.5.7** ⁸.

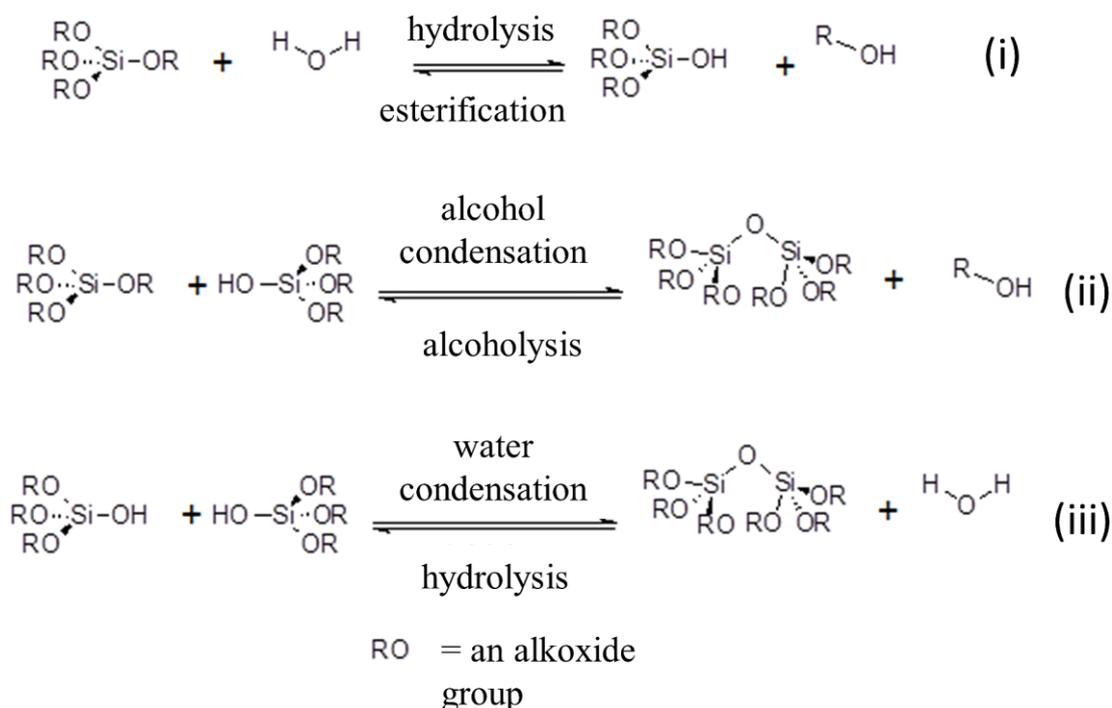


Fig. 5.7: Mechanism describing the three main reactions occurring during silica sol formation ⁸.

Under most conditions, reactions (ii) and (iii) commence before reaction (i) is complete ⁸. Further reaction of the alkoxide groups on the siloxane (Si – O – Si) products (ii) and (iii), with silanol groups, leads to polycondensation reactions that result in the formation of small silica particles. These small silica particles, dispersed within the continuous water and alcohol liquid phase, form a colloidal system; a silica sol ¹¹. Through a phenomenon known as Ostwald ripening, whereby the smaller silica particles are more soluble than larger silica particles due to the system minimising surface free energy ¹², larger and larger silica particles form. These larger silica particles join together covalently, through polycondensation reactions, to form a silica network, which contains entrapped water and alcohol molecules ¹³. Continued polycondensation reactions occur leading to strengthening of the forming gel. This is known as aging. Finally a drying step, whereby the entrapped water and alcohol molecules are removed, results in the final silica sol-gel ¹³.

The resulting silica sols can be spin deposited or dip coated onto a surface to form thin films. Further aging of the deposited sol and densification by heat treatment results in the formation of porous thin films known as sol-gel thin films. If a silica sol-gel thin film was fabricated using a silica sol synthesised from a tetraalkoxysilane, then the surface of the thin film will be hydroxylated and thus be

hydrophilic. This type of silica sol-gel thin film would be suited for use in a sensor for water vapour¹⁴. However, these hydroxylated silica surfaces can be functionalised with a vast range of functionalised groups to favour sensing of a wide range of gases^{15,16}. If the silica sol-gel thin film was fabricated using a silica sol synthesised from an organoalkoxysilane, the surface of the thin film will be covered with the organic group of the organoalkoxysilane precursor. The surface of these sol-gel thin films will then display hydrophilicity or hydrophobicity depending on the nature of the organic functional group. Thus these sol-gel thin films would be suitable for the sensing of a variety of gases, depending on the functional group.

In addition to the variety of surfaces available, the low-temperature synthesis reaction pathway of silica sol-gels allows for the encapsulation of chemical or biological, utilised for sensing of particular gases¹⁷, that would be denatured at the temperatures encountered in conventional glass manufacture (> 1000 °C)¹¹.

5.2.4 Polymer over layers

An alternative approach for improving the sensitivity is through the use of an over layer made from a material known as a polymer. Where sol-gel films can be considered as porous, polymer films, whilst not necessarily porous, can be considered to be permeable to gases and vapours¹⁸. Thus, the polymer film can act as a high surface area to increase the number of analyte gas molecules within the evanescent wave interaction volume. However, polymer over layers differ to sol-gel over layers, in that polymer over layers can expand and/or contract in the presence of vapours and gases, whereas sol-gels are rigid. The ability of polymer, over layers to swell or contract upon exposure to vapours and gases have been utilised in conductometric sensors¹⁹⁻²¹. The insulating polymer over layer is loaded with a conductive material. When exposed to a particular analyte, the polymer over layer swells and thus causing a change in conductivity. However, swelling of polymer over layers has also been utilised for optical sensing of vapours. For example, Ksendzov *et. al.* utilised a polymer over layer in an optical ring-resonator sensor for sensing of isopropanol vapour²². The swelling and refractive index change of the polymer upon exposure to isopropanol vapour caused a change in the optical output²². Therefore, it was proposed that the use of a polymer over layer would be a suitable strategy. A brief introduction to polymers, polymer dissolution and swelling

is given below. Further comprehensive polymer chemistry and theory can be found in the literature ^{23,24}.

5.2.4.1 Polymer theory

Polymers are organic or inorganic macromolecules comprised of a periodic structure of repeating smaller units known as monomers and can be of biological or man-made origin. The repeating units form long chains of lengths that are at least an order of magnitude greater than the width ²³. The polymer chains consist of many chemical variations such as a range of molecular weights, different degrees of branching and interconnection between chains ²³. Polymeric systems also exhibit many physical variations in the conformations of the individual chains and the alignment and subsequent organisation of neighbouring chains ²³, e.g. polymer chains may be physically entangled ²⁵.

Polymers do not dissolve in a manner similar to non-polymeric materials. Polymer dissolution involves diffusion of the solvent molecules in between the polymer chains, polymer chain disentanglement and diffusion of the polymer chains into the bulk liquid solvent ²⁵. Polymers in a glass-like state contain free volume. This free volume is comprised of channels and holes of molecular size within the bulk polymer ²⁵. Upon exposure to a thermodynamically suitable solvent, the solvent molecules diffuse into the channels and holes and chain disentanglement and diffusion of polymer chains into the bulk liquid solvent begin ²⁵.

If a polymer layer is exposed to solvent vapour, diffusion of solvent molecules into the free volume occurs with subsequent disentanglement of polymer chains and partial dissolution of the polymer, but, due to the absence of a bulk liquid solvent phase, little to no diffusion of polymer chains into the solvent occurs. The diffusion of solvent molecules into the polymer layer causes a change in the refractive index of the polymer layer to occur. Firstly, the diffusing solvent molecules displace gas molecules within the free volume of the polymer and thus cause an increase in the refractive index of the polymer layer; solvent refractive indices are higher than the refractive indices of gases as shown in **Table 5.1** above. Conversely, the second effect of diffusion of the solvent molecules into the polymer is the increase in the volume of the polymer layer; swelling of the polymer layer ²². The increase in volume causes a decrease in density and thus a decrease in refractive index. These

two effects of solvent diffusion on the refractive index of polymer layers suggest the use of polymer layers for the refractometric sensing of solvent vapours and other volatile organic compounds. In addition, by tailoring the functional groups present on the polymer chains, selective choice of which solvents are thermodynamically suitable for swelling and partial dissolution of the polymer over layer can be achieved. This approach has been successfully utilised for the generation of optical fibre volatile organic compound sensors²⁶. For these reasons, the use of a polymer over layer as a transduction layer for the refractometric sensing of solvent vapour with a planar integrated optical Bragg grating sensor was also investigated in this work.

1. R. A. Macrae, E. T. Arakawa, and M. W. Williams, *J. Chem. Eng. Data*, 1978, **23**, 189–190.
2. R. Stenutz, *Tables Chem.*, 2013.
3. S. S. Kurtz, A. E. Wikingsson, D. L. Camin, and R. A. Thompson, *J. Chem. Eng. Data*, 1965, **10**, 330–334.
4. G. W. C. Kaye and T. H. Laby, *Tables of Physical and Chemical Constants*, Longman, 16th edn., 1995.
5. R. M. Parker, J. C. Gates, M. C. Grossel, and P. G. R. Smith, *Appl. Phys. Lett.*, 2009, **95**, 173306.
6. M. N. Ghazzal, O. Deparis, J. De Coninck, and E. M. Gaigneaux, *J. Mater. Chem. C*, 2013, **1**, 6202.
7. C.-S. Chu, *Appl. Opt.*, 2011, **50**, 145–151.
8. C. J. Brinker and G. . Scherer, *Sol-gel science The Physics and Chemistry of Sol-Gel Processing*, Academic Press Inc. (London) Ltd., London, 1990.
9. J. D. Wright and N. A. J. M. Sommerdijk, *Sol-Gel Materials Chemistry and Applications*, Taylor & Francis, London, 2001.
10. C. J. Brinker and G. . Scherer, *Sol-gel science The Physics and Chemistry of Sol-Gel Processing*, Academic Press Inc. (London) Ltd., London, 1990.
11. J. D. Wright and N. A. J. M. Sommerdijk, *Sol-Gel Materials Chemistry and Applications*, Taylor & Francis, London, 2001.

12. M. M. Curtin Carter, N. S. McIntyre, H. W. King, and A. R. Pratt, *J. Non. Cryst. Solids*, 1997, **220**, 127–138.
13. J. Lin and C. Brown, *Trends Anal. Chem.*, 1997, **16**, 200–211.
14. J. P. Singh, S. Tao, and C. B. Winstead, 2005.
15. P. K. Jal, S. Patel, and B. K. Mishra, *Talanta*, 2004, **62**, 1005–28.
16. I. M. El-Nahhal and N. M. El-Ashgar, *J. Organomet. Chem.*, 2007, **692**, 2861–2886.
17. P. C. a Jerónimo, A. N. Araújo, and M. Conceição B S M Montenegro, *Talanta*, 2007, **72**, 13–27.
18. S. A. Stern and J. R. Fried, in *Physical Properties of Polymers Handbook*, ed. J. E. Mark, Springer New York, New York, 2nd edn., 2007, pp. 1033–1047.
19. M. A. Ryan, M. L. Homer, M. G. Buehler, K. S. Manatt, B. Lau, D. Karmon, and S. Jackson, in *Proc. 28th Int. Conf. on Environmental systems*, Society for Automotive Engineers, Warrendale, PA, 1998, p. 981564.
20. M. C. Lonergan, E. J. Severin, B. J. Doleman, S. A. Beaber, R. H. Grubb, and N. S. Lewis, *Chem. Mater.*, 1996, **8**, 2298–2312.
21. S. V. Patel, M. W. Jenkins, R. C. Hughes, W. G. Yelton, and A. J. Ricco, *Anal. Chem.*, 2000, **72**, 1532–1542.
22. A. Ksendzov, M. L. Homer, and A. M. Manfreda, *Electron. Lett.*, 2004, **40**, 2–3.
23. A. J. Peacock and A. Calhoun, *Polymer Chemistry Properties and Applications*, Carl Hanser Verlag, Munich, 1st edn., 2006.
24. J. E. Mark, Ed., *Physical Properties of Polymers Handbook*, Springer New York, New York, 2nd edn., 2007.
25. B. A. Miller-Chou and J. L. Koenig, *Prog. Polym. Sci.*, 2003, **28**, 1223–1270.
26. G. Schwotzer, I. Latka, H. Lehmann, and R. Willsch, *Sensors Actuators B. Chem.*, 1997, **38-39**, 150–153.

6. Mesoporous thin films and relative humidity sensing

6.1 Introduction

In the previous chapter the theory behind the proposal of increasing sensitivity of planar Bragg grating sensors through use of the ‘3D sensing volume’, along with materials such as sol-gel thin films and polymer films that would allow for utilisation of the ‘3D sensing volume’, were described. Due to potential cross-sensitivity and/or poisoning of sensing elements on sensors, the presence of water vapour in mixtures of analyte gases needed to be considered¹. Therefore investigation into the Bragg wavelength shift response of a Bragg grating device modified with a porous sol-gel thin film exposed to water vapour was investigated. During this work a planar Bragg grating relative humidity sensor was developed.

Within this chapter the development of the relative humidity sensor, which utilised the concept of the ‘3D sensing volume’ is described. The resulting sensor was robust, reusable and had a response time < 1 min. The fabrication of the sensor was achieved by modification of a planar Bragg grating chip with a thin film of a sol-gel. Firstly, a range of different types of silica sol-gel were fabricated and systematically characterised until a suitable silica sol-gel was synthesised that allowed for fabrication of reproducibly robust and porous thin films. A Bragg grating sensor chip was then modified with a thin film of this silica sol-gel and the Bragg wavelength shift response of this sensor chip to changes in relative humidity was investigated. A relationship between Bragg wavelength shift and increasing relative humidity for the sol-gel covered Bragg gratings was discovered, but it was soon determined that this silica sol-gel was hydrolytically unstable over time which significantly reduced sensitivity. Therefore, grafting of aluminium oxide onto the thin films of the silica sol-gel was explored as a method of improving the stability. In addition to improving the hydrolytic stability of the silica sol-gel, grafting with aluminium oxide also

doubled the sensitivity of the Bragg grating device to changes in relative humidity. Repeatable and reproducible measurements of changes in relative humidity were achieved with the aluminosilicate sol-gel modified device in a flow system and in the 'static' ambient laboratory environment over an 11 hour period. Contamination of the aluminosilicate sol-gel thin film did occur but full restoration of sensitivity was repeatedly achieved by rinsing with solvents (e.g. methyl ethyl ketone, MEK) commonly used in chemistry and electronics processing laboratories². Overall a robust and reusable relative humidity planar Bragg grating sensor, with a response time of < 1 min was achieved.

Note 1: In all Figures, unless explicitly stated, the x-axis error bars represent the average associated uncertainty of an average %RH value calculated from a range of %RH values measured with the *Testo 625* relative humidity sensor which is quoted as having an accuracy of ± 2.5 %RH³. The y-axis error bars represent the associated average uncertainty of an average Bragg wavelength shift calculated for either the uncovered or covered Bragg gratings at a particular %RH value.

Note 2: The file name of the associated spectra and/or characterisation data is given in the text at appropriate points. The file names given refer to the file names of the spectra/data that are located on the attached spectra CD. The file names are in italic font.

6.2 Development of the sol-gel sensing thin film

6.2.1 Undoped silica sol-gel (1)

The sol-gel thin films that were first investigated during this project were silica sol-gel thin films synthesised using tetraethyl orthosilicate (TEOS).

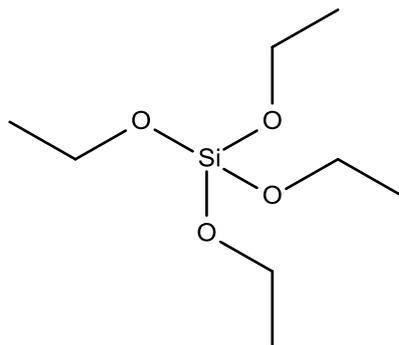


Fig.4.1: Structure of tetraethyl orthosilicate, TEOS.

The thin films of the undoped silica sol-gel (**1**) were fabricated by spin deposition of undoped ethanolic silica sol (**0.5**) and subsequent heat treatment at 75 °C for 20 hours. (**0.5**) was synthesised by acidic hydrolysis of TEOS using ethanol as a co-solvent and was left to age/stir for 6 days. The ^1H and ^{13}C NMR spectra of (**0.5**) only showed signals consistent with ethanol (^1H NMR spectrum \rightarrow *DJW.6066.Undoped TEOS silica sol (0.5).1H NMR.MA1213DJW1.010.esp* and ^{13}C NMR spectrum \rightarrow *DJW.6066.Undoped TEOS silica sol (0.5).13C NMR.ma1213djwt1.011.esp*). Despite the absence of signals due to TEOS in the NMR spectra, it cannot be stated from this result that the hydrolysis of TEOS had proceeded. This is because ethanol, the co-solvent, was in huge excess compared to the other reagents at the start of the reaction. In addition the amount of ethanol in (**0.5**) further increases during the course of the reaction; ethanol is a side-product of the hydrolysis of TEOS. Thus, it is more likely that the absence of the peaks due to TEOS is due to the very large amplitude of the ethanol peaks caused by the huge excess of ethanol. However, a split strong trough at 1080 cm^{-1} and 1044 cm^{-1} , assigned to Si – O – Si stretches in long siloxane chains, and a strong trough at 879 cm^{-1} , assigned to amorphous silica, in the FT-IR spectrum of (**0.5**), confirmed the presence of silica species (FT-IR spectrum \rightarrow *DJW.6066.Undoped TEOS silica sol (0.5).FT-IR*). These characteristic IR signals indicated that the hydrolysis of TEOS to form siloxane linkages and silica particles had occurred.

To form the thin films of (**1**), (**0.5**) was spin deposited onto silica substrates that were pre-treated in “piranha” solution: a 3:1 ratio of 98% v/v sulphuric acid & hydrogen peroxide aqueous solution (20 volumes). The thin films were then baked for 20 hours at 75 °C. The resulting thin films of (**1**) were clear and colourless by eye.

Characterisation by melting point analysis and IR spectroscopy confirmed that **(1)** was solid silica (FT-IR spectrum \rightarrow *DJW.6066.Undoped TEOS silica sol-gel (1).FT-IR*). However, the thin films of **(1)** also exhibited large cracks and the thin film appeared to be ‘flaking’ away from the substrate as shown in the scanning electron micrograph (**Fig.6.2**) below.

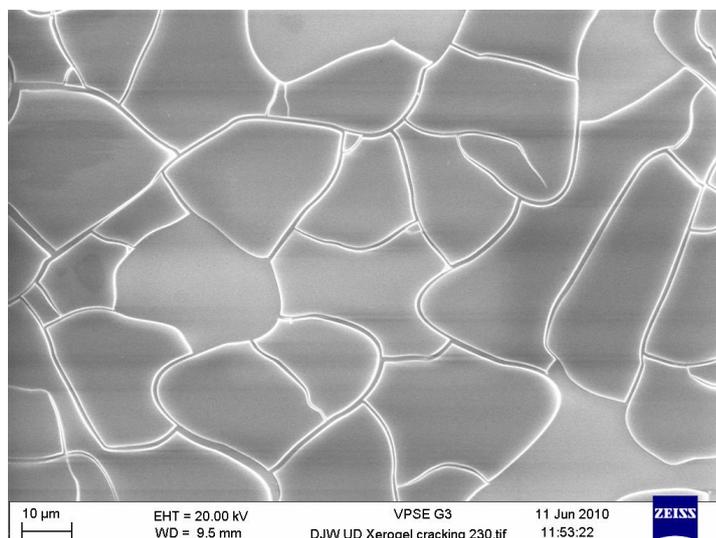


Fig.6.2: Scanning electron micrograph of a thin film of **(1)** showing cracking and areas where sections of **(1)** that had become removed. The streaking on the micrograph is an artefact due to surface charging. The micrograph was collected whilst operating the SEM in variable pressure mode.

These cracks are discontinuities in refractive index that the evanescent wave of the optical mode would encounter. Therefore this could lead to significant scattering losses, thus diminishing the reflected signals from the Bragg gratings. In addition, the robustness and lifetime of the thin film of **(1)** is severely limited due to the observation that removal of sections of **(1)** occurs during or after cracking. Therefore another type of silica sol-gel that did not exhibit cracking features upon heat treatment/densification was required.

6.2.2 Undoped methyl-functionalised silica sol-gel (2)

In the literature, silica sol-gels synthesised from trimethoxy(methyl)silane (MTMS) have been used in the fabrication of bespoke optical components as it has been shown that MTMS sol-gels do not exhibit cracking upon heat treatment/densification⁴. Furthermore, there is an example in literature of an MTMS based silica sol-gel that exhibited superhydrophobicity after post-synthesis with alkylsilanes⁵; superhydrophobicity would minimise the effect of water vapour when

refractometrically sensing other gases and vapours. Thus, the use of MTMS silica sol-gels was explored.

The thin films of the undoped methyl-functionalised silica sol-gel (**2**) were fabricated by spin deposition of undoped methyl polysiloxane sol (**1.5**) and subsequent heat treatment at 70 °C for 2 hours. (**1.5**) was synthesised using a modified ‘fast sol-gel’ method ⁴; hydrolysis of neat MTMS with water at 73 °C for 20 mins. On the ¹H NMR spectrum of (**1.5**) there was a broad singlet at 4.47 ppm which was attributed to a silanol functional group proton (**Fig.6.3**); this suggests that some degree of hydrolysis of MTMS had occurred (¹H NMR → *DJW.6625.32.MTMS silica sol (1.5).1H NMR.AP0413DJW1.0.10.esp*).

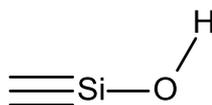


Fig.6.3: A silanol functional group. ≡ represents the remaining three bonds from silicon to other atoms.

The ¹³C NMR of (**1.5**) showed the presence of 6 singlet signals between 50.78 – 49.99 ppm (¹³C NMR → *DJW.6625.32.MTMS silica sol (1.5).13C NMR.positive ppm.AP0413DJW1.011.esp*). These signals have been attributed to Si – O – **CH₃** carbon of MTMS molecules in six different possible stages of hydrolysis as shown below in **Fig.6.4**. The position of the functional groups around the central silicon atom does not matter.

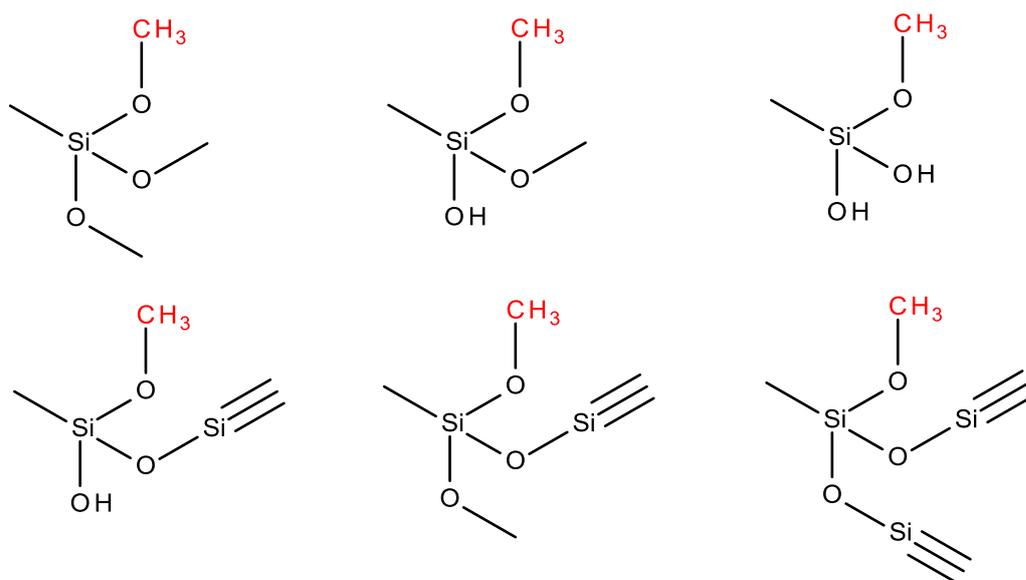


Fig.6.4: The six signals in the ^{13}C NMR of (1.5), between 50.78 – 49.99 ppm, are attributed to the Si – O – CH_3 carbon of a MTMS molecules which can be in one of six different permutations of degree of hydrolysis, all of which are shown in this figure. The position of the functional groups around the central silicon atom does not matter. \equiv represents the remaining three bonds from silicon to oxygen atoms.

Additionally there were fourteen singlet signals in the region between $\sim 3.00 - \sim 7.00$ ppm (^{13}C NMR \rightarrow DJW.6625.32.MTMS silica sol (1.5).13C NMR.negative ppm.AP0413DJW1.011.esp). These signals are in the region typical for carbon atoms which are directly bonded to a silicon atom. Ten of these signals have been attributed to the Si – CH_3 carbon of MTMS molecules in ten different possible stages of hydrolysis as shown below in Fig.6.5. The position of the functional groups around the central silicon atom does not matter.

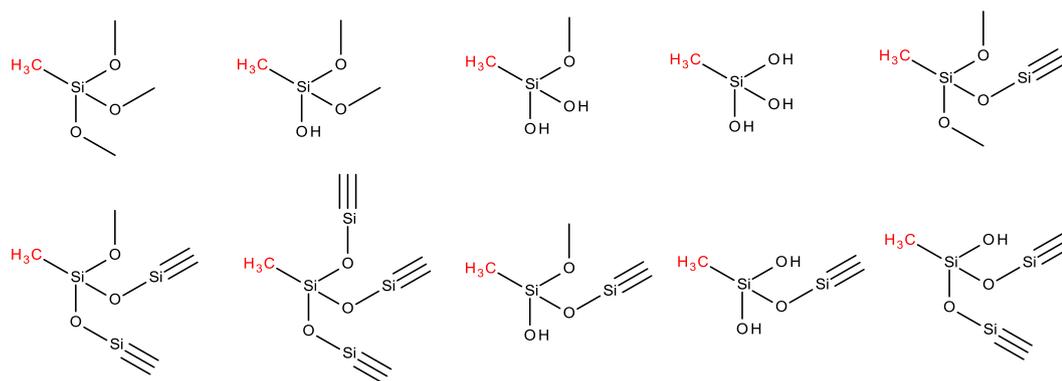


Fig.6.5: Ten of the signals in the $-3.00 - -7.00$ ppm region in the ^{13}C NMR of **(1.5)** are attributed to the Si – CH_3 carbon of a MTMS molecules which can be in many different permutations of hydrolysis, as shown in this figure. The position of the functional groups around the central silicon atom does not matter. \equiv represents the remaining three bonds from silicon to oxygen atoms.

These signals in the ^{13}C NMR suggest that hydrolysis of MTMS had occurred and that polysiloxane species had been formed in the sol.

Thin films of **(2)** were fabricated by spin deposition of **(1.5)** and subsequent heat treatment at $70\text{ }^\circ\text{C}$ for 2 hours. Synthesis of undoped methyl-functionalised silica sol-gel **(2)** was confirmed by the melting point analysis and IR spectroscopy. The melting point of the solid was $> 300\text{ }^\circ\text{C}$ which suggests that the solid is not organic and is inorganic silica; the literature value of the melting point of silica is $1723\text{ }^\circ\text{C}$ ⁶. Furthermore, a strong and broad absorption trough at 1023 cm^{-1} in the FT-IR spectrum of **(2)** confirmed that long chains of Si – O – Si bonds were present in the solid. In addition, strong absorptions at 1270 cm^{-1} and 776 cm^{-1} (both attributed to the Si – C bond) and a weak absorption at 2969 cm^{-1} (C – H stretch) confirmed the presence of methyl group directly bonded to silicon within the silica solid (FT-IR spectrum \rightarrow *DJW.6625.32.MTMS fast sol-gel (2).FT-IR*).

The thin films of **(2)** were transparent by eye and crucially did not display any crack features as shown in **Fig.6.6** below. However, the thin films were uneven and did display some bubble/hole-like features (see **Fig.6.6**); these features may have caused optical scattering. In addition it was found that the reproducibility in terms of the robustness of thin films of **(2)** was low; scratch-tests with plastic and/or metal tweezers revealed some films of **(2)** were softer than other samples. This was initially attributed to degradation of the MTMS starting material but even with

robust control of the reaction conditions and a fresh stock of MTMS the reproducibility issue was not resolved.



Fig.6.6: (Left) Photograph of a thin film of (2) on a soda glass substrate demonstrating the high degree of transparency of the thin films at visible wavelengths and the lack of macro crack features. (Right) A photograph of a thin film of (2) that had been coloured with a blue dye (on a soda glass substrate) highlighting the bubble-like/hole features in the thin films of (2).

A further disadvantage was that thin films of (2) were not porous. The non-porous nature of thin films of (2) was determined by comparison of refractive index values. The refractive index of the thin film of (2) was measured using a Metricon prism coupler. Using a prism coupler, the refractive index and thickness of thin films of dielectric materials can be determined^{7,8}. Briefly, the coupling of light (usually a laser) into the thin film is governed by the angle of incidence, θ , of the light onto the base of the prism as shown in **Fig.6.7** below.

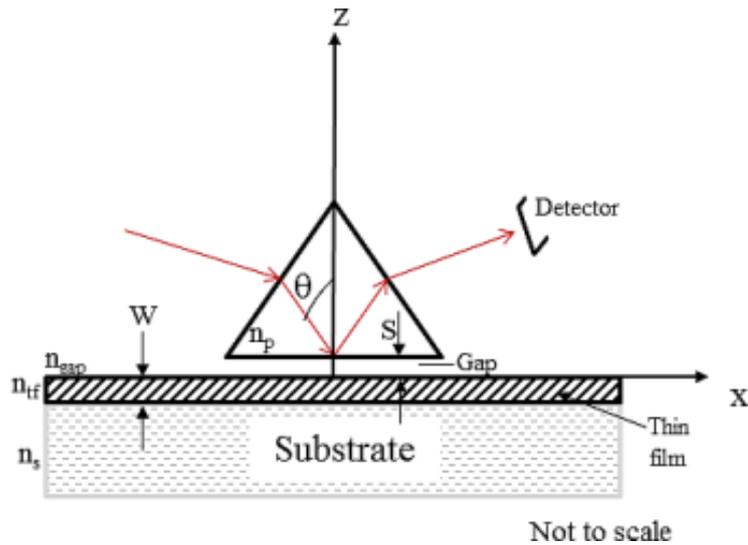


Fig.6.7: Schematic of the prism coupling technique used to determine the refractive index of the thin film (n_{tf}) and the thickness of the thin film (W). There is an air gap (Gap) of width S and refractive index n_{gap} between the prism (refractive index n_p) and the thin film. At certain values of the angle of incidence, θ , coupling of the laser light (red arrows) into the thin film causing excitation of propagating thin film modes occurs and thus the power recorded at the detector is at a minimum.

At most values of θ , total internal reflection occurs and the magnitude of the reflected optical power is recorded at the detector. However, at certain values of θ , strong coupling of light into the thin film occurs resulting in excitation of the first order and higher order propagating modes within the thin film. At these values of θ , the reflected power at the detector is at a minimum and thus dips in the reflected power spectrum are observed. Knowing these values of θ , and with appropriate signal processing and calculation, the refractive index and thickness of a thin film can be determined. More information on this technique, including the mathematics used to calculate the refractive index and the thickness of a thin film is given in the work of Ulrich *et. al.*^{7,8}.

The refractive index of a thin film of (2) was experimentally measured to be 1.402 ± 0.002 and the literature value for the refractive index value of a non-porous MTMS sol-gel thin film = 1.399 ⁹. Therefore an alternative reproducible method to produce robust porous sol-gel thin films for gas sensing was required.

6.2.3 Undoped MTMS silica solid (3)

Highly porous silica sol-gel thin films made from MTMS were next investigated. Briefly, MTMS was hydrolysed with an aqueous solution of oxalic acid for 24 hours

to yield a sol (**2.5**). Characterisation of (**2.5**) by ^1H NMR showed that some hydrolysis of MTMS had occurred due to the presence of a broad shoulder peak at 4.57 ppm which is attributed to a silanol proton (^1H NMR spectrum \rightarrow *DJW.6625.32.Fast sol-gel powder sol (2.5).1H NMR.ap1713dhw5.010.esp*). A cluster of signals between 50.8-50.3 ppm in the ^{13}C NMR spectrum were attributed to the Si – O – CH_3 carbon of MTMS molecules in different stages of hydrolysis as shown above in **Fig.6.4**. In addition a cluster of 10 signals between \sim 3.50-7.20 ppm are attributed to the Si – CH_3 carbon of MTMS molecules in various different stages of hydrolysis as shown above in **Fig.6.5** (refer to *DJW.6625.32.MTMS silica sol (1.5).13C NMR.positive ppm.AP0413DJW1.011.esp* and *DJW.6625.32.MTMS silica sol (1.5).13C NMR.negative ppm.AP0413DJW1.011.esp*). These signals strongly suggest that some degree of hydrolysis of MTMS has occurred but the reaction had not gone to completion at this point; confirmed by the observation that the sol was still a liquid and had not formed a cross-linked silica solid.

After 24 hours, gelation was initiated by the addition of 11M $\text{NH}_4\text{OH}_{(\text{aq.})}$ solution to (**2.5**) and the reaction was left to stand for \sim 60 hours without stirring to afford a white solid monolith. This monolith was mechanically ground into the white solid powder (**3**). The synthesis of (**3**) was confirmed by melting point analysis and IR spectroscopy. The melting point of (**3**) was > 300 $^\circ\text{C}$. Measurement of melting points above 300 $^\circ\text{C}$ was not possible, however a melting point >300 $^\circ\text{C}$ suggests that (**3**) was inorganic silica and not an organic side product.. Therefore, the nature of (**3**) was elucidated with IR spectroscopy. The presence of a strong absorption feature at 1014 cm^{-1} in the IR spectrum of (**3**) confirmed that long and branched chains of Si – O – Si bonds were present. In addition the presence of the methyl group was confirmed by the strong absorptions at 1270 cm^{-1} and 762 cm^{-1} (Si – C bond stretches) and the weak absorption at 2971 cm^{-1} (C – H stretch)(FT-IR spectrum \rightarrow *DJW.6625.31.Fast sol-gel MTMS solid (3).FT-IR*)

Thin films of (**3**) were formed by spin deposition of sonicated methanol suspensions containing varying masses of undoped MTMS silica solid (**3**). The sol-gel thin films were then dried in ambient conditions. All of the thin films exhibited a granular/powdery structure when observed visually and by visual microscopy which suggests that the films display a high degree of porosity (**Fig.6.8** below). However, the largest particles from the sol-gel thin films were easily removed when the thin

film was directly exposed to a flow of nitrogen gas and the thin films were also partially removed when mechanically rubbed with an acetone soaked cleaning bud. Upon rinsing with acetone the thin films were fully removed. These observations suggest the thin films of (3) were not chemisorbed onto the substrate surface via (Si – O – Si) bonds.

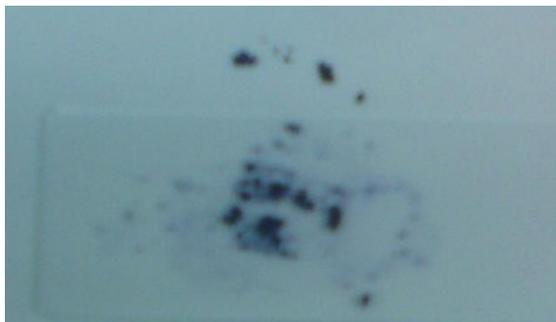


Fig.6.8: Powdery appearance of an attempted film of (3) on a soda glass slide. The solid was dyed with a blue dye to enable visualisation of the resultant films.

Overall, the macroporous sol-gel thin films fabricated using this method would be not suitable for application to a Bragg grating sensor as a sensing thin film. The micron scale particles within the thin films of (3) could cause scattering losses and the thin films would not be suitable for gas or liquid flow sensing applications due to easy removal from the substrates.

Thus an alternative type of sol-gel thin film that was porous but also highly robust was required for liquid or gas flow sensing experiments.

6.2.4 Undoped mesoporous silica sol-gel thin film (4)

An alternative method for the formation of mesoporous silica sol-gel thin films is the template method. Briefly, surfactant molecules are dissolved in the sol at concentrations (c_0) below the critical micelle concentration (cmc) of the surfactant, $c_0 \ll \text{cmc}$. When the sol is deposited via spin coating or dip coating the evaporation of the solvent causes the concentration of the surfactant to be greater than the cmc and micelles of the surfactant molecules form within the wet sol-gel thin film; the micelles template a structure of pores within the sol-gel thin film. Upon calcination in air, the silica structure is consolidated and the organic surfactant molecules are removed via combustion, leaving behind the pore structure within the silica sol-gel thin film. This is known as the evaporation induced self-assembly (EISA) method¹⁰.

To investigate this method, a thin film of (4) was fabricated by using modified procedures from the literature ^{11,12,13}. Briefly, tetraethyl orthosilicate (TEOS), dissolved in ethanol was hydrolysed with HCl_(aq.) at reflux under a nitrogen atmosphere. The resulting sol was then cooled to room temperature, the concentration of HCl was increased to 7.34 mM with stirring under nitrogen and the sol was ‘aged’ without stirring at 60 °C for 15 minutes in ambient conditions. To this sol, ethanol (3 volumes) was added and the organic surfactant cetyltrimethylammonium bromide (CTAB) was added to afford (3.5). The concentration, c_0 , of CTAB was 0.07. This concentration is reported to result in a bicontinuous worm-like mesoporous structure within the sol-gel thin films upon spin or dip coating¹¹.

Characterisation of (3.5) demonstrated that the hydrolysis of TEOS had occurred. Similar to (0.5) the ¹H and ¹³C NMR spectra of (3.5) only showed signals consistent with ethanol; again ethanol was in a huge excess (¹H NMR spectrum → *DJW.6066.85.CTAB templated TEOS silica sol (3.5).1H NMR.AP3012DJW1.010.esp*). However, strong absorptions at 1200 cm⁻¹ and 1080 cm⁻¹ in the FT-IR spectrum of (3.5) assigned to asymmetric Si – O – Si stretches and symmetric stretches in cyclic structures respectively, confirmed the formation of siloxane species indicating that the hydrolysis of TEOS had occurred to some degree (FT-IR spectrum → *DJW.6066.85.CTAB templated TEOS silica sol (3.5).FT-IR*).

Thin films of (4) were formed by spin deposition of (3.5) onto a silica substrate (which had been previously treated with “piranha” solution, a 3:1 ratio of 98% v/v sulphuric acid & hydrogen peroxide aqueous solution (20 volumes)) at 2000 rpm for 1 min followed by calcination at 400 °C for 1 hour (heating rate 1.5 °C / min) in a N₂/O₂/Ar atmosphere. With these spin deposition conditions the average thickness of a thin film of (4) was ~200-250 nm (2000-2500 Å) and the average surface roughness (R_a) ~20 nm (~200 Å). These thickness and surface roughness measurements were collected by contact surface profilometry over the step edge of the thin film. In this technique a stylus is placed in contact with the surface of interest and then is translated horizontally across the surface akin to how a phonograph needle is translated across a record on a turntable. Changes in the Z axis (defined here as the ‘height’ axis), due to peaks and troughs present on the surface, are generally recorded as changes in capacitance. With signal processing this data is

converted into information about the profile of the surface, including the average surface roughness (R_a)^{14,15,16}. The average surface roughness (R_a) is defined the arithmetic mean of the profile data. A typical surface profile over the step edge of a thin film of (4) is shown below in **Fig.6.9**.

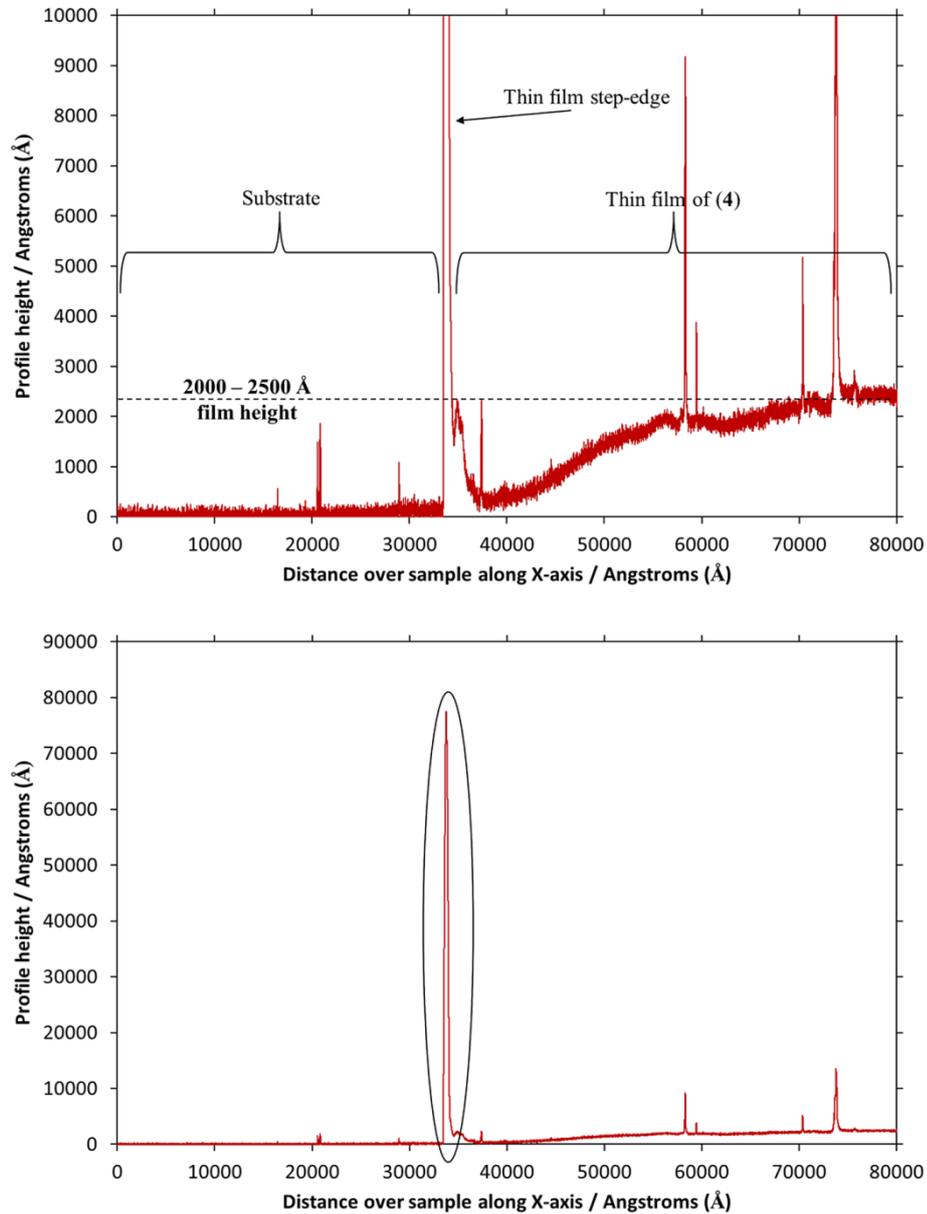


Fig.6.9: (Top) An average (from 3 traces) step profile of the step-edge of a typical thin film of (4), at one location, on a substrate showing the step-edge feature and a film height (relative to the substrate level) of ~2000-2500 Å. Measurement of step height from left to right along x-axis. (Bottom) Highlighting the step-edge feature which is approximately 80000 Å and is formed by accumulation of (3.5) against the Capton® polyimide tape mask (used to mask areas on the substrate) during spin deposition of (3.5). Several

To enable characterisation of (4) with conventional chemical characterisation techniques, thin films of (4) were scraped with metal scalpel blades and the flakes of solid collected were ground to afford a white powder. This powder was then characterised by IR spectroscopy and melting point analysis. The melting point was found to be $> 300\text{ }^{\circ}\text{C}$; this suggested that the solid was not an organic by-product and the solid could have been silica (4). The presence of a strong and very broad peak at 1019 cm^{-1} in the FT-IR spectrum of the solid, which is attributed to Si – O – Si chain stretches (the broadness of the peak indicates very long and branched silica chains), confirmed that (4) had been formed (FT-IR spectrum \rightarrow *DJW.6625.32.CTAB templated TEOS silica sol-gel (4).FT-IR*).

Thin films of (4) were clear and colourless and crucially did not display any crack or bubble/hole-like features as shown in **Fig.6.10** below.

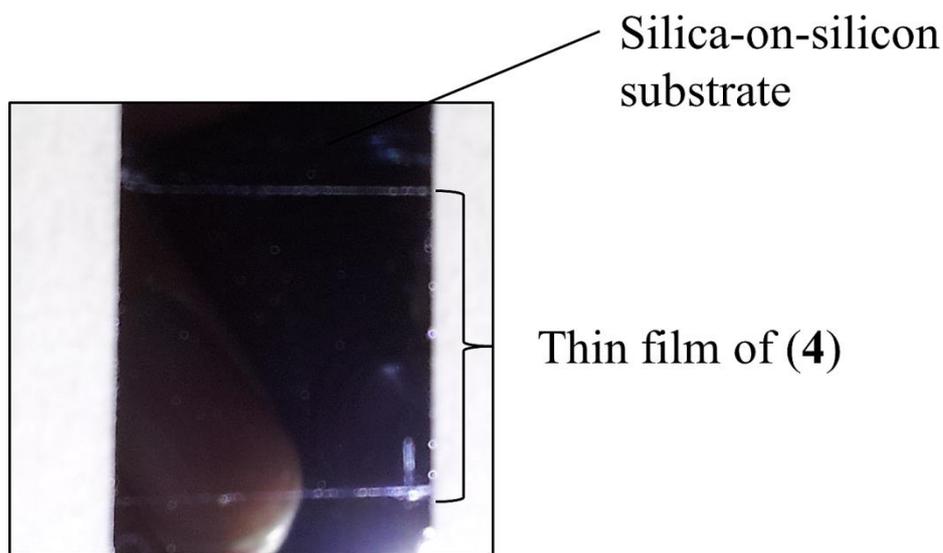


Fig.6.10: A clear and colourless thin film of (4) on a reflective silica-on-silicon, thus highlighting the high transparency of the thin films of (4) and the lack of crack or hole-like features.

The sol-gel thin films were only slightly scratched with plastic tweezers with no associated removal of the thin film. In addition, no morphological changes were observed by eye or visual microscopy after sonication of a thin film of (4) in acetone for 25 mins. Atomic force microscopy (AFM) was also used to characterise the thin films of (4).

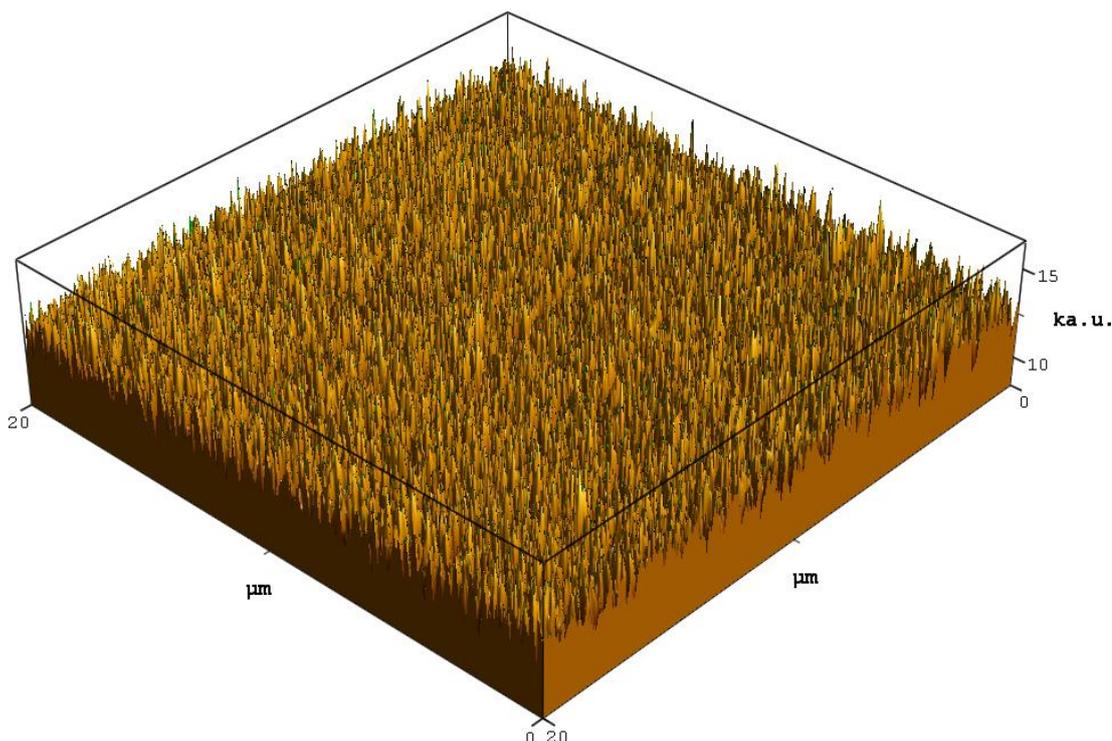


Fig.6.11: Atomic force micrograph of the surface of a thin film of (4) highlighting the roughness of the surface, which is comprised of peaks and troughs.

As is evident from **Fig.6.11** above the surface of the sample of a thin film of (4) is comprised of peaks and troughs which give rise to a high surface area. This suggests that thin films of (4) would be suitable for sensing applications but the porosity of the thin films of (4) still had to be determined.

6.2.5 Determination of the porous nature of thin films of (4)

Firstly, scanning electron microscopy (SEM) was attempted to visualise pores within the thin film. However, no pore features were observed. This was attributed to the pore features being an order of magnitude smaller than the resolution limit of the scanning electron microscope that was used; the expected diameter of the pores is ~ 3 nm¹¹ and the resolution limit of a conventional SEM (i.e. not a field-emission scanning electron microscope) is ~ 10 nm¹⁷. Therefore another method was needed to determine if the thin films of (4) were porous.

In the literature, the porous nature of mesoporous silica sol-gel thin films has been confirmed by doping with a highly coloured dye; the pores allowed for ingress of the dye into the thin films and thus resulted in colouration of the thin film¹¹. This method was used to determine if the thin films of (4) were porous. To determine if

methylene blue was encapsulated within the pores of (4) and not adsorbed on the surface of the silica, another thin film of a silica sol-gel (NP) was synthesised as per the experimental procedure for (4) apart from addition of CTAB surfactant; no pore templating and formation would occur. The thin films of (4) and (NP) (~300 nm thick) were immersed in an aqueous solution of methylene blue chloride (pH 6.6); the chloride salt of a highly coloured organic dye (Fig.6.12 below).

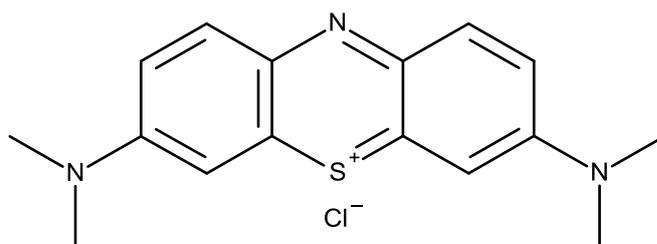


Fig.6.12: Structure of methylene blue chloride.

The aqueous solution of methylene blue was pH = 6.6 to ensure the silica surface was predominantly negatively charged thus enabling ion – ion interactions with the methylene blue cation (the isoelectric point of silica is between pH 1.8 – 2.5)¹¹. After 20 mins with stirring, the thin films were removed from the solution. The thin film of (4) was intense blue whereas the thin film of (NP) only exhibited a very slight blue colouration. The intense blue colouration of (4) persisted with copious rinsing with de-ionised water and drying under a stream of nitrogen gas. In contrast, the intensity of the very slight blue colouration of (NP) decreased further upon copious washing with de-ionised water. Both thin films were then characterised with transmission mode UV-Visible spectroscopy.

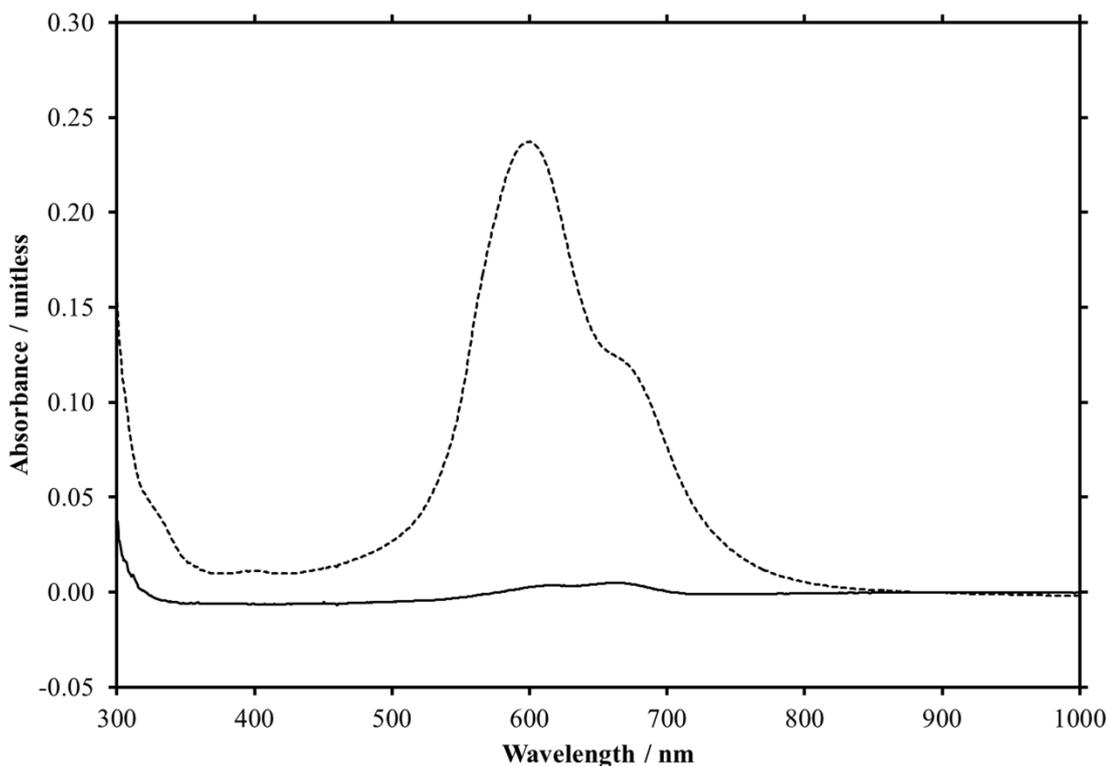


Fig.6.13: Intense absorption due to methylene blue encapsulated within the pores of the templated thin film of (4) but little to no methylene blue associated absorption features for the non-templated non-porous thin film sample (NP).

Colouration of the thin film of (4) due to the presence of methylene blue, thus formation of (5), was confirmed with UV-Visible spectroscopy; an intense absorption feature at $\lambda_{\max} = 600 \text{ nm}$ & $\lambda_{2\text{nd}(\text{shoulder})} = 665 \text{ nm}$ in excellent agreement with the literature¹¹. In contrast the spectrum of (NP) showed a very weak absorption feature due to methylene blue; this is attributed to methylene blue physically adsorbed on the surface of (NP) only. The greater magnitude of the absorption feature due to methylene blue for (5) compared to (NP) is attributed to a much greater quantity of methylene blue encapsulated within the pores of (5) than the quantity of methylene blue physically adsorbed on the surface of (NP). This demonstrates that the template method is a successful method for producing porous thin films and that thin films of (4) were porous and suitable for sensing applications.

Further attempts to characterise the nature of the pore structure within the thin films of (4) were made with X-ray diffractometry (XRD). Thin film X-ray diffraction (XRD) studies were performed with Dr. Mark Light (Department of Chemistry, University of Southampton) in attempt to calculate the diameter of the pores within a mesoporous thin film of (4). However, the XRD traces collected showed no

diffraction peaks attributed to long range ordered pore structures. An example XRD trace is shown below in **Fig.6.14**.

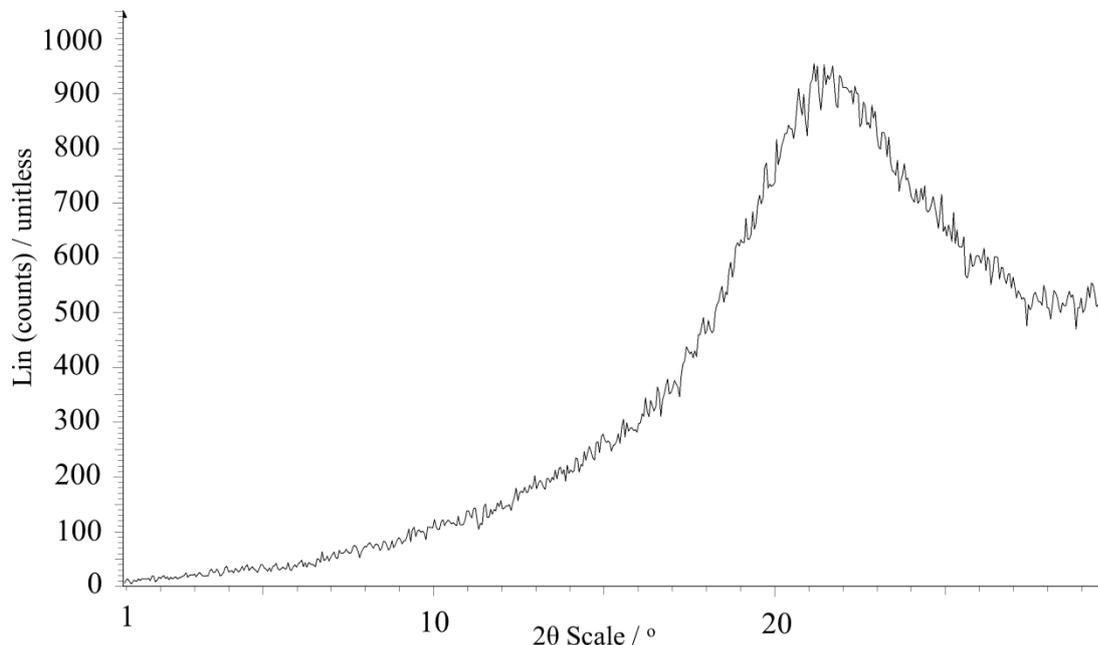


Fig.6.14: X-ray diffraction (XRD) trace collected from thin film of (4) (~250 nm thick) adhered on a silica-on-silicon substrate using a *Bruker Gadds* diffractometer running in pseudo-parallel beam geometry. There are no peak features within the 2θ region of interest which was determined to be 2° - 5° from the literature (knowing that the concentration of the CTAB surfactant in the sol before spin coating = 0.07 M). The broad peak at $\sim 22^\circ$ is attributed to a common feature in XRD traces for amorphous materials¹⁸.

In the XRD traces there were no peaks within the 2θ region of interest which was determined from the literature to be 2 - 5° (knowing the concentration of the CTAB surfactant in the sol before spin coating $c_o = 0.07$ M)¹¹. This result indicated that there was no long-range ordered pore network within the thin films of (4), or there were no pores. The latter had been disproven by the observations made in the dye ingress experiments, therefore the absence of diffraction peaks in the 2 - 5° 2θ region was explained by the absence of a long-range ordered pore network. The absence of a long-range ordered pore network within thin films of (4) was attributed to the spin-deposition method that was used; no ramp-up rate from 0 to 2000 rpm. It was proposed that no ramp-up rate led to changes to the structural form of the micelles formed during the EISA process. With no ramp-up rate, the spin rate increased from 0 rpm to 2000 rpm in a time, t , estimated to be $t < 0.1$ s. It is proposed that $t < 0.1$ s is insufficient for a long-range ordered micellar worm-like

network to form before the critical micelle concentration is surpassed due to the rapid spin-off of the sol (3.5) and/or evaporation of ethanol and the shear forces exerted on the sol. Thus an amorphous disordered micelle network is formed. This argument is supported by the work of Pan *et. al.* in which it was reported that spin rate has an effect on the mesostructure formed due to changing ethanol evaporation rates and shear forces¹⁹. The broad peak at $\sim 22^\circ$ is attributed to a common diffraction peak in XRD traces for amorphous materials¹⁸.

6.3 Development of a Bragg grating sensor relative humidity sensor

6.3.1 Planar Integrated Bragg grating sensor modified with a thin film of (4) as a relative humidity (%RH) sensor

It has been demonstrated previously that planar integrated Bragg grating sensors, of the type used herein, are sensitive to physically adsorbed water²⁰. When layers of adsorbed water build up on the surface of the Bragg grating device, air (refractive index ~ 1.00) is replaced by water (refractive index 1.33) and thus the effective refractive index, n_{eff} , encountered by the evanescent wave of the optical mode increases. This causes a corresponding increase in the Bragg wavelength.

It was proposed that the large surface area of the thin film of (4) would further increase the sensitivity of the planar integrated Bragg grating sensors devices to adsorbed water vapour. It was argued that due to the large surface area of a thin film of (4) compared to the planar surface of an unmodified Bragg sensing device the evanescent wave of the optical mode will experience a larger effective refractive index due to more physisorbed water per square unit area. Therefore to understand the effect of concentration of water vapour in a carrier gas on Bragg wavelength shift, an experiment was designed whereupon a device modified with a thin film of (4) (shown below in **Fig.6.15**) was exposed to varying concentrations of water vapour in nitrogen carrier gas and interrogated at 1550 nm.

Now that the porous nature of thin films of (4) had been established, the suitability of thin films of (4) for sensing was investigated. A thin film of (4) was applied to the surface of a planar integrated Bragg grating sensor chip as per the procedure given in the Experimental Details chapter. The thickness of the thin film of (4) was measured

using stylus profilometry. At multiple locations (3-5 locations) on the sample an average (from 3 step profile traces) step profile of the step-edge of a the thin film of (4) was determined. The average thickness of the film, calculated from the multiple average height profiles, was 230 ± 27 nm. The large associated error is attributed to the significant topographical waviness of the thin film surface which was measured with the step profiler; waviness is defined as variation in the height of the sample surface over long wavelength regimes²¹ The Bragg grating device contained eight Bragg gratings equally spaced along a waveguide. The thin film of (4) was applied to the device so that the central four Bragg grating were covered and the remaining four Bragg gratings, two gratings on either side of the thin film were uncovered. This is shown in **Fig.6.15** below.

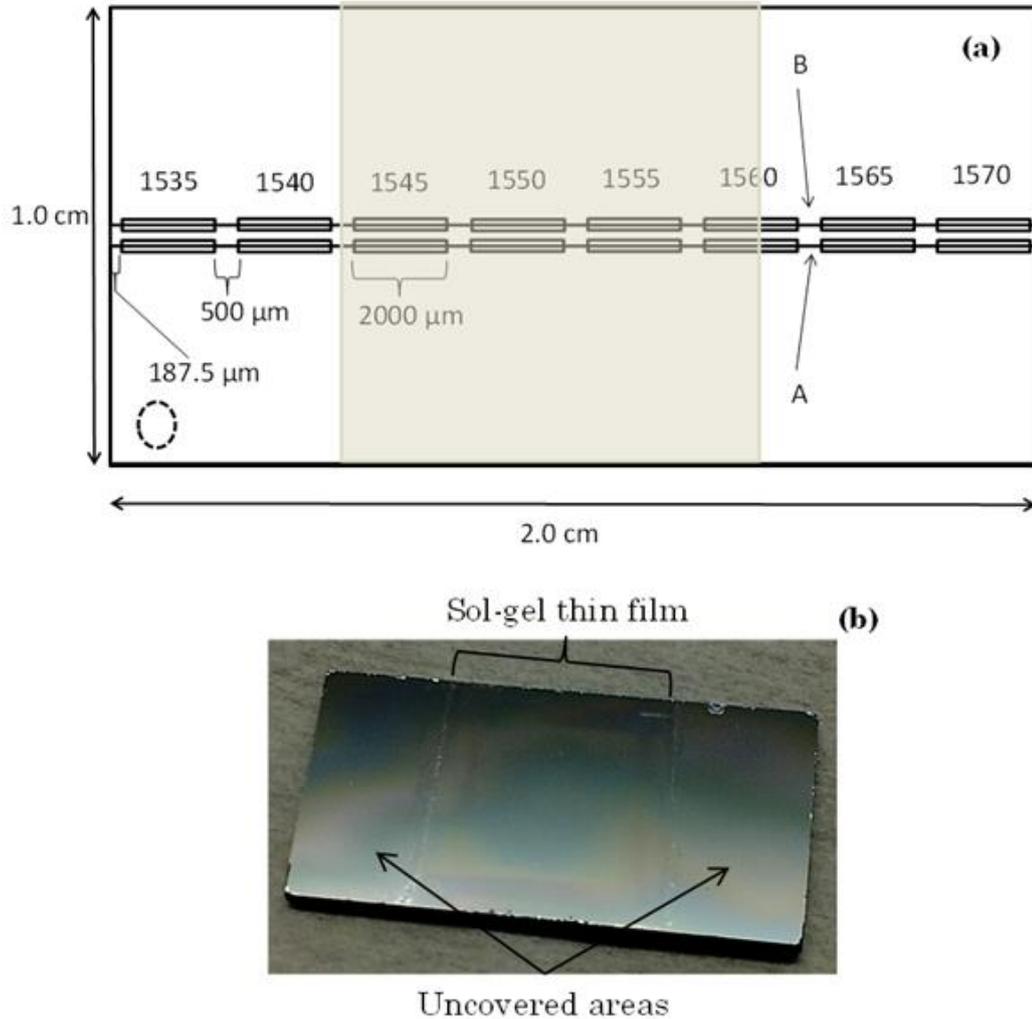


Fig.6.15: (a) Schematic of the initial water vapour sensing Bragg device highlighting the thin film of (4) on top of the device (light grey colour) thus showing the Bragg gratings that were covered and which were uncovered. A and B are the waveguides written into the device. The rectangles along A and B represent the Bragg gratings; the number above each Bragg grating is the Bragg wavelength of that grating (units = nm) and is used for identification. The hashed circle shows which end facet was pigtailed. **NB** Bragg grating 1560 was partially covered by the thin film of (4). (b) A photograph of Bragg device modified with the thin film of (4).

By only covering the central four Bragg gratings with the thin film of (4), the peripheral Bragg gratings on either side were then used for self-referencing against other environmental fluctuations; primarily temperature. It should be noted that the Bragg gratings at the extremities of the device, while suitable for temperature referencing, exhibited spectral fringes which degraded the quality of fitting. As such,

these gratings (1535 nm and 1570 nm) were not used explicitly for referencing but did allow for further confirmation of thermal trends that were observed.

This Bragg grating device modified with the porous thin film of (4) was then used in moisture vapour sensing (optical hygrometry) experiments:

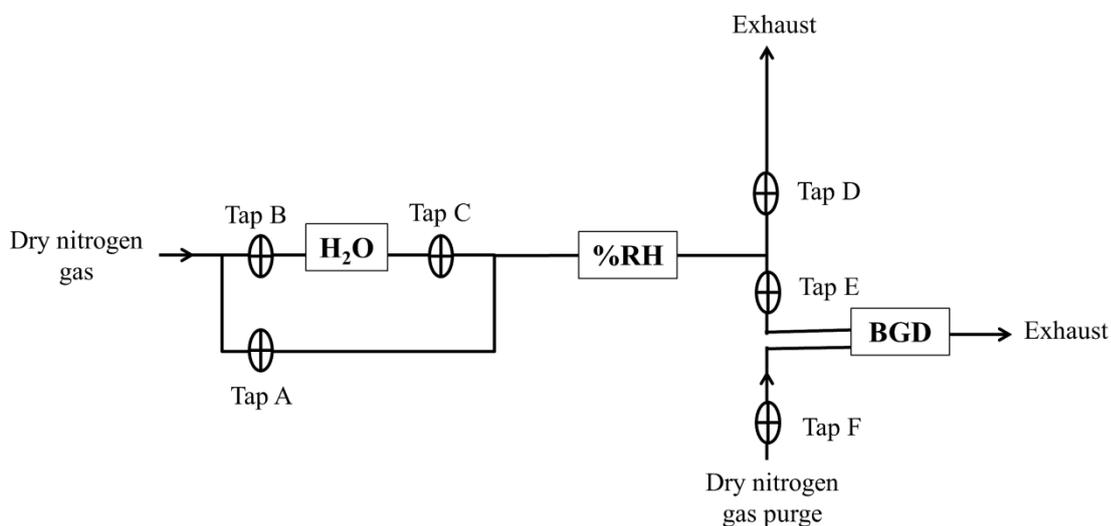


Fig.6.16: Schematic of the optical relative humidity sensing experiment. Nitrogen gas containing water vapour was generated by bubbling dry nitrogen gas through the reservoir of de-ionised water ('H₂O'). '%RH' represents the commercial electronic reference hygrometer and 'BGD' is the flow cell containing the integrated optical Bragg grating device. A second nitrogen purge was used to maintain a dry atmosphere between measurements.

A schematic of the gas delivery apparatus for optical hygrometry experiments is shown above in **Fig.6.16**. The integrated optical Bragg grating device ('BGD') was mounted within a flow cell and interrogated optically whilst exposed to alternating flows of either dry or moist nitrogen gas. The temperature within the flow cell was monitored via a thermocouple. The %RH level of the dry nitrogen gas was <0.5 %RH as measured with a commercial electronic reference hygrometer.

To achieve a flow of moist nitrogen gas, the nitrogen carrier gas was introduced by bubbling dry nitrogen gas (typical flow rate $\sim 3.5 \text{ L min}^{-1}$) through a reservoir of deionised water ('H₂O'). The moisture content in the nitrogen gas was altered by changing the temperature of the water in the reservoir. This was achieved through use of an external water bath; the temperature of which was increased or decreased with either a hotplate or addition of ice respectively. After exposure to moist nitrogen gas, the integrated Bragg grating hygrometer device ('BGD') was returned

to its initial state by purging with a flow of dry nitrogen gas ($>5 \text{ L min}^{-1}$). Before a humidity sensing measurement was recorded, a stable %RH value for the moist nitrogen gas flow was first achieved by altering the water bath temperature and referenced against an in-line electronic commercial Testo 625 hygrometer ('%RH'). Once a constant relative humidity, %RH, value was achieved, the moist nitrogen gas was introduced into the cell containing the 'BGD'. Whilst the vapour flow was stabilising, the sensor device was kept under the bypass dry nitrogen flow to avoid contamination. The full spectrum of the reflected peaks of the Bragg gratings was sampled every 20-25 seconds via an optical spectrum analyser (OSA). The average shift in Bragg wavelengths, upon exposure of the 'BGD' to changes in humidity were calculated by subtraction of an average over at least 3 mins of the Bragg wavelength measured during exposure to moist nitrogen gas from the average of the stable background that was measured under dry nitrogen before and after, allowing thermal effects to be minimised.

The 'BGD' was then exposed to cycles of either dry nitrogen gas or nitrogen gas which contained a controlled concentration of water vapour whilst interrogated optically in the infrared region ($\sim 1550 \text{ nm}$) throughout. By comparing the observed Bragg wavelength shift with the relative humidity recorded by an electronic hygrometer located in-line, the sensitivity of the device to changes in humidity were probed. **Fig.6.17** below highlights the recovery of the Bragg wavelength shift response of both the covered and uncovered Bragg gratings back to the 0 %RH baseline value after exposure to increased relative humidity.

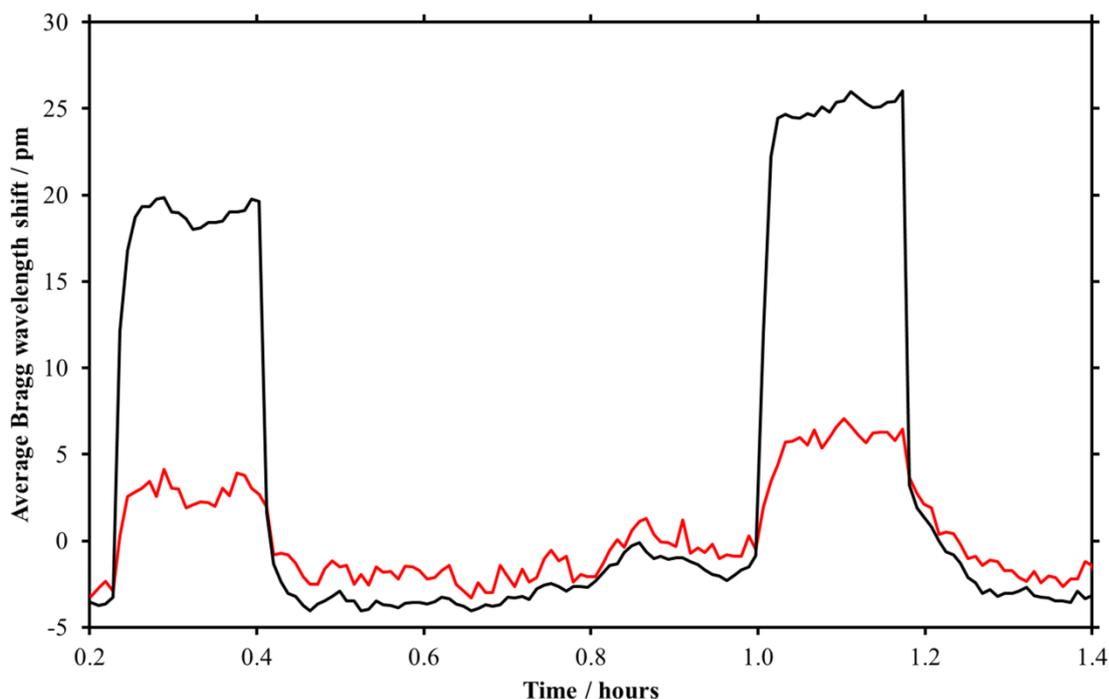


Fig.6.17: The average Bragg wavelength shifts of Bragg gratings covered with a thin film of (4) (black line) and uncovered Bragg gratings (red line) when exposed to different relative humidities, highlighting the recovery when exposed to changes in relative humidity from a baseline value of 0 %RH and then back to 0 %RH.

To determine the Bragg wavelength shift of both the covered and uncovered Bragg gratings caused by exposure to a change in %RH the following calculation method was used. Firstly, the average Bragg wavelength shifts for all the covered Bragg gratings and the average Bragg wavelength shifts for all the uncovered Bragg gratings were calculated. The magnitude of the overall Bragg wavelength shift for either a uncovered or covered Bragg grating was then calculated by subtraction of the average of the baseline values (recorded at 0 %RH) before and after a sensing event away from the average of the stable Bragg wavelength values recorded during the sensing event. This calculation is explained pictorially in **Fig.6.18** below.

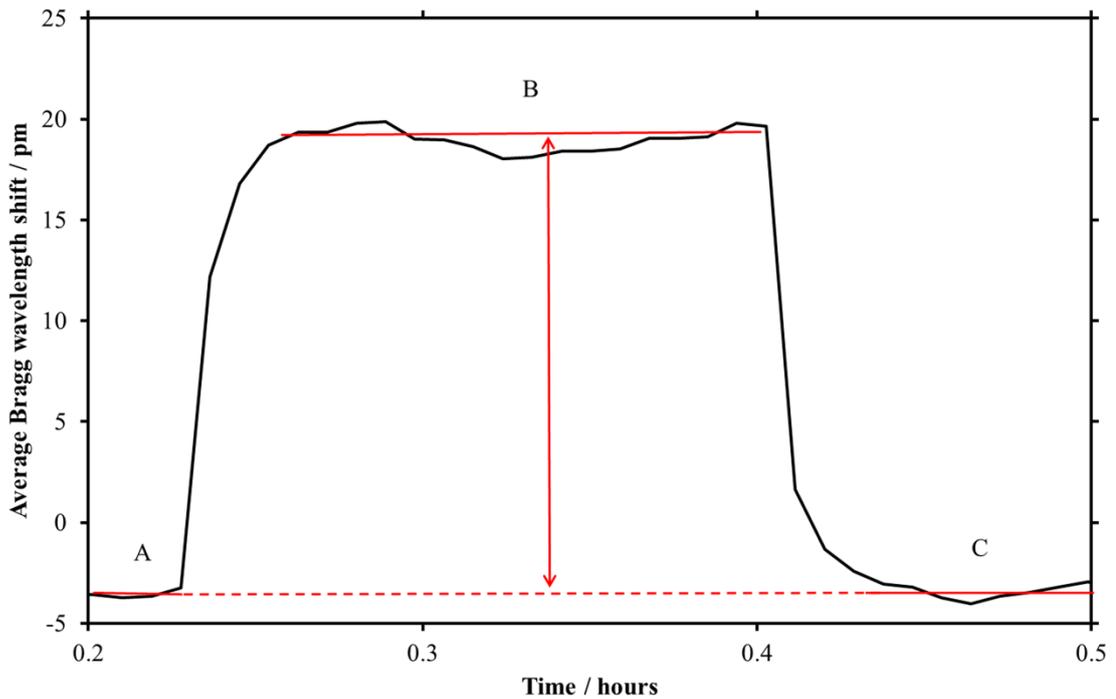


Fig.6.18: Pictorial example of calculation method used to determine the magnitude of a Bragg wavelength shift caused by a change in relative humidity. The average of the stable baseline (0 %RH) Bragg wavelength values at regions A and C was calculated and then subtracted from the average Bragg wavelength value in region B.

It was found that there was a linear response between the magnitude of the average Bragg wavelength shifts recorded by the sol-gel covered Bragg gratings upon increasing the relative humidity from 3 to 90 %RH. In contrast, the magnitudes of the Bragg wavelength shifts measured with the uncovered Bragg gratings was ~5 pm for all values of relative humidity above 3 %RH. This independence between Bragg wavelength shift and humidity for the uncovered Bragg gratings is attributed to a rapid saturation of the unmodified sensor surface with water, with further subtle variations in the average Bragg wavelength shift primarily due to changes in temperature during the experiment. This is shown in **Fig6.19** below.

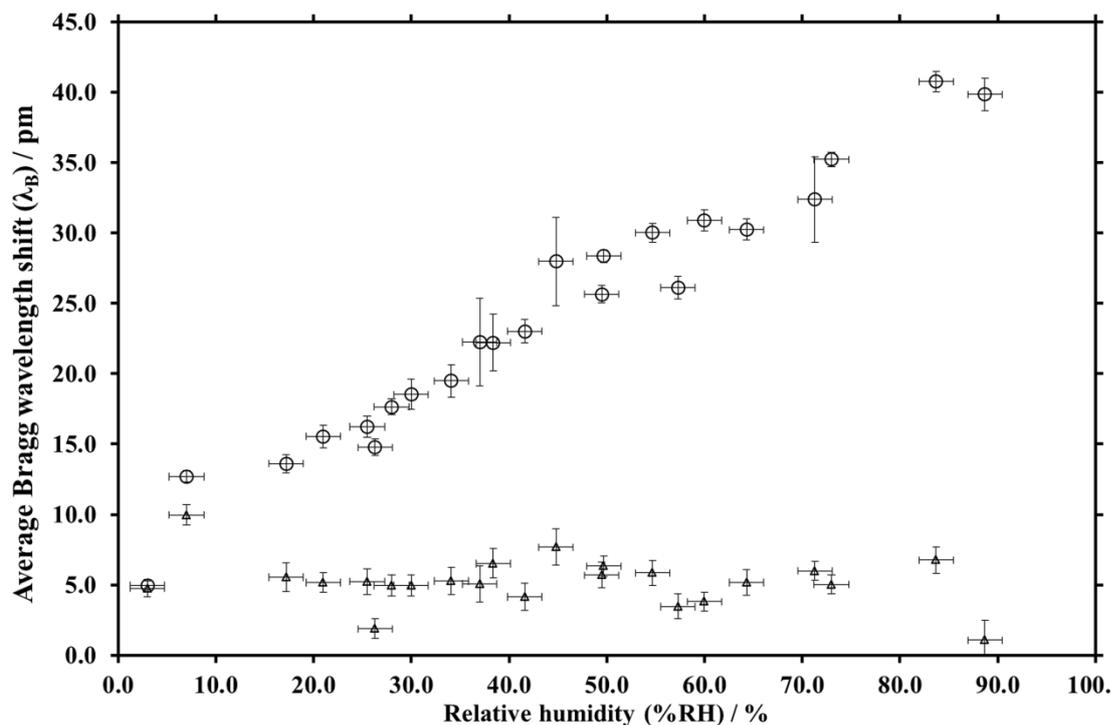


Fig.6.19: The average Bragg wavelength shift of the Bragg gratings covered with the thin film of (4) (circles) increases when exposed to increasing relative humidity, %RH. In contrast the uncovered Bragg gratings (triangles) show no response to humidity change.

Temperature referencing was achieved by a first-order subtraction of the average Bragg wavelength shift for the uncovered region from the average Bragg wavelength shift of the covered region. This temperature referencing method is based on a good first approximation that the average $\delta n/\delta T$ that the optical mode experiences in the region covered with the ~ 250 nm thickness thin film is comparable to that of the uncovered region. Thus changes in temperature should affect all gratings equally and so full compensation for such fluctuations was achieved passively and on-chip. After applying on-chip referencing, the linearity of the average Bragg wavelength shift with increasing humidity was found to be improved, with the linear regression coefficient of determination (R^2) increasing from 0.96 to 0.98. The sensitivity of the hygrometer was calculated to be $0.4 \text{ pm} / \%RH$, at the resolvable limit of the Bragg grating.

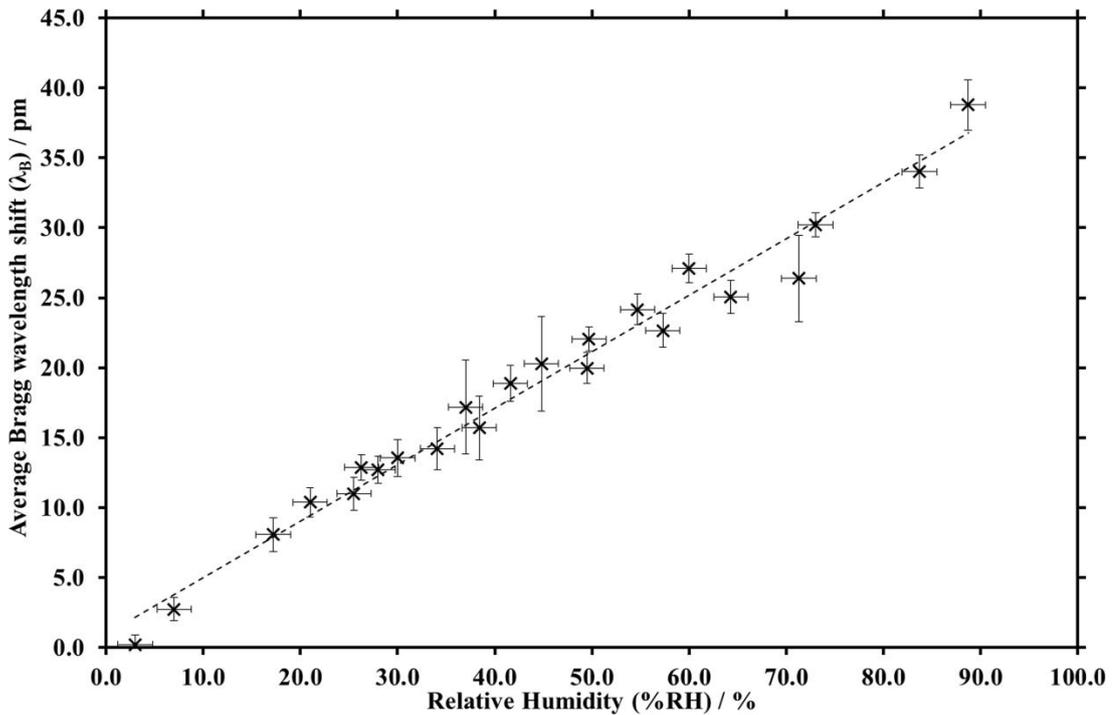


Fig.6.20: After subtraction of the average Bragg wavelength shifts of the uncovered reference Bragg gratings an improved linear response to increasing relative humidity was observed, further demonstrating on-chip thermal compensation.

Despite an ideal linear response of the sensor to relative humidity, a shortcoming of this sensor was that the sensitivity was found to have decreased by ~50% over a period of ~2 weeks in ambient humidity which also included 2-3 days use of the sensor in experiments where > 90 %RH. It was proposed that the cause of this decrease in sensitivity could be due to two factors; (i) residual moisture in the pores of the thin film of (4) resulting in a decrease of the active sensing area or (ii) degradation of the thin film of (4). To test factor (i) the sensor device was heated to 50 °C for 24 hours in air. However, a repeat sensing experiment after this drying step revealed that no improvement in sensitivity had occurred. It must be noted that a higher temperature could not be used as the optical pigtail glue would have undergone thermal degradation. Therefore the device was then dried *in vacuo* in a desiccator for 24 hours but again the device was not returned to the original sensitivity state.

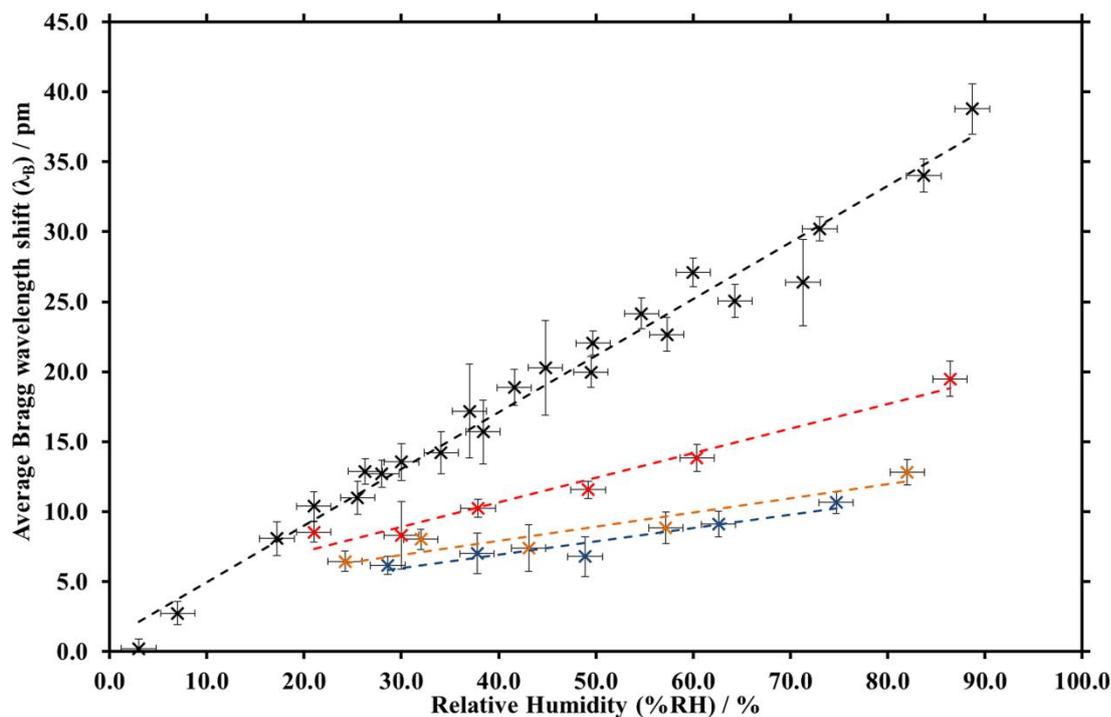


Fig.6.21: The original data (X) which was temperature and strain referenced against the uncovered Bragg gratings, data from experiment during which the reduction in sensitivity was noted (X, temperature and strain referenced), the sensing response after drying at 50 °C for 24 hours (X, temperature and strain referenced) and after drying in an evacuated desiccator for 24 hours (X, temperature and strain referenced).

Despite attempts at ‘drying’ the thin film of (4) no improvement in sensitivity was achieved which suggested that factor (ii) was the cause of the decrease in sensitivity. Surface profilometry of the thin film of (4) demonstrated that the thickness of the thin film had decreased by ~25% relative to the initial thickness. It has been reported in the literature that the thickness of silica sol-gel thin films decreases until a stable thickness is reached due to exposure to ambient humidity²². Furthermore, it is known that the thickness of silica sol-gel thin films rapidly decreases upon immersion in aqueous solutions²³. Thus it was proposed that the decrease in sensitivity was due to the decrease in film thickness which was caused by pore collapse/hydrolytic degradation.

6.3.2 Planar Integrated Bragg grating sensor modified with a thin film of (6) as a relative humidity (%RH) sensor

To improve the viability of mesoporous sol-gel thin films for use as the active sensing elements for refractometric Bragg gratings sensors a solution to the issue of hydrolytic degradation was required. In the literature it has been demonstrated that

the hydrolytic stability of silica sol-gel thin films is significantly improved upon ‘doping’ or ‘grafting’ with aluminium oxide²³. The aluminium oxide ‘doping treatment’ is a pre-fabrication process; the precursor of aluminium oxide is incorporated into the sol that is used to fabricate the sol-gel thin film. To achieve this, aluminium chloride is added to the initial sol reaction whereupon the aluminium chloride is hydrolysed in the acidic aqueous conditions and is incorporated within the silica sol-gel matrix as aluminium oxide upon calcination²³. However, it has been demonstrated in the literature that inclusion of aluminium oxide, within the silica sol-gel structural matrix, changes the structure (size and shape) of the porous network within the sol-gel due to the trigonal planar geometry of the ‘AlO₃’ unit compared to the tetrahedral ‘SiO₄’ unit as shown below in **Fig.6.22** below²³.

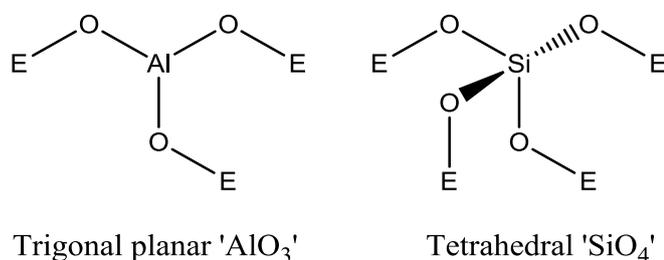


Fig.6.22: The geometries of the ‘AlO₃’ and ‘SiO₄’ structural units within an aluminium oxide ‘doped’ mesoporous sol-gel thin film. ‘E’ represents either an Al or Si atom. The trigonal planar geometry of an ‘AlO₃’ unit within the silica network changes the shape and sizes of the pores within the thin film compared to the shape and sizes of the pores within a pure silica mesoporous sol-gel thin film.

Inclusion of aluminium oxide within the sol-gel matrix would result in the pore morphology within the sol-gel thin film to be different compared to the pore morphology within a thin film of (4) which may have caused a difference in sensitivity to relative humidity. Thus a direct comparison of the sensitivities between a thin film of (4) and the thin film of an aluminium oxide treated sol-gel thin film would not be possible. In addition, the fabrication of thin films of (4) in a repeatable and reproducible manner was facile. Therefore the ‘doping’ technique was not utilised.

In contrast, the ‘grafting’ technique is a post-fabrication technique and it has been reported in the literature that changes to the pore morphology do not occur²⁴. This is because the pore morphology has already formed within the thin film and thus is not affected by the presence of the trigonal ‘AlO₃’ unit. It has been proposed that the

aluminium oxide is grafted homogeneously as a monolayer on the walls of the pores and the external surfaces of the thin film²⁴. Therefore, this method was chosen to increase the hydrolytic stability of the silica thin films.

To test the 'grafting' procedure a ~220 nm thick thin film of (4) on a FHD silica was immersed in an aqueous solution of 'hydrolysed aluminium chloride' (~ 60 mg mL⁻¹) for 6 hours at 80 °C with occasional agitation. In the literature this method had been shown to result in aluminium oxide 'grafted' thin films of silica sol-gel that subsequently did not decrease in thickness even when immersed in aqueous buffer solution for at least 1 week; 1 week was the maximum time measured within the literature study²³. To consolidate the aluminium oxide 'grafting' the thin film was calcined at 450 °C for 3 hours (heating rate 1.0 °C min⁻¹) in an atmosphere of N₂:O₂:Ar, 2.1 : 0.6 : 0.5 L min⁻¹ approx. flow rates). Characterisation by energy dispersive X-ray spectroscopy (EDX) on multiple spots of the sample showed that an aluminium oxide grafted silica sol-gel thin film had been successfully fabricated. The EDX spectra are shown below in **Fig.6.23**.

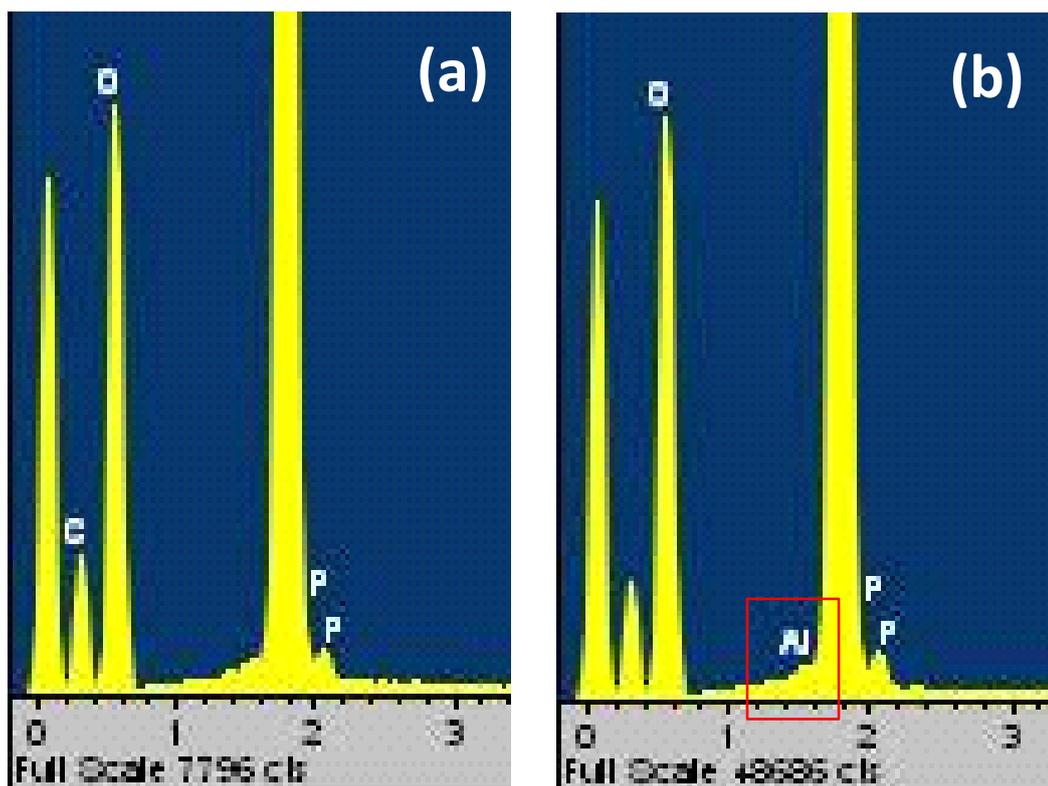


Fig.6.23: Comparison of EDX spectra collected from (a) blank FHD wafer (left) and (b) the aluminium oxide grafted silica sol-gel thin film on a FHD wafer (right). A small peak (highlighted by the red box) corresponding to the aluminium $K\alpha$ emission = 1.486 keV is present in spectrum (b) but no such feature is present in spectrum (a). The corresponding weight percentage of aluminium within the aluminium oxide grafted sol-gel = 0.21 ± 0.03 % (2100 ppm). The large broad peak on both spectra is the silicon $K\alpha$ emission = 1.739 keV. The peak at 2.013 keV corresponds to the $K\alpha$ emission of phosphorous; phosphorous is one of the dopants in the FHD wafer substrate. Each sample was coated in 77 nm of carbon.

A small peak corresponding to the aluminium $K\alpha$ emission = 1.486 keV was present in the EDX spectrum confirming the conversion of the thin film of (4) to (6). The corresponding weight percentage of aluminium (calculated by the INCA EDX software) within the aluminium oxide grafted sol-gel = 0.21 ± 0.03 % (2100 ppm). The magnitude of the thickness of the thin film of (6) is very small compared to the dimensions of the interaction volume of the electron beam. Thus it is proposed that the aluminium $K\alpha$ emission signal is due to deposition of alumina throughout the thin film and not just on the surface. It must be noted that this is a very crude calculated estimate of the weight percentage of aluminium oxide grafted onto the thin film of (4). This is because most of the X-ray photons received at the detector (the count of these photons are used by the algorithm within the INCA EDX

software to calculate the relative peak intensities) would have been emitted from within substrate due to a large percentage of the interaction volume of the electron beam being present within the silica substrate.

The thin film of (6) was characterised by surface profilometry. It was found that thickness of thin film had decreased from an average thickness before aluminium oxide grafting of 221 ± 36 nm to an average thickness after grafting of 143 ± 26 nm. It was proposed that the decrease in thickness was due to one of two factors; (i) partial solubilisation/degradation of the thin film during the grafting reaction or (ii) the extra calcination step causing further consolidation/collapse of the thin film structure.

To investigate factor (ii), a thin film of (4) was fabricated on a silica soda glass substrate as per the procedure given in the Experimental Details section below. The average thickness of the thin film was measured using step profilometry and was 263 ± 48 nm. The aluminium oxide ‘grafting’ reaction was NOT performed but the thin film of (4) was then calcined at 450 °C for 3 hours as per the calcination conditions given in the procedure for (6) in the Experimental Details section below. The average thickness of the thin film was then measured using step profilometry and was determined to be 235 ± 17 nm. The thicknesses of the thin film before and after the second calcination step are in reasonable agreement within associated error. Thus this result suggests the main cause of the thickness decrease measured after the aluminium oxide grafting reaction is due to partial solubilisation/degradation of the silica thin films within the aqueous condition of the aluminium oxide grafting reaction.

An attempt to prevent the thickness decrease during the ‘grafting’ reaction was made by changing the reaction solvent from water to dry ethanol and performing the reaction under a nitrogen atmosphere reaction to minimise exposure to water vapour. It is known that ethanol reacts with aluminium chloride to form ethoxide derivatives²⁵. It was proposed that the ‘aluminium ethoxide’ derivatives would react with the silanol groups on the surface of the silica thin film and then upon calcination in ‘air’ become grafted as aluminium oxide. However, despite the exclusion of water from the reaction conditions, it was shown by step profilometry measurements after the grafting reaction, that the thickness of the thin film had decreased. This suggests that

degradation and partial solubilisation of the thin film by ethanol had occurred. Thus it was determined that mesoporous silica slowly dissolves under these reaction conditions, regardless of whether water is excluded or not, until the protective aluminium oxide layer is fully formed.

To enable for direct comparison of a thin film of (4) to a thin film of (6) for sensing the decrease in thickness during the ‘grafting’ had to be overcome. To compensate for this erosion, a thin film of (4) of ~300 nm thickness was initially prepared on a ‘BGD’ sensor device by deposition at a lower spin speed. This film subsequently reduced in thickness to 260 ± 24 nm. Thus a thin film of (6) for relative humidity sensing was fabricated that was of comparable thickness to the thin film of (4) used in the first iteration of the Bragg grating relative humidity sensor. In this way direct comparison between the thin film sensing elements was possible.

The ‘BGD’ modified with the thin film of (6) was then used in relative humidity sensing experiments as per the procedure in the Experimental Details chapter. The sensing experiment was conducted in the range of 0-100 %RH and was repeated multiple times. At all relative humidity values the average Bragg wavelength shift for the uncovered Bragg gratings was ~5-10 pm, therefore was independent of relative humidity. The average Bragg wavelength shift for the uncovered Bragg gratings at each %RH value is mainly attributed to the physical adsorption of multilayers of water vapour on the surface (thickness $\ll 1$ nm). However, as the average uncovered Bragg wavelength is independent of %RH it is suggested that the uncovered surface quickly saturates with water vapour at low %RH values. Changes in temperature and strain within the sensor chip are also factors; i.e. the uncovered Bragg gratings acted as temperature and strain reference gratings. Therefore, by subtracting the average Bragg wavelength shift for an uncovered Bragg grating at a certain %RH value from the average Bragg wavelength shift for the covered Bragg gratings at the same %RH value gave the following plot (**Fig.6.24**).

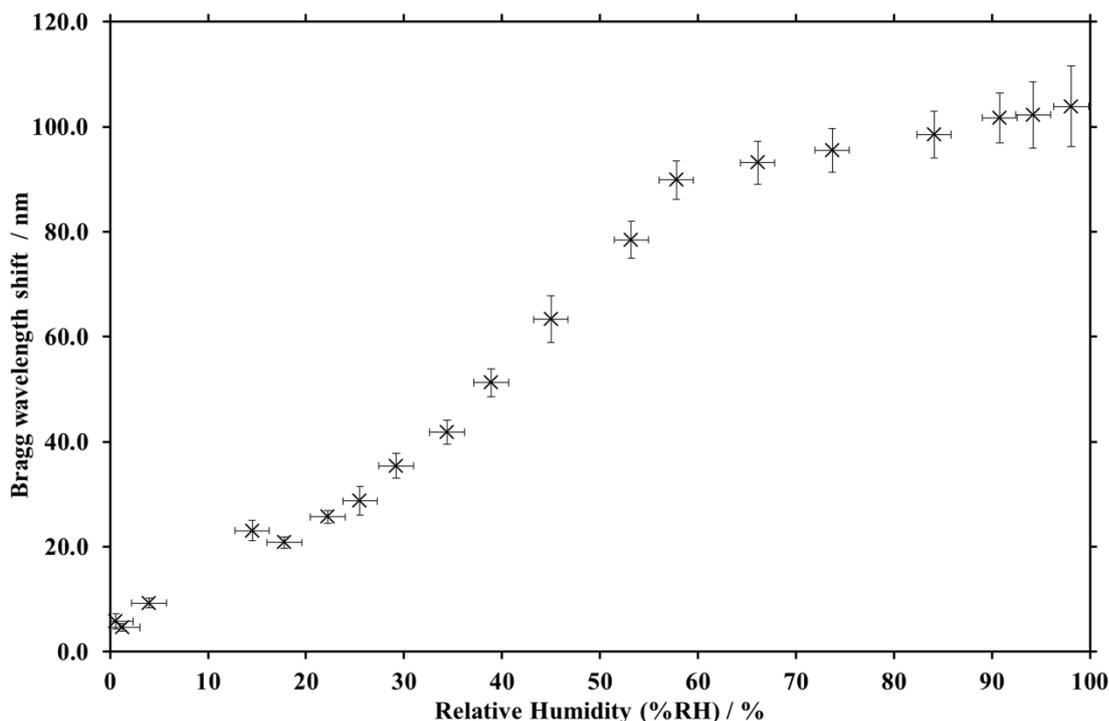


Fig.6.24: Relationship between Bragg wavelength shift measured with Bragg gratings covered with a thin film of (6) (~260 nm thick) and relative humidity (%RH) after temperature and strain effect referencing.

Whilst the behaviour of the uncovered reference gratings was unchanged, it was found that the sensitivity to changes in humidity for the covered gratings had increased and the relationship was no longer found to be linear, but instead exhibited a more complex behaviour between relative humidity and the average Bragg wavelength shift (**Fig.6.24**).

The hydrolytic stability of the thin film of (6) was then investigated. The 'BGD' was exposed to 100 %RH continuously for 2 hours and then three repeats of the moisture sensing experiment were performed. With subtraction of the average Bragg wavelength shift for an uncovered Bragg grating at a certain %RH value from the average Bragg wavelength shift for the covered Bragg gratings at the same %RH value gave the following plot (**Fig.6.25**).

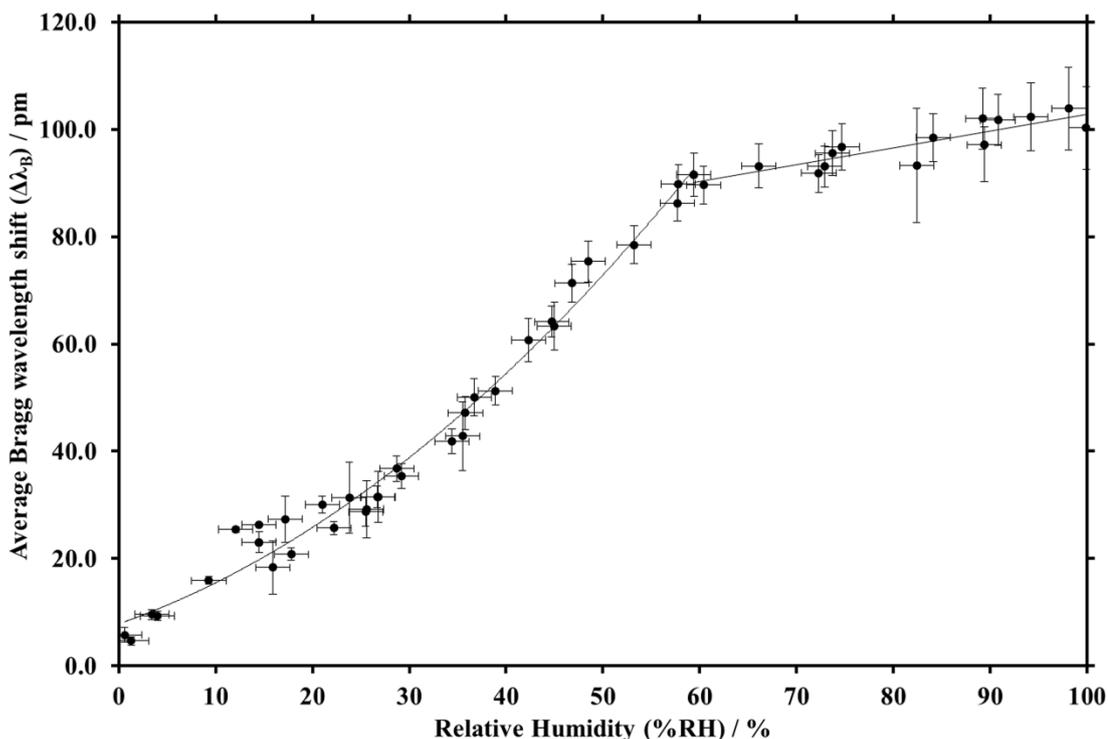


Fig.6.25: Three sensing experiments from 0-100 %RH were conducted and no change in the sensing response of the device was measured despite prolonged exposure to high relative humidity (>95 %RH) and ambient relative humidity (all the data collected temperature compensated is shown above). Lines are guides for the eye only.

As is evident from **Fig.6.25** above, despite exposure to 100 %RH for 2 hours, storage in ambient relative humidity ~45 %RH, and a range of %RH values (5-95 %RH) in each sensing repeat experiment, the sensitivity of the ‘BGD’ modified with the thin film of (6) was maintained. This result demonstrates that grafting of aluminium oxide onto a thin film of (4) to form (6) improves the hydrolytic stability of the sol-gel thin film sensing element.

In the region 0-60 %RH, the ‘BGD’ modified with the thin film of (6) exhibited sensitivity of 0.69 ± 0.05 %RH/pm; 3 times greater than the sensitivity of the ‘BGD’ when modified with a thin film of (4) (2.47 ± 0.18 %RH/pm). The increase in sensitivity is attributed to the thin film of (6) having a higher refractive index compared to the thin film of (4). The higher refractive index of the thin film of (6) ‘pulls’ the optical mode further out of the waveguide core. Thus a greater proportion of the power within the evanescent wave interacts with the sol-gel sensor layer. The higher refractive index of (6) was confirmed by monitoring the Bragg wavelength shift caused by deposition of the thin film of (4) and comparing this to the Bragg

wavelength shift during the fabrication of thin film of (6) on the same Bragg grating device. The final Bragg wavelength shift after fabrication of the thin film of (6) was ~370 pm whilst the final Bragg wavelength shift after deposition of the thin film of (4) was ~270 pm. It is known that the larger the change in refractive index the larger the Bragg wavelength shift. It must be noted that the difference in sensitivity could be explained by a difference in thickness between the two layers. However, the thicknesses of the thin film of (4) (233 ± 27 nm) and the thin film of (6) (260 ± 27 nm) were in reasonable agreement (within associated errors) and thus the increase in sensitivity was not attributed to a comparative increase in thickness.

By performing a linear regression on the data in the range 0-60 %RH and using the calculated standard error of the Bragg wavelength shift, a calculation of the precision of the aluminosilicate modified thin film device at room temperature was possible. The calculation yielded a value of ± 0.3 %RH. This precision value is only accurate at room temperature (~ 21 °C) due to the relationship between absolute concentration of water vapour in air and the temperature of the air. At lower temperatures it is expected that the precision of the device would worsen. At 4 °C, the absolute concentration of water in air drops by a factor of three from its room temperature value (~ 21 °C)²⁶, therefore the precision of the device is expected to worsen to ± 0.9 %RH. Above ~60 %RH there is a reduction in sensitivity exhibited by the aluminosilicate device which is shown as the shallower gradient on the plot (**Fig.6.25**); this was demonstrated in all three data sets. This limits operation at high water concentrations and thus would limit operation at higher temperatures; however it would be relatively simple to make a less sensitive device by reducing the porosity of the active sensing sol-gel thin film.

Above ~60 %RH there was a reduction in sensitivity which is shown as the shallower gradient on the plot. This was demonstrated in all three data sets. It is proposed that at relative humidity values less than 60 %RH the response of the device follows a similar trend as evident in **Fig.6.20**. As the relative humidity increases, the amount of water ($n \sim 1.33$) within the pores of the thin film of (6) also increases and displaces nitrogen gas ($n \sim 1.00$). The result of this is that the average refractive index (n_{eff}) of the thin film increases and thus the optical mode is 'pulled' further and further out of the waveguide. The extent of the evanescent wave within the thin film increases, i.e. more of the evanescent wave of the optical mode

encounters the increasing refractive index of the thin film, which in turn increases the sensitivity of the optical mode to further increases in refractive index. Thus the magnitude of the Bragg wavelength shift increases in a quadratic manner as shown in **Fig.6.25** above. When relative humidity values were > 60 %RH, it is proposed that saturation of the pores had occurred and only multilayers of adsorbed water formed on the surface of the thin film of **(6)**. This is supported by the work of Al-Abadleh where it was demonstrated that above 70 %RH, formation of a liquid-like water layers occurred on aluminium oxide surfaces²⁷; it is known that water is readily adsorbed on aluminium oxide²⁸. The larger error bars calculated for the data at the highest %RH values also suggest that multilayers of water are forming; it has been demonstrated previously that uneven coverage of the sensor surface with droplets of condensed water leads to increased uncertainty in the value of the Bragg wavelength²⁰. It is proposed that the difference in sensitivity between the thin films of **(6)** and **(4)** is due to a larger rate of water adsorption on the aluminium oxide surface of **(6)** compared to the silica surface of **(4)**. This leads to saturation of the aluminium oxide surface of **(6)** at %RH $< 100\%$ whereas it is proposed that the thin film of **(4)** was never saturated under the conditions that were used in these experiments. This is corroborated by the literature values of the heats of adsorption for water on silica and aluminium oxide which are ~ 59 kJ mol⁻¹²⁹ and ~ 70 kJ mol⁻¹³⁰ respectively. The greater the magnitude the value of the heat of adsorption of water the more favoured adsorption becomes and thus the equilibrium shifts towards adsorption of water on the surface of the thin film.

6.3.2.1 Sensor response time determination

The response time of the device in the flow system was then determined. Three independent sensing events were performed; in each the relative humidity was stepped from 0 %RH to 90 %RH and the time taken for a stable Bragg wavelength shift to be achieved at 90 %RH (starting from 0 %RH) was recorded. In the literature the response time of a gas sensor is defined as the time taken to achieve 90 % of the final stable change of a sensor after a step increase of the concentration of the analyte gas³¹. Therefore an average time was calculated from the time taken in each experiment for the Bragg wavelength shift to reach 90% of the full stable Bragg wavelength shift due to exposure to 90 %RH (starting from 0 %RH) as highlighted

in **Fig.6.26** below. For the ‘BGD’ modified with a thin film of (6) (~260 nm thick) 90 % of the final constant Bragg wavelength value was reached in 54 secs.

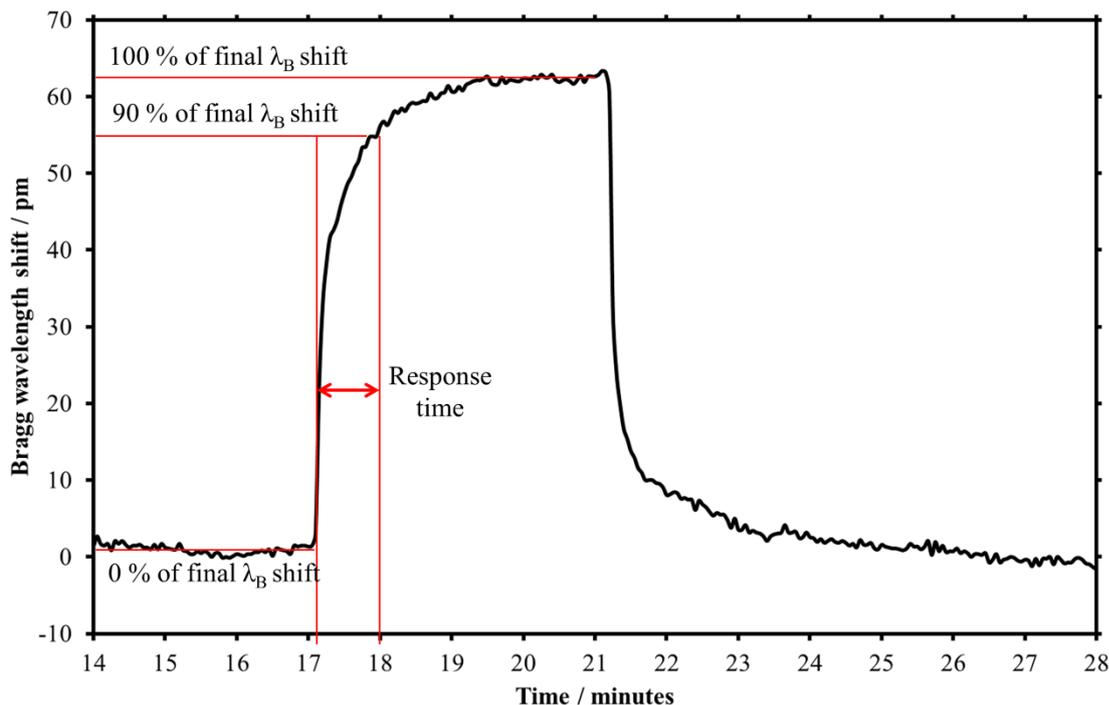


Fig.6.26: The definition of the response time of the ‘BGD’ during a change from 0-90 %RH. The Bragg wavelength shifts from the sol-gel covered Bragg grating were recorded every three seconds.

This definition of sensor response time is suitable for this ‘BGD’ sensor because 90 % of the average Bragg wavelength shift is sufficient to differentiate between all %RH values; an identical response curve would be generated but just at Bragg wavelength shift values 10% lower than the values in **Fig.6.25** above. Therefore the viable response time of this relative humidity sensor is < 1 min.

6.3.2.2 Long-term hygrometry experiment in a ‘static’ environment

To further confirm the long-term operation and stability of this optical hygrometer, its application outside of a flow system was investigated. The Bragg grating hygrometer device was installed in the ‘static’ ambient environment of the open laboratory and the Bragg wavelength shift was sampled every 30 seconds over an eleven hour period whilst the relative humidity recorded from the commercial electronic hygrometer (in close proximity to the Bragg grating sensor device) was manually sampled every 30 minutes. After referencing changes in temperature using the technique described above, the Bragg grating wavelength shift response due to

changes in relative humidity was revealed. The processed data collected over the course of the eleven hour period is shown in **Fig.6.27** below.

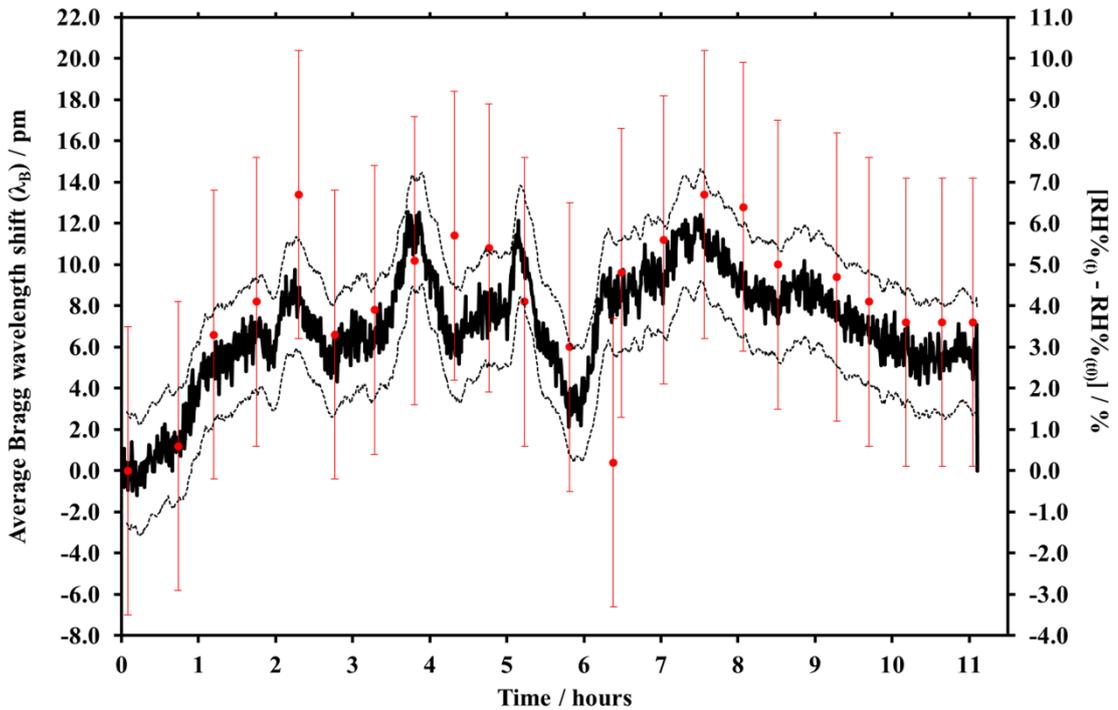


Fig.6.27: Excellent agreement between the Bragg wavelength shift of the Bragg grating relative humidity sensor (black line) with the commercial *Testo 625* electronic hygrometer (red dots) relative to the initial value, when both devices were exposed to the ambient open laboratory atmosphere for 11 hours. The range of the associated error of the Bragg grating humidity sensor is given between the two dashed black lines. The accuracy of each measurement using the electronic hygrometer is shown by the red vertical error bars.

It was found that the temperature-referenced Bragg wavelength shifts data were in good agreement with the %RH change data as recorded with the *Testo 625* commercial hygrometer within the associated accuracy error of each measurement. Excellent agreement and lack of drift of the Bragg wavelength shift data over the eleven hour period demonstrated that the thermal compensation afforded by on-chip reference gratings is a sufficient method to compensate for refractive index changes due to temperature change in ‘static’ sensing environments as well as ‘flow’ sensing environments.

6.3.2.3 Surface contamination and cleaning of the device with organic solvent rinsing.

Over several weeks of regular use in sensing experiments, a loss of sensitivity to humidity was noted but it was not accompanied by a reduction in film thickness unlike the silica analogue. The cause of this was attributed to grease within the laboratory nitrogen gas lines liberated under high flow and adsorbing in the pores and on the surface of the thin film of (6).

However, it was found that full sensitivity to changes in humidity could be repeatedly and completely restored, by rinsing the planar device with organic solvent. *In-situ* refractive index monitoring during a rinsing cycle of methyl ethyl ketone followed by isopropanol revealed the removal of a contaminant, as shown by the negative Bragg wavelength shift in **Fig.6.28**, plotted after reference against the temperature-compensation Bragg gratings. It should be noted that whilst the reference returned to its initial value, this was only once all solvent had evaporated and the effects of evaporative cooling had diminished. However, these evaporation and cooling effects would be experienced by all gratings equally - further illustrating the need for on-chip compensation. It was found that the alumina-grafted sol-gel layer was resistant to a wide range of organic solvents, including methyl ethyl ketone, isopropanol, methanol, dichloromethane, *n*-hexane, acetone, xylenes and water with no decrease in film thickness being detected after prolonged exposure.

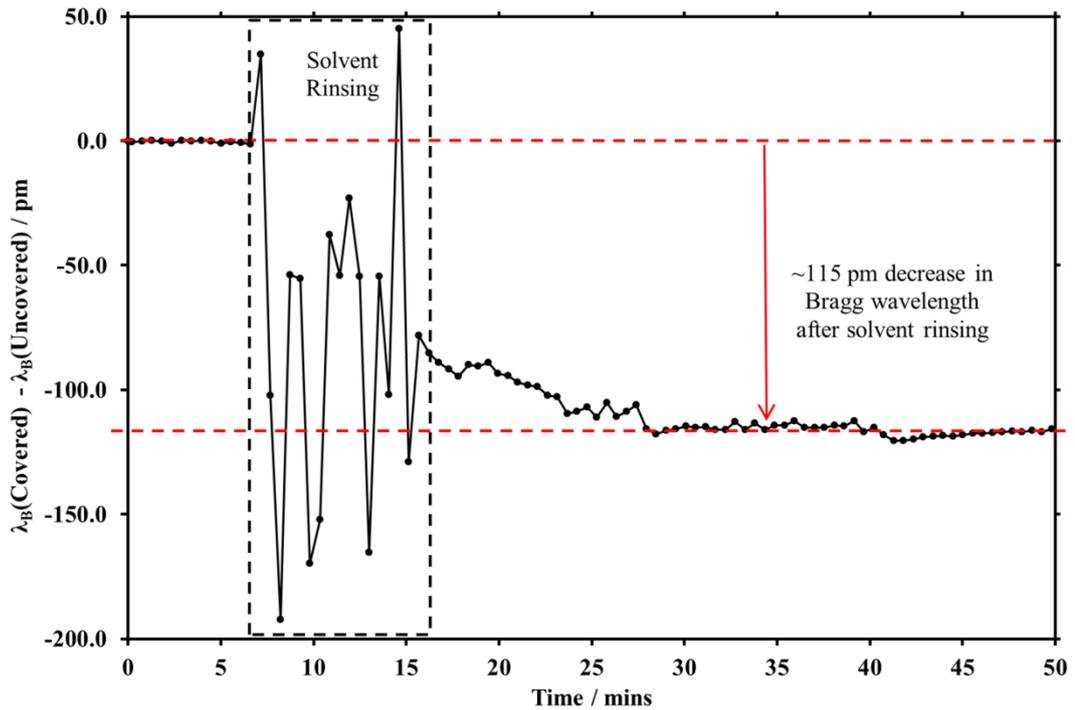


Fig.6.28: Indication of the removal of surface contamination due to the stable decrease in Bragg wavelength that occurred after rinsing the contaminated aluminosilicate thin film Bragg grating hygrometer with methyl ethyl ketone (MEK). The sharp jumps in refractive index within the hashed region correspond to the individual solvent wash/rinse steps.

6.4 Conclusion

It has been demonstrated that a planar integrated Bragg grating sensor chip fabricated using the direct UV-writing approach can be modified with a mesoporous silica sol-gel thin film. Such a device was sensitive to changes in relative humidity over a wide humidity range; however hydrolytic degradation of the sol-gel required the additional grafting of aluminium oxide to the porous surface to ensure long-term stability. Grafting with aluminium oxide also offered the additional benefits of enhanced sensitivity, up to 3 times that of the silica analogue thin film, and allowed for application of the sensing at elevated humidity levels. The sensitivity of the aluminium oxide modified thin film device, in the range 0-65 %RH, was determined to be 0.69 ± 0.05 %RH/pm. Compared to photonic crystal fiber-based humidity sensors reported in the literature, the device described herein is less intrinsically sensitive³². However, with further optimisation of the film thickness and enhancement of the evanescent modal overlap the sensitivity of this first proof-of-concept device technique can be improved.

Long-term measurement in ‘static’ ambient environment indicated that the thermal compensation afforded by on-chip reference grating was sufficient to prevent any drift in calibration. As with all hygrometers, contamination of the sensor occurred, but for the reported device this was easily removed by rinsing with organic solvent with the sensitivity being repeatedly and reproducibly restored.

The facile fabrication techniques, robustness, and associated advantages of the planar integrated optical format (as highlighted in **Chapter 3**) makes the sensor device modified with a thin film of (6) a viable humidity sensor that offers advantages over the current electrical devices in a range of domestic, commercial and industrial settings. When this is combined with the previously reported methods for monitoring temperature³³, pressure³⁴, and chemo/bio-detection³⁵ the suitability of integrated optical Bragg grating devices for highly multiplexed sensor devices within distributed networks becomes apparent. In addition, through this work the Bragg wavelength response of a planar Bragg grating device modified with sol-gel thin film of silica and an aluminosilicate analogue to changes in relative humidity from 0-100 %RH has been established. This allows for refractive index changes caused due to changes in humidity to be referenced and removed from Bragg wavelength shifts measured with Bragg grating sensor device modified with sol-gel thin films.

- (1) *Advanced gas sensing: the electroadsorptive effect and related techniques*; Doll, T., Ed.; 1st ed.; Kluwer Academic Publishers, 2003; p. 202.
- (2) Thompson, R. T. In *Electronic Materials Handbook: Volume 1 Packaging*; Minges, M. L., Ed.; ASM International, 1989; pp. 670–675.
- (3) Testo Limited Testo 625 - Humidity/Temperature - Testo Limited <http://www.testolimited.com/p/227/testo-625-humiditytemperature> (accessed Apr 22, 2013).
- (4) Haruvy, Y.; Webber, S. *Chem. Mater.* **1991**, *3*, 501–507.
- (5) Rao, A. V.; Lathe, S. S.; Dhere, S. L.; Pawar, S. S.; Imai, H.; Ganesan, V.; Gupta, S. C.; Wagh, P. B. *Appl. Surf. Sci.* **2010**, *256*, 2115–2121.
- (6) Carney, C. M.; Parthasarathy, T. a.; Cinibulk, M. K. *J. Am. Ceram. Soc.* **2011**, *94*, 2600–2607.
- (7) Tien, P. K.; Ulrich, R. *J. Opt. Soc. Am.* **1970**, *60*, 1325–1337.

- (8) Ulrich, R.; Torge, R. *Appl. Opt.* **1973**, *12*, 2901–8.
- (9) Yildirim, A.; Budunoglu, H.; Deniz, H.; O. Guler, M.; Bayindir, M. *ACS Appl. Mater. Interfaces* **2010**, *2*, 2892–2897.
- (10) Brinker, C. J.; Lu, Y.; Sellinger, A.; Fan, H. *Adv. Mater.* **1999**, *11*, 579–585.
- (11) Levchenko, T.; Plyuto, Y.; Kovtyukhova, N. *J. Sol-Gel Sci. Technol.* **2007**, *43*, 269–274.
- (12) Lu, Y.; Ganguli, R.; Drewien, C. A.; Anderson, M.; Brinker, C. J.; Gong, W.; Guo, Y.; Soyez, H.; Dunn, B.; Huang, M.; Zink, J. I. *Nature* **1997**, *389*, 364–368.
- (13) Tao, S.; Li, G.; Zhu, H. *J. Mater. Chem.* **2006**, *16*, 4521.
- (14) Mills, M. *Basic structure of a stylus profilometer.*; 2005; pp. 1–4.
- (15) Rideout, D. Rough Talk: Understanding Surface Metrology Tools <http://www.qualitydigest.com/inside/twitter-ed/rough-talk-understanding-surface-metrology-tools.html> (accessed Apr 29, 2013).
- (16) Bennett, J. M.; Dancy, J. H. *Appl. Opt.* **1981**, *20*, 1785–802.
- (17) Mao, H. Nanoporous Polymers with Functionalized One-dimensional and Three-dimensional Channels from Ordered Block Copolymer Templates, ProQuest, 2006, p. 322.
- (18) Cullity, B. D. *Elements of X Ray Diffraction*; 1st ed.; Addison-Wesley: Reading, Massachusetts, U.S.A., 1956; p. 531.
- (19) Pan, J. H.; Lee, W. I. *Bull. Korean Chem. Soc.* **2005**, *26*, 418–422.
- (20) Sparrow, I.; Emmerson, G.; Gawith, C.; Smith, P. *Sensors Actuators B Chem.* **2005**, *107*, 856–860.
- (21) Stephenson, D. A.; Agapiou, J. S. *Metal Cutting Theory and Practice*; CRC Press, 2005; Vol. 72, p. 864.
- (22) McDonagh, C.; Sheridan, F.; Butler, T.; MacCraith, B. D. *J. Non. Cryst. Solids* **1996**, *194*, 72–77.
- (23) Dunphy, D. R.; Singer, S.; Cook, A. W.; Smarsly, B.; Doshi, D. A.; Brinker, C. J. *Langmuir* **2003**, *19*, 10403–10408.
- (24) Cónsul, J. M. D.; Baibich, I. M.; Benvenuti, E. V.; Thiele, D. *Quim. Nova* **2005**, *28*, 393–396.
- (25) Jr, W. H. S.; Frantz, S.; Chung, H. T. *Polym. Degrad. Stab.* **1997**, *56*, 103–108.

- (26) Kaye, G. W. C.; Laby, T. H. *Table of Physical & Chemical Constants*; Longman: London, 1971.
- (27) Al-Abadleh, H. A.; Grassian, V. H. *Langmuir* **2003**, *19*, 341–347.
- (28) Peri, J. B. *J. Phys. Chem.* **1965**, *69*, 211–219.
- (29) Puibasset, J.; Pellenq, R. J.-M. *J. Chem. Phys.* **2003**, *118*, 5613.
- (30) Tarasevich, Y. I.; Polyakova, I. G.; Polyakov, V. E. *Theor. Exp. Chem.* **2000**, *36*, 113–116.
- (31) *Selected Topics in Advanced Solid State and Fibre Optic Sensors*; Vaezi-Nejad, S. M., Ed.; IET, 2000; pp. 215–243.
- (32) Zheng, S.; Zhu, Y.; Krishnaswamy, S. *Sensors Actuators B. Chem.* **2013**, *176*, 264–274.
- (33) Parker, R. M.; Gates, J. C.; Grossel, M. C.; Smith, P. G. R. *Sensors Actuators B Chem.* **2010**, *145*, 428–432.
- (34) Holmes, C.; Carpenter, L. G.; Gates, J. C.; Smith, P. G. R. *J. Micromechanics Microengineering* **2012**, *22*, 025017.
- (35) Parker, R. M.; Gates, J. C.; Wales, D. J.; Smith, P. G. R.; Grossel, M. C. *Lab Chip* **2013**, *13*, 377–85.

7. Sensing of solvent vapours using a polysiloxane thin film as the active sensing element

7.1 Introduction

In **Chapter 6**, the theory behind the proposal of increasing sensitivity of planar Bragg grating sensors through use of the ‘3D sensing volume’ was discussed. Within this chapter, the development of a Bragg grating refractometric solvent vapour sensor, which utilised the concept of the ‘3D sensing volume’ is described. The sensor was fabricated by spin deposition of a thin film of a hydrophobic siloxane polymer onto the surface of a planar Bragg grating sensor chip. The Bragg wavelength shift response of this sensor chip, when exposed to organic solvent vapours in nitrogen carrier gas, was investigated. A complex relationship between Bragg wavelength shift and the relative hydrophobicity of each solvent was discovered. The resulting sensor was robust, reusable and had a response time (t_{90}) ~ 1.5 min.

Note: The file name of the associated spectra and/or characterisation data is given in the text at appropriate points. The file names given refer to the file names of the spectra/data that are located on the attached spectra CD. The file names are in italic font.

7.2 Development of the siloxane polymer

7.2.1 Synthesis of poly(methylhydro)-co-poly(methyloctyl)siloxane (8):

The type of polymer chosen to fabricate the active sensing element of a Bragg grating refractive index sensor for flammable solvent vapours was a polydimethylsiloxane (PDMS) derivative. Polydimethylsiloxane is an organosilicon polymer comprised of repeating units of ‘dimethylsiloxane’ $-\text{[Si(CH}_3)_2 - \text{O]}-$ and the chains are typically capped with trimethylsilyl groups as shown in **Fig.7.1** below.

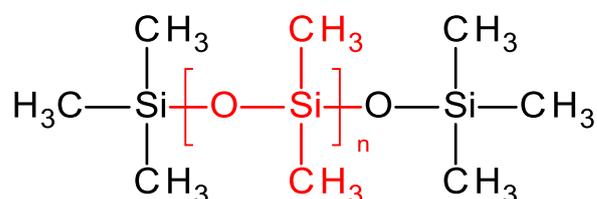


Fig.7.1: Structural formula of polydimethylsiloxane. The repeating unit of ‘dimethylsiloxane’ is highlighted in red. The trimethylsilyl capping groups are depicted in black.

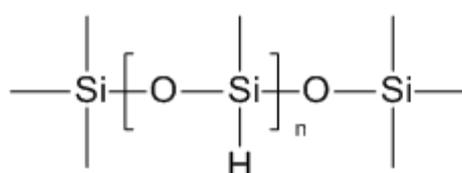
PDMS is an inherently hydrophobic polymer. This is due to the presence of methyl groups along the backbone of the polymer chains ¹. It is expected that the hydrophobic nature of PDMS would favour interaction with the vapours of hydrophobic solvents found in hydrocarbon fuels, rather than residual moisture. This is corroborated by the work of Whitesides *et.al.*, in which it was demonstrated that hydrophobic non-polar solvents swell PDMS to a greater extent than polar solvents, including water ². However, if the pendant groups of the ‘dimethylsiloxane’ repeating unit are changed for pendant groups which are more hydrophobic, then the extent of swelling is increased ³. In this work a polysiloxane was modified with *n*-octyl side chains. The aim was to increase the hydrophobicity of the polysiloxane backbone chains, relative to PDMS, and thus further favour interaction with greasy hydrophobic solvent molecules.

7.2.1.1: Hydrosilylation

The procedure used to synthesise the polymer was taken from the work of Marciniak *et al.* where a hydrosilylation reaction between poly(methylhydro)siloxane and oct-1-ene was used to introduce octyl functional groups along the length of the polymer

Chapter 7: Sensing of solvent vapours using a polysiloxane thin film as the active sensing element

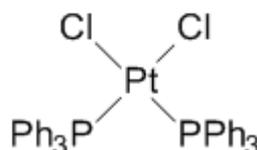
chain ⁴. The term hydrosilylation refers to the reaction whereupon organic or inorganic silicon hydrides add across double or triple bonds, particularly carbon – carbon or carbon – heteroatom double or triple bonds ⁵. Despite the first recorded example of a hydrosilylation reaction proceeding via a radical reaction pathway, most examples of hydrosilylation reaction feature the use of catalyst, in particular transition metal catalysts and the reactions proceed via a heterolytic mechanism ⁵. In this work a catalyst was used; *cis*-dichlorobis(triphenylphosphine)platinum(II). The silicon hydride was polymethylhydrosiloxane and the alkene was oct-1-ene.



polymethylhydrosiloxane



oct-1-ene



cis-dichlorobis(triphenylphosphine)platinum(II)

Fig.7.2: Reagents and the catalyst used in the hydrosilylation reaction.

7.2.1.1.1: Synthesis of the catalyst, (7)

cis-dichlorobis(triphenylphosphine)platinum(II)

The catalyst, *cis*-dichlorobis(triphenylphosphine)platinum(II) (7), was synthesised, as per the procedure given in **Chapter 10: Experimental Details**, in excellent yield (98 %) in a separate project in collaboration with Priscilla Quainoo (Project student, University of Southampton). The structure of (7) was determined by ¹H, ¹³C and ³¹P NMR, FT-IR spectroscopy and melting point analysis (¹H NMR → DJW.6674.11.Pt

cat. (7).1H NMR.ap0913djw1.010.esp) (^{13}C NMR \rightarrow DJW.6674.11.Pt cat. (7).13C NMR.ap0913djw1.011.esp) (^{31}P NMR \rightarrow DJW.6674.11.Pt cat. (7).31P NMR.ap0913djw1.012.esp) (FT-IR spectrum \rightarrow DJW.6674.11.Pt cat. (7).FT-IR) These data matched with the reported literature values and thus confirmed that (7) was *cis*-dichlorobis(triphenylphosphine)platinum(II), the desired isomeric product .

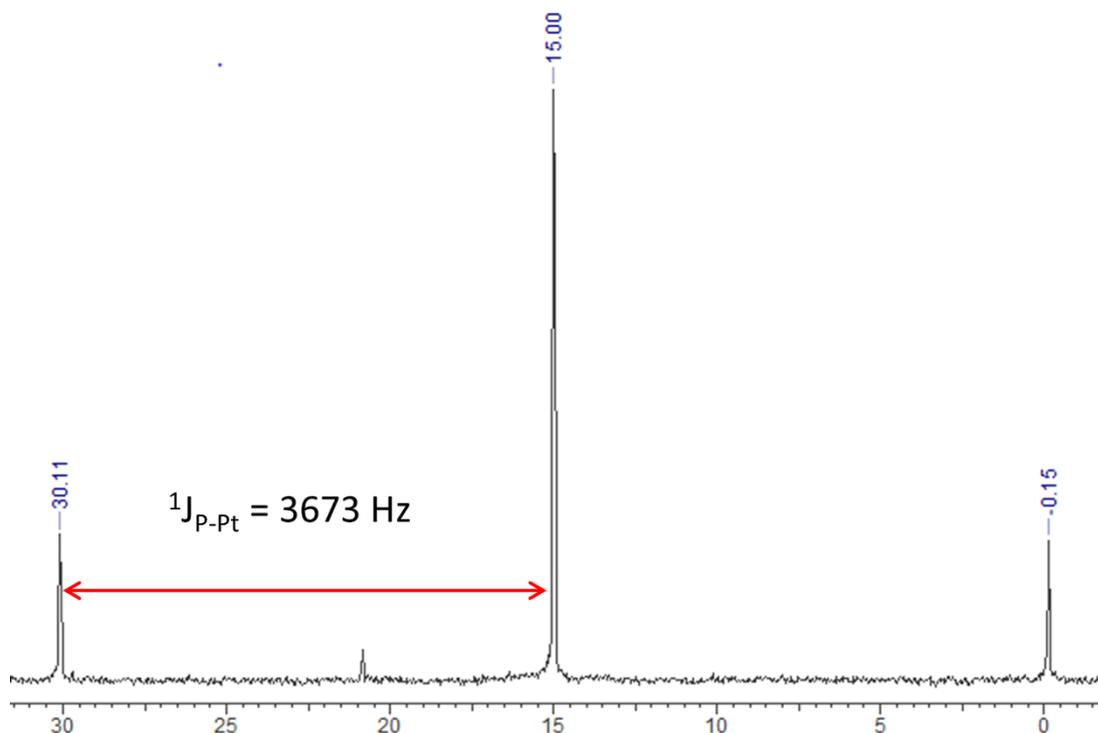


Fig.7.3: $^{31}\text{P}\{^1\text{H}\}$ NMR spectrum for (7), confirming the synthesis of *cis*-dichloro-bis(triphenylphosphine)platinum(II). The single resonance peak at 15.0 ppm is characteristic for ^{31}P in *cis*-dichlorobis(triphenylphosphine)platinum(II). The satellite peaks at 30.1 and -0.15 ppm respectively are due to through-bond one-bond coupling between ^{31}P (natural abundance $\sim 100\%$, $S = 1/2$) and ^{195}Pt (natural abundance $\sim 34\%$, $S = 1/2$) with a coupling constant of $^1J_{\text{P-Pt}} = 3673$ Hz.

7.2.2: Synthesis and characterisation of poly(methylhydro) – co – poly(methyloctyl) siloxane

A procedure, from the literature, for the synthesis of poly(methyloctyl)siloxane from oct-1-ene and polymethylhydrosiloxane using a different platinum catalyst was modified and used to synthesise (8) ⁴. The reaction was performed as per the procedure given in **Chapter 9** below (solvent = toluene, 100 °C, 6 hours, air). However, complete conversion of all silicon hydride functional groups to pendant octyl groups was not achieved as is evident in the ^1H NMR spectrum shown below in **Fig.7.4** (^1H NMR spectrum \rightarrow DJW.6625.10.poly(methyloctyl)siloxane (8).1H NMR 7percent conversion.ja2313djw1.010.esp).

Chapter 7: Sensing of solvent vapours using a polysiloxane thin film as the active sensing element

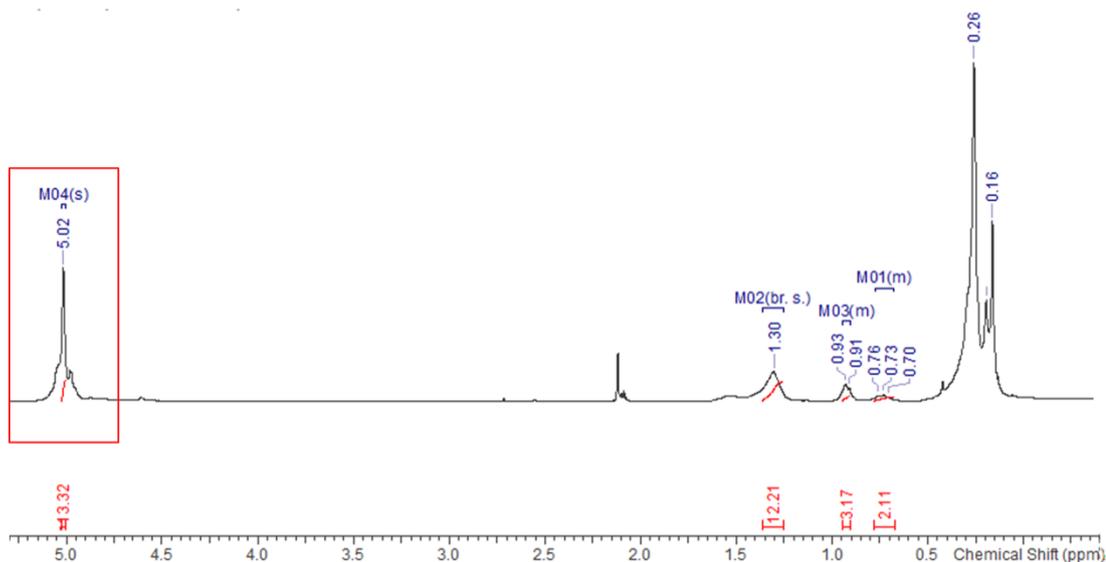


Fig.7.4: The presence of a broad peak at 5.02 ppm (highlighted by the red box), attributed to the Si – H group, on the ^1H NMR spectrum of poly(methylhydro) – *co* – poly(methyloctyl) siloxane confirmed incomplete conversion of the hydride groups to octyl groups during the 6 h reaction. The broadness of the peaks is a common feature of ^1H NMR spectra of polymers.

The broad signal at 5.02 ppm in the ^1H NMR spectrum is attributed to the hydride proton of a Si – H group. This confirms incomplete conversion of the hydride groups to octyl groups during the 6 h reaction. The presence of a strong intense stretch at 2164 cm^{-1} in the FTIR spectrum, attributed to a Si – H bond stretch, also indicates that incomplete conversion of the hydride functional groups to octyl groups had occurred (FT-IR spectrum \rightarrow *DJW.6066.100.poly(methyloctyl)siloxane.FT-IR 7 percent conversion*).

Using copolymer ^1H NMR analysis, (whereupon the magnitudes of the integrals of characteristic and well defined proton signals from each component of a copolymer are utilised to calculate the no.# moles of each component within the total copolymer) the mole % of poly(methyloctyl)siloxane was calculated to be 7 %. Incomplete conversion was attributed to two factors; (i) the poor solubility of *cis*-dichlorobis(triphenylphosphine)platinum(II) in toluene ⁶ and (ii) performing the reaction with the reaction vessel open to the ambient atmosphere rather than in a sealed-tube reaction vessel ⁴. It is well known that the kinetics of reactions can increase if performed in sealed-tube reaction vessels. This is because the pressure of the gases/vapours within a sealed tube vessel increase upon heating ⁷. This can cause superheating of the solvent which leads to rate enhancements as can be explained by

Chapter 7: Sensing of solvent vapours using a polysiloxane thin film as the active sensing element

the Arrhenius equation⁸. Use of a sealed reaction vessel was avoided due to safety concerns but an attempt to account for the rate enhancement afforded by reaction in a sealed vessel was made by repeating the reaction with identical conditions but just for a longer duration. The reaction was worked-up after 24 hours and the viscous oily polymer was characterised. Again, the data from FT-IR and ¹H NMR spectroscopic measurements demonstrated that incomplete conversion of the hydride functional groups to *n*-octyl functional groups had occurred. The presence of a strong intense stretch at 2164 cm⁻¹ in the FTIR spectrum, attributed to a Si – H bond stretch indicates that incomplete conversion of the hydride functional groups to octyl- had occurred (FT-IR spectrum → *DJW.6625.20.poly(methyloctyl)siloxane.FT-IR 15 percent conversion*). This is further corroborated by the presence of a broad peak at 5.01 ppm in the ¹H NMR spectrum which is also attributed to the hydride proton, shown in **Fig.5** below (¹H NMR spectrum → *DJW.6625.20.poly(methyloctyl)siloxane (8).1H NMR 15percent conversion.ja2313djw1.010.esp*). Using copolymer ¹H NMR analysis, the mole % of poly(methyloctyl)siloxane was calculated to be 15 %.

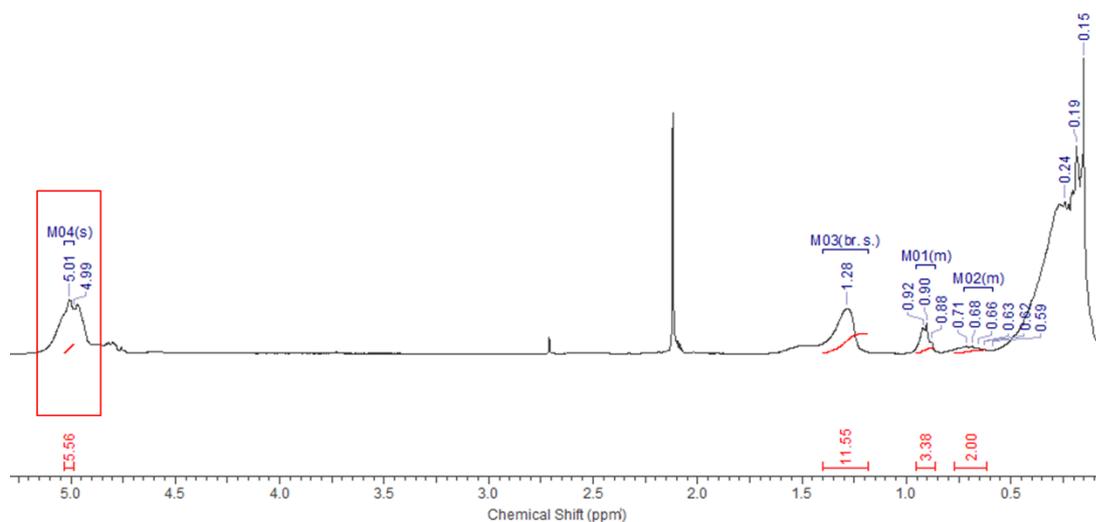


Fig.7.5: The presence of a broad peak at 5.01 ppm (highlighted by the red box), attributed to the Si – H group, on the ¹H NMR spectrum of poly(methylhydro) – co – poly(methyloctyl) siloxane confirmed incomplete conversion of the hydride groups to octyl groups during the 24 h reaction. The broadness of the peaks is a common feature of ¹H NMR spectra of polymers.

Despite a longer reaction time (24 hrs > 6 hrs), incomplete conversion of hydride to octyl still occurred. Again the two proposed causative factors were the poor solubility of (7) in toluene and performing the reaction with the reaction vessel open

Chapter 7: Sensing of solvent vapours using a polysiloxane thin film as the active sensing element

to the ambient atmosphere rather than in a sealed-tube reaction vessel. The mole% conversion had approximately doubled with a fourfold increase in reaction time. Therefore, for 100% mole% conversion the reaction, under the conditions stated in **Chapter 9** below, would have to proceed for 1 week. A faster reaction rate could be achieved by changing the conditions of the reaction; sealed reaction vessel and use of a different hydrosilylation catalyst that is more soluble in toluene.

However, it was decided that 100% mole% conversion was needed as both PMHS and PDMS are soluble in different solvents and thus swell by different magnitudes when exposed to these solvents⁹. Therefore, it was decided that having a copolymer of both poly(methylhydro)siloxane and poly(methyloctyl)siloxane would enable sensitivity to a wider range of solvent vapour than selective use of just one of the polymers.

7.2.3 Physical characterisation of poly(methylhydro)-co-poly(methyloctyl)siloxane (8):

(8) was dissolved in *tert*-butyl alcohol (~17 % w/w) at ~45 °C to form clear and colourless viscous solution. Thin films of (8) were achieved by spin deposition. *Tert*-butyl alcohol (TBA) was chosen as the solvent because the spin deposition parameters to deposit thin films of PDMS with well-defined thicknesses, using TBA as a solvent, are well documented¹⁰. Spin deposition at 2000 rpm for 60 s yielded clear and colourless thin films of (8). The thin films were subsequently ‘cured’ for 24 hours at 100 °C to yield robust thin films of (8). It was observed that when thin films of (8) were ‘cured’ for durations shorter than 24 hours, the thin films were easily mechanically damaged, but the damage was partially reversible. This partial reversibility is attributed to the viscosity of the polymer being sufficiently low enough to allow for reflowing.

After ‘curing’ the thickness of thin films of (8) was measured. Contact surface profilometry was unsuitable for determining the thickness of the thin films due to mechanical damage of the thin film of (8) caused by the stylus. Therefore the thickness of the thin films was determined in collaboration with Peter Cooper (PhD Student, University of Southampton) using an optical profilometry technique known as scanning white light interferometry (SWLI). SWLI is a non-contact, three-dimensional optical method for measuring the thickness and metrology of surface

Chapter 7: Sensing of solvent vapours using a polysiloxane thin film as the active sensing element

layers. An excellent introduction to SWLI is given by Wood ¹¹, but the essentials of the technique are described herein. Briefly illumination from a white light source is passed through a filter and a microscope objective lens before incident on the sample surface. The microscope objective lens is coupled with a beam splitter to allow for some of the white light to be reflected from a reference mirror. The light incident on the surface of the sample reflects back and recombines with the reference beam. The recombined beams create bright and dark bands called “fringes” due to the principle of superposition. The fringes make up the ‘interferogram’; the spacing of the fringes is related to the topography of the surface. The fringe pattern is captured on a CCD camera array for software analysis. Several ‘interferogram’ frames (containing the intensity data of the fringe pattern) are obtained for each point to allow for software calculation/recreation of the surface of the sample. The frames are then processed through an algorithm to convert the intensity signals into topographical data. The appropriate solution was chosen, from several solutions that were generated from the software by Peter Cooper (PhD Student, University of Southampton).

Using SWLI it was determined that the average thickness of the thin film of **(8)** spin deposited on the Bragg wavelength sensor device using the conditions mentioned above was $\sim 1.4 \mu\text{m}$. As the thickness is greater than $1 \mu\text{m}$, the evanescent wave of the optical mode was expected to be fully within the thin film of **(8)**; any optical mode will fully encounter any change in thickness due to swelling upon exposure to solvent vapours.

The refractive index of the thin film of **(8)** was then measured (in collaboration with Dr James Gates, University of Southampton) at 633 nm and 1553 nm using a *Meticon* Prism coupler, the background theory of which is given above in **Chapter 4**. The refractive index of the thin film **(8)** at 633 nm = 1.4424 (*Meticon Spectrum* \rightarrow *DJW.6625.20.poly(methyloctyl)siloxane (8).Meticon Prism Coupling Spectrum*) and at 1553 nm = 1.4397. These experimental values of the refractive index further corroborated that **(8)** is a copolymer of poly(methylhydro)siloxane and poly(methyloctyl)siloxane; the values of the refractive index at 633 nm and 1553 nm both lie between the literature refractive index values for poly(methylhydro)siloxane ($n = 1.398 @ 589 \text{ nm}$) ¹² and poly(methyloctyl)siloxane ($n = 1.4450 @ 589 \text{ nm}$) ³.

7.3 Refractometric sensing of organic vapours

7.3.1 Organic vapour sensing experimental set-up and procedure :

The experimental was set-up as shown in **Fig.6** below. Full details of the gas sensing experiments are given in **Chapter 10** below, however the assumptions and reasoning behind the design of the experiment and how this affected the results are discussed here.

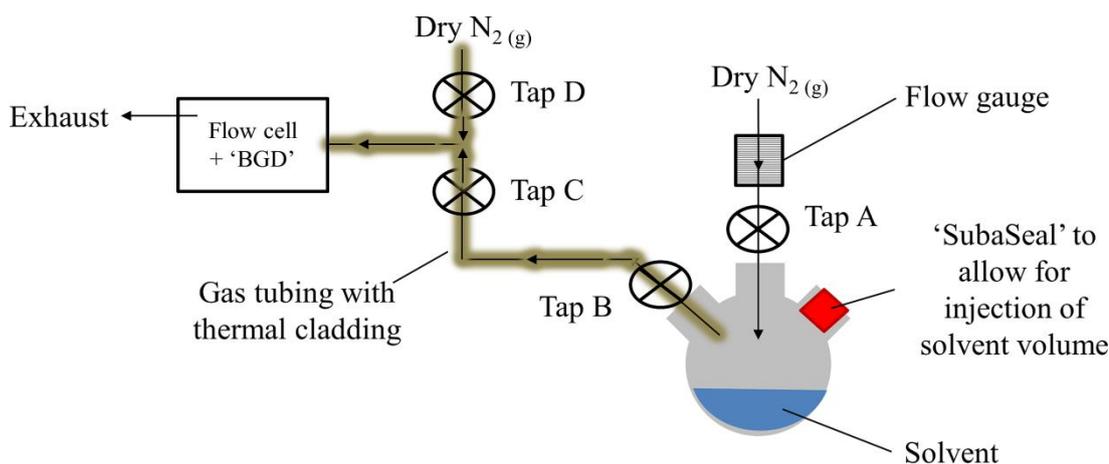


Fig.7.6: Schematic of the solvent vapour sensing experimental set-up. The flow of nitrogen gas through the reservoir of solvent was ~ 1.5 L/min.

The experimental gas sensing set-up used herein was based on an organic vapour sensing experiment within the peer-reviewed literature¹³. However, an advantage of the set-up used herein, compared to the literature, was that the solvent reservoir was held at a temperature which was > 20 °C than the boiling point of the chosen analyte solvent. This ensured that the solvent was boiling. In the literature example the solvent reservoir was held at 80 °C for all analyte solvents¹³.

The Bragg grating sensor device modified with the thin film of (8), labelled as 'BGD', was placed in a flow cell; the temperature within the flow cell was monitored throughout the experiment with a thermocouple. This allowed for the magnitude of Bragg wavelength shifts recorded with the uncovered reference Bragg gratings to be corroborated with the measured temperature changes during a sensing event, knowing that the temperature coefficient of FHD silica is ~ 10 pm °C⁻¹¹⁴. Erroneous Bragg wavelength shift due to contamination of the sensing layer were minimised by continuous exposure of the 'BGD' to a flow of dry nitrogen gas (> 5 L min⁻¹) to prevent contamination of the thin film of (8). For sensing events, the

Chapter 7: Sensing of solvent vapours using a polysiloxane thin film as the active sensing element

'BGD' was exposed to a flow of organic solvent vapour in dry nitrogen carrier gas. A three neck flask was used as the reservoir for the liquid solvent analytes and was preheated to temperatures > 20 °C higher than the boiling point of the chosen analyte solvent for at least 20-30 mins (e.g. for dichloromethane (boiling point ~ 40 °C) the three neck flask was heated to ~ 60 - 65 °C). *NOTE:* Extra care was taken when carbon disulphide (CS_2) was used as the analyte solvent; it was ensured that the temperature of the flask did not exceed the relatively low autoignition temperature of CS_2 : ~ 90 °C¹⁵. When the flask was at appropriate temperature, analyte solvent (3 mL) was injected into the three neck flask via the 'Suba Seal'. Within a few seconds, the liquid solvent began bubbling and condensation of liquid was seen around the top of the flask. At this point it was assumed that a saturated atmosphere of solvent vapour in nitrogen had formed within the flask. At this point, the dry nitrogen gas flow over the 'BGD' was removed and Tap D was shut (the identity of each tap is shown in **Fig.7.6** above). Taps B, C and then A were then opened in quick succession followed immediately by application of a flow of dry nitrogen carrier gas (~ 1.5 L min^{-1}) over the volume of the analyte solvent as shown in **Fig.7.6** above, which in turn then flowed over the 'BGD'. The length of gas piping between the flow cell (containing the 'BGD') and the reservoir was kept to a minimum (~ 20 cm) and was insulated with lagging to prevent cooling and condensation of solvent vapour before reaching the 'BGD'. During sensing events it was noted that the volume of liquid solvent decreased with continued nitrogen carrier gas flow; this indicated that evaporation of the analyte solvent was occurring. The flow of nitrogen carrier gas through the reservoir flask was maintained for at least 5 mins after it was first observed that all the liquid solvent had evaporated. This was to ensure that condensed solvent vapour within the pipes was purged and passed over the 'BGD'. This enabled the following assumption to be made; the Bragg wavelength shifts recorded for the vapours of different solvents were due to the properties of the solvent and not due to differences in the volume of each different vaporized solvent passed over the 'BGD'. After five minutes Tap C was shut, the flow of dry nitrogen carrier gas through the flask was ceased, Tap D was opened and the flow of dry nitrogen gas (> 5 L min^{-1}) was reintroduced to the flow cell before finally Tap A and Tap B were shut. This procedure was repeated for every sensing event to enable direct comparison of the Bragg wavelength shifts recorded upon exposure to different solvent vapours. A sufficient period (usually 10-15 mins) of dry nitrogen gas was allowed between

Chapter 7: Sensing of solvent vapours using a polysiloxane thin film as the active sensing element

sensing events to ensure Bragg wavelength shift values had returned to stable baseline levels.

It must be noted that with this particular experimental set-up, the vapour vented to the external atmosphere, i.e. vented into atmospheric pressure. Therefore the vapour pressure was not constant. One way to overcome this would be to expose the sensor to a closed system with a solvent vapour-rich atmosphere at a constant vapour pressure solvent as used in the Reid Method (an American National Standard) ¹⁶. However, the advantage of the experimental method reported herein is that this set-up allows for the compatibility of the Bragg solvent vapour sensor to gas flow systems to be demonstrated.

7.3.2: Solvent vapour sensing results:

For each solvent, at least three ‘sensing events’ were performed. A ‘sensing event’ is defined as exposure of the ‘BGD’ to the vapour of an individual solvent. For each ‘sensing event’ the change in Bragg wavelength was calculated for both the thin film covered and uncovered Bragg gratings. These values were calculated by subtraction of an average baseline Bragg wavelength value (average of the baseline Bragg wavelength values before and after a sensing event) from the average peak Bragg wavelength shift during a sensing event. These calculations were identical to the calculation outlined in **Chapter 4** above. Then for each sensing event the difference in Bragg wavelength shift, $\Delta\lambda_B$, was calculated by subtraction of the average Bragg wavelength shift value for thin film covered Bragg gratings from the average Bragg wavelength shift value for uncovered Bragg gratings. Therefore for each sensing event there was a corresponding $\Delta\lambda_B$ value and thus for each solvent there were at least values of $\Delta\lambda_B$. The resulting average Bragg wavelength shift for each solvent, average $\Delta\lambda_B$, was calculated using the three values of $\Delta\lambda_B$ determined. Associated errors were propagated throughout. The average Bragg wavelength shift values (average $\Delta\lambda_B$) for uncovered and thin film covered Bragg gratings when exposed to each solvent are shown below in **Fig.7.7**:

Chapter 7: Sensing of solvent vapours using a polysiloxane thin film as the active sensing element

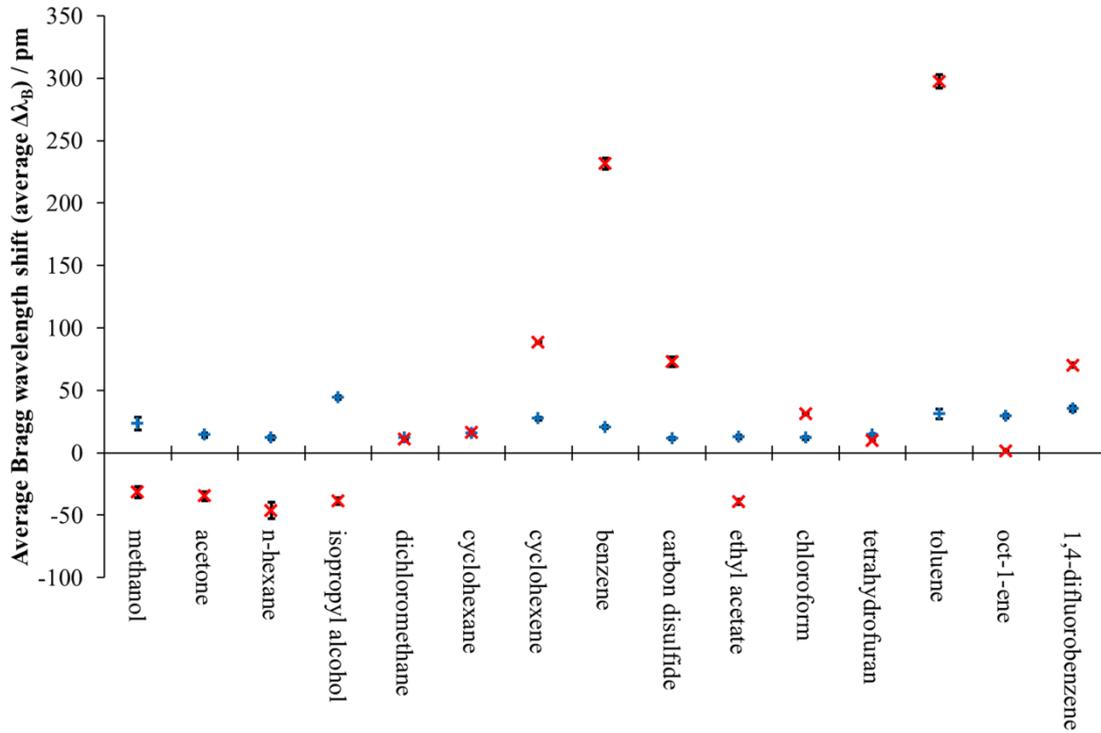


Fig.7.7: Blue crosses (+) are the average Bragg wavelength shift values (average $\Delta\lambda_B$) for the uncovered Bragg gratings and the red crosses (x) are the average Bragg wavelength shift values for the thin film covered Bragg gratings. For all solvents, the average $\Delta\lambda_B$ of the uncovered Bragg gratings are positive, whereas on the other hand, the average $\Delta\lambda_B$ values of the thin film Bragg gratings are either negative or positive depending on the solvent. The associated errors in average $\Delta\lambda_B$ for both uncovered and covered are included.

As is demonstrated in **Fig.7** above, for all solvents, the average $\Delta\lambda_B$ of the uncovered Bragg gratings are positive. On the other hand, the average $\Delta\lambda_B$ values of the thin film Bragg gratings are either negative or positive depending on the solvent. This is attributed to a thin film of condensed solvent forming on the surface when solvent vapour is flown over the 'BGD' during a sensing event. This layer of solvent replaces the nitrogen atmosphere close to the sensor surface. Because all of the solvents are of larger magnitude refractive indices than nitrogen gas, ($n = 1.0003$ @ 1550 nm)¹⁷, this causes an positive increase in Bragg wavelength as explained by,

$$\lambda_B \propto n_{eff}$$

Eqn.7.1

Chapter 7: Sensing of solvent vapours using a polysiloxane thin film as the active sensing element

where λ_B is the Bragg wavelength shift and n_{eff} is the effective index encountered by the optical mode. It may be expected that the magnitude of the Bragg wavelength shift would be proportional to the refractive index of the solvent; the same volume of each solvent was vaporised and thus the thin layer formed of each solvent would be the same volume. However, when the average $\Delta\lambda_B$ values for the uncovered Bragg gratings are plotted against the refractive index of the solvents there is no correlation as shown in **Fig.7.8** below.

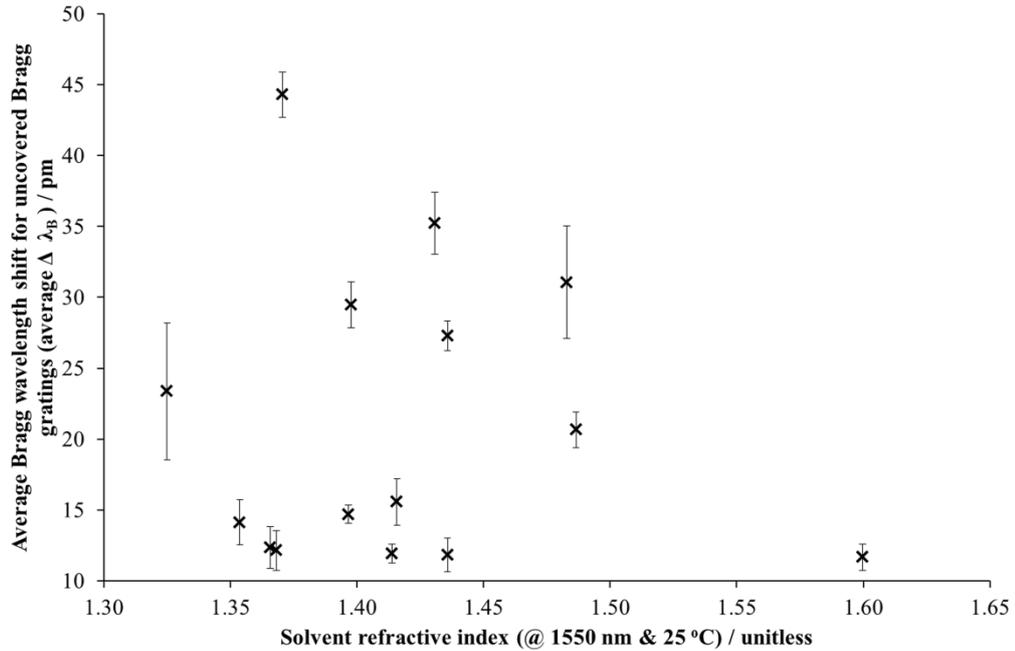


Fig.7.8: No correlation between the average $\Delta\lambda_B$ of the uncovered Bragg gratings and the refractive indices of the different solvents.

The lack of correlation is explained by the much larger effect of changes in temperature and strain on the Bragg wavelength shifts.

For the thin film covered Bragg gratings it would be expected that the layer of condensed solvent between the polymeric chains of the thin film would always increase n_{eff} and thus a positive Bragg wavelength shift would occur. However, for some solvents, a negative average $\Delta\lambda_B$ was calculated. This suggests that the properties of the solvents and the interaction of the solvents with the thin film of polymer are important factors. However, care must be taken as temperature and strain effects have not yet been referenced and removed from these Bragg wavelength shift values for the thin film Bragg gratings.

Chapter 7: Sensing of solvent vapours using a polysiloxane thin film as the active sensing element

To account for temperature and strain effects, the first order and linear referencing method introduced in **Chapter 6** was used; for each solvent the average $\Delta\lambda_B$ value for the uncovered Bragg gratings was subtracted from the average $\Delta\lambda_B$ value for the covered Bragg gratings. The resulting referenced $\Delta\lambda_B$ for each solvent are shown below in **Fig.7.9**.

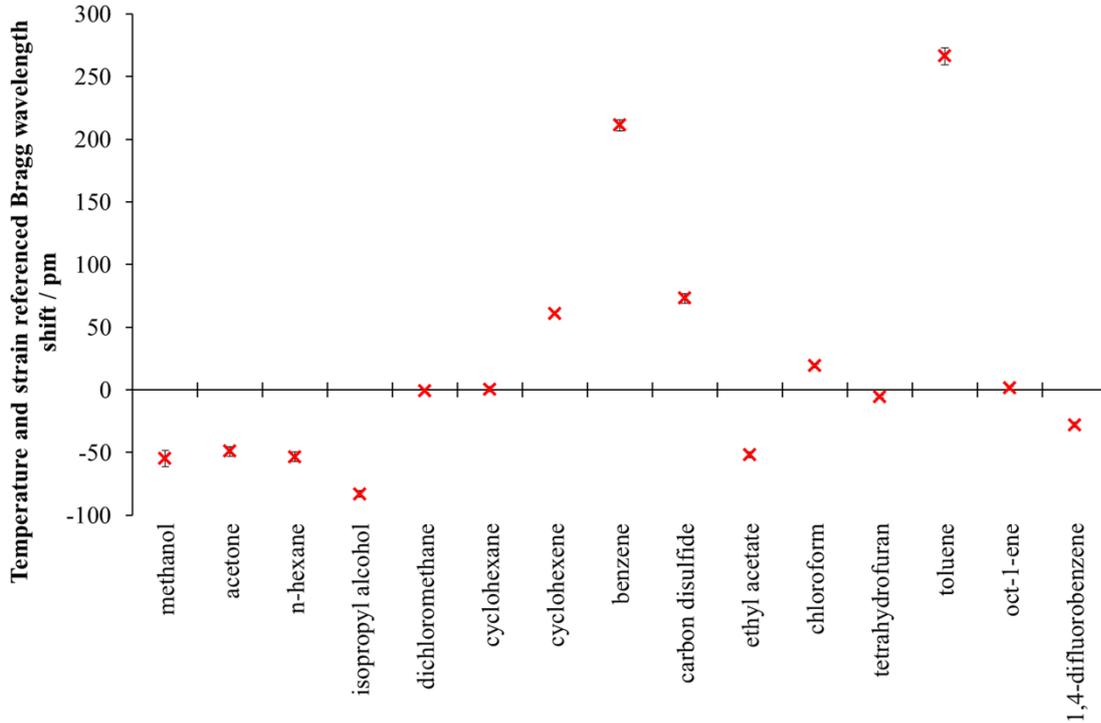


Fig.7.9: Overall Bragg wavelength shifts due to exposure to the vapours of different solvents.

Associated errors are shown by the black error bars.

After referencing for changes in temperature and strain, the overall Bragg wavelength shift for some solvents is negative whereas for the other solvents the shifts are positive.

These results highlight a complex interaction of solvent vapour with the thin film of (8). If thin layers of solvent were forming on top of the thin film of (8) it would be expected that the referenced $\Delta\lambda_B$ values would be positive for all solvents. The thin layer of solvent would increase n_{eff} by displacing nitrogen from near the surface of the thin film; the refractive index of all the solvents is greater than the refractive of nitrogen gas. However, when the referenced $\Delta\lambda_B$ values are plotted against the refractive indices of the solvents, apart from carbon disulfide which was deemed to be an outlier, (**Fig.7.10** below) it is clear that this is not the sensing mechanism that is occurring.

Chapter 7: Sensing of solvent vapours using a polysiloxane thin film as the active sensing element

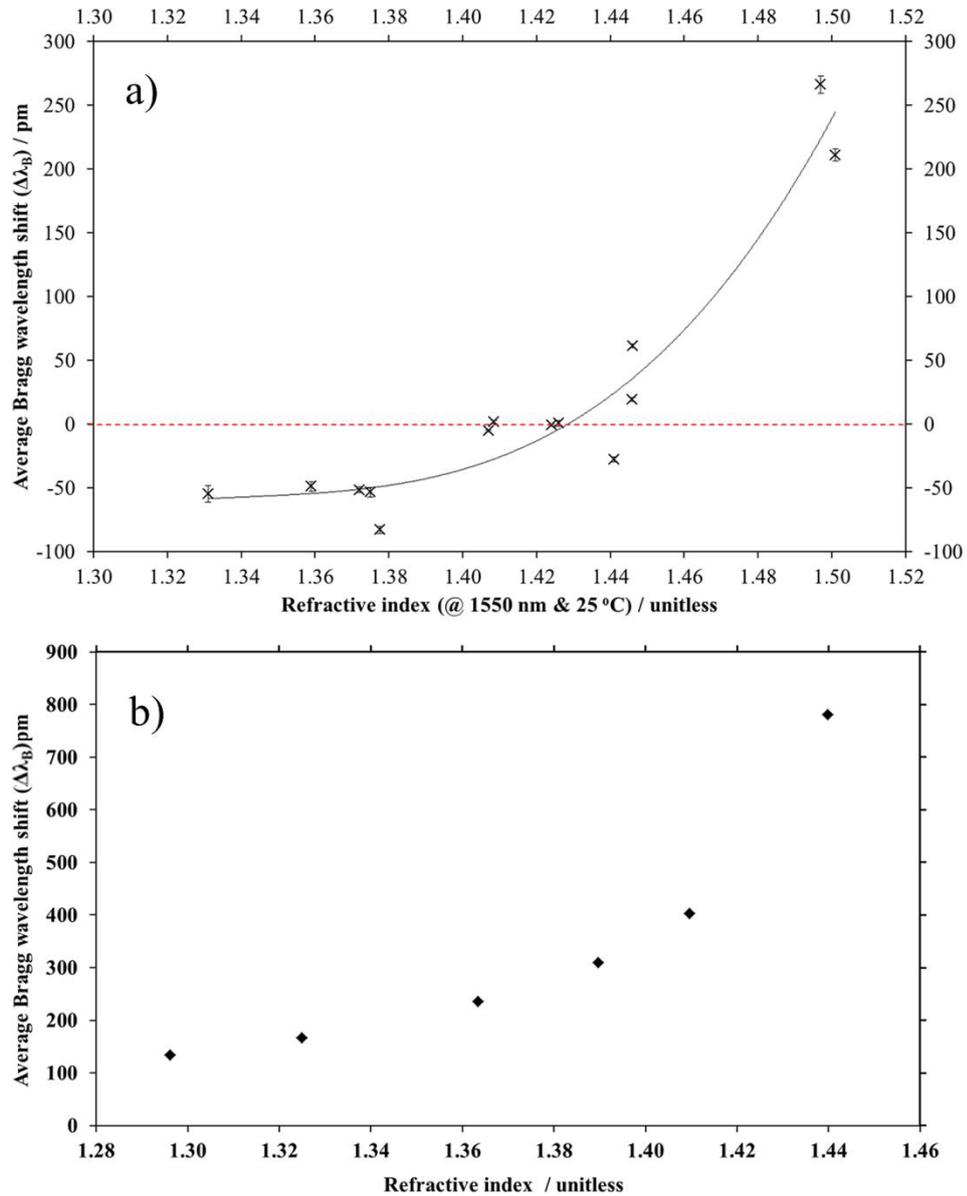


Fig.7.10:(a) The relationship between the reference $\Delta\lambda_B$ values and the refractive index (at 1550 nm) of the solvents tested (apart from carbon disulfide, which was an outlier) showing both negative and positive reference $\Delta\lambda_B$ values. This demonstrates a complex sensing mechanism (the curved line is a guide for the eye). If a thin layer of solvent was forming, then the relationship between these variables would be similar to the relationship shown in **(b)**; refractive index matching liquids of different refractive indices on top of a uncovered Bragg grating sensor resulting in positive Bragg wavelength shifts in all cases.

As is shown in **Fig.7.10(a)**, despite all of the solvents having a refractive index greater than nitrogen gas, there are some negative reference $\Delta\lambda_B$ values. If a thin layer of solvent was forming then a similar plot to **Fig.7.10(b)** (liquids of different refractive indices on top of a uncovered Bragg grating sensor) would be expected; all

Chapter 7: Sensing of solvent vapours using a polysiloxane thin film as the active sensing element

the reference $\Delta\lambda_B$ values would be positive. Therefore this corroborates that a more complex sensing mechanism is occurring.

The model of the formation of a thin layer of solvent on top of the polymer thin film does not explain the experimental results. Thus it is proposed that there is an interaction of the solvent vapours with the thin film of **(8)** which gives rise to the observed experimental result.

It is known that both PDMS and PMHS polymers swell in the presence of solvent vapours^{2,6}, therefore it is postulated that solvent vapours swell the thin film of **(8)**, and the extent of swelling is dependent on the solvent.

During swelling, two things would occur: (i) solvent molecules would displace the molecules of nitrogen in between the polymer chains and thus increase the average n_{eff} of the thin film of **(8)** and (ii) the thickness of the thin film of **(8)** would increase thus causing the density to decrease. Factor (i) would cause an increase in n_{eff} whereas factor (ii) would cause a decrease in n_{eff} . However, it would be expected that magnitude of the change in n_{eff} due to factor (i) would be larger than the magnitude of the change in n_{eff} due to factor (ii); therefore all values of referenced $\Delta\lambda_B$ should be positive. This is not found to be true experimentally. Therefore, it is proposed that the magnitudes of factors (i) and (ii) are determined by the properties of the solvent, i.e. how well does a particular solvent solvate the polymer and thus to what extent do solvent molecules displace nitrogen molecules in between the polymer chains. It is postulated that this subsequently causes a trade-off between factor (i) and (ii). A very 'good' solvent for the polymer would solvate the polymer readily and thus a large number of solvent molecules would displace nitrogen molecules and thus the magnitude of (i) > (ii), whereas few molecules of a very 'poor' solvent would displace nitrogen molecules, but this would still cause some swelling, thus factor (i) < (ii).

To determine what a 'good' or a 'poor' solvent is for this polymer system, the correlations between the reference $\Delta\lambda_B$ values and intrinsic properties of the solvents were investigated. With reference to the literature, wherein Lowe *et. al.* reported a holographic Bragg grating optical sensor based on swelling of a polymer layer¹⁸, appropriate solvent property descriptors were chosen. The intrinsic solvent property

Chapter 7: Sensing of solvent vapours using a polysiloxane thin film as the active sensing element

descriptors were boiling point, the logarithm of the octanol water partition coefficient of the solvent ($\log K_{ow}$) and the Hildebrand solubility parameter.

7.3.2.1 Solvent boiling point

The boiling point of a substance is defined as the temperature at which the saturated vapour pressure of the substance becomes equivalent to the pressure of the surrounding medium (typically the atmosphere). At this point the evaporation rate of the substance is at its highest magnitude; the intermolecular forces between the molecules are broken. Therefore the boiling point of a solvent can also be used as a crude overall description of the total magnitude of intermolecular forces between solvent molecules. The magnitude of the average intermolecular interaction between the solvent molecules is due to types of intermolecular interactions (such as hydrogen bonding, dipole-dipole interactions and Van de Waal's forces) that are present. Grossly it can be stated, that at a certain pressure, if a solvent has a higher boiling point then the magnitude of the average intermolecular forces is relatively larger than for a solvent with a lower boiling point. The types of intermolecular forces afforded by each solvent also affects the ability of that solvent to solubilise a solute; in this case the solute is poly(methylhydro) – *co* – poly(methyloctyl)siloxane (**8**). Therefore to investigate, the reference $\Delta\lambda_B$ values for the covered Bragg gratings were plotted against the boiling points of the solvents used in the sensing experiment.

Chapter 7: Sensing of solvent vapours using a polysiloxane thin film as the active sensing element

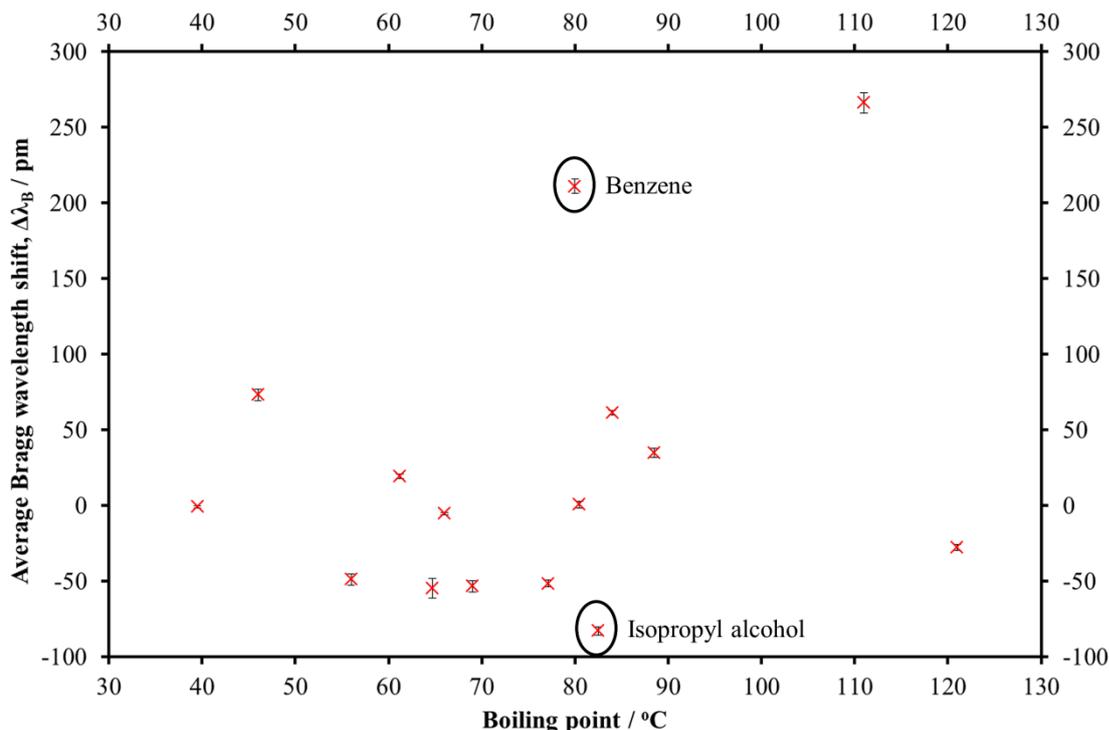


Fig.7.11: No correlation between the reference $\Delta\lambda_B$ values for the solvents that were used in the sensing experiments and the boiling points of the solvents. The associated errors for the average reference $\Delta\lambda_B$ value are shown by the black error bars.

As is evident, there is no correlation between the average reference $\Delta\lambda_B$ value and the boiling point of the solvent. This is attributed to the boiling point of a solvent being a poor descriptor of the ability of the solvent to solubilise the polymer, which is corroborated in the literature for swelling of polymer by volatile organic compounds in the liquid state¹⁸. This is because as stated above, the boiling point of a solvent is dependent on the total intermolecular forces, but not does discriminate between the different types of intermolecular forces. For example, the solvents highlighted with a black circle in **Fig.7.11** above, benzene and isopropyl alcohol, both have very similar boiling points; 80.1 °C and 82.5 °C respectively. However, the average reference $\Delta\lambda_B$ shift for both solvents is vastly different; 211 pm for benzene and -83 pm for isopropyl alcohol. This is attributed to the different intermolecular forces present between the molecules of benzene and between the molecules of isopropyl alcohol. For all molecules there are Van de Waal's forces, however in addition, for benzene, there are π - π stacking interactions, and for isopropyl alcohol there are dipole-dipole interactions plus hydrogen bonding. From this comparison it can be stated that the nature of the different types of intermolecular forces present has an effect on the degree of solubilisation of the

Chapter 7: Sensing of solvent vapours using a polysiloxane thin film as the active sensing element

polymer which in turn determines the magnitude of the Bragg wavelength shift. Therefore a better descriptor of the solvation ability of the solvents was required.

7.3.2.2: Octanol water partition coefficient (K_{ow}) of the solvent

The octanol water partition coefficient (K_{ow}) of a substance is defined as the ratio of the concentration of a chemical in two immiscible phases, which are in equilibrium and at a specified temperature. For the octanol/water partition coefficient the phases are *n*-octanol & water¹⁹. For a given chemical, A, the ratio is given by,

$$K_{ow} = \frac{[A]_{n-octanol}}{[A]_{water}}$$

Eqn.7.2

Where $[A]_{n-octanol}$ and $[A]_{water}$ are the concentration of compound A in the *n*-octanol phase and the water phase respectively.

For ease of comparison of the K_{ow} values of different chemicals, the logarithm of the K_{ow} is taken. $\log_{10} K_{ow}$ values are quantitative thermodynamic measures of the hydrophobic (or lipophilic) / hydrophilic behaviour of a chemical; the larger the $\log_{10} K_{ow}$ value the more hydrophobic the chemical. It is predicted that the polymer (**8**) will swell the most when exposed to solvents with high $\log_{10} K_{ow}$ values, based on the solubilities of PDMS and PHMS^{2,6}.

Therefore, experimental values of $\log_{10} K_{ow}$, for the solvents used in these sensing experiments, were taken from the literature²⁰ and plotted against the reference Bragg wavelength shift values as shown in **Fig.7.12** below.

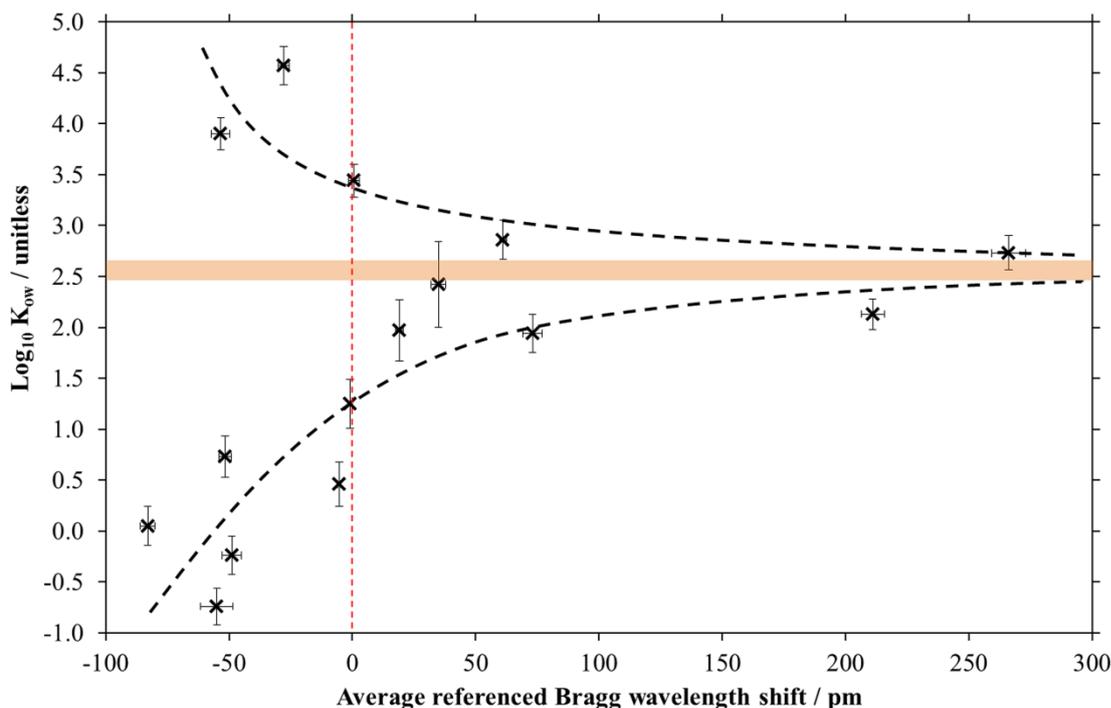


Fig.7.12: Relationship between $\text{Log}_{10} K_{ow}$ and the average referenced Bragg wavelength shift highlighting the asymptotic behaviour approaching the range of $\text{log}_{10} K_{ow}$ values of PDMS (shown by the salmon pink highlighted area)²¹. The dashed black lines are guides for the eyes only. The dashed red line denotes the position of zero on the x-axis. Associated errors are represented by the black error bars.

The relationship between $\text{log}_{10} K_{ow}$ values and the average reference Bragg wavelength shift values is complex and shows asymptotic behaviour around $\text{log}_{10} K_{ow} \approx 2.5$, forming a narrow range of $\text{log}_{10} K_{ow}$ values. This narrow band of $\text{log}_{10} K_{ow}$ values matches with the $\text{log}_{10} K_{ow}$ value range in the literature for PDMS = (2.47 – 2.62). The solvents with similar $\text{log}_{10} K_{ow}$ values, benzene ($\text{log}_{10} K_{ow} = 2.13$) and toluene ($\text{log}_{10} K_{ow} = 2.73$) cause the largest magnitude positive Bragg wavelength shifts. This is to be expected as compounds with very similar $\text{log}_{10} K_{ow}$ values will readily dissolve in one another; this is corroborated by the use of toluene as the reaction solvent for the synthesis of **(8)** due to facile dissolution of the starting material PMHS. Both benzene and toluene are relatively hydrophobic solvents therefore it could be postulated that **(8)** is the most soluble in hydrophobic solvents and not hydrophilic solvents. Corroboration of this is afforded by the small magnitude negative average referenced Bragg wavelength shifts when the sensor device was exposed to the vapour of hydrophilic solvents such as methanol ($\text{log}_{10} K_{ow} = -0.73$) and isopropyl alcohol ($\text{log}_{10} K_{ow} = 0.05$). However, the relationship

Chapter 7: Sensing of solvent vapours using a polysiloxane thin film as the active sensing element

between hydrophobicity and average referenced Bragg wavelength shift is not that simple. This is highlighted by the negative and small magnitude average referenced Bragg wavelength shifts when the sensor device is exposed to solvents that are more hydrophobic than benzene or toluene; n-hexane ($\log_{10} K_{ow} = 3.90$) and oct-1-ene ($\log_{10} K_{ow} = 4.57$).

The model postulated to explain this behaviour is based on the solvating ability of the solvents based on the $\log_{10} K_{ow}$; the solvating ability determines the quantity of solvent that ingresses into the thin film of (8). The quantity of solvent determines the extent of the trade-off between the n_{eff} increase due to solvent molecules displacing nitrogen molecules and the n_{eff} decrease due to swelling of the polymer thin film. It is proposed, based on the data displayed in **Fig.7.12** above, solvents with $\log_{10} K_{ow}$ values similar to the $\log_{10} K_{ow}$ value range of PDMS (2.47 – 2.62) solvate (8) well. Large positive average referenced Bragg wavelength shifts are the result of this due to a large quantity of solvent within the thin film of (8). The large quantity of solvent molecules results in a large n_{eff} increase then the slight n_{eff} decrease due to swelling. In contrast, solvents with $\log_{10} K_{ow}$ values that are either relatively smaller or larger in magnitude solvate (8) poorly and thus result in small negative average referenced Bragg wavelengths. In this case the extent of swelling is greater than the slight increase in n_{eff} due to a relatively small quantity of solvent molecules displacing nitrogen gas molecules.

7.3.2.1 Hildebrand solubility parameter, δ_H :

To better describe the solvation of the thin film of (8) and the subsequent Bragg wavelength shifts, a more robust descriptor of the solvation ability of the solvents was required. A descriptor commonly used to describe the intermolecular forces of a solvent, and thus the ability of the solvent to solvate polymers, is the Hildebrand solubility parameter, δ_H . The Hildebrand solubility parameter, δ_H , is defined as the square root of the cohesive energy density of the solvent and has units of $\text{Pa}^{1/2}$. The cohesive energy density, C_p , of a solvent is defined as the following ratio,

$$C_p = \frac{(\Delta H_v - RT)}{V_m}$$

Eqn.7.3

Chapter 7: Sensing of solvent vapours using a polysiloxane thin film as the active sensing element

where ΔH_v is the enthalpy of vaporization of the solvent, R is the ideal gas constant, T , is the temperature of the system and V_m is the molar volume of the solvent. The cohesive density describes the amount of energy required for separation of a unit volume of molecules in such a manner that each molecule is then separated at an infinite distance (starting at the equilibrium distance) from each of the other molecules; becoming an ideal gas.

The Hildebrand solubility parameters were plotted against the average reference Bragg wavelength shifts for each solvent to investigate if there was a significant relationship between the variables. However, solvents containing hydrogen bond donor groups (methanol and isopropyl alcohol) were not included; the derivation of the Hildebrand solubility parameter does not take into account hydrogen bonding²². The δ_H values for the solvents were taken from the comprehensive work of Abboud & Notario²³, except for oct-1-ene and 1,4-difluorobenzene. The δ_H values for oct-1-ene and 1,4-difluorobenzene were calculated using **Eqn.7.3** above and the value of ΔH_v for each solvent from the literature^{24,25}.

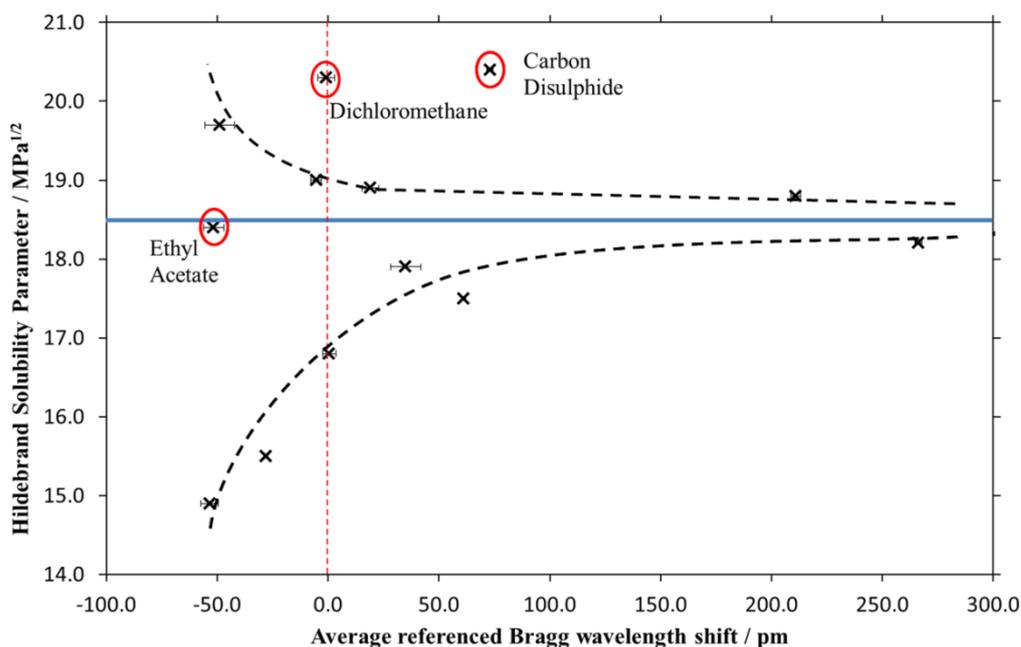


Fig.7.13: Relationship between the Hildebrand solubility parameter, δ_H , and the average referenced Bragg wavelength shift (for the non-hydrogen bonding solvents) highlighting the asymptotic behaviour approaching $\delta_H \approx 18.5 \text{ MPa}^{1/2}$ (shown by the thick blue line). The dashed black lines are guides for the eyes only. The dashed red line denotes the position of zero on the x-axis. Associated errors are represented by the black error bars and outliers are circled in red with the solvent name given besides the outlier datum.

Chapter 7: Sensing of solvent vapours using a polysiloxane thin film as the active sensing element

The relationship between the δH values and the average reference Bragg wavelength shift values is complex and shows asymptotic behaviour around $\delta H \approx 18.5 \text{ MPa}^{1/2}$. However, the overall shape of the plot, and asymptotic behaviour, corroborates with a plot in the literature describing the change in hologram playback wavelength in relation to the Hildebrand solubility parameter of various solvents¹⁸. However, there are some significant outliers, which are circled in red. Carbon disulphide can be discounted on the basis that it is an inorganic compound; all the other solvents which are organic solvents. The outlier behaviour of ethyl acetate and dichloromethane is explained by the relatively high relative polarities of these solvents; polarity affects the solvating power of a solvent in a manner that is not fully taken into account by the Hildebrand solubility parameter²⁶.

The solvents with similar δH values, benzene ($\delta H = 18.8 \text{ MPa}^{1/2}$) and toluene ($\delta H = 18.2 \text{ MPa}^{1/2}$) resulted in the largest magnitude positive Bragg wavelength shifts. This is to be expected as compounds with very similar δH values will readily dissolve in one another; this is corroborated by the use of toluene as the reaction solvent for the synthesis of **(8)**. This suggests that the δH value of **(8)** is $\approx 18.5 \text{ MPa}^{1/2}$, however no comparable value in the literature was found. In contrast, solvents with vastly different δH value to the proposed δH value of **(8)** result in small or negative magnitude average reference Bragg wavelength shifts.

The quantity of solvent determines the extent of the trade-off between the n_{eff} increase due to solvent molecules displacing nitrogen molecules and the n_{eff} decrease due to swelling of the polymer thin film. It is proposed, based on the data displayed in **Fig.7.13** above, solvents with δH values similar to the proposed δH value of **(8)**, solvate **(8)** well. Large positive average referenced Bragg wavelength shifts are the result of this due to a large quantity of solvent molecules displacing nitrogen molecules within the thin film of **(8)**. The large quantity of solvent molecules results in a large n_{eff} increase that is greater than the slight n_{eff} decrease due to swelling. In contrast, solvents with δH values that are either relatively smaller or larger in magnitude, solvate **(8)** poorly and thus result in small or negative magnitude average referenced Bragg wavelength shifts. The effect of swelling on n_{eff} is greater than the slight increase in n_{eff} due to a relatively small quantity of solvent molecules displacing nitrogen gas molecules.

7.3.2.2: Sensor response time determination

The response time of the device in the flow system was then determined. Three independent sensing events were performed; in each event the sensor device was switched from exposure to dry nitrogen gas to nitrogen gas saturated with toluene vapour and the time taken for a stable Bragg wavelength shift to be achieved when exposed to the vapour saturated gas (starting from a stable baseline value in dry nitrogen) was recorded. In the literature the response time of a gas sensor is defined as the time taken to achieve 90 % of the final stable change of a sensor after a step increase of the concentration of the analyte gas²⁷. Therefore an average time was calculated from the time taken in each sensing event for the Bragg wavelength shift, of a Bragg grating covered with (8), to reach 90% of the full stable Bragg wavelength shift, as highlighted in **Fig.7.14** below. For the ‘BGD’ modified with a thin film of (8) (~1.2 μm thick) 90 % of the final constant Bragg wavelength value was reached in ~100 s. It is proposed a thinner film of (8) would allow for a faster response time due a shorter time for the solvent to diffuse into the thin film layer.

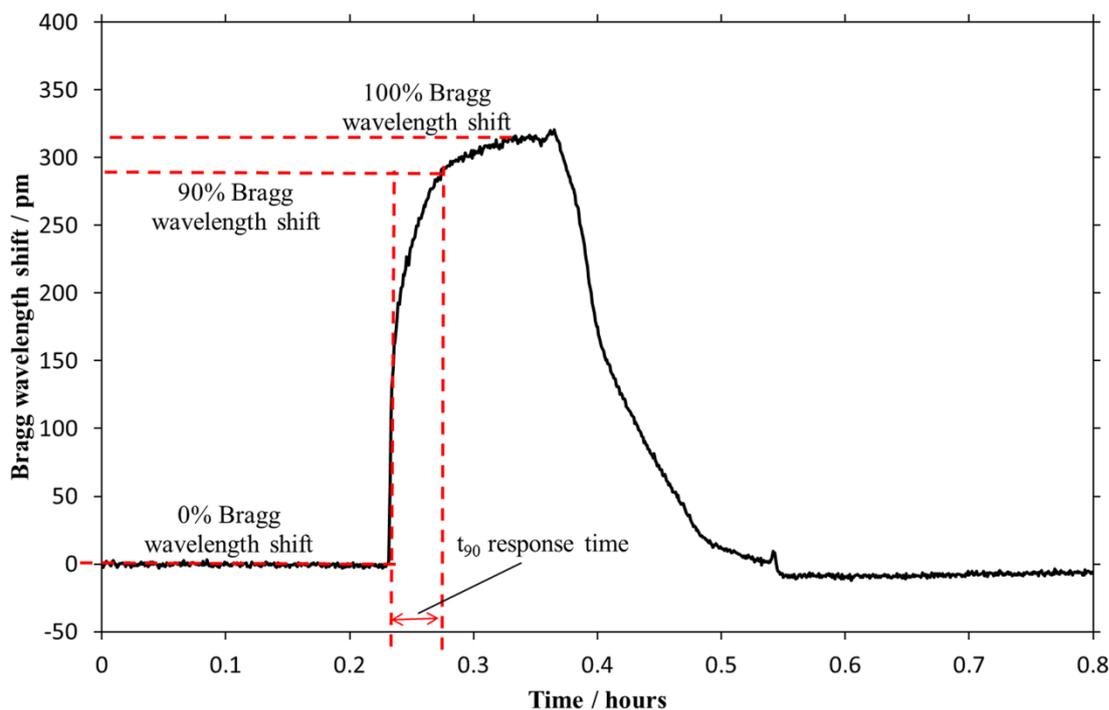


Fig.7.14: The definition of the response time of the ‘BGD’ during a switch from dry nitrogen gas to toluene vapour saturated nitrogen gas. The Bragg wavelength shifts from the polymer covered Bragg grating were recorded every three seconds.

7.3.3: QSAR approach to enable prediction of Bragg wavelength shifts:

The approach used in 5.3.2 above enabled the modelling and understanding of how different solvents affect the magnitude of Bragg wavelength shifts measured with a Bragg grating device modified with a thin film of (8). However, this approach did not generate a linear relationship between Bragg wavelength shift and the solvent parameters; a simple linear relationship would have facilitated prediction of Bragg wavelength shifts for particular solvents, measured with this system. In addition, this approach did not allow for specific sensing of solvent vapours to be achieved; due to the shape of the curves, certain Bragg wavelength shift values would correspond to more than one solvent (see Fig.7.12 and Fig.7.13 above). Therefore, a quantitative structural analysis relationship (QSAR) study was performed to determine a linear regression model between the parameters of the solvents and the Bragg wavelength shifts.

Quantitative structural analysis relationships (QSAR) are a type of regression model which relates a set of “descriptor” variables (X values) to the response variable (Y value). In chemistry, a descriptor is usually a real physico-chemical or theoretical property of a chemical, for example the boiling point or the count of hydrogen bond acceptor functional groups a molecule possesses. In a QSAR model, a chemical can be described by many descriptors.

In this work, a set of descriptors, which described both physico-chemical and theoretical properties of the solvents, were related to the average referenced Bragg wavelength shift using multiple variable linear regression. The properties that were used to describe the solvents are listed below in Table.7.1.

Chapter 7: Sensing of solvent vapours using a polysiloxane thin film as the active sensing element

Chemical Descriptor	Physico-chemical or theoretical property?	Description
1) Surface Tension	Physico-chemical	The surface tension describes the energy required to form an interface between the bulk solvent and the surrounding environment, usually the atmosphere.
2) Freezing point	Physico-chemical	The temperature at which the chemical changes state from a liquid to a solid
3) Boiling point	Physico-chemical	The temperature at which the chemical changes state from a liquid to a gas
4) Hildebrand Solubility Parameter	Physico-chemical	The square root of the cohesive energy density. The cohesive energy density describes the energy required to separate a unit volume of molecules to infinite separation from neighbouring molecules.
5) Molecular Weight	Physico-chemical	Relative molecular mass of the chemical.
6) $\text{Log}_{10} K_{ow}$	Physico-chemical	A quantitative thermodynamic measure of the hydrophobic / hydrophilic behaviour of a chemical.
7) Refractive index (1550 nm)	Physico-chemical	The refractive index of the chemical at 1550 nm.
8) Topological Polar Surface Area (TPSA)	Theoretical property	TPSA is a measure of the polar surface area of a molecule.
9) Number of rotatable bonds	Theoretical property	A topological parameter that describes molecular flexibility. A rotatable bond is defined as a single, non-ring bond to a non-terminal heteroatom.

Chapter 7: Sensing of solvent vapours using a polysiloxane thin film as the active sensing element

10) Number of hydrogen bond donor groups	Theoretical property	The number of –OH or –NH(R) groups within the molecule that are able to act as hydrogen bond donor groups.
11) Number of hydrogen bond acceptor groups	Theoretical property	The number of nitrogen atoms in the molecule substituted by a hydrogen or aliphatic chain or the number of oxygen atoms in the molecule that are bonded to a carbon atom by a double bond or substituted by a hydrogen or aliphatic chain. Oxygen atoms that are directly bonded to an atom which is itself doubly bonded to another atom and oxygen atoms in an aromatic system are not counted. In this study, carbon disulfide, S=C=S, and 1,4-difluorobenzene were counted as possessing two H-bond acceptor groups each. There is evidence of weak hydrogen bond acceptor behaviour of the C=S groups in carbon disulfide and the C-F bonds in 1,4-difluorobenzene in the literature ^{28,29} .
12) Ring double bond equivalents value	Theoretical property	The ring double bond equivalents value gives an indication of the unsaturation of a molecule. The number gives the total sum of double bonds, rings and twice the number of triple bonds within a molecule.

Table.7.1: List of the chemical descriptors used in the QSAR study reported herein.

Chemical descriptors (1) through to (4) and (6) were chosen because these descriptors begin to describe the intermolecular forces between the solvent molecules; the magnitudes of these descriptors depend on the strength of the intermolecular forces. The value of descriptor (1) for each solvent were sourced from

Chapter 7: Sensing of solvent vapours using a polysiloxane thin film as the active sensing element

the literature³⁰⁻⁴³. The value of descriptors (2) and (3) for each solvent were easily sourced from the Sigma-Aldrich UK website⁴⁴. Values for descriptor (4), as mentioned in section 5.3.2.1 above, were taken from the comprehensive work of Abboud & Notario²³, apart from oct-1-ene and 1,4-difluorobenzene; the values for oct-1-ene and 1,4-difluorobenzene were calculated using **Eqn.3** above and values of ΔH_v taken from the literature^{24,25}. The $\log_{10} K_{ow}$ values, descriptor (6), were taken from the literature²⁰.

Chemical descriptor (5) was calculated by hand. Descriptor (7) was chosen because refractive index is the integral physic-chemical property that is being investigated in this work. Values for (7) were determined by taking n_D values (where n_D is the refractive index of a material at the sodium D-line wavelength) from the Sigma-Aldrich website⁴⁴ and then converting these values into the refractive index at 1550 nm by use of an in-house Excel calculation spreadsheet which utilised Cauchy's equation⁴⁵; the Cauchy's equation predicts the refractive index of a material at a certain wavelength⁴⁶.

Chemical descriptors (8) through (12) were chosen as these begin to describe the functional groups present and the overall structure of the molecules and how this impacts on the steric bulk of the molecules and the intermolecular forces between the molecules. Descriptors (8) & (9) were calculated using the *Molinspiration* online chemical descriptor tool⁴⁷ Descriptors (10) & (11) were calculated and checked by hand. Descriptor (12) value were calculated using the following formula:

$$RDBE = C - \frac{H}{2} - \frac{X}{2} + N + 1$$

Eqn.7.4

where C , H , X , N are the number of carbon atoms, hydrogen atoms, halogen atoms and nitrogen atoms respectively in the molecule.

The descriptor values, for all the solvents, are given below in **Table.7.2**.

Chapter 7: Sensing of solvent vapours using a polysiloxane thin film as the active sensing element

SOLVENT	DESCRIPTOR											
	1	2	3	4	5	6	7	8	9	10	11	12
methanol	24.6	175.15	337.85	29.7	32.04	-0.74	1.3250	20.228	0	1	1	0
acetone	23.9	179.15	329.15	19.7	58.08	-0.24	1.3538	17.071	0	0	1	1
n-hexane	28.8	178.15	342.15	14.9	86.18	3.90	1.3682	0	3	0	0	0
isopropyl alcohol	26.6	183.65	355.15	23.7	60.10	0.05	1.3706	20.228	0	1	1	0
dichloromethane	27.0	176.15	313.05	20.3	84.93	1.25	1.4138	0	0	0	0	0
cyclohexane	22.8	278.65	353.85	16.8	84.16	3.44	1.4158	0	0	0	0	1
cyclohexene	25.9	169.65	356.15	17.5	82.14	2.86	1.4358	0	0	0	0	2
benzene	17.9	278.65	353.15	18.8	78.11	2.13	1.4865	0	0	0	0	4
carbon disulfide	27.4	161.65	319.15	20.4	76.14	1.94	1.5997	0	0	0	2	2
ethyl acetate	31.6	189.15	350.15	18.4	88.11	0.73	1.3658	26.305	2	0	2	1
chloroform	21.2	210.15	334.15	18.9	119.38	1.97	1.4358	0	0	0	0	0
tetrahydrofuran	26.5	165.15	339.15	19.0	72.11	0.46	1.3967	9.234	0	0	1	1
toluene	21.2	180.15	383.65	18.2	92.14	2.73	1.4829	0	0	0	0	4
oct-1-ene	22.6	172.15	395.65	15.5	112.24	4.57	1.3977	0	5	0	0	1
1,4-difluorobenzene	27.9	260.15	361.65	17.9	114.09	2.42	1.4308	0	0	0	0	4

Table.7.2: The values of the chemical descriptors for each of the solvents investigated. The chemical descriptors are as follows: (1) surface tension / dyne cm⁻¹, (2) freezing point / K, (3) boiling point / K, (4) Hildebrand solubility parameter / MPa^{1/2}, (5) molecular weight / gmol⁻¹, (6) log₁₀ K_{ow} / unitless, (7) refractive index at 1550 nm / unitless, (8) topographical polar surface area (TPSA) / unitless, (9) number of rotatable bonds / unitless, (10) number of hydrogen bond donor groups / unitless, (12) number of hydrogen bond acceptor groups / unitless & (13) ring double bond equivalents / unitless

Once all the descriptor values had been sourced from the literature, or calculated, the QSAR model building process began.

Chapter 7: Sensing of solvent vapours using a polysiloxane thin film as the active sensing element

Firstly, the order of the solvents listed in **Table.7.2** was randomized to ensure any unseen ordering of the data was removed. Then the coefficient of variance for each descriptor was determined by use of the following equation,

$$\text{coefficient of variance} = \frac{\text{Standard Deviation}}{\text{Average}}$$

Eqn.7.5

The coefficient of variance is a measure of the spread in the data. If the coefficient of variance tends towards zero, then this indicates that there is little or no spread in the data set. Therefore that data set is not suitable to be included in the regression model. The absolute magnitudes of the coefficients of variation for the descriptors are given below in **Table.7.3**.

Descriptor	Absolute magnitude of the coefficient of variation (to 3.s.f)
Surface tension (1)	0.165
Freezing point (2)	0.207
Boiling point (3)	0.0629
Hildebrand solubility parameter (4)	0.184
Molecular weight (5)	0.276
$\log_{10} K_{ow}$ (6)	0.854
Refractive index (7)	0.0476
Number of rotatable bonds (8)	2.24
Number of hydrogen bond donor groups (9)	2.64
Number of hydrogen bond acceptor groups (10)	1.39
Ring double bond equivalents (11)	1.07

Table.7.3: The coefficients of variation for each of the descriptors were compared and it was determined that the two lowest values of coefficient of variation were for ‘Boiling point’ and ‘Refractive index’ (highlighted in red).

The two descriptors, ‘Boiling point’ and ‘Refractive index’ had the smallest magnitude absolute coefficient of variation values. Therefore these two descriptors were removed from this QSAR model.

Chapter 7: Sensing of solvent vapours using a polysiloxane thin film as the active sensing element

The values of the remaining descriptors were then scaled using the unit variance scaling method. This method involved dividing every value of a descriptor by the standard deviation for that chemical descriptor. This ensured that any descriptor with larger magnitude values did not dominate the regression model.

Pairwise correlations between the chemical descriptors were then checked by creating a correlation matrix. The resulting correlation matrix and the key to the terms is shown below in **Fig.15**.

	A	B	C	D	E	F	G	H	I	J
A		0.175	0.027	0.155	-0.062	-0.374	-0.584	-0.365	0.114	0.559
B	0.175		-0.211	0.278	0.248	-0.277	-0.232	-0.177	-0.407	0.445
C	0.027	-0.211		-0.742	-0.794	0.577	-0.457	0.842	0.410	-0.277
D	0.155	0.278	-0.742		0.702	-0.604	0.356	-0.655	-0.468	0.278
E	-0.062	0.248	-0.794	0.702		-0.780	0.541	-0.565	-0.601	0.280
F	-0.374	-0.277	0.577	-0.604	-0.780		-0.047	0.589	0.693	-0.382
G	-0.584	-0.232	-0.457	0.356	0.541	-0.047		-0.181	-0.086	-0.222
H	-0.365	-0.177	0.842	-0.655	-0.565	0.589	-0.181		0.255	-0.378
I	0.114	-0.407	0.410	-0.468	-0.601	0.693	-0.086	0.255		-0.205
J	0.559	0.445	-0.277	0.278	0.280	-0.382	-0.222	-0.378	-0.205	

Fig.7.15: The correlation matrix for the remaining ten chemical descriptors. The correlations range from -1 to 1 including 0, where -1 = perfect anti - correlation between two descriptors, 0 = no correlation between two descriptors and 1 = perfect correlation between the two descriptors. The black squares represent the correlations between a descriptor and itself, which = 1.00 by definition.

Due to symmetry, the two halves of the correlation matrix, about the line of black squares, are identical. The red squares represent the cases where there is very significant anti - correlation or correlation ($|0.70| < \text{absolute magnitude of correlation coefficient}$). The chemical descriptors are as follows: (A) surface tension / dyne cm^{-1} , (B) freezing point / K, (C) Hildebrand solubility parameter / $\text{MPa}^{1/2}$, (D) molecular weight / gmol^{-1} , (E) $\log_{10} K_{ow}$ / unitless, (F) topographical polar surface area (TPSA) / unitless, (G) number of rotatable bonds / unitless, (H) number of hydrogen bond donor groups / unitless, (I) number of hydrogen bond acceptor groups / unitless & (J) ring double bond equivalents / unitless.

From visual inspection of the correlation matrix, it was decided that the most pairwise correlated descriptors were the Hildebrand solubility parameter, molecular weight, $\log_{10} K_{ow}$ and number of hydrogen bond donor groups. These descriptors were removed from the QSAR model building process. The most pairwise correlated descriptors were removed because very significant correlation or anti - correlation

Chapter 7: Sensing of solvent vapours using a polysiloxane thin film as the active sensing element

between descriptors can influence the statistics that describe the regression models. Six chemical descriptors then remained in the QSAR model building process.

The QSAR model was derived by multiple successive multiple linear regressions of the data. At first all six remaining chemical descriptors were included and a multiple linear regression was performed. The p – value (which is linked to the t – statistic) was visually inspected for each descriptor; the largest p – value suggests that descriptor is the least significant for that regression model. The chemical descriptor which had the largest magnitude p – value was removed from future multiple linear regressions. Then a multiple linear regression was performed with the remaining five descriptors, the p – values were visually inspected and the chemical descriptor with the largest magnitude p –value was removed so four chemical descriptors were left. This process, known as backward step regression model building⁴⁸, was continued until only three chemical descriptors remained, all of which had p – values that were 10^{-3} in magnitude; the smaller the magnitude of the p-value, the more significant the descriptor is for the regression model. The derived regression model equation, using the backwards step regression approach, is given below:

$$Y = (1.661 \times \text{Surface Tension}) - (1.392 \text{TPSA}) + (1.604 \times \text{RDBE}) - 12.285$$

Eqn.7.6

Where Y is the predicted cube root of the Bragg wavelength shift, *Surface Tension* is the surface tension value for a particular solvent, *TPSA* is the value of the scalar quantity topographical polar surface area of the solvent and *RDBE* is the value of ring and double equivalents for the solvent. It should be noted that the predicted Y values are scalar. The unit variance scaling step results in the scaled descriptor values becoming unitless because each value is divided by the standard deviation of that descriptor; the standard deviation has the same units as each individual descriptor value and by unit calculus the units cancel out.

The predicted Y values, for each solvent, were calculated using **Eqn.7.6** above. The cube rooted values of the average referenced Bragg wavelength shift values were plotted against the predicted Y values, as shown in **Fig.7.16** below.

Chapter 7: Sensing of solvent vapours using a polysiloxane thin film as the active sensing element

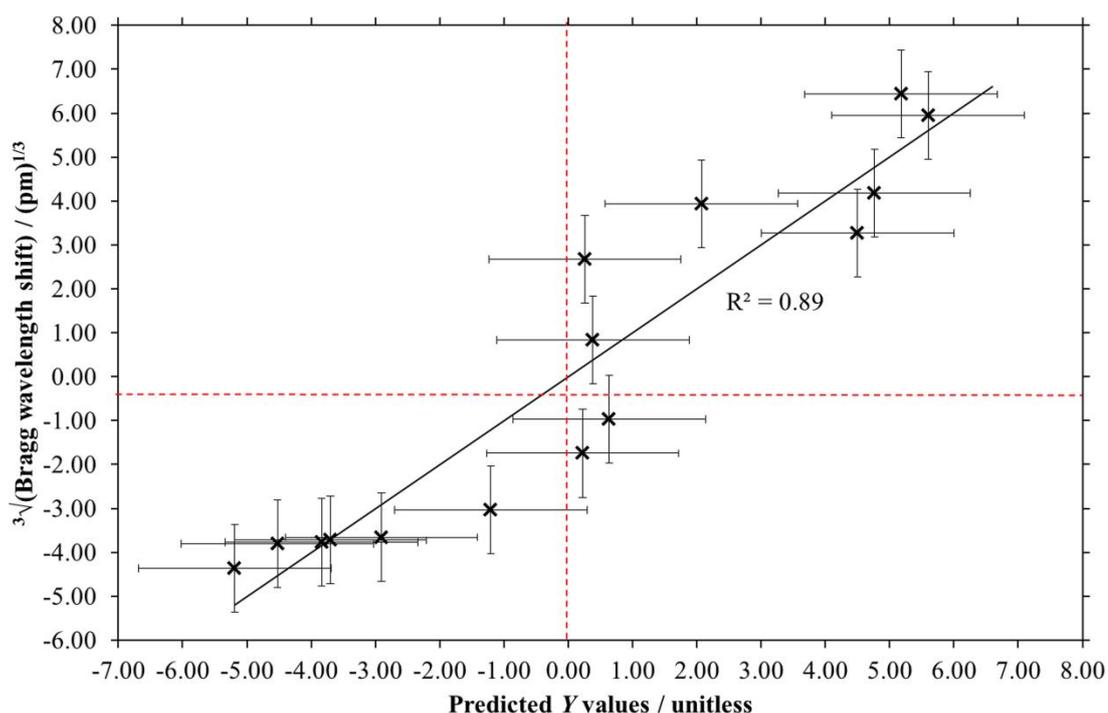


Fig.7.16: The resulting linear trend from the QSAR regression model. $R^2 = 0.89$. The predicted Y values, for each solvent, were calculated using **Eqn.6** above and plotted against the corresponding experiment average referenced Bragg wavelength shift. The red dashed lines represent the position of zero on both axes. The vertical error bars represent the cube rooted value of the associated errors in the Bragg wavelength shift values and the horizontal error bars represent the standard error, calculated from the regression model, of the predicted Y values.

The overall linear behaviour of the model allows for a particular Bragg wavelength shift value to correspond to a single solvent, rather than the two solvents as would result from the curves plotted in **Fig.7.12** and **Fig.7.13** above. In addition, the model allows for the prediction of the resulting average referenced Bragg wavelength shift value upon exposure of the BGD to the vapours of a solvent not tested in these experiments. The linear model reasonably fits the data and explains the change in the cube root of the average referenced Bragg wavelength shift upon exposure of the BGD to vapours of different solvents; the model is reasonably robust. This is corroborated by the magnitude of the R^2 value from the regression model, $R^2 = 0.89$; this linear regression model describes 89% of the variation in the cube rooted average referenced Bragg wavelength shift values. Furthermore, the predictive power of the model was determined by calculation of the Q^2 value, which can take a value between 0 and 1. A Q^2 value of zero shows no predictive ability in the model whereas a value of one shows perfect predictive ability. The Q^2 value was calculated as per **Eqn.7.7** below,

$$Q^2 = \frac{(SD - PRESS)}{SD}$$

Eqn.7.7

where SD is the squared deviation of the observed experimental values and is given by ⁴⁹:

$$SD = \sum_{i=1}^n (y_i - y)^2$$

Eqn.7.8

where y_i are the experimentally observed values (the average reference Bragg wavelength shift values) and y is the average of the experimental observed values.

$PRESS$ is defined as:

$$PRESS = \sum_{i=1}^n (y_i - \hat{y}_i)^2$$

Eqn.7.9

where again, y_i are the experimentally observed values (the average reference Bragg wavelength shift values) and \hat{y}_i are the predicted cube rooted Bragg wavelength shift values.

Performing this calculation yielded a Q^2 value for this particular linear regression model = 0.89; the model can robustly predict the cube rooted average referenced Bragg wavelength shift 89% of the time.

To further test the robustness of the regression model, the similarity of the solvents, in terms of the values of *Surface Tension*, *TPSA* and *RDBE* for each solvent in this 3D descriptor space, was measured. The similarity of the set of solvents was 0.06; there was only 6% similarity between the solvents. This result is important as it

shows the linear regression model was built on a diverse set of molecules and thus is widely applicable and robust.

7.4 Conclusions and Further Work

It has been demonstrated that a planar integrated Bragg grating sensor chip, fabricated using the direct UV-writing approach, can be modified with a siloxane polymer, which was a derivative of poly(hydromethyl)siloxane (PHMS). The derivative polymer was successfully synthesised by using a hydrosilylation reaction approach to functionalise the PHMS backbone with *n*-octyl functional groups, confirmed by NMR and FTIR spectroscopy. The resulting polymer was poly(hydromethyl) – *co* – poly(methyloctyl)siloxane (**8**) which contained a 15% mole percentage of the poly(methyloctyl) monomer, as calculated by copolymer NMR analysis. The original aim was to completely replace all of the silicon hydride functional groups with *n*-octyl groups, i.e. 100% mole percentage of the poly(methyloctyl) monomer; the result would have been a relatively hydrophobic polymer which would favour interaction with hydrophobic hydrocarbon solvent vapours. The incomplete conversion, within the timeframes investigated in this work, was attributed to the poor solubility of the catalyst in the reaction solvent and conducting the reaction at atmospheric pressure instead of in a sealed reaction vessel. It is proposed that to achieve 100% conversion, in a reasonable timeframe i.e. an overnight reaction or 24 h, another catalyst, which is more soluble in the reaction solvent (toluene), should be used. Despite incomplete conversion, the resulting copolymer (**8**) was deemed suitable for solvent vapour sensing as it contained both PHMS and PMOS monomer units; the differing hydrophobicities of the monomer units will favour interaction with different solvents and thus increase the range of solvents that can be sensed.

Upon exposure to nitrogen gas saturated with the vapours of different solvents, both negative and positive Bragg wavelength shifts of differing magnitudes were measured with the BGD modified with a thin film of (**8**). Upon investigation into the sensing mechanism it was revealed that the magnitude and the sign of the Bragg wavelength shift was due to the solubility of (**8**) in the solvent vapours; this was quantified through the use of $\log_{10} K_{ow}$ and Hildebrand solubility parameters values.

Chapter 7: Sensing of solvent vapours using a polysiloxane thin film as the active sensing element

A QSAR approach was utilised to create a multiple variable linear regression model, built from parameters that chemically described the solvents. The resulting linear regression model further confirmed that the solubility of the thin film of **(8)** in the different solvents was due to the properties of the solvent and was the main cause of the Bragg wavelength shifts of differing magnitude. Furthermore, the linear regression model equation allows for prediction of the Bragg wavelength shifts that would be measured with this iteration of the sensor device for any given solvent which has known values of surface tension, topographical polar surface area and ring double bond equivalents. The values for these properties are easily accessible; surface tensions of many common solvents are readily available in the literature and the TPSA & RDBE values are easily calculated using common and easy to use chemical software (and available online for free in the case of *molinspiration*⁴⁷).

The study of the interaction of solvent vapour with thin films is important for applications such as photolithography and membrane fabrication/science⁵⁰. Despite the slow response time of this current iteration of a planar Bragg grating organic solvent vapour sensor compared to state-of-the-art sensors in the literature, the facile fabrication techniques and associated advantages of the planar integrated optical format (as highlighted in **Chapter 3**) makes this sensor device modified with a thin film of **(8)** a viable organic vapour sensor that offers advantages over the current electrical devices in a range of domestic, commercial and industrial settings⁵¹. However, it should be briefly stated that the particular ‘state-of-the-art’ work from the literature cited above dealt with polymer thin films of only 6-8 nm thick, an order of 10^3 thinner than the thin film presented in this chapter; it would be expected that the literature sensor would have a much faster response time.

When the above advantages are combined with the previously reported methods for monitoring temperature¹⁴, pressure⁵², and chemo/bio-detection⁵³ the suitability of integrated optical Bragg grating devices for highly multiplexed volatile organic compound sensor devices within distributed networks becomes apparent.

Chapter 7: Sensing of solvent vapours using a polysiloxane thin film as the active sensing element

1. J. C. McDonald, D. C. Duffy, J. R. Anderson, D. T. Chiu, H. Wu, O. J. Schueller, and G. M. Whitesides, *Electrophoresis*, 2000, **21**, 27–40.
2. J. N. Lee, C. Park, and G. M. Whitesides, *Anal. Chem.*, 2003, **75**, 6544–54.
3. K. L. Plett, PhD Thesis, Queen's University, 2008.
4. B. Marciniak, J. Gulinski, L. Kopylova, H. Maciejewski, M. Grundwald-Wypianska, and M. Lewandowski, *Appl. Organomet. Chem.*, 1997, **11**, 843–849.
5. B. Marciniak, H. Maciejewski, C. Pietraszuk, and P. Pawluc, *Hydrosilylation: A Comprehensive Review on Recent Advances*, Springer, 2009.
6. S. Guizzetti, M. Benaglia, and J. S. Siegel, *Chem. Commun. (Camb.)*, 2012, **48**, 3188–3190.
7. I. A. Leenson, *J. Chem. Educ.*, 2005, **82**, 241–245.
8. B. M. Khadilkar and V. R. Madyar, *Synth. Commun.*, 1999, **29**, 1195–1200.
9. S. Guizzetti, M. Benaglia, and J. S. Siegel, *Chem. Commun.*, 2012, **48**, 3188–3190.
10. J. H. Koschwanetz, R. H. Carlson, and D. R. Meldrum, *PLoS One*, 2009, **4**, e4572.
11. S. Wood, *MICROmanufacturing*, 2009, 19–21,47.
12. Sigma-Aldrich, 2013.
13. L. I. B. Silva, T. A. P. Rocha-Santos, and A. C. Duarte, *Glob. NEST J.*, 2008, **10**, 217–225.
14. R. M. Parker, J. C. Gates, M. C. Gossel, and P. G. R. Smith, *Sensors Actuators B Chem.*, 2010, **145**, 428–432.
15. P. Patnaik, *A Comprehensive Guide to the Hazardous Properties of Chemical Substances*, John Wiley & Sons, 2007.
16. ASTM International, *American National Standard: D 323 - 99a Standard Test Method for Vapor Pressure of Petroleum Products (Reid Method)*, 1999.
17. M. Polyanskiy, *RefractiveIndex.INFO*, 2013.
18. J. L. Martínez-Hurtado, C. A. B. Davidson, J. Blyth, and C. R. Lowe, *Langmuir*, 2010, **26**, 15694–15699.
19. V. L. Cunningham, in *Pharmaceuticals in the Environment: Sources, Fate, Effects and Risks*, ed. K. Kümmerer, Springer, 2004, p. 19.

Chapter 7: Sensing of solvent vapours using a polysiloxane thin film as the active sensing element

20. J. Sangster, *LOGKOW - Sangster Res. Lab.*, 2013.
21. J. D. Wang, N. J. Douville, S. Takayama, and M. ElSayed, *Ann. Biomed. Eng.*, 2012, **40**, 1862–73.
22. B. A. Miller-Chou and J. L. Koenig, *Prog. Polym. Sci.*, 2003, **28**, 1223–1270.
23. J.-L. M. Abboud and R. Notario, *Pure Appl. Chem.*, 1999, **71**, 645–718.
24. V. Svoboda, V. Charvátová, V. Majer, and V. Hynek, *Collect. Czechoslov. Chem. Commun.*, 1982, **47**, 543–549.
25. G. Liesmann and W. Schmidt, in *Data Compilation of the Saechsische Olefinwerke Boehlen Germany*, 1995.
26. J. Burke, in *The Book and Paper Group ANNUAL: Volume Three*, CoOL, 1984.
27. S. M. Vaezi-Nejad, Ed., *Selected Topics in Advanced Solid State and Fibre Optic Sensors*, IET, 2000.
28. A. B. Sannigrahi and A. K. Chandra, *Bull. Chem. Soc. Jpn.*, 1967, **40**, 1344–1349.
29. P. C. Singh, M. Ray, and G. N. Patwari, *J. Phys. Chem. A*, 2007, **111**, 2772–2777.
30. A. Villares, B. Giner, H. Artigas, C. Lafuente, and F. M. Royo, *J. Solution Chem.*, 2005, **34**, 185–198.
31. C. Bermudez-Salguero, A. Amigo, and J. Gracia-Fadrique, *J. Chem. Eng. Data*, 2010, **55**, 2905–2908.
32. J. E. Shewmaker, C. E. Vogler, and E. Roger Washburn, *J. Phys. Chem.*, 1954, **58**, 945–947.
33. J. Koefoed and J. V. Villadsen, *Acta Chem. Scand.*, 1958, **12**, 1124–1126.
34. H. M. Trimble, *J. Phys. Chem.*, 1928, **32**, 1211.
35. W. F. Seyer and E. G. King, *J. Am. Chem. Soc.*, 1933, **55**, 3140–3144.
36. E. Jimenez, H. Casas, L. Segade, and C. Franjo, *J. Chem. Eng. Data*, 2000, **45**, 862–866.
37. I. L. Acevedo, G. C. Pedrosa, and M. Katz, *J. Solution Chem.*, 1990, **9**, 911–921.
38. J. Aracil, G. Luengo, B. S. Almeida, M. M. T. da Gama, R. G. Rubio, and M. D. Pena, *J. Phys. Chem.*, 1989, **93**, 3210–3218.

Chapter 7: Sensing of solvent vapours using a polysiloxane thin film as the active sensing element

39. J. L. Zurita, M. L. G. de Soria, M. A. Postigo, and M. Katz, *J. Solution Chem.*, 1987, **16**, 163–170.
40. R. S. Myers, B. A. Berenbach, and H. L. Clever, *J. Chem. Eng. Data*, 1969, **14**, 91.
41. A. Ahosseini, B. Sensenich, L. R. Weatherley, and A. M. Scurto, *J. Chem. Eng. Data*, 2010, **55**, 1611–1617.
42. M. Hadded, A. Mayaffre, and P. Letellier, *J. Chim. Phys. Physico-Chimie Biol.*, 1989, **86**, 525–538.
43. L. F. Transue, E. Roger Washburn, and F. H. Kahler, *J. Am. Chem. Soc.*, 1942, **64**, 274.
44. Sigma-Aldrich, 2013.
45. J. C. Gates, University of Southampton.
46. R. E. Sah, J. Zhang, J. M. Deen, J. Yota, and A. Toriumi, *ECS Trans.*, 2009, **19**, 467–477.
47. Molinspiration Cheminformatics, 2013.
48. A. R. Leach and V. J. Gillet, *An Introduction to Chemoinformatics*, Kluwer Academic Publishers, Dordrecht, 2003.
49. R. Carbo-Dorca, R. Carbo, D. Robert, L. Amat, X. Girones, and E. Besalu, *Molecular Quantum Similarity in QSAR and Drug Design*, Springer UK, 2000.
50. G. J. Price and J. M. Buley, *Progress Org. Coatings*, 1991, **19**, 265–274.
51. İ. Çapan, Ç. Tarımcı, M. Erdoğan, and A. K. Hassan, *Mater. Sci. Eng. C*, 2009, **29**, 1114–1117.
52. C. Holmes, L. G. Carpenter, J. C. Gates, and P. G. R. Smith, *J. Micromechanics Microengineering*, 2012, **22**, 025017.
53. R. M. Parker, J. C. Gates, D. J. Wales, P. G. R. Smith, and M. C. Grossel, *Lab Chip*, 2013, **13**, 377–85.

8 Utilising the relation between n and κ to achieve refractometric sensing

8.1 Introduction

In **Appendix 1**, the relationship between a colour change in a material and the associated refractive index change in that material is described using the relation between the refractive index, n , and the absorption coefficient, κ . In addition, the proposal of refractometric gas sensing by indirect measurement of the associated refractive index change upon a change of colour in material is also proposed. Within this chapter, the development of a planar integrated optical Bragg grating refractometric gas sensor, which utilised the concept of a measureable refractive index change upon a colour change, is described. The sensor was fabricated by spin deposition of a thin film of a mesoporous silica sol-gel and subsequent doping of the thin film with an organic pH chromic dye. The Bragg wavelength shift response of this sensor chip, at 1550 nm and 780 nm, when exposed to ammonia or hydrogen chloride fumes, was investigated.

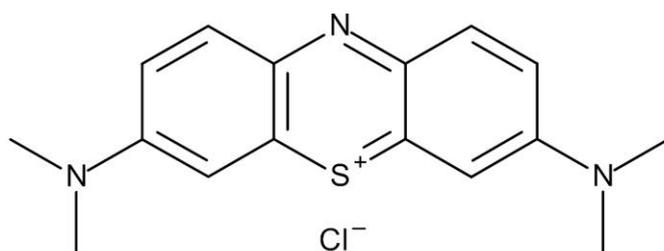
Note: The file name of the associated spectra and/or characterisation data is given in the text at appropriate points. The file names given refer to the file names of the spectra/data that are located on the attached spectra CD. The file names are in italic font.

8.2 Fabrication of a pH chromic thin film

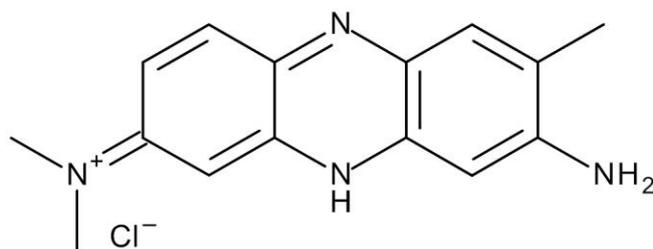
To achieve the aims set out in **Appendix 1**, a suitable pH chromic dye, that changes colour in pH conditions that are compatible with the thin film, was required. Therefore, as a mesoporous silica thin film was to be used as the thin film matrix, the chosen dye had to possess a colour change at pH values below pH $\sim 9 - 10$; higher pH values lead to the basic hydrolysis and degradation of silica. After interrogation

of the pH indicator literature, the most suitable dye, in terms of pH range and colour changes, was neutral red.

Neutral red (N8,N8,3-trimethylphenazine-2,8-diamine) is a phenazine based organic dye that is used for histochemical staining. It is also used as a pH indicator; the dye can be one of three colours depending on the pH. At $\text{pH} < 2$, neutral red is an intense blue colour, between $\text{pH} \sim 2$ and $\text{pH} 8.6$ it is pink/red (hence the trivial name) and at $\text{pH} > 8.6$ it is yellow. Therefore, neutral red satisfies the requirement of colour changes occurring below pH values $\sim 9 - 10$. In addition, the phenazine structure of neutral red is structurally similar to methylene blue (a phenothiazine based organic dye) (**Fig.8.1** below), which had already been successfully loaded into a mesoporous silica thin film (see **Chapter 6**). Therefore, this favoured successful loading of neutral red into the mesoporous silica thin film.



N3,N3,N7,N7-tetramethylphenothiazin-5-ium-3,7-diamine chloride
(methylene blue chloride)



(8-amino-7-methyl-10H-phenazin-2-ylidene)-dimethyl-ammonium chloride
(neutral red chloride)

Fig.8.1: The similar chemical structures of neutral red chloride salt (bottom) and methylene blue chloride salt (top) and the respective IUPAC names.

Neutral red chloride was loaded into the mesoporous silica sol-gel thin film using the procedure given in **Chapter 10**. Loading was confirmed by the presence of absorption features typical to neutral red in the transmission UV-Vis spectrum. The UV-Vis transmission spectrum was collected after excess physisorbed neutral red had been removed by rinsing with de-ionised water. It had been confirmed that neutral red doped mesoporous silica (**9**) had been successfully fabricated.

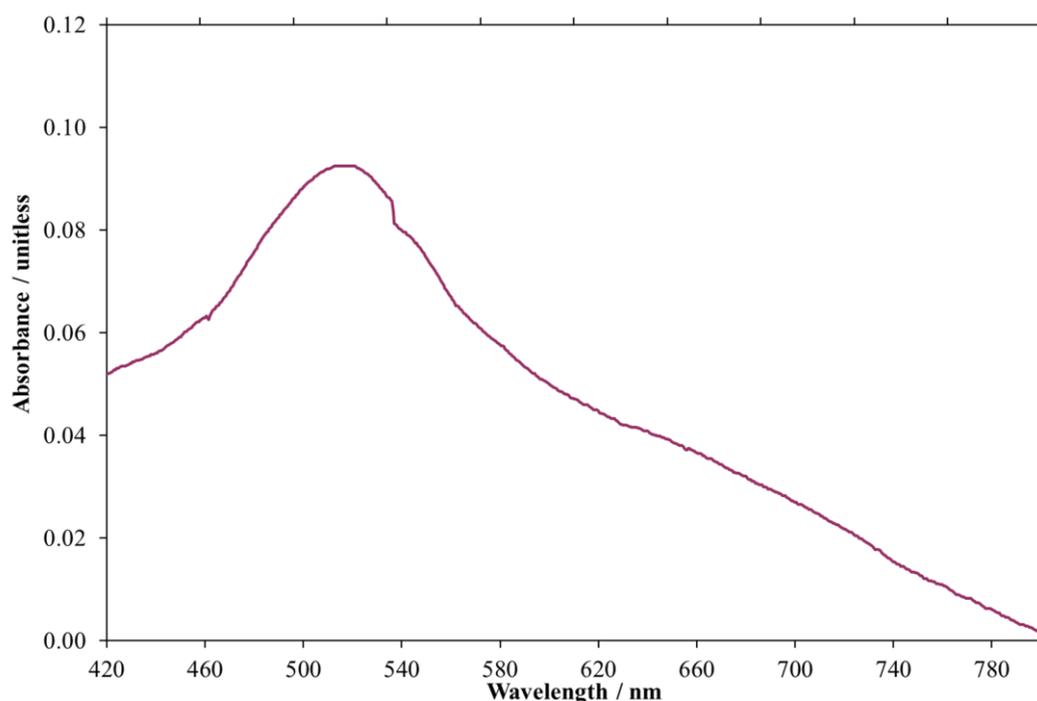


Fig.8.2: Visible absorption spectrum of encapsulated neutral red chloride in a mesoporous silica sol-gel thin film. The value of $\lambda_{\text{max}} \sim 520$ nm for encapsulated neutral red in air is in agreement with the solution phase $\lambda_{\text{max}} \approx 520$ nm for neutral red in pH = 7.0 aqueous solution. Note: The discontinuity at ~ 540 nm was a systematic spectrometer artefact.

8.3 Investigation into the pH chromic behaviour of (**9**)

8.3.1 Visible spectroscopy study

After encapsulation of neutral red in a mesoporous silica sol-gel to form (**9**) had been successfully demonstrated, the ability of encapsulated neutral red to exhibit pH chromic behaviour was investigated. To facilitate pH chromic behaviour the sample of (**9**) was exposed to an acidic gas (hydrogen chloride fumes), a basic gas (ammonia fumes) and neutral air.

In air the sample of (9) was pink. Upon exposure to ammonia fumes (9) reversibly changed colour from pink to yellow. Upon exposure to hydrogen chloride fumes (9) reversibly changed colour pink to blue respectively. The colour changes are shown in the photographs in **Fig.8.3** below. The time taken to change colour, by eye, was in the order of 1-2 secs.

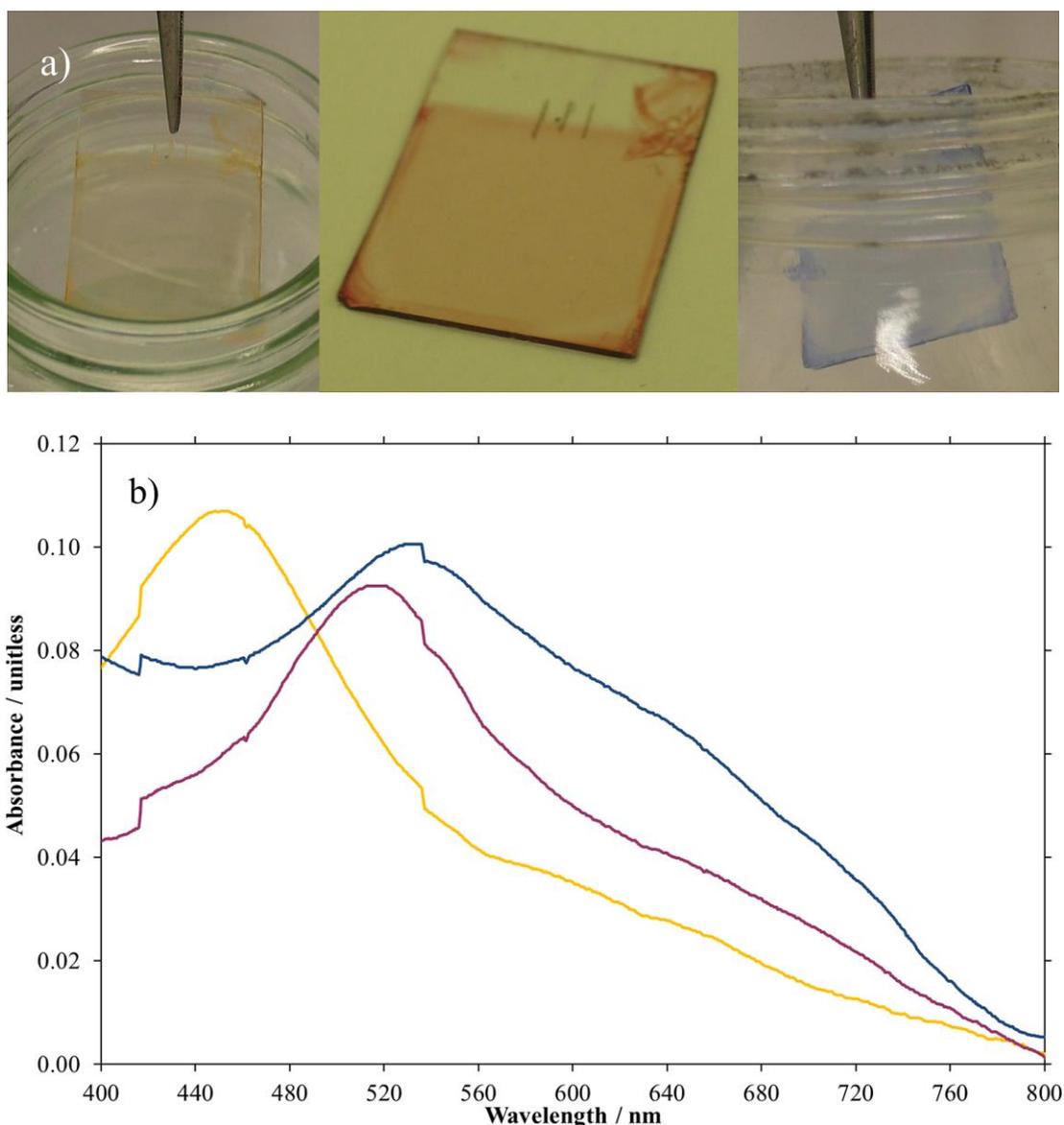


Fig.8.4: (a) The pH chromic behaviour of neutral red encapsulated in a mesoporous silica sol-gel thin film. (Left) Yellow when (9) was exposed to ammonia fumes, (middle) pink when (9) was in ambient lab air and (right) blue when (9) was exposed to hydrogen chloride fumes. (b) Visible spectra of encapsulated neutral red chloride in the three different colour states: yellow when exposed to ammonia fumes (yellow spectrum), pink when exposed to neutral air (pink spectrum) and blue when exposed to hydrogen chloride fumes (blue spectrum). **Note:** The discontinuities at ~ 415 & ~ 540 nm were systematic spectrometer artefacts. Data collected in partnership with Mr James Field, a Nuffield summer project student.

The repeatability and reproducibility of these colour changes was then investigated by collection of transmission UV-visible spectra during exposure to a cycle of lab air (neutral), hydrochloric acid vapour, lab air, ammonia vapour, and then the cycle

repeated. The thin film was exposed to/purged with air for at least 3 minutes to avoid reaction of the hydrogen chloride and ammonia gases to form ammonium chloride salt on the thin film, which could have potentially blocked the pores of the thin film. For each step in the exposure cycle, the colour changes were confirmed by eye before the spectrum was collected. The wavelength at which maximum absorbance was measured was determined for each individual exposure step and these values are plotted below in **Fig.8.5**.

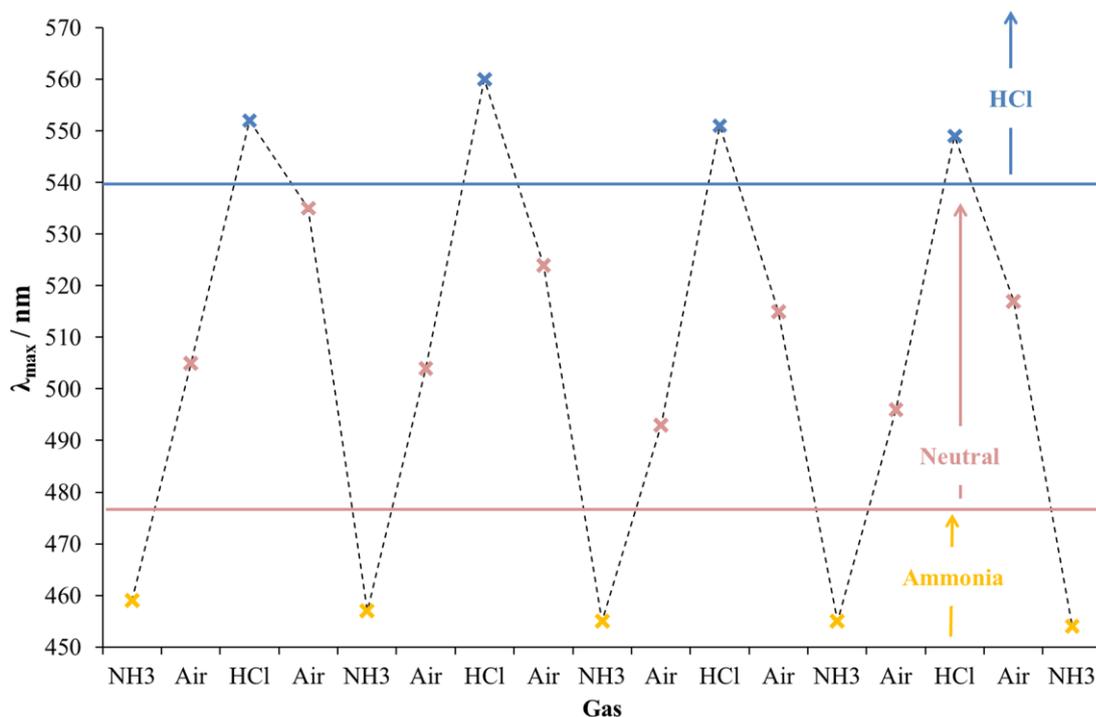


Fig.8.5: The repeatability and reproducibility of the colour changing process upon exposure of (9) to different gases as labelled on the plot, where ‘Neutral’ is ambient lab air and ‘HCl’ is hydrogen chloride. (X) = (9) in a yellow state, (X) = (9) in a pink state and (X) = (9) in a blue state. Data collected in partnership with Mr James Field, a Nuffield summer project student.

The thin film of (9) demonstrated good repeatability and reproducibility, in terms of pH chromism. Thus a thin film of (9) was proposed as a suitable and reusable active sensor element for a pH responsive Bragg grating sensor.

8.3.2 Refractometric sensing at 1550 nm

8.3.2.1: ‘Moist’ ammonia fume sensing

A thin film of (9), ~90 nm thick (measured with surface profilometry), was deposited on the surface of a Bragg grating sensor chip as per the procedure given in **Chapter**

10. The sol-gel thin film was deposited in such a manner that some Bragg gratings were left uncovered to act as temperature and strain reference gratings.

In initial gas sensing experiments, the chosen analyte gas was ammonia. Ammonia is a biologically important gas; the quantity of ammonia in exhaled breath can be used to give a measure of the progression of kidney disease¹. Before such low concentrations of ammonia (such as the concentration in exhaled breath) could be tested, initial ammonia sensing experiments were performed whereupon the Bragg grating sensor device was exposed to the headspace above a volume of 38% v/v aqueous ammonia solution for various durations, whilst interrogated at 1550 nm and visually observed for any colour changes.

When exposed to ammonia fumes the thin film rapidly changed (~ 1 s) colour from pink to and yellow, and vice versa when removed to ambient air. In addition, Bragg wavelength shifts of ~10 pm were measured, upon exposure to ammonia, with the thin film covered Bragg gratings. Upon removal to ambient air, the Bragg wavelength values, measured with the thin film covered gratings, returned to a pre-exposure baseline value. However, Bragg wavelength shifts of ~30 pm were measured, upon exposure to ammonia, with the uncovered reference Bragg gratings. In addition, the Bragg wavelengths of the uncovered Bragg gratings also returned to baseline values upon removal to ambient air. It was proposed that the Bragg wavelength shifts measured with the uncovered Bragg gratings were caused by adsorption of water vapour and changes in temperature. Therefore, it could not be determined whether or not the Bragg wavelength shifts measured with the thin film covered Bragg grating were due to adsorption and ingress of water into the thin film or due to the observed colour changes. Bragg wavelength shifts related to the colour change may have occurred, but were masked by the Bragg wavelength shifts caused by water adsorption.

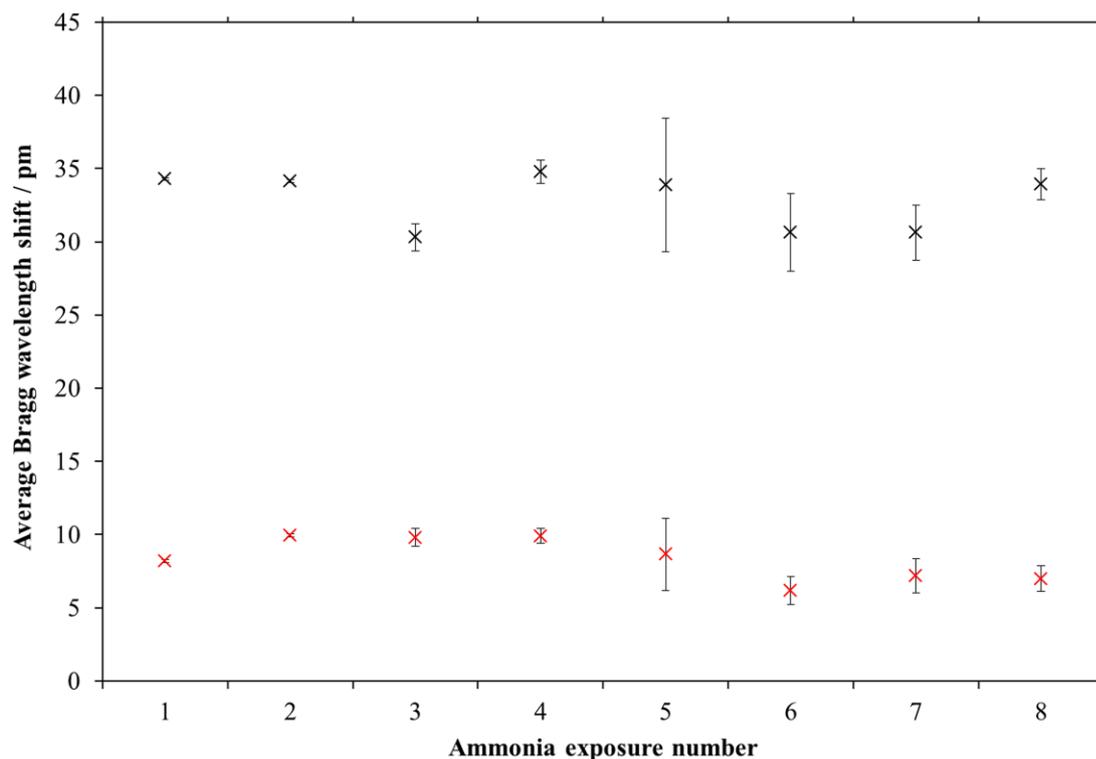


Fig.8.6: Average Bragg wavelength shifts for the uncovered (×) and thin film covered (×) Bragg gratings during exposure to ammonia fumes above 38 %v/v ammonia solution. The error bars represent the associated errors.

8.3.2.2: ‘Dry’ ammonia fume sensing

To remove the effect of water vapour and minimise the effect of temperature, the experimental set-up was changed so that the device, modified with a thin film of (9), was exposed to cycles of either dry nitrogen or dry ammonia gas in nitrogen carrier gas. The dry nitrogen carrier gas was heated to ~ 25 °C and had a moisture content of 0.0 %RH, as measured with a commercial in-line hygrometer. The dry mixture of ammonia gas in nitrogen carrier gas was achieved by firstly passing the dry nitrogen gas over 38% w/v aqueous ammonia solution to form a ‘wet’ gas mixture and then passing this ‘wet’ mixture through a 30 cm long column of sodium hydroxide pellets to dry the ammonia in nitrogen gas mixture (relative humidity < 0.5 %RH, ~ 25 °C).

Using this experimental set-up, no Bragg wavelength shifts greater in magnitude than the ± 3 pm noise were measured upon exposure to the mixture of ammonia gas in nitrogen gas or pure dry nitrogen despite colour changes of pink to yellow and vice versa occurring. The data is shown in **Fig.8.7** below.

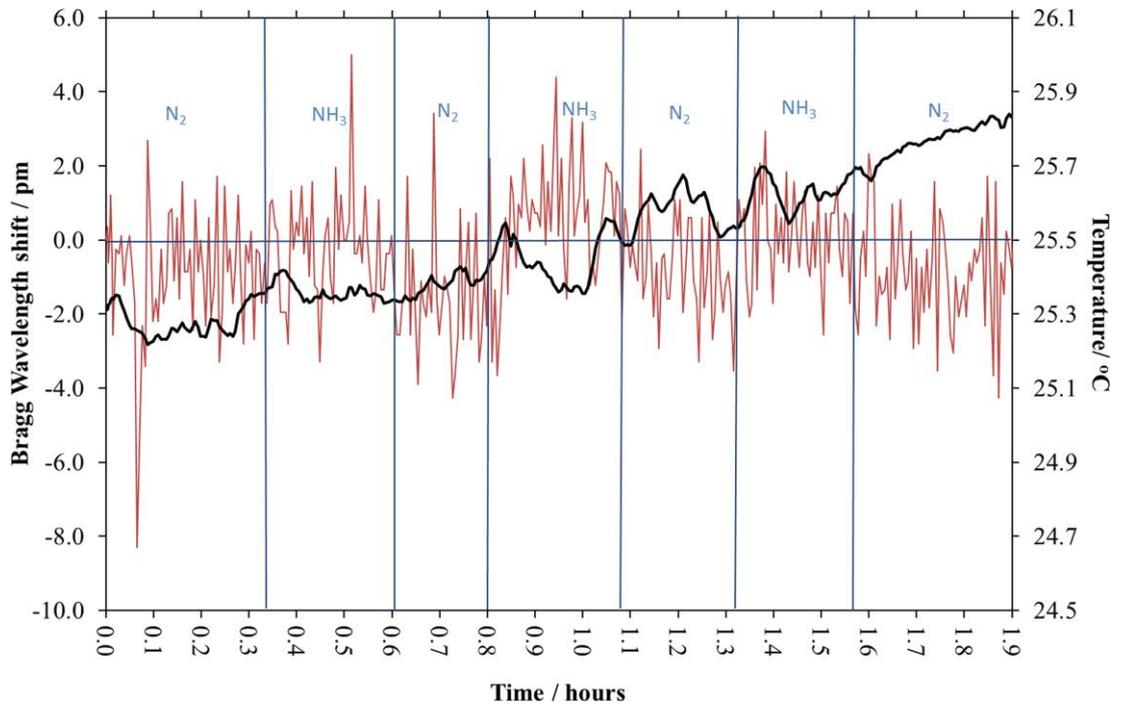


Fig.8.7: No Bragg wavelength step shifts were measured with a thin film covered Bragg grating (red line) when exposed to cycles of dry ammonia gas and dry nitrogen (demarcated with the vertical blue lines). The corresponding changes in temperature are given by the black line (scaled to 1 °C = 10 pm). The horizontal blue line represents 0 pm Bragg wavelength shift.

From this result it was deduced that the Bragg wavelength shifts measured with the thin film covered and uncovered Bragg gratings in the previous dunk experiments were due to water adsorption/desorption and temperature changes. In addition, this result led to the hypothesis that the observed visible colour changes (absorption changes) from pink ($\lambda_{\text{max}} = 516 \text{ nm}$) to yellow ($\lambda_{\text{max}} = 452 \text{ nm}$) and vice versa, do not result in a measurable refractive index change at 1550 nm which can be measured with this iteration of planar integrated Bragg grating devices. Furthermore, it was proposed that the absorption changes in the 450 – 550 nm region did not affect a change in refractive index at the interrogation wavelength 1550 nm. By interrogating the Bragg gratings at a wavelength closer to the absorption changes would ensure any resulting refractive index changes could be measured at the new interrogation wavelength.

8.4 Mathematical modelling of refractive indices

8.4.1 Fitting of Lorentzian functions to absorbance features

To validate this hypothesis, modelling of the associated refractive index profile of the thin film of (9) in each of the three different colour states was performed with Dr. Chris Holmes. Firstly, the attenuation coefficients (in units of m^{-1}) at different wavelengths between 300 nm and 800 nm were calculated for each of the colour states. This was achieved by dividing the absorbance values from the UV-Visible spectrum data for each colour state (recorded at 0.5 nm increments) by the thickness of the thin film of (9) in m, measured by step profilometry; this assumes the thin films are solid. The resulting values were the attenuation coefficients, in m^{-1} , at each 0.5 nm wavelength increment.

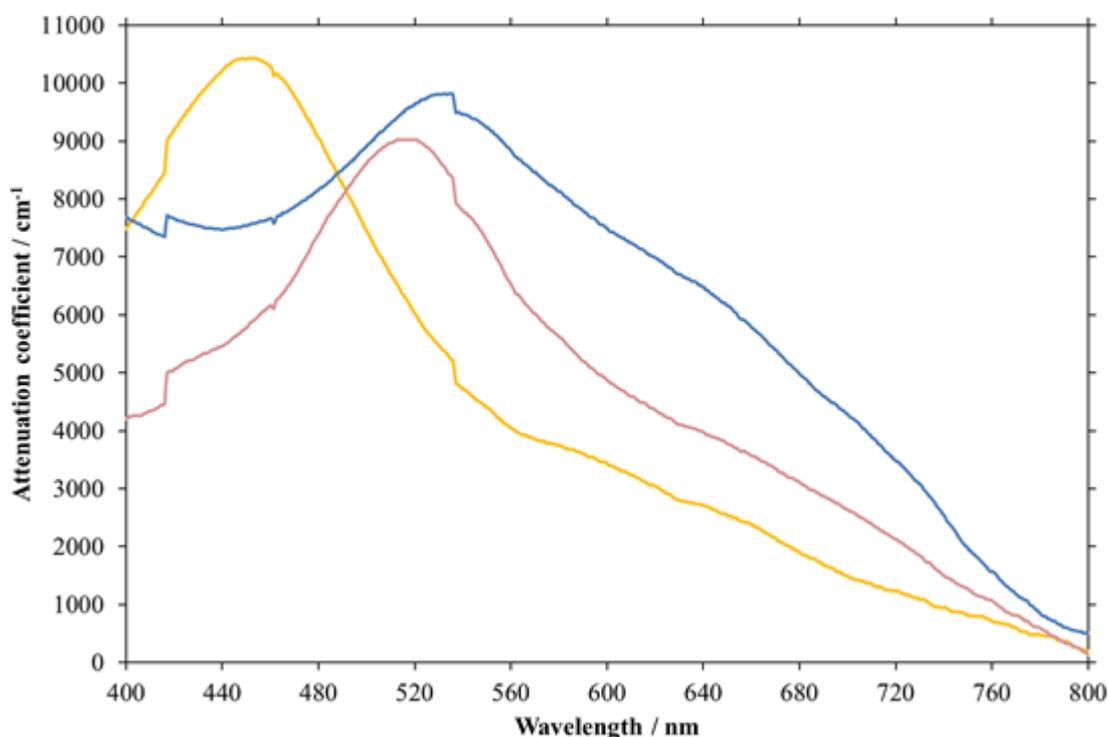


Fig.8.8: The attenuation coefficients for the yellow state of (9) (yellow line), the pink state of (9) (pink line) and the blue state of (9) (blue line). The discontinuities at ~ 420 nm and ~ 530 nm are systematic artefacts from the UV-Visible spectroscopy data, originally arising from the photospectrometer.

To model the refractive index profile of the three colour states, this attenuation coefficient data and a *MATLAB* code written by Holmes² for the modelling of the dispersion of different materials based on a single resonance absorption feature. Using this code, an iterative process of fitting Lorentzian peaks to the attenuation

coefficient data was performed until a best fit was achieved by visual inspection. These fitted Lorentzian single resonance peaks were then used to calculate the corresponding dispersion curves through use of the Cauchy integral theorem that is a programmed function within the *MATLAB* software. The best fit Lorentzian peaks for the three colour states and the resulting dispersion curves are shown below in **Fig.8.9** and **Fig.8.10** respectively.

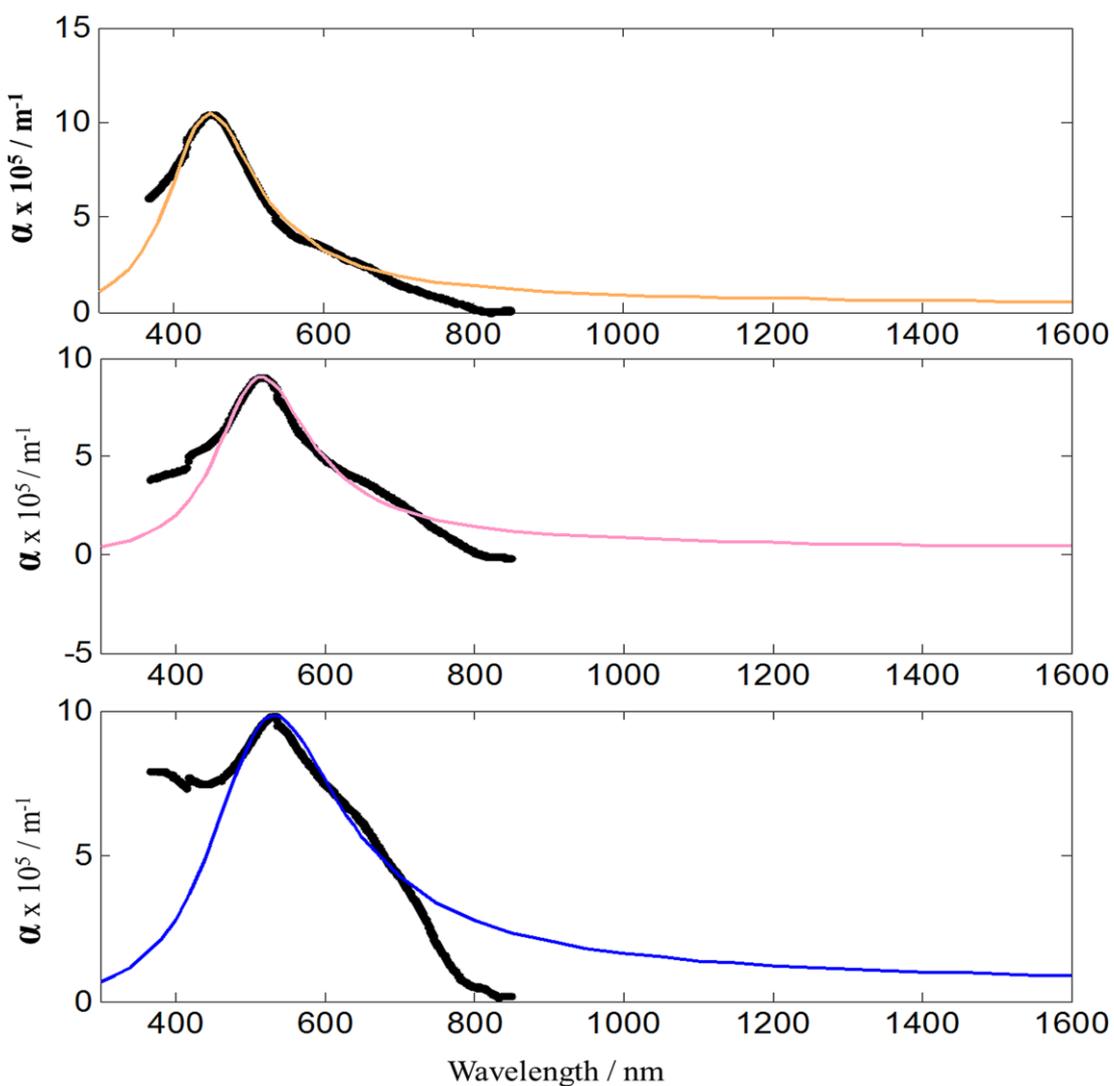


Fig.8.9: In all plots the black line represents the attenuation coefficient data for a particular colour state of (9) and the coloured line represents the visually inspected best-fit Lorentzian peak. (Top) the yellow state of (9) when exposed to ammonia fumes, (middle) the pink state of (9) when exposed to neutral air, (bottom) the blue state of (9) when exposed to fumes of hydrogen chloride.

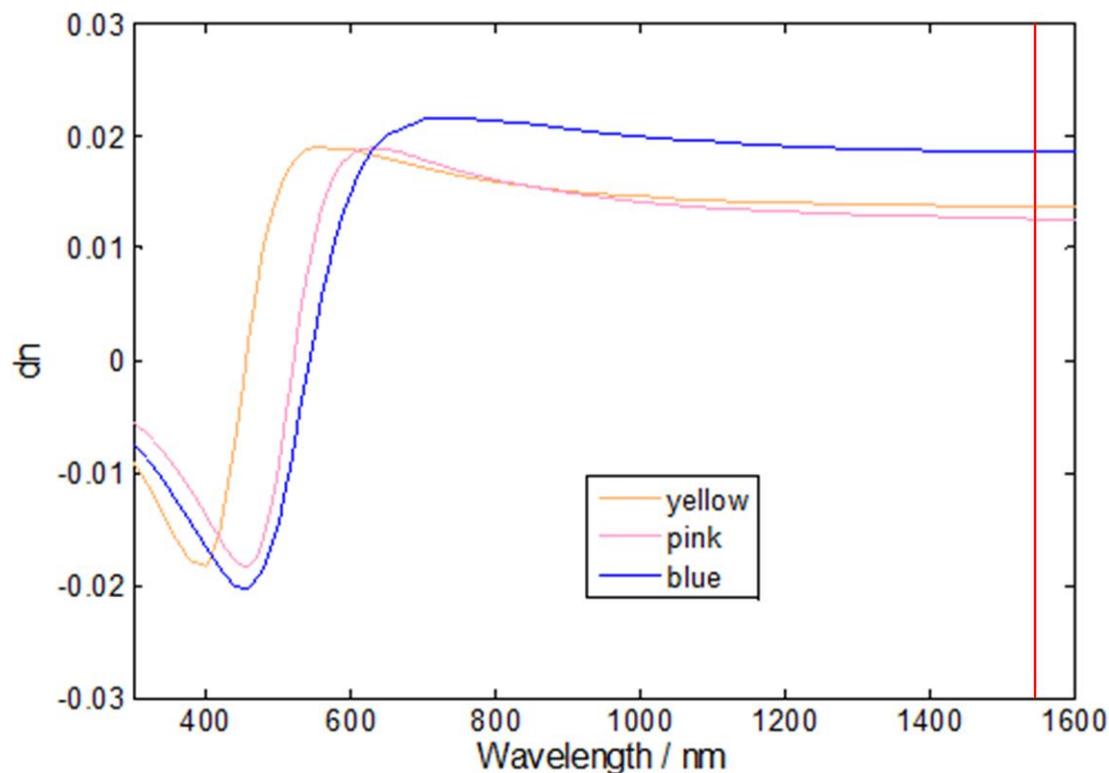


Fig.8.10 The resulting dispersion curves calculated using the Cauchy Principle Integral and the single resonance Lorentzian peaks fitted to the attenuation coefficient data. The yellow curve is the dispersion curve of the ‘yellow’ colour state of (9) when exposed to ammonia fumes, the pink curve is the dispersion curve of the ‘pink’ colour state of (9) when exposed to neutral air and the blue curve is the dispersion curve of the ‘blue’ state of (9) when exposed to hydrogen chloride fumes. The vertical red line represents the position of the interrogation wavelength = 1550 nm.

However, upon inspection the calculated dispersion curves did not predict the experimentally determined refractive index change at 1550 nm upon a change from the pink to the yellow state. The magnitude of the difference in refractive index, dn , between the pink and yellow in the calculated dispersion curves above is $+1.5 \times 10^{-3}$, which corresponds to change in Bragg wavelength shift of ~ 10 pm. This corresponding Bragg wavelength shift for the refractive index change was obtained by reading off the corresponding Bragg wavelength shift value from a straight line with a gradient equivalent to the gradient of the RI calibration curve (shown in **Fig.8.11** below) located at a refractive index value of 1.400. The changes in refractive index were added to the estimated starting refractive index of the layer = 1.400. This refractive index value (1.400) is a good estimate as this was the measured refractive index of a similar methylene blue doped sol-gel layer fabricated in **Chapter 6**. This predicted shift is different to the experimental result which

showed that there was no shift in Bragg wavelength at 1550 nm, greater than the ± 3 pm noise, caused by the colour change from pink to yellow. The source of this discrepancy was determined to be due to the poor description of the absorption features as a single resonance feature with a Lorentzian peak. As is evident in **Fig.8.9** above, there is very poor fit between the Lorentzian peak and the absorption spectrum line shape away from the λ_{\max} values; the absorption spectra are comprised of a convolution of several absorption resonances and not just one absorption.

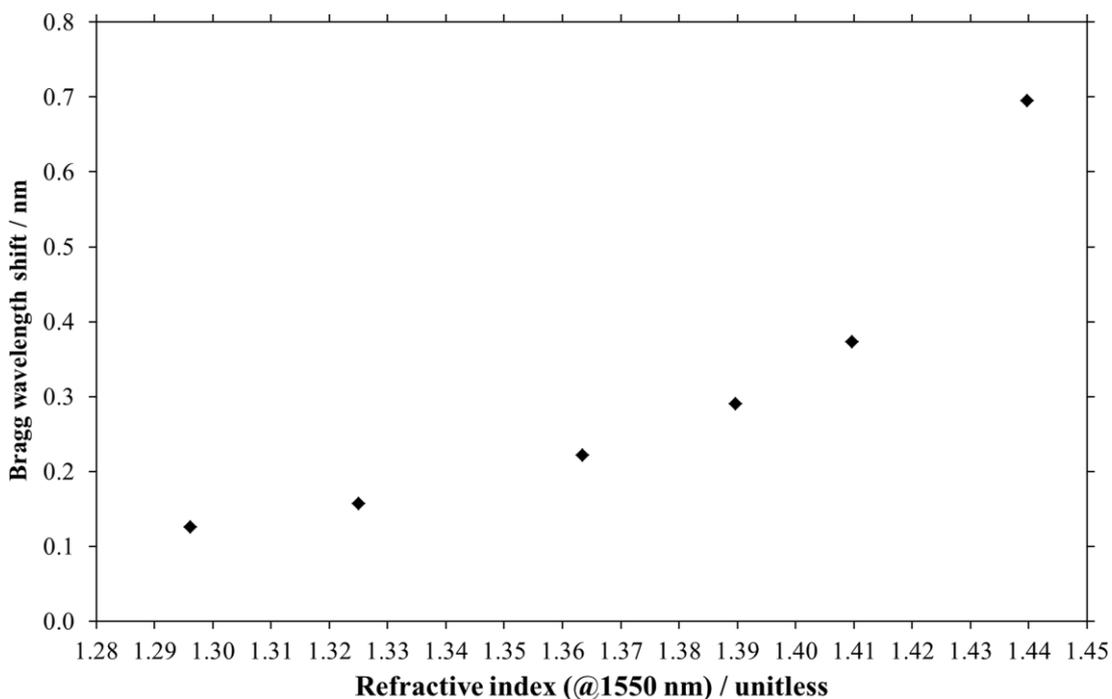


Fig.8.11: Refractive index calibration curve for the TE mode.

8.4.2 Fitting of Voigt functions to absorbance features

The spectral line shape of a molecular absorption feature is affected by many physical processes. These physical processes introduce spectral line shape broadening. The types of broadening are lifetime broadening, Doppler broadening, pressure broadening and proximity broadening. In the solid phase, pressure broadening and proximity broadening dominate. To achieve spectral line fitting there are three main types of functions used, Lorentzian, Gaussian and Voigt. For the absorption spectra of (9) in the different colour states it was determined that a Voigt function would achieve the best fit of the spectral line shapes. This is because the Voigt function is a theoretical description of spectral line shape broadening and also allows for good quality fits to experimental data³.

A Voigt function is a convolution of a Lorentzian and Gaussian function and is useful in the study of stellar atmospheres, x-ray spectra and plasma spectra ⁴. In addition, Willer *et al* fitted Voigt functions to recorded spectra to extract information about the absorbing species ⁵. In this work, a numerical approximation to the Voigt function, known as the casual Voigt function proposed by de Sousa *et. al.* and a Fadeeva function was used to fit to the spectral line shapes of the three colour states of (9) ³. The resulting fitted Voigt function curves are shown below in **Fig.8.12**.

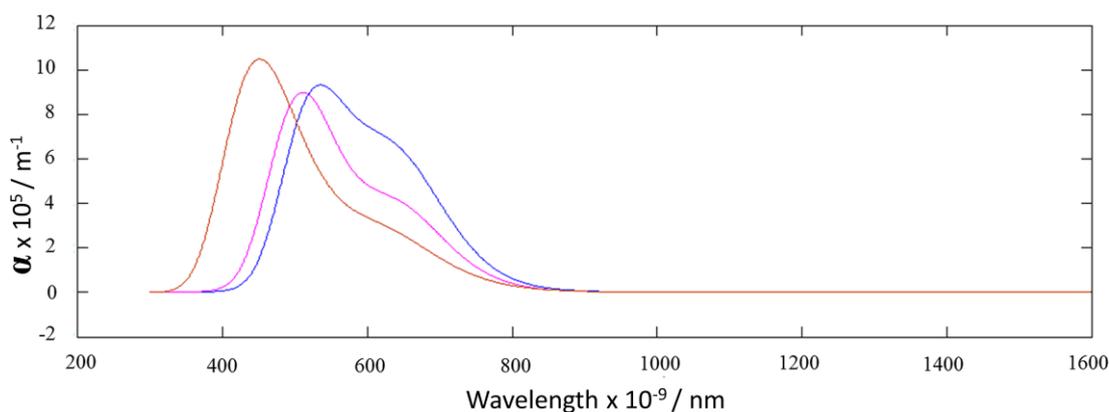


Fig.8.12: The Voigt functions fitted to the spectral line shapes of the absorption features of the three different colour states of (9), where α is the attenuation coefficient. The orange line represents the ‘yellow’ state of (9) when exposed to ammonia, the pink line represents the ‘pink’ state of (9) when exposed to neutral air and the blue line represents the ‘blue’ state of (9) when exposed to hydrogen chloride.

The calculated refractive index profiles from the fitted absorption curves are shown below in **Fig.8.13**

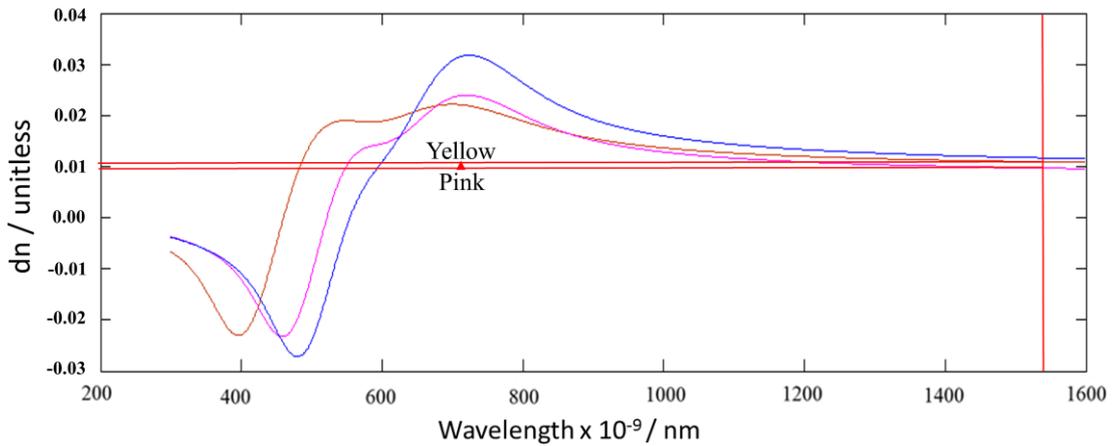


Fig.8.13: The modelled dispersion curves for the three colour states of (9) after fitting the absorption peak features with Voigt functions. The vertical red line denotes the position of the interrogation wavelength = 780 nm. The horizontal red lines denote the difference in refractive index of the pink and blue states $\sim 1 \times 10^{-3}$, at 1550 nm

Upon inspection, the dispersion curves calculated from the Voigt function fitted absorption feature peaks predicted the experimentally determined refractive index change at 1550 nm upon a change from the pink to the yellow state. The magnitude of the difference in refractive index, dn , between the pink and yellow from the calculated dispersion curves above is $\sim 1.0 \times 10^{-3}$, which corresponds to change in Bragg wavelength shift of ≤ 5 pm. This was obtained by reading off the corresponding Bragg wavelength shift value from a straight line with a gradient equivalent to the gradient of the RI calibration curve (shown in **Fig.8.13** above) located at a refractive index value of 1.400. This predicted shift of ~ 5 pm is in good agreement with the experimental result which showed that there was no shift in Bragg wavelength at 1550 nm with the associated error of ± 3 pm (noise).

However, taking the difference between the refractive index values of the pink and yellow curves at 780 nm predicts a change in refractive index of $\sim 1.5 \times 10^{-3}$ which corresponds to a Bragg wavelength shift of ~ 10 pm. To test this, the sensor device was interrogated at 780 nm. At 780 nm the second-order harmonic Bragg peaks of the Bragg gratings were generated and quantified in the same manner.

8.5 Refractometric sensing at 780 nm

8.5.1 ‘Moist’ ammonia fume refractometric sensing at 780 nm

The device was pigtailed with a 780 nm pig-tail and inserted into the 780 nm optical set-up shown in **Chapter 11** below. The device was repeatedly exposed to ambient atmosphere or ‘dunked’ into the vapour space above 38% aqueous ammonia solution. Colour changes from pink to yellow and vice versa were observed, however no Bragg wavelength shifts greater than the ± 10 pm noise were measured with the thin film (9) covered Bragg grating as shown in **Fig.8.14** below.

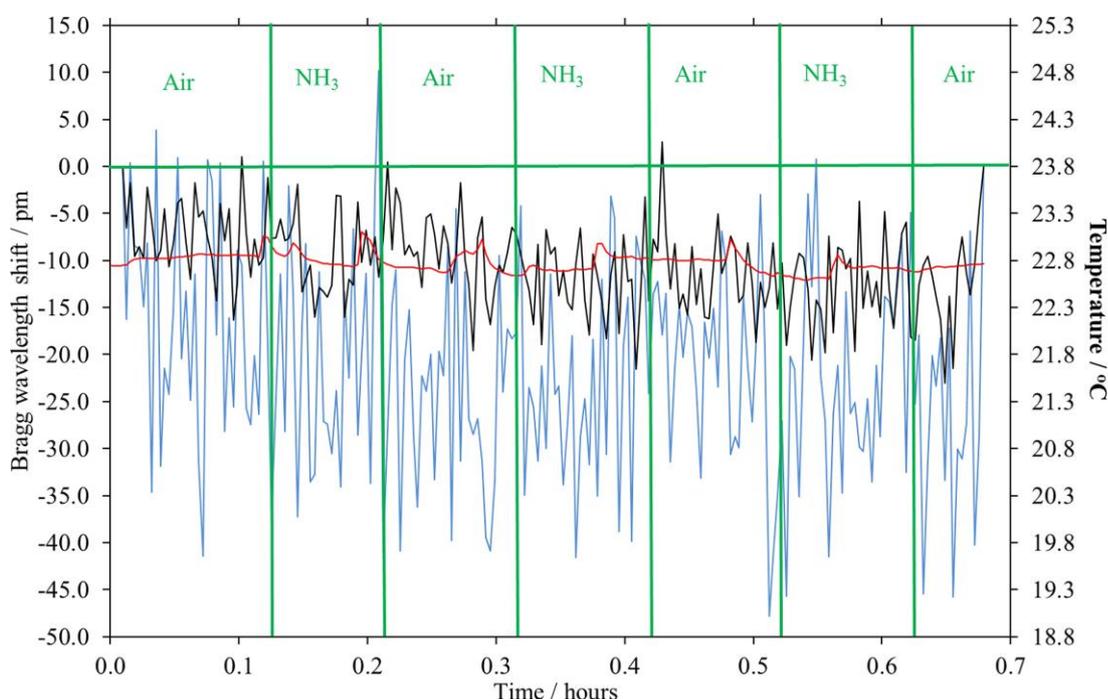


Fig.8.14: No Bragg wavelength step shifts were measured at 780 nm with a thin film covered Bragg grating (black line) or an uncovered Bragg grating (blue line), when exposed to cycles of dry ammonia gas and dry nitrogen (demarcated with the vertical green lines). The corresponding changes in temperature are given by the red line (scaled to $1\text{ }^{\circ}\text{C} = 10\text{ pm}$). The horizontal green line represents 0 pm Bragg wavelength shift.

A lack of an accompanying refractive index change, upon colour change, would lead to no corresponding Bragg wavelength shift. However, the Kramers-Kronig relation (as detailed above **Chapter 8**) states that the absorption spectrum of a molecule is related to the refractive index of that molecule. Therefore a change in the absorption spectrum will always result in a change to the refractive index profile of the molecule. Therefore, it was proposed that the cause of this null result was due to the colour change from pink to yellow corresponding to a change in refractive index that

caused a Bragg wavelength shift smaller or equal to the +/- 10 pm noise; as predicted from the modelled refractive index curves. The signal to noise level at 780 nm prevented resolving a Bragg wavelength shift due to the colour change. The increased noise level is due to two factors. Firstly the sensor device utilised was specifically written for interrogation at 1550 nm. Thus, when interrogated at 780 nm the optical loss was high due to the waveguide supporting multiple modes at 780 nm. This was further compounded by the inherent increased optical loss of shorter wavelengths propagating in a material due to increased Rayleigh scattering. Rayleigh scattering loss scales by λ^{-4} , the shorter the wavelength the larger the optical loss.

8.5.2 'Moist' hydrogen chloride fume refractometric sensing at 780 nm

However, it was clear from the predicted refractive index curves (**Fig.8.13** above) that a colour change from pink to blue, caused by exposure to hydrogen chloride gas, would cause a change in refractive index of **(9)** $> 1.5 \times 10^{-3}$. This would result in a Bragg wavelength shift > 10 pm; greater than the noise of +/- 10 pm. Therefore, the experiment was repeated but with 38% w/v ammonia solution replaced with 35% v/v hydrochloric acid as a source of hydrogen chloride fumes.

When the device was 'dunked' into the hydrogen chloride fumes a colour change from pink to blue in the thin film of **(9)**, was observed. In addition, a Bragg wavelength shift of ~ 40 pm (greater in magnitude than the +/- 10 pm noise) was measured with a Bragg grating covered by the thin film of **(9)**. This experiment was repeated twice more and Bragg wavelength shifts of ~ 24 pm and ~ 20 pm were measured. However, corresponding Bragg wavelength shifts of 69 pm, 38 pm and 46 pm respectively were measured with an uncovered Bragg gratings. This suggested that moisture ingression and/or temperature changes caused a change in refractive index and subsequent Bragg wavelength shift and not the colour change. The average Bragg wavelength shifts measured with the uncovered Bragg gratings and the Bragg gratings covered with the thin film of **(9)** are shown below.

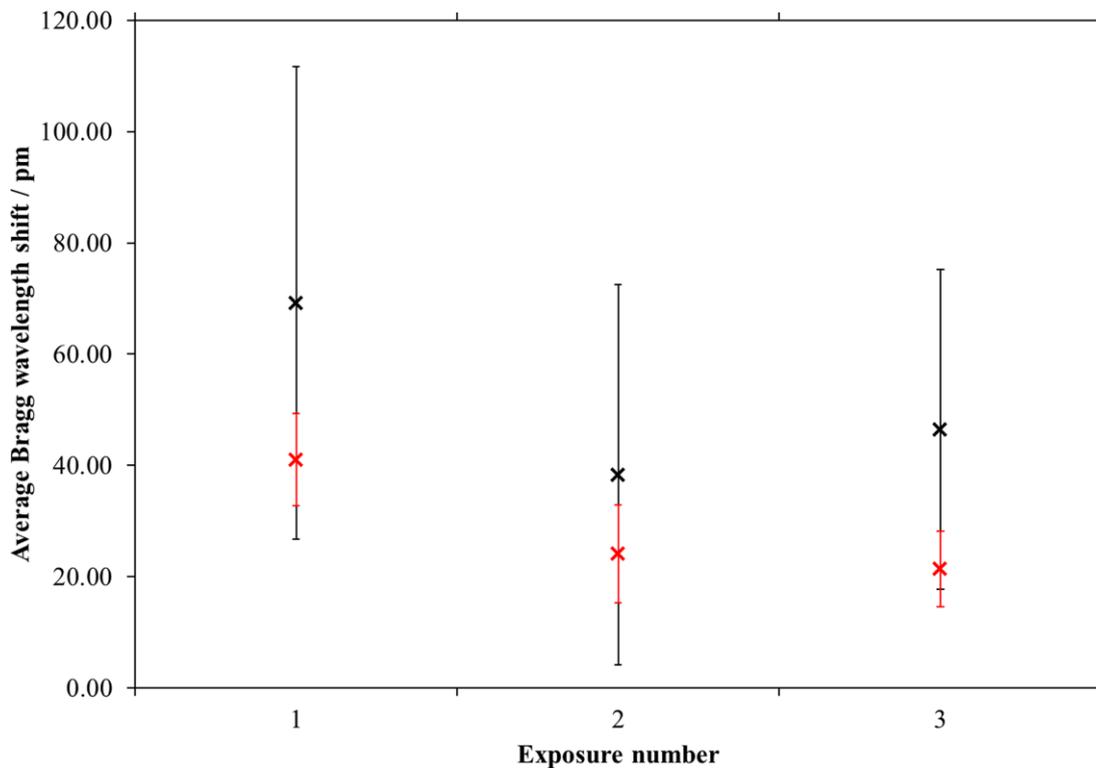


Fig.8.15: Bragg wavelength shift measured with the uncovered Bragg gratings (×) and the Bragg gratings covered with the thin film of (9) (×). The black error bars represent the associated errors of the Bragg wavelength shifts of the uncovered Bragg gratings and the red vertical errors bars represent the associated errors of the thin film covered Bragg gratings.

However, as is evident in **Fig.8.15** above, the associated errors of the Bragg wavelength shifts measured with the uncovered Bragg gratings were 3 – 4 times greater than the associated errors of the Bragg wavelength shifts measured with the thin film covered Bragg gratings. The cause of the large associated errors was investigated and it was determined that poor fitting of a Gaussian function to the Bragg grating peaks in the *LabView* software occurred upon exposure to hydrogen chloride fumes. This was due to a decrease in Bragg peak amplitude upon exposure, for the peaks of both of the uncovered and covered Bragg gratings as shown in **Fig.8.16** below.

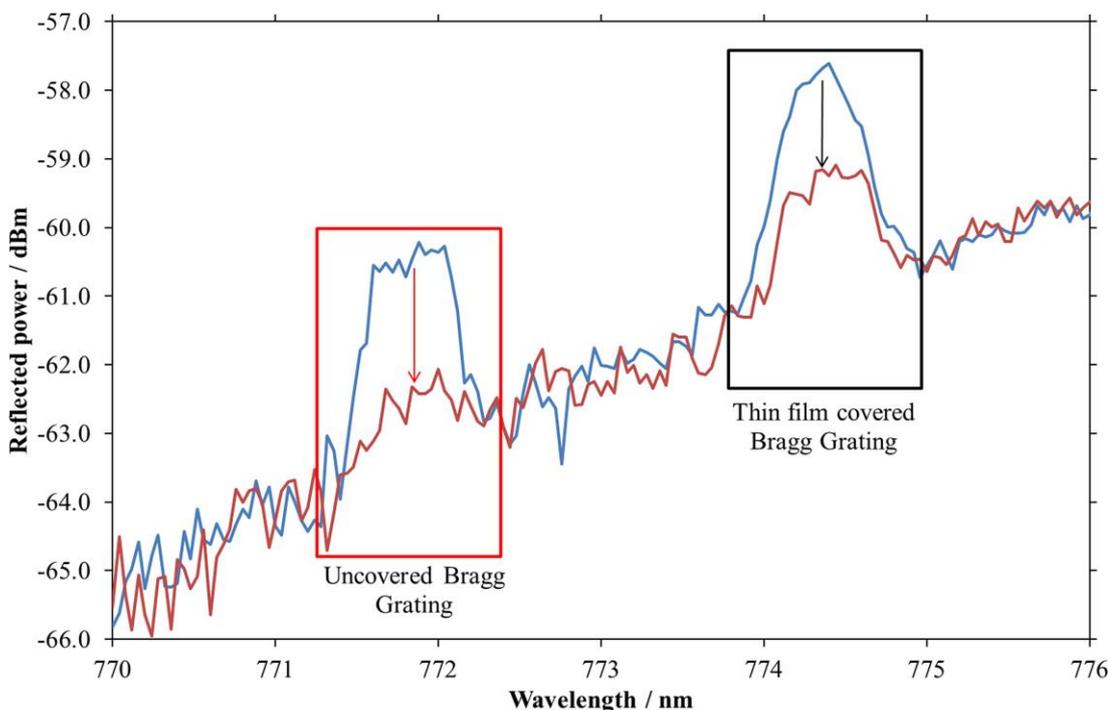


Fig.8.16: Decrease in Bragg peak amplitude upon exposure to hydrogen chloride fumes. The blue line represents the Bragg grating spectrum recorded in air and the maroon line represents the Bragg grating spectrum recorded during exposure to hydrogen chloride fumes.

The decrease in amplitude of the Bragg peaks for the uncovered Bragg grating caused the Bragg peak to disappear amongst the background noise. Therefore, the wavelength shifts measured for the uncovered Bragg gratings were measurements of random variations in the background noise and not Bragg wavelength shifts, thus will be disregarded in further analysis.

Despite a decrease in the amplitude of the Bragg grating covered by the thin film of (9), sufficient fitting of a Gaussian function to the Bragg peak in the *LabView* software was possible, allowing for measurement of Bragg wavelength shifts.

The average Bragg wavelength shift measured with the Bragg grating covered with the thin film of (9) was (29 ± 5) pm. However, the average temperature change upon exposure to hydrogen chloride fumes must also be taken into account. The average temperature change during the exposure = (0.56 ± 0.36) °C. Using the first-order approximation of $\Delta 1 \text{ oC} = \Delta 10 \text{ pm}$ shift, this average temperature change upon exposure corresponds to an average Bragg wavelength shift of (5.6 ± 3.6) pm. Taking a Bragg wavelength shift of ~ 6 pm due to temperature change, suggests that the average Bragg wavelength shift measured with the thin film covered Bragg

gratings, after accounting for the Bragg wavelength shift due to temperature change, was ~ 24 pm. Using the modelled refractive index curves in **Fig.8.13** above, the colour change from pink to blue would cause a change in refractive index of $\sim 7 \times 10^{-3}$, which would correspond to a Bragg wavelength shift of ~ 40 pm. With temperature change taken into account, the proposed Bragg wavelength shift due to colour change of ~ 24 pm is in reasonable agreement with the modelled Bragg wavelength shift. However, the Bragg wavelength shift may not have been caused by the colour change, even with temperature compensation applied. The Bragg wavelength shift may also have been caused by adsorption of water vapour as was determined in the ammonia ‘dunk’ exposure experiments. The decrease in Bragg peak amplitude, as shown in **Fig.8.16** above, upon exposure to the hydrogen chloride vapours, corroborates this hypothesis. This is because a plausible mechanism for the amplitude decrease is due to water ingress into the thin film, causing the effective index within the sol-gel thin film to increase, causing more of the optical mode to be ‘pulled’ out of the waveguide and thus resulting in less reflected power.

The effect of water ingress into the mesoporous silica sol-gel thin film, on the measured Bragg wavelength shift, can be estimated by use of the relative humidity sensing results reported in **Chapter 6** for a Bragg grating sensor device covered in a silica sol-gel thin film. By determining the average %RH during the hydrogen chloride fume sensing experiments, a value for the expected Bragg wavelength shift due to moisture ingress into the silica sol-gel thin film can be made. Firstly, the following values need to be determined: the average temperature, T , during the sensing experiments, the value of the partial pressure of water above the hydrochloric acid solution and the saturation vapour pressure of water vapour at temperature T .

The relative humidity, %RH, at a given temperature, T , is given by:

$$\%RH = \frac{p_w}{p_s} \times 100$$

Eqn.8.1

Where p_w is the partial pressure of water vapour at temperature T , and p_s is the saturated vapour pressure of water at temperature T . Firstly, the temperature T needs

to be defined. During exposure of the Bragg grating, the temperature was 23 – 24 °C, which for the following calculations will be taken as 25 °C. Therefore $T = 25 \text{ °C} = 298.15 \text{ K}$. The saturated vapour pressure of water is given by the following equation ⁶:

$$p_s = \exp \left(\frac{\left(77.3450 + 0.0057T - \left(\frac{7235}{T} \right) \right)}{T^{8.2}} \right)$$

Eqn.8.2

where T is the temperature in K and p_s is in Pa. Therefore, at 298.15 K the saturated vapour pressure of water, $p_s = 3158.502 \text{ Pa}$ and with unit conversion from Pa to mmHg = 23.69 mmHg.

The hydrochloric acid solution used was 34 %v/v. With reference to the literature, the partial pressure of water vapour above a 34 %v/v aqueous solution of hydrochloric acid, at 25 °C, is given as 5.35 mmHg ⁷. Using **Eqn.8.1** the %RH during the hydrogen chloride exposure experiments can be estimated as 22.6 %RH. With reference to the results in **Chapter 6** for a Bragg grating sensor device covered with a silica sol-gel thin film a value of 22.6 %RH corresponds to a Bragg wavelength shift of ~ 10 pm, after referencing for temperature. However, it must be noted the neutral red doped silica thin film (~100 nm thick) was thinner than the silica thin film used in Chapter 6 (~250 nm); it is expected that the sensitivity of the thinner silica film to relative humidity will be less than the sensitivity of the thicker silica film; less porous thin film in the evanescent wave interaction volume and thus less adsorbed water. Therefore a reasonable estimate of the Bragg wavelength shift due to moisture ingress would be ~4 – 5 pm as the neutral red doped thin film was approximately half the thickness of the silica sol-gel thin film used on the relative humidity sensor device. Therefore, by subtracting 4 – 5 pm from the average Bragg wavelength shift (~24 pm after temperature and strain referencing) of the Bragg gratings covered in the neutral red doped sol-gel thin film, gives a Bragg wavelength shift of ~20 pm. This overall shift, after removal of temperature and moisture effects, is in good agreement with the modelled Bragg wavelength shift of ~30 pm at the interrogation wavelength of 780 nm due to the colour change of

neutral red from pink to blue. This suggests that the ~20 pm Bragg wavelength shift, after removal of moisture and temperature effects, was due to the associated refractive index change caused by the colour change.

However, it must be noted that treatment of the moisture ingress effect assumes that the response of a neutral red doped silica thin film will be equivalent to an undoped silica sol-gel thin film. The presence of neutral red molecules in the pores of the sol-gel thin film may either increase or decrease the quantity of water that ingresses into the pores of the sol-gel thin film compared to an undoped thin film. It is known that the diameter of the pores, within the silica sol-gel thin films used in this work, are ~3 nm⁸. It is known in the literature⁹ that the molecular dimensions of neutral red are $(7.4 \times 3.45 \times 1.9)$ Å. Therefore two or three molecules of neutral red can fit into a pore, which reduces the volume within the pore that can be occupied by water molecules. Therefore, it is suggested that the presence of neutral red within the pore of the silica sol-gel reduces the quantity of water within the sol-gel thin film, thus reducing the sensitivity of the thin film covered Bragg gratings in the neutral red PH sensor device, to water vapour. Therefore, the contribution of the relative humidity to the Bragg wavelength shift, upon exposure to hydrogen chloride fumes, maybe overestimated in the calculation presented above.

Thus, it can be stated that a proof-of-concept Bragg grating refractometric gas sensor that utilises a change in the absorption coefficient of a material to induce a measurable refractive index change at 780 nm, due to exposure to a gas, has been achieved.

Better agreement between the measured Bragg wavelength shift and the predicted Bragg wavelength shift could be achieved by implementing the following optimisations of this experiment. Firstly, by further optimisation of the fitting of the Voigt function to the absorbance peak features, more accurate dispersion curves will be obtained through the *MatLab* calculation. From these more accurate dispersion curves, more accurate Bragg wavelength shifts can be predicted. Secondly, an experimentally measured value of the %RH above the hydrochloric acid solution could be used, instead of a calculated %RH value, to predict the resulting relative humidity contribution to the measured Bragg wavelength shift upon exposure to hydrogen chloride fumes. Thirdly, if Bragg wavelength shift vs. relative humidity

data for a Bragg grating sensor device modified with a silica sol-gel thin film of ~100 nm thick was obtained and plotted, then this data could be used to predict the expected Bragg wavelength shift due to moisture ingress. Thus, a more accurate prediction of the Bragg wavelength shift, due to the associated refractive index change caused by the colour change, could then be made. Despite the statement above that the effect of relative humidity on the pH sensor device maybe overestimated, to confirm that the colour change and not moisture ingress was the cause of the Bragg wavelength shift, the experiment could be performed with dry hydrogen chloride fumes.

8.6 Colour change refractometric sensing of volatile organic compounds (VOCs) at 1550 nm

Despite the achievement of sensing of gas utilising the resultant change in refractive index upon a colour change, it had been achieved at 780 nm. This was necessary, as the changes to the absorption spectrum of neutral red, upon exposure to hydrogen chloride fumes, occur in the visible region of the EM spectrum. Therefore, the extent of the resulting change in refractive index was only quantifiable in the visible region and not in the near-infrared, as shown by the modelling refractive index in **Fig.8.13** above. However, the extent of standard and comparatively cheap optical characterisation equipment operates over the telecoms band, especially at 1550 nm. Therefore, to achieve gas sensing using standard telecoms equipment, a gas receptor molecule that exhibited absorbance changes in the near-infrared region near to 1550 nm, upon interaction with an analyte gas, was required.

8.6.1 Lutetium bisphthalocyanine

One class of molecules, which have significant absorption features in the near-infrared region are the lanthanide bisphthalocyanines. These molecules are sandwich complexes of a lanthanide metal ion, usually in the 3⁺ charge state, between two organic macrocycles known as phthalocyanines.

Phthalocyanines are intensely coloured macrocycles (see **Fig.8.17** below) that can coordinate more than 70 of the elements in the periodic table ¹⁰. Phthalocyanines coordinated to metal cations, known as metal phthalocyanines (see **Fig.8.17** below), have been demonstrated in the literature as active sensing elements for detection of VOCs ¹¹.

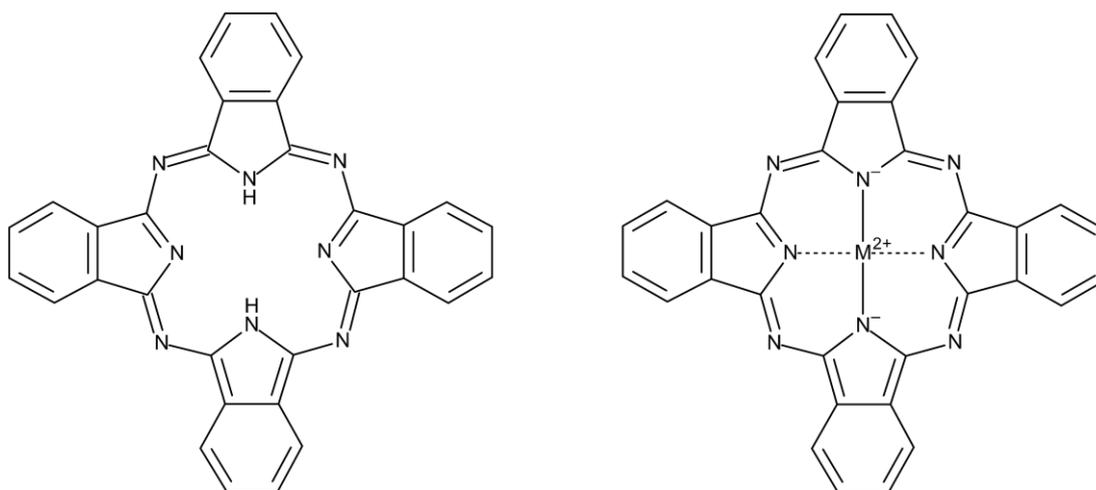


Fig.8.17: Hydrogen phthalocyanine and a metal phthalocyanine overall neutral complex, consisting of the phthalocyanine dianion and a divalent metal cation

Cations, with small ionic radii, fit within the plane of the phthalocyanine macrocycle ring, whereas cations with large ionic radii sit outside of the plane of the phthalocyanine macrocycle ring. Relatively larger (in terms of ionic radius) lanthanide trivalent cations sit outside of the plane allowing for another dianion phthalocyanine macrocycle ring to sit above, thus forming a sandwich complex. These sandwich complexes are named lanthanide bisphthalocyanines an example of which (Lutetium bisphthalocyanine) is shown below in **Fig.8.18**.

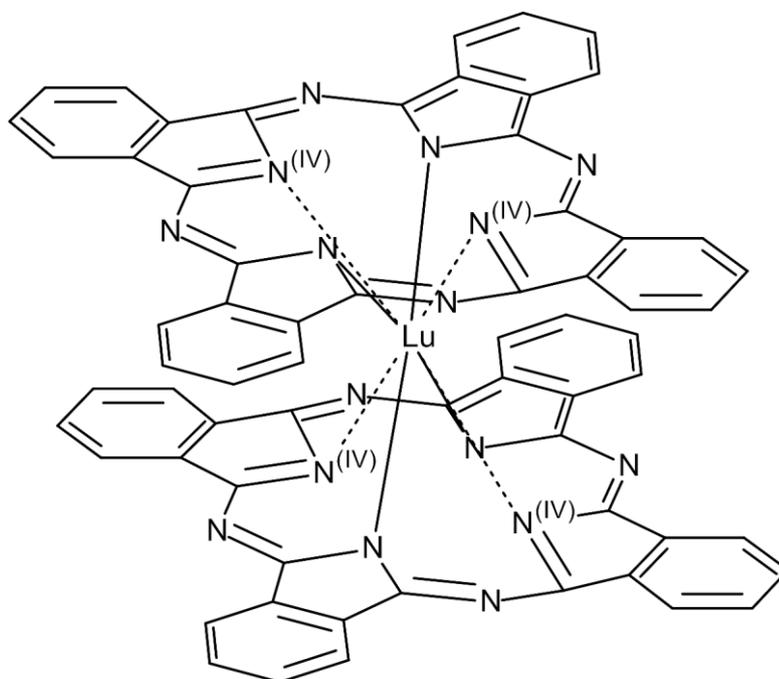


Fig.8.18: The molecular structure of lutetium bisphthalocyanine, a bisphthalocyanine sandwich complex

In particular lutetium bisphthalocyanine is a vapochromic chemical species, i.e. undergoes an absorption change in the near-infrared region (~1420 nm) when exposed to certain organic vapours¹². The vapochromic behaviour of lutetium bisphthalocyanine was demonstrated in the work of Bariáin *et. al.* whereupon an optical-fibre sensor, the end facet of which was modified with a Langmuir-Blodgett film of lutetium bisphthalocyanine, was fabricated and used to sense VOCs¹². This sensor worked by detecting the decrease in the magnitude of the reflected power from the end facet, which was caused by the decrease in the absorbance at ~1420 nm and subsequent change in the refractive index of the lutetium bisphthalocyanine, upon exposure to vapour of oxygenated solvents¹². Bariáin *et. al.* determined that the largest decreases in magnitude of the reflected power, and thus the largest changes in refractive index of a film of lutetium bisphthalocyanine occurred upon exposure to the most oxidising oxygenated solvents¹². Therefore, lutetium bisphthalocyanine was chosen as a suitable gas receptor molecule for refractometric VOC sensing with planar integrated optical Bragg grating sensors at 1550 nm.

8.6.1.1: Synthesis of lutetium bisphthalocyanine (10)

Lutetium bisphthalocyanine was synthesised in a poor yield of < 5% by the procedure given in **Chapter 10**; it is well documented that lanthanide bisphthalocyanines are difficult to synthesise in any appreciable yield¹³. Successful synthesis of lutetium bisphthalocyanine was confirmed by UV-Vis spectroscopy, ¹H NMR, IR spectroscopy and elemental analysis. (¹H NMR spectrum → *DJW.6625.21.LuPc 2 (10).1H NMR.MA1913DJW1.010.ESP*), (FT-IR spectrum → *DJW.6625.28.LuPc2 (10).FT-IR*) & (Elemental analysis → *DJW.6625.21.LuPc2 (10).Elemental Analysis Report*).

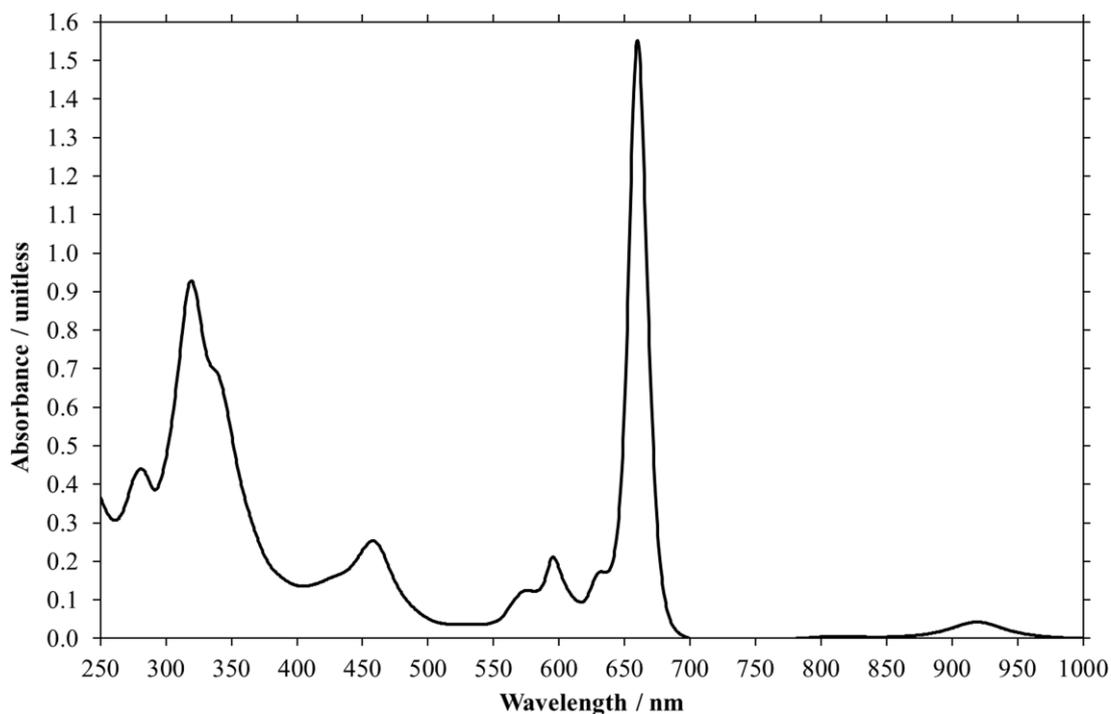


Fig.8.19: UV-Visible spectrum of (10), which matched with the literature reported spectrum for lutetium bisphthalocyanine.

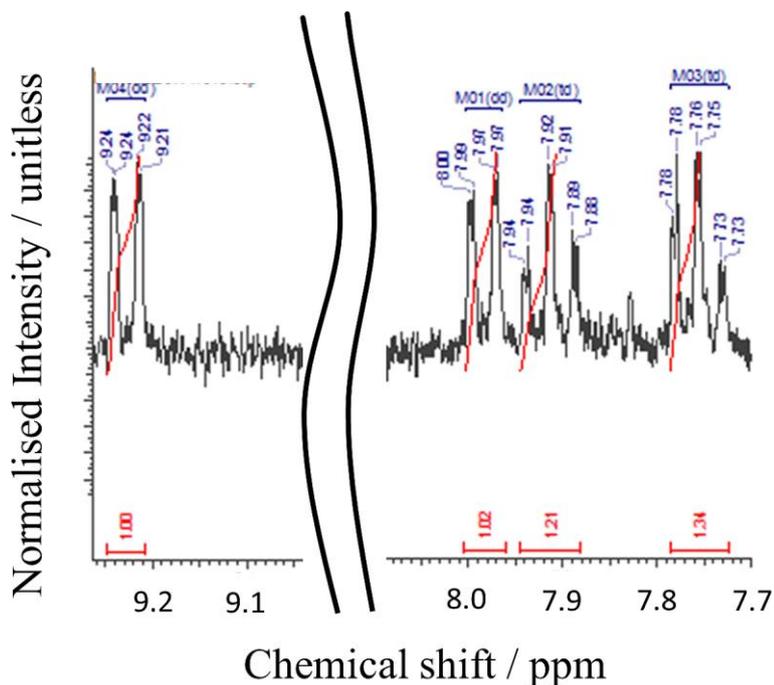


Fig.8.20: A section of the aromatic proton region of the ^1H NMR of (10) displaying characteristic proton peaks typical of lutetium bisphthalocyanine. The 'squiggly' lines represent a discontinuity along the x-axis; there were no proton signal peaks in this region.

The elemental analysis results showed that the sample of (10) contained $\sim 70\%$ lutetium bisphthalocyanine species and $\sim 30\%$ lutetium monophthalocyanine

species. It was deemed that despite the monophthalocyanine impurity, 70 % of the bisphthalocyanine sandwich complex would be sufficient for optical sensing of VOCs.

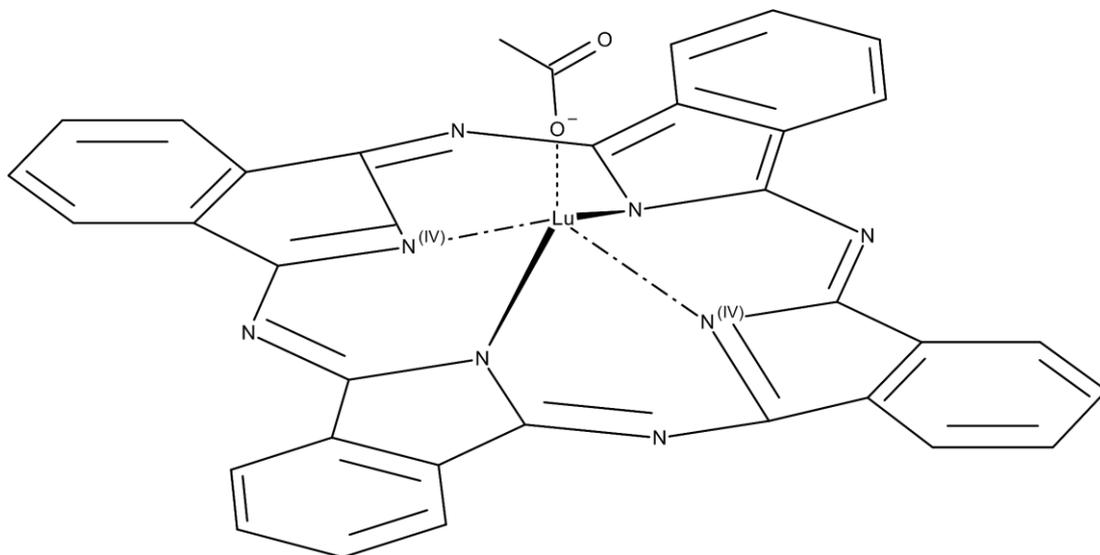


Fig.8.21: Lutetium monophthalocyanine acetate. The lutetium(III) cation sits out of the plane of the phthalocyanine macrocycle and in this example an axially co-ordinated acetate anion is present.

8.6.1.2: Fabrication of the film of (10) for sensing

A thin film of lutetium bisphthalocyanine was fabricated by dissolution of (10) in chloroform (12 mg/ml concentration) and subsequent spin deposition of the solution at 1000 rpm for 1 min before drying in ambient condition for ~ 12 hours. This yielded a pale green film on the surface of the Bragg grating sensor which partially covered the top surface of the sensor; some Bragg gratings were covered with the thin film of (10) and the other Bragg gratings were not. This allowed for on-chip referencing of changes in temperature and other physical effects in the same manner as described above, and in **Chapters 6 & 7**.

8.6.2 VOC sensing experiments at 1550 nm

8.6.2.1 VOC sensing at 1550 nm in a gas flow system

The sensing experiment was performed as described in section **10.4.12** and was identical to the equipment set-up used for VOC sensing in **Chapter 7** and as shown in **Fig.8.22** below. It should be noted that the solvent reservoir was held at a temperature which was $> 20\text{ }^{\circ}\text{C}$ than the boiling point of the chosen analyte solvent, this ensured that the solvent was boiling.

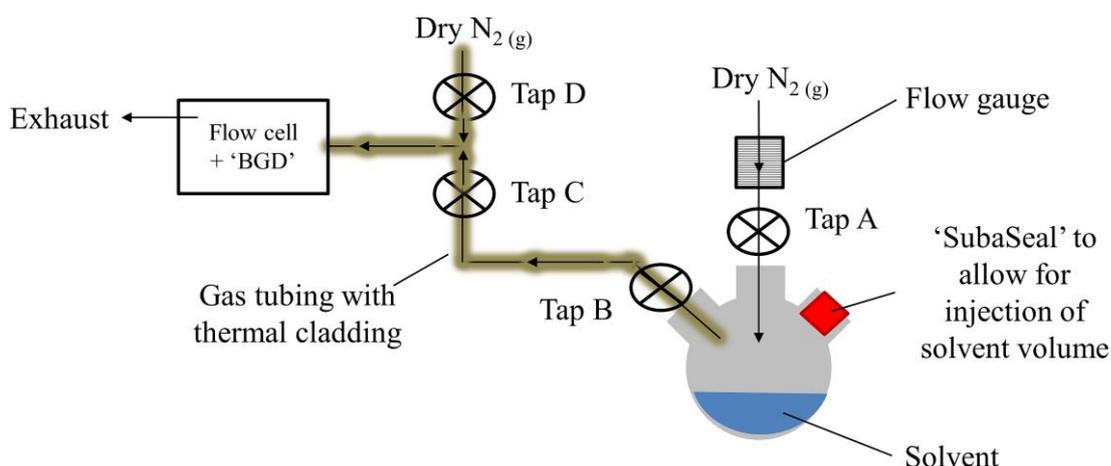


Fig.8.22: Schematic of the solvent vapour sensing experimental set-up, using the Bragg grating sensor device modified with a film of (10). The flow of nitrogen gas through the solvent reservoir was approximately 1.5 L/min.

The Bragg grating sensor device modified with the thin film of (10), labelled as 'BGD', was placed in a flow cell. The temperature within the flow cell was monitored throughout the experiment with a thermocouple. This allowed for the magnitude of Bragg wavelength shifts recorded with the uncovered reference Bragg gratings to be corroborated with the measured temperature changes during a sensing event, knowing that the temperature coefficient of FHD silica is $\sim 10 \text{ pm } ^\circ\text{C}^{-1}$ ¹⁴. Contamination of the sensing layer of (10) was minimised by continuous exposure of the 'BGD' to a flow of dry nitrogen gas ($> 5 \text{ L min}^{-1}$). For sensing events, the 'BGD' was exposed to a flow of organic solvent vapour in dry nitrogen carrier gas. A three neck flask was used as the reservoir for the liquid solvent analytes and was preheated to temperatures $> 20 \text{ }^\circ\text{C}$ higher than the boiling point of the chosen analyte solvent for at least 20-30 min (e.g. for dichloromethane, boiling point $\sim 40 \text{ }^\circ\text{C}$, the three neck flask was heated to $\sim 60\text{-}65 \text{ }^\circ\text{C}$). When the flask was at appropriate temperature, analyte solvent (3 mL) was injected into the three neck flask via the 'Suba Seal'. Within a few seconds, the liquid solvent began bubbling and condensation of liquid was seen around the top of the flask. At this point it was assumed that a saturated atmosphere of solvent vapour in nitrogen had formed within the flask. At this point, the dry nitrogen gas flow over the 'BGD' was removed and Tap D was shut (the identity of each tap is shown in **Fig.8.22** above). Taps B, C and then A were then opened in quick succession followed immediately by application of a flow of dry nitrogen carrier gas ($\sim 1.5 \text{ L min}^{-1}$) over the volume of the analyte solvent as shown in **Fig.8.22** above, which in turn then flowed over the 'BGD'. The length of gas

piping between the flow cell (containing the 'BGD') and the reservoir was kept to a minimum (~20 cm) and was insulated with lagging to prevent cooling and condensation of solvent vapour before reaching the 'BGD'. During sensing events it was noted that the volume of liquid solvent decreased with continued nitrogen carrier gas flow; this indicated that evaporation of the analyte solvent was occurring. The flow of nitrogen carrier gas through the reservoir flask was maintained for at least 5 min after it was first observed that all the liquid solvent had evaporated. This was to ensure that condensed solvent vapour within the pipes was purged and passed over the 'BGD'. This enabled the following assumption to be made; the Bragg wavelength shifts recorded for the vapours of different solvents were due to the properties of the solvent and not due to differences in the volume of each different vaporized solvent passed over the 'BGD'. After five minutes Tap C was shut, the flow of dry nitrogen carrier gas through the flask was ceased, Tap D was opened and the flow of dry nitrogen gas ($> 5 \text{ L min}^{-1}$) was reintroduced to the flow cell before finally Tap A and Tap B were shut. This procedure was repeated for every sensing event to enable direct comparison of the Bragg wavelength shifts recorded upon exposure to different solvent vapours. A sufficient period (usually 10-15 min) of dry nitrogen gas was allowed between sensing events to ensure Bragg wavelength shift values had returned to stable baseline levels.

It must be noted that with this particular experimental set-up, the vapour vented to the external atmosphere, i.e. vented into atmospheric pressure. Therefore the vapour pressure was not constant. However, the advantage of this experimental set-up is that the compatibility of the Bragg sensor, modified with a film of (10), to gas flow systems could be demonstrated.

The 'BGD' was exposed to methanol, hexane and dichloromethane vapours. These particular solvents were chosen to enable the response of the thin film of (10) to the vapours of different types of solvent (an oxygenated solvent, a hydrocarbon solvent and a chlorinated solvent) to be determined. Referencing of temperature and physical changes was achieved as previously described. The average Bragg wavelength shifts for the thin film covered Bragg gratings, after referencing for changes in temperature and other physical effects had been applied, are shown below in **Fig.8.23**.

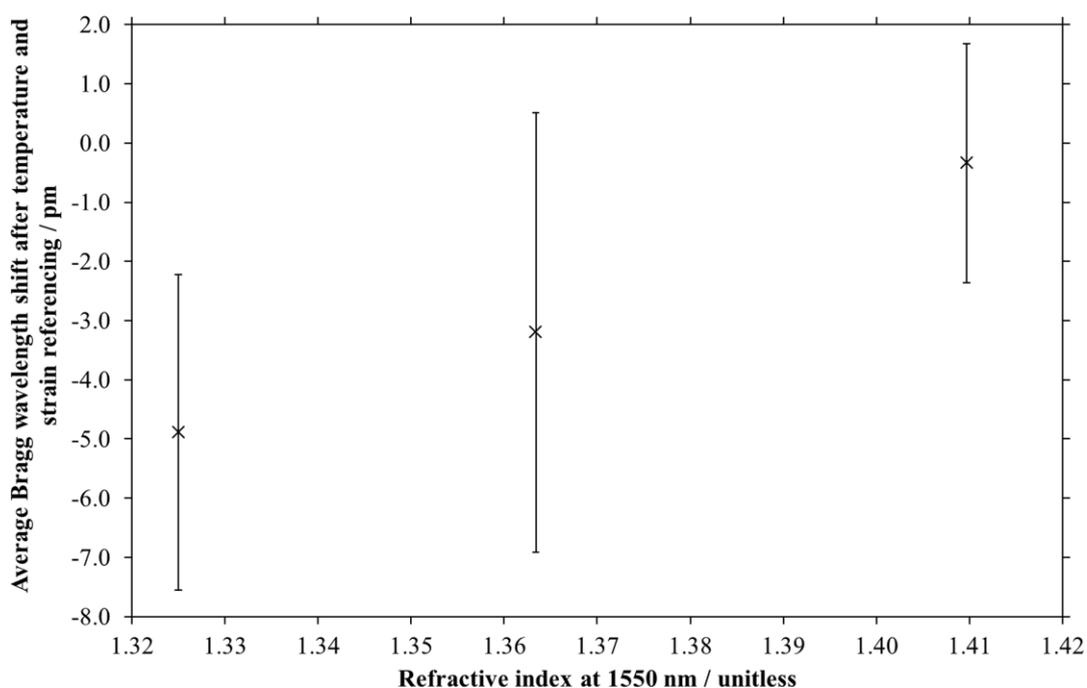


Fig.8.23: Within associated error, the average (three measurements) Bragg wavelength shifts of Bragg gratings covered with a film of **(10)** upon exposure to methanol (n at 1550 nm = 1.3250, left datum), n -hexane (n at 1550 nm = 1.3634, middle datum) and dichloromethane (n at 1550 nm = 1.4097, right datum) were similar. The error bars represent the associated error for each datum.

With reference to the work by Bariáin *et. al.*¹², it was expected that methanol, the only oxygenated solvent analyte in this experiment, should cause the largest magnitude decrease in absorption, thus the largest decrease in refractive index and thus the largest negative Bragg wavelength shift. However, as is evident in **Fig.8.23** above, the average Bragg wavelength shift values for each solvent, after referencing for temperature and physical effects, were in excellent agreement within associated error and were tending towards 0 pm. This suggests that no significant change in absorbance and thus no associated change in refractive index occurred at ~1420 nm, upon exposure to the vapours of the different solvents.

Two factors, which may have caused no measurable change in refractive index upon exposure of the sensor modified with the film of **(10)** to the vapours of different solvents, were proposed. Firstly, it was proposed that the method of deposition of the film of **(10)** may have affected the solid state near-infrared absorption spectrum of lutetium bisphthalocyanine. It has been reported by Apetrei *et. al.* that Langmuir-Blodgett thin film of lutetium bisphthalocyanines display broader and red-shifted absorbance peaks compared to films deposited by spin deposition¹⁵. Therefore, it

was proposed that absorption peak feature at ~1420 nm for a Langmuir-Blodgett deposited thin film of lutetium bisphthalocyanine, reported by Bariáin *et. al.*, may be at a lower wavelength value and may be less broad in the spin deposited thin film used in the work herein. This may result in no change of refractive index at the interrogation wavelength of 1550 nm; analogous to the ammonia sensing work reported above.

The second variable was the magnitude of the exposure time to the solvent vapour. In this experiment the sensor device was exposed to a flow of vapour of a solvent in nitrogen carrier gas for a total of 10 min for each solvent. In contrast, the solvent vapour exposure time in the work of Bariáin *et. al.* was on the order of hours and was a static exposure set-up as opposed to a flow system ¹². Therefore it was proposed that no appreciable change in refractive index occurred during the exposure to solvent vapour due to an insufficient exposure time.

8.6.2.2: Prolonged ‘dunk’ VOC sensing at 1550 nm experiment

To determine if the first factor caused no measurable change of refractive index the following experiment was performed. Bragg grating sensor device modified with a film of (10) was exposed to the vapour headspace above a volume of acetic acid, at a temperature of ~23 °C, for ~1.5 hours. Acetic acid was chosen as the analyte solvent because the greatest attenuation of the reflected power in the work of Bariáin *et. al.* was achieved upon exposure of the lutetium bisphthalocyanine film to acetic acid ¹². The difference between the average Bragg wavelength shift measured with the uncovered Bragg gratings and the average Bragg wavelength shift of the film covered Bragg gratings, over the duration of the experiment is shown below in **Fig.8.24**.

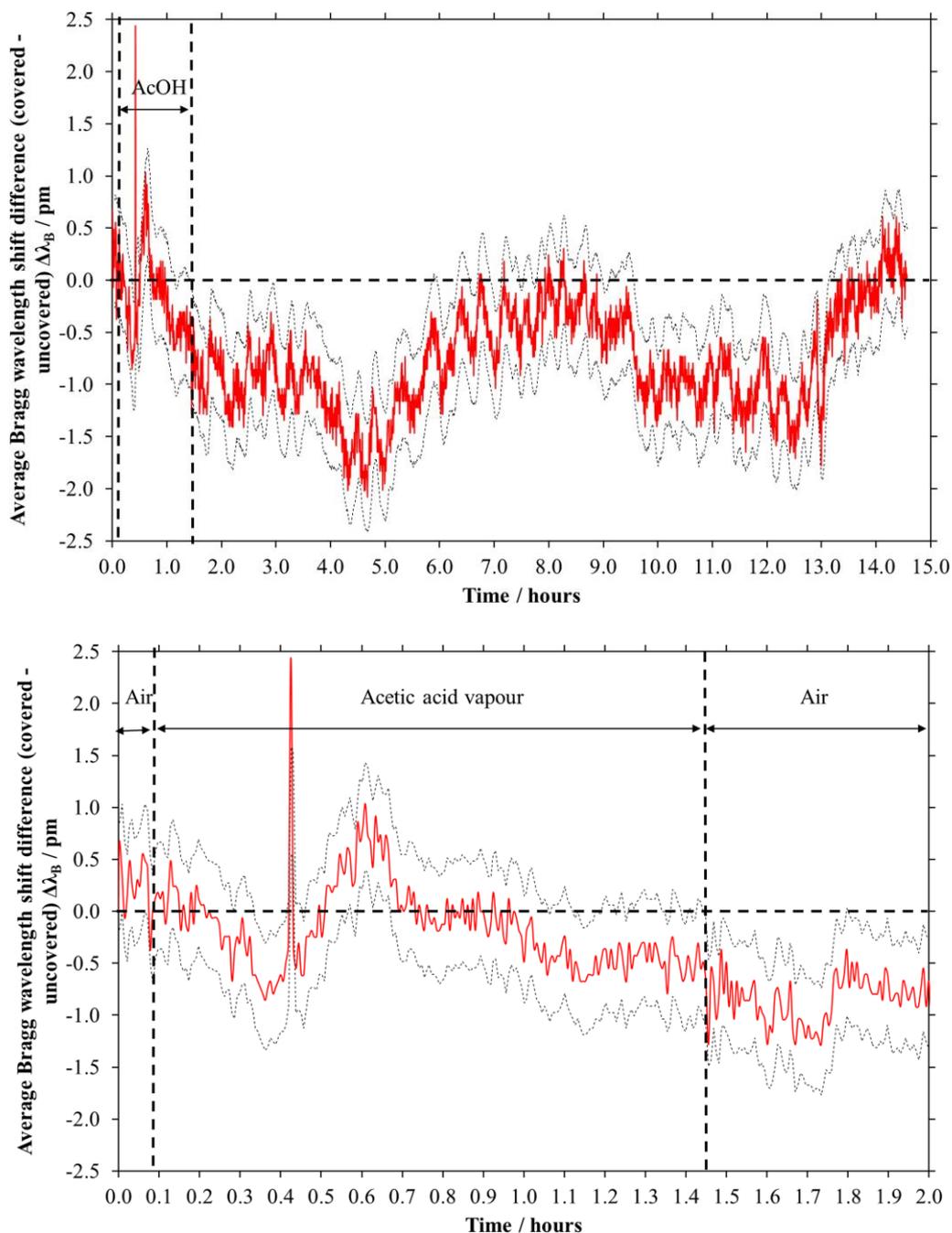


Fig.8.24: (Top) The difference between the average Bragg wavelength shift of the covered Bragg gratings and the average Bragg wavelength shift of the uncovered Bragg gratings was ~ 0 pm over the ~ 15 hr period of the acetic acid dunk experiment. The horizontal dashed line represents zero on the y-axis and the vertical dashed line denote the region where the sensor device was exposed to acetic acid vapours. (Bottom) The ~ 1.5 hour exposure to acetic acid vapour where the difference between the average Bragg wavelength shift for the covered Bragg gratings and Bragg wavelength shift of the uncovered Bragg gratings ~ 0 pm. The horizontal dashed line represents zero on the y-axis and the vertical dashed line denote the region where the sensor device was exposed to acetic acid vapours. In both plots the sharp spike at 0.4 h was a random outlier.

Despite a prolonged exposure (~1.5 h) of the Bragg grating sensor device modified with a film of (10) to acetic acid vapour the difference between the average Bragg wavelength shift measured with the uncovered Bragg gratings and the average Bragg wavelength shift of the film covered Bragg gratings was ~0 pm. After removal of the BGD from the acetic acid vapour headspace, Bragg wavelength measurement was continued for a further ~12 h to determine whether any Bragg wavelength shifts occurred due to removal from the acetic acid vapour and subsequent evaporation of acetic acid from the film of (10). However, as is evident in **Fig.8.24(Bottom)**, there was no overall difference between the Bragg wavelength shifts measured with the covered and uncovered Bragg grating upon removal, thus suggesting that removal from the vapour and evaporation of the acetic acid did not alter the optical properties of the lutetium bisphthalocyanine molecules.

The result from this sensing experiment suggests that the exposure time of the BGD to solvent vapour was not a contributing factor to the lack of a significant Bragg wavelength shift difference between covered and uncovered Bragg gratings.

8.6.2.3: Near-infrared spectroscopy of a film of (10)

To determine whether the spin deposited film of (10) differed optically to the Langmuir-Blodgett film of lutetium bisphthalocyanine in the literature, a film of (10) of was spin deposited onto a glass slide as per the spin deposition procedure used to deposit a film of (10) onto the Bragg grating sensor. The colouration of the resulting thin film of (10) was barely visible with the naked eye. This suggests that the film of (10) was very thin. The UV-visible-NIR absorption spectrum of the spin deposited film of (10) was then collected.

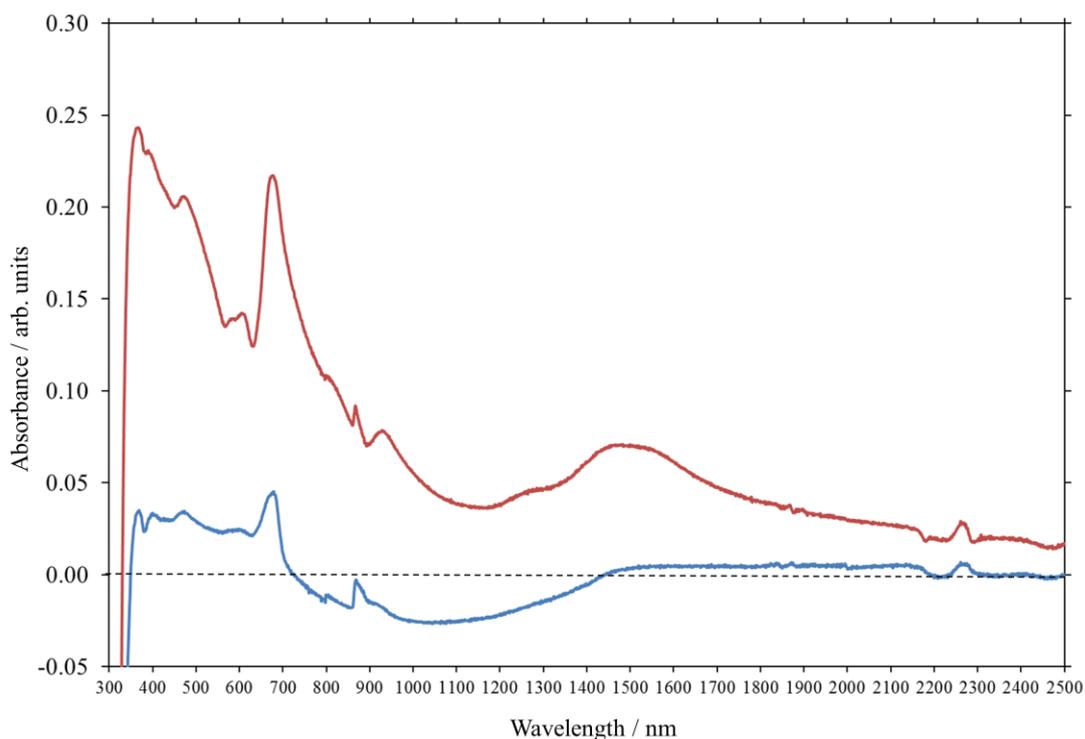


Fig.8.25: Transmission UV-Visible-NIR spectra of (blue line) a thin film of (10) which was fabricated using the spin deposition conditions used to produce the thin film of (10) on the Bragg grating sensor and for (red line) a evaporation deposited layer of (10). The negative absorption of the blue line spectrum is attributed to an etalon fringe period effect imposed on the spectra. Taking this into consideration, the spin deposited thin film of (10) displays little to no absorption at ~ 1420 nm whereas the evaporative deposited thin film does display a significant broad absorption at 1420. The substrates in both cases were soda glass microscope slides, hence the nonsense value below 350 nm.

As is evident in **Fig.8.25** above, there is little to no absorption at ~ 1420 nm for the thin film of lutetium bisphthalocyanine that was spin deposited (blue line). Therefore, due to the lack of a significant absorption peak there would be no associated change in the magnitude of absorption at ~ 1420 nm, therefore a significant change in refractive index at the interrogation wavelength of 1550 nm would not occur and thus no significant Bragg wavelength shift would occur. It was proposed that the absence of a significant absorption at ~ 1420 nm was due to the thickness of the spin deposited film of (10); a thin film of (10), tending towards the thickness of a few molecular layers, would have a small absorption cross-section (10). This was confirmed by the almost absence of colour in the thin film when observed by eye. In contrast, the layer of (10) that was fabricated by evaporative deposition was dark green by eye; a thicker film resulting in a greater absorption

cross-section, as confirmed by the spectrum (red line) in **Fig.8.25** above, which displays a significant absorption at ~ 1420 nm.

As identical spin deposition conditions were employed for the film of **(10)** on the Bragg grating sensor, it was proposed that the film of **(10)** on the Bragg grating sensor was of equivalent thickness to the thin film of **(10)** that was fabricated for the transmission spectra experiments above. Thus absorption due to **(10)** at ~ 1420 nm was insignificant and thus no significant change in refractive index at 1550 nm occurred. This was further compounded by the small interaction surface area between the evanescent wave and the thin film of **(10)**. The dimensions of the waveguide under the thin film of **(10)** are $\sim 4 \times 10^{-6}$ m by $\sim 5 \times 10^{-4}$ m resulting in an interaction surface area of 2×10^{-10} m², whereas the interaction surface area for the light in the UV-visible-NIR transmission spectroscopy was 2.5×10^{-8} m², a factor of 100 larger (assuming the beam spot was $\sim 5 \times 10^{-4}$ m by $\sim 5 \times 10^{-4}$ m).

Therefore, for a viable planar Bragg grating refractometric sensor for volatile organic compounds, a thicker film of lutetium bisphthalocyanine is required. The waveguide dimensions would remain equivalent, but the extent of the evanescent wave interaction volume would increase. To achieve this evaporative deposition could be used to deposit a thicker film of **(10)**. However, reproducibility in terms of thin film topography and thickness is hard to achieve with the evaporative deposition technique. To fabricate a planar optical integrated Bragg grating sensor with lutetium bisphthalocyanine as the active sensor element it is proposed that the evanescent wave interaction volume would need to be increased. This could be achieved through use of a sol-gel doped with/functionalised with lutetium bisphthalocyanine or a film of a polymer that is functionalised with lutetium bisphthalocyanine.

8.7 Conclusions and Further Work

It has been demonstrated that a planar integrated Bragg grating sensor chip, fabricated using the direct UV-writing approach, can be modified with a mesoporous sol-gel thin film doped with a pH chromic organic dye or a thin film of lutetium bisphthalocyanine. These sensors were then utilised to determine whether the change in refractive index of a material that occurs upon a colour change in the material

could be used to achieve refractometric sensing of gases with a planar Bragg grating sensor device.

The sol-gel thin film was doped with neutral red, a pH chromic organic dye that displays three colour states across a wide pH range, to form (8). Initial sensing experiments focussed on the sensing of ammonia, an alkaline gas that has medical significance. Initial exposure sensing experiments at 1550 nm were dominated by physisorption of water moisture. The sensor response to dry ammonia gas was then investigated, but it was found that no significant Bragg wavelength shift occurred upon colour change; the interrogation wavelength of 1550 nm was too far away from the change in absorption. These sensing experiments demonstrated the need to use an interrogation wavelength that is located close to the absorption change when utilising the Kramers-Kronig relation for refractometric sensing; this was confirmed by mathematical modelling of the dispersion curves of the thin film of (8).

An interrogation wavelength of 780 nm was then used, but it was found that the predicted change of 10 pm due to the colour change caused by exposure to ammonia in a 'dunk' exposure experiment was covered by the increased noise in the 780 nm experiments. Therefore, despite the medical significance of ammonia, focus was switched to the sensing of hydrogen chloride gas so that proof-of-concept was achieved. The colour change upon exposure to hydrogen chloride was predicted to cause a Bragg wavelength shift of ~35 pm and during a 'dunk' exposure experiment to hydrogen chloride fumes, a Bragg wavelength shift of ~20 pm was measured, after accounting for the effect of temperature change and moisture ingress upon the Bragg wavelength shift. Thus, a proof-of-concept Bragg grating refractometric gas sensor, that utilised the change in the absorption coefficient of neutral red upon exposure to hydrogen chloride fumes to induce a measurable refractive index change at 780 nm, due to exposure to a gas, was demonstrated.

Better agreement between the measured Bragg wavelength shift and the predicted Bragg wavelength shift could be achieved by implementing the experimental optimisations given above. In addition, future work would focus on confirming that the colour change, not moisture ingress, was the cause of the Bragg wavelength shift. To achieve this, the experiment would be performed with dry hydrogen chloride fumes that could be generated by drying a small volume of aqueous

hydrochloric acid solution on calcium chloride leading to the generation of hydrogen chloride gas. This gas could be further dried by passage through a column of granular calcium chloride.

For a suitable demonstration of this principle at telecoms wavelengths, a suitable probe molecule for organic vapour that would result in a refractive index change at 1550 nm upon changing colour was required. Lutetium bisphthalocyanine (LuPc₂) was chosen as the suitable probe molecule as thin films of LuPc₂ have been demonstrated in the literature as vapochromic materials at telecoms wavelengths¹². Lutetium bisphthalocyanine was successfully synthesised, as confirmed by UV-Visible and IR spectroscopy, melting point analysis, ¹H NMR and elemental analysis. A thin film of LuPc₂ was then spin deposited onto a Bragg grating sensor chip, but upon exposure to the vapour of different organic solvents, no overall Bragg wavelength shift was measured. By replicating the thin film of LuPc₂ on a transparent substrate and performing transmission NIR spectroscopic measurements, it was determined that the magnitude of the absorption cross-section of the LuPc₂ thin film was too small for a significant colour change to occur. Thus, no significant change in refractive index occurred and thus no overall Bragg wavelength shift occurred.

Therefore, for a viable planar Bragg grating refractometric sensor operating at 1550 nm, for volatile organic compounds, a thicker film of lutetium bisphthalocyanine is required. The waveguide dimensions would remain equivalent, but the extent of the evanescent wave interaction volume would increase due to the increased thickness of the active sensing film. This could be achieved through use of a sol-gel or polymer film that is doped with, or functionalised with lutetium bisphthalocyanine.

Upon fabrication of either a polymer or sol-gel layer, which is functionalised with lutetium bisphthalocyanine, a potentially robust and sensitive planar integrated optical Bragg grating sensor for volatile organic compounds will be realised. The facile fabrication techniques and associated advantages of the planar integrated optical format makes a sensor device modified with a robust and thick film of a material containing lutetium bisphthalocyanine a viable organic vapour sensor that offers advantages over the current electrical devices in a range of domestic, commercial and industrial settings. When combined with the previously reported

methods for monitoring temperature¹⁴ and pressure¹⁶, the suitability of integrated optical Bragg grating devices as sensors for physical and chemical stimuli, within distributed and multiplexed networks becomes apparent.

1. G. Rolla, M. Bruno, L. Bommarito, E. Heffler, N. Ferrero, M. Petrarulo, C. Bagnis, M. Bugiani, and G. Guida, *Eur. J. Clin. Invest.*, 2008, **38**, 728–33.
2. C. Holmes, PhD Thesis, University of Southampton, 2009.
3. D. De Sousa Meneses, G. Gruener, M. Malki, and P. Echegut, *J. Non. Cryst. Solids*, 2005, **351**, 124–129.
4. S. P. Limandri, R. D. Bonetto, H. O. Di Rocco, and J. C. Trincavelli, *Spectrochim. Acta Part B At. Spectrosc.*, 2008, **63**, 962–967.
5. U. Willer, D. Scheel, I. Kostjucenko, C. Bohling, W. Schade, and E. Faber, *Spectrochim. Acta. A. Mol. Biomol. Spectrosc.*, 2002, **58**, 2427–32.
6. G. Vladilo, G. Murante, L. Silva, A. Provenzale, G. Ferri, and G. Ragazzini, *Astrophys. J.*, 2013, **767**, 65.
7. P. E. Liley, G. H. Thomson, D. G. Friend, T. E. Daubert, and E. Buck, in *Perry's Chemical Engineer's Handbook*, eds. R. H. Perry, D. W. Green, and J. O. Maloney, McGrawHill, New York, 7th edn., 1999, pp. (2–1) – (2–374).
8. T. Levchenko, Y. Plyuto, and N. Kovtyukhova, *J. Sol-Gel Sci. Technol.*, 2007, **43**, 269–274.
9. M. K. Singh, *Photochem. Photobiol.*, 2000, **72**, 438–443.
10. H. Amouri and M. Gruselle, *Chirality in Transition Metal Chemistry: Molecules, Supramolecular Assemblies and Materials*, John Wiley & Sons, 2008, vol. 1.
11. S. Kasap and P. Copper, Eds., *Springer Handbook of Electronic and Photonic Materials*, Springer, New York, 1st Ed., 2006.
12. C. Bariáin, I. R. Matías, C. Fernández-Valdivielso, F. J. Arregui, M. L. Rodríguez-Méndez, and J. a. de Saja, *Sensors Actuators B Chem.*, 2003, **93**, 153–158.
13. M. Linaje, M. C. Quintanilla, A. González, J. L. del Valle, G. Alcaide, and M. L. Rodríguez-Méndez, *Analyst*, 2000, **125**, 341–346.
14. R. M. Parker, J. C. Gates, M. C. Grossel, and P. G. R. Smith, *Sensors Actuators B Chem.*, 2010, **145**, 428–432.

15. C. Apetrei, M. Nieto, M. L. Rodríguez-Méndez, and J. A. de Saja, *J. Porphyr. Phthalocyanines*, 2011, **15**, 908–917.
16. C. Holmes, L. G. Carpenter, J. C. Gates, and P. G. R. Smith, *J. Micromechanics Microengineering*, 2012, **22**, 025017.

9 Conclusions

9.1 Conclusions

In this work, the technique of direct UV-writing has been used to simultaneously define optical waveguides and short-period Bragg gratings (spaced along the length of the waveguides) within a photosensitive planar germanosilicate glass layer that is on top of a silica-on-silicon substrate. The waveguides are written due to the induced localised refractive index increase within the photosensitive glass layer, caused by exposure to a tightly focussed UV beam at 244 nm. The Bragg gratings, within the waveguides, are created by precise modulation of the interference pattern produced when two focussed and coherent UV laser beams (244 nm) are overlapped. The resulting Bragg gratings typically have Bragg wavelength values between 1400 – 1700 nm; within the near-infrared region.

The resulting reflectance spectra of these Bragg gratings were analysed remotely via an optical fibre pigtail and commercially available telecoms measurement equipment. This allowed for sub-picometre resolution of the peak Bragg wavelengths of the Bragg gratings.

As the Bragg gratings reside within the germanosilicate top layer of the waveguide structure, the evanescent waves within the Bragg gratings interact with the surrounding chemical environment. Any change in this chemical environment causes a change in the effective index of the Bragg grating. To satisfy the Bragg condition (see **Chapter 2**) the Bragg wavelength shifts in a corresponding manner. By measuring the Bragg wavelength shifts allows for indirect measurement of the change in refractive index; the Bragg gratings act as refractometers.

These planar integrated optical Bragg grating sensors allowed for novel gas sensors to be designed. In addition, gas sensing is required in a vast range of fields, such as in medicine, industry and in health and safety monitoring. However, due to the inherent lower density of gases compared to liquids, and relatively very slight differentiation between molecules of different gases, in terms of shape and size, meant that an alternate strategy to achieve enhanced sensitivity to gases was required.

9.1.1 Sol-gel thin films as the active sensor element

One approach to overcome these difficulties in gas sensing, which has been successfully demonstrated, was the application of a porous thin film on top of the core layer of the sensor. Through pseudo-confinement of gas molecules within the pores of the thin and subsequent interaction of gas molecules with the surface of the thin film, a larger number of gas molecules were within the penetration height of the evanescent wave, which is normal to the plane of the waveguide. Relative to a Bragg grating sensor with no thin film overlayer, the increased number of gas molecules within the extent of the evanescent wave, due to the thin film, resulted in a larger change of effective index and thus a larger shift in the Bragg wavelength. An increase in sensitivity was achieved.

A mesoporous silica sol-gel thin film was applied to the waveguide layer of a topless Bragg grating sensor chip. The thin film was applied in such a manner that some of the Bragg gratings were covered and the others were left exposed. The resulting sensor device was then exposed to changes in relative humidity from 0 – 100 %RH, where it was found that the exposed Bragg gratings demonstrated an average peak Bragg wavelength shift of 5 pm at all relative humidity values. On the other hand, the thin film covered Bragg gratings demonstrated a linear response of increasing Bragg wavelength shift with increasing relative humidity. This clearly demonstrated the thin film extended the sensitivity range of the covered Bragg gratings.

The suitability of this device as relative humidity sensor was investigated, but it was found that a decrease in sensitivity caused by hydrolytic degradation of the silica sol-gel thin occurred after two weeks of infrequent exposure to high relative humidity values. A replacement aluminosilicate sol-gel thin film, of equivalent thickness, was applied to the surface of the waveguide layer to remedy the issue of hydrolytic

degradation. In addition, the sensitivity of the sensor device was found to have increased due to the higher refractive index of alumina. The response of the sensor to changes in relative humidity was demonstrated in both a flow system and in the ‘static’ ambient laboratory atmosphere. The sensitivity of the relative humidity sensor was 0.69 ± 0.05 %RH/pm and the T_{90} response time was < 1 min. In addition this sensor allowed for the quantification of the effect of relative humidity on peak Bragg wavelength shift when a porous thin film is used as the active sensing element. Water moisture is typically present in analyte gases and this data allows for referencing of Bragg wavelength shifts caused by water moisture when sensing other gases.

9.1.2: Polymer thin film as the active sensing element

The second approach was the use of a thin film of a siloxane polymer for sensing of volatile organic compound (VOC) vapours. It was proposed that a thin film of a polymer, would swell by differing amounts when exposed to the vapours of different VOCs. This would cause a density change within the polymer thin film and a subsequent change in refractive index, in addition to the increased sensitivity due to the larger interaction volume.

A thin film (~ 1 μm), of an *n*-octyl group functionalised derivative of poly(hydromethyl)siloxane, was applied on top of the waveguide layer in a manner so as to achieve covered Bragg gratings for sensing and exposed Bragg gratings for temperature and strain referencing. The resulting sensor was exposed to the vapours of different organic solvents and both positive and negative magnitude peak Bragg wavelength shifts were measured. It was proposed that the negative Bragg wavelength shifts were caused by solvents with ‘poor solvating power’ for the polymer. These solvents subsequently caused the refractive index decreasing effect of swelling to dominate the refractive index increasing effect of solvent molecules displacing gas molecules. In contrast, for the positive Bragg wavelength shifts it was proposed that the vice versa argument held true.

Solvent properties such as $\log_{10} K_{ow}$ and the Hildebrand solubility parameter, δ_H , were used to quantify ‘solvating power’ and determine the effect on the sign and magnitude of the measured Bragg wavelength shifts. It was found that solvents with a similar $\log_{10} K_{ow}$ value to poly(dimethyl)siloxane, a derivative of PHMS, caused

the largest magnitude positive Bragg wavelength shifts. This was due to these solvents having the largest ‘solvating power’ for the polymer.

However, the relationships between a solvent property parameter and the Bragg wavelength shifts were non-linear, where some Bragg wavelength values could be caused by more than one solvent. This made prediction of Bragg wavelength shifts for this system non-trivial. Therefore a linear regression model for predicting the Bragg wavelength shifts for this system, based on properties of the analyte solvents, was developed by the use of QSAR and a backwards regression model approach. The resulting linear regression equation explained 89% of the variability in the Bragg wavelength shifts when the device was exposed to vapours of the solvents used in these experiments ($R^2 = 0.89$) and a high predictive ability ($Q^2 = 0.89$).

This proof-of-concept work demonstrated that a swellable polymer layer, deposited on the waveguide layer of a planar integrated optical Bragg grating sensor, is a viable approach for sensing and differentiation of different VOCs. However, further optimisation of the experimental setup is required to determine the sensor response at different concentrations of VOC vapour.

9.1.3: Utilising the Kramers-Kronig relation

The Kramers-Kronig relation relates the absorption features of a material to the refractive index of that material. A change to the inherent absorbance feature of a material at a certain wavelength, i.e. the absorbance peak shifting to a different wavelength or an absorbance magnitude change, results in a change to the refractive index of the material at that wavelength. Therefore, if a change to the inherent absorbance feature of a chemical was achieved by the interaction with a gaseous species, this would be a potentially selective method of gas sensing.

A proof-of-concept sensor device was fabricated by application of a silica sol-gel thin film to the waveguide layer in a similar manner used to create the relative humidity sensor. However, this mesoporous sol-gel thin film was doped with neutral red, an organic pH indicator dye. Upon exposure to hydrogen chloride fumes, the neutral red molecules immobilised in the pores of the sol-gel thin film visibly changed colour from pink to blue; a change to the absorption spectrum of neutral red induced by a reaction with gaseous hydrogen chloride. By modelling the refractive

index change, through the use of numerical solution models for the Kramers-Kronig method, a corresponding Bragg wavelength shift of ~ 25 pm was predicted at 780 nm. The sensor device was then interrogated at 780 nm, a wavelength near to the main absorption peak of the blue state neutral red molecule, and it was found that the colour change from pink to blue and vice versa, produced absolute Bragg wavelength shifts of ~ 25 pm in good agreement with the predicted value from the numerical modelling of the refractive index shift. This proof-of-concept of device demonstrated that utilising the Kramers-Kronig relation is a viable method of gas sensing using planar integrated optical Bragg grating sensors.

However, before this particular sensor design becomes a viable sensor for acidic gases, further optimisation is needed. For example, the period of the Bragg gratings in the sensor chip used were set for satisfying the Bragg condition at wavelengths centred around 1550 nm. The Bragg gratings were satisfactorily interrogated at 780 nm, by making use of an inherent frequency doubling effect, but the quality of the reflected signal was comprised. This would be overcome through the use of a Bragg grating sensor chip written for operation at 780 nm. In addition, the neutral red is not covalently bonded to the surface of the pores within the thin film, thus can be removed upon rinsing with water or other solvents. This seriously reduces the stability and reproducibility of this particular design of the acidic gas sensor. However, this could be overcome by use of a neutral red derivative that has a functional group to enable covalent bonding to the thin film surface, but is not a functional group that participates in, or affects, the pH chromism of the neutral red skeleton. The proposed synthetic route to such a neutral red derivative is highlighted below in section 9.2 below.

9.2 Further work

In this section further work that would optimise the sensors demonstrated in this work will be discussed. In addition other potential approaches to selective gas sensing using planar integrated optical Bragg grating sensor is also discussed.

9.2.1: Optimising the relative humidity sensor

9.2.1.1: Sensitivity and resolution limit improvement

The relative humidity sensor reported in **Chapter 6** has a resolution of 0.3 %RH at 21 °C. This resolution limit is comparable to the resolution limits of relative humidity sensors reported in the literature, but still could be improved to enable detection of incremental changes in relative humidity. A lower resolution limit would be obtained by increasing the sensitivity of the sensor device to water vapour. To achieve this, the penetration depth of the evanescent wave could be increased by application of a high index thin overlayer, such as tantalum pentoxide, on top of the waveguide layer. The use of a tantalum pentoxide high overlayer has been demonstrated previously to significantly increase the sensitivity of planar integrated optical Bragg grating sensors^{1,2}. With subsequent application of the aluminosilicate mesoporous thin film on top of the tantalum pentoxide sensing of relative humidity would be enabled, and the increased sensitivity would enable a lower resolution limit to be achieved.

9.2.1.2: Hydrolytic stability investigation

Despite showing no decrease in sensitivity for > 1 month, the hydrolytic stability of the aluminosilicate sol-gel thin film active sensing element at high relative humidity values could be investigated for an increased time period. This would enable conclusions on the operational lifetime of such a sensor to be drawn.

9.2.2: Optimising the volatile organic compound vapour sensor

Several optimisations are required to make the sensor reported in **Chapter 7** a viable sensor for the detection of VOCs in the field.

9.2.2.1: Sensing of vapours at different concentrations

An investigation into the response of the sensor device to different concentrations to particular VOCs is required. This will enable the sensitivity and resolution limit to be determined and for comparison of these values to VOC sensors that are commercially available, or reported in the literature. However, with the experimental set-up utilised in this work, precise concentrations of VOC vapours in nitrogen

carrier were hard to achieve. However, through the use of mass flow controllers, different concentrations would be achieved.

9.2.2.2: Polymer thin film thickness

It is proposed that the thickness of the polymer film has an effect on the sensitivity and response time of the proposed organic vapour sensor. A thin film would decrease the active sensing volume, as outlined in **Chapter 5** above, and thus decrease the overall sensitivity of the sensor. In contrast, a film which has a thickness \gg than the penetration height of the evanescent wave would increase in the response time of sensor and may even reduce the sensitivity. The response time would increase because the diffusion time of solvent molecules into the region of interaction with the evanescent wave, i.e. the rate determining step, would be greatly increased. In addition if the thickness of the polymer is too great, any swelling or solubilisation of the polymer layer may occur only in the top part of the thin film, which maybe out the region of interaction with the evanescent wave. Therefore a serious of thicknesses should be trialled to determine the optimal thickness of polymer thin film in terms of overall sensitivity and fastest response time.

9.2.2.3: Sensitivity improvement

The penetration height of the evanescent wave could be increased by application of a high index thin overlayer (in the order of ~ 10 's nm), such as tantalum pentoxide, on top of the waveguide layer. The use of a tantalum pentoxide high overlayer has been demonstrated previously to significantly increase the sensitivity of planar integrated optical Bragg grating sensors ^{1,2}. With subsequent application of the polymer thin film on top of the tantalum pentoxide overlayer, sensing of organic vapours would be enabled with increased sensitivity.

9.2.2.4: Optimisation of the polymer synthesis

To increase the mol% of the (methyloctyl)siloxane monomer that is achievable in a reasonable timescale, the optimisation of the hydrosilylation reaction is required. Choosing a solvent in which the catalyst is more soluble, will increase the number of catalytic species in solution available for reaction at any one moment and thus decrease the reaction time required to achieve 100 % conversion of poly(hydromethyl)siloxane to poly(octylmethyl)siloxane. The timescale required to

achieve 100% conversion using the current reaction set-up given in **Chapter 10** below is approx. 1 week.

However, it must be noted that the hydrophobicity of poly(octylmethyl)siloxane is predicted to be larger than the co-polymer used in this work. Therefore, the sensitivity of the sensor to solvents with inherent hydrophobicity greater than that of toluene or benzene would increase; the range of volatile organic compounds that can be detected would change.

9.2.3: Optimising the pH chromic refractometric sensor

Several optimisations are required to make the sensor reported in **Chapter 8** a viable sensor for the detection of acidic gases in the field.

9.2.3.1: Design of a 780 nm device with additional absorption loss measurement capability

As demonstrated in **Chapter 8**, the interrogation wavelength of the pH chromic refractometric sensor device needs to be close to the resonance wavelength of the organic dye. For neutral red, the most suitable interrogation wavelength is 780 nm. However, in **Chapter 8** the sensor device utilised was specifically written for interrogation at 1550 nm. Thus, when interrogated at 780 nm the optical loss was high due to the waveguide, which supports single modes at 1550 nm, supporting multimodes at 780 nm. This was further compounded by the inherent increased optical loss of smaller wavelengths propagating in a material due to increased Rayleigh scattering, which scales with λ^{-4} ; the smaller the wavelength the larger the optical loss via Rayleigh scattering.

Therefore, the first proposed improvement is the use of a Bragg grating sensor chip which has been written for interrogation at 780 nm, thus avoiding the loss of optical power by excitation of multiple other modes which are not the desired fundamental modes. The second proposed improvement is to create an ‘absorbance loss Bragg grating sensor device’, based on the work of Rogers *et.al.*³. The proposed ‘absorbance loss’ device is shown below in **Fig.9.1**.

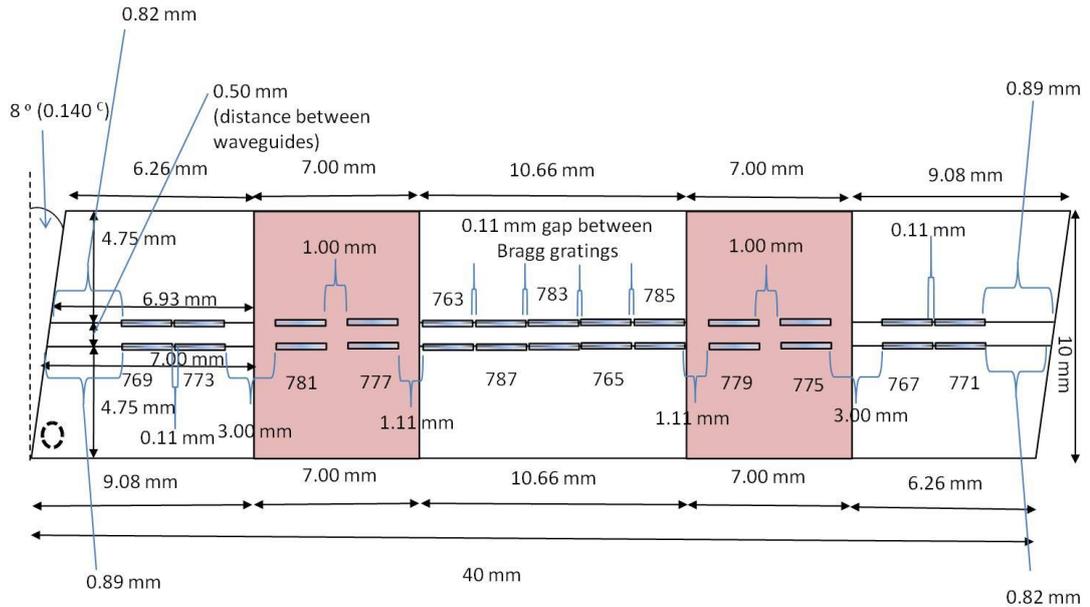


Fig.9.1: Schematic of the proposed refractometric & absorbance loss based pH sensor for sensing of acidic gases at 780 nm. The pink rectangles represent the areas to be coated with sol-gel thin films.

One strip will be undoped and the other strip of thin film will be doped with neutral red. The horizontal blue rectangles represent the Bragg gratings and the unitless numbers, above and below the Bragg gratings, are the corresponding Bragg wavelengths. The dashed line circle in the bottom left of the diagram is an indicator to enable determination of which end facet to pigtail.

This ‘absorbance loss’ device would function as a refractometric sensor in the same manner as the other Bragg grating sensors, in this work, have functioned. However, in addition, this device would also allow for the quantification of changes in the magnitude of the propagation loss, at 780 nm, along the waveguide, using the technique proposed by Rogers *et.al.*³ Assuming the change in the magnitude of the propagation loss was solely due to exposure to HCl (g), the absorbance losses across both the undoped and neutral red doped sol-gel thin films can then be determined. The propagation loss along the length of the waveguide would be measured from both opposing launch directions thus allowing the propagation loss along different lengths of the waveguide to be determined. This method is non-destructive, refractometric and crucially is independent of coupling loss and variability in the Bragg gratings³.

9.2.3.2: Synthesis of a neutral red derivative capable of covalent attachment to the matrix of the mesoporous thin film

In this work, neutral red was only held within the pores by physisorption, thus it could easily be removed by rinsing with, or immersion in a variety of solvents including water. Thus the durability and the reproducibility of the current sensor design are very poor.

To overcome this covalent attachment of neutral red to the aluminosilicate sol-gel thin film would prevent removal of the dye and thus increase the durability of the sensor. Therefore, a neutral red derivative with a functional group facilitating attachment to the sol-gel surface is desired. However, the ideal derivative must have similar pH chromic behaviour compared to neutral red. Thus the amine functional groups, which participate in the pH chromism of neutral red, must not be chemically altered. The structure of the proposed neutral red derivative is shown below in **Fig.9.2**. However, during attachment of the neutral red derivative onto the surface of the sol-gel, the primary amine group must be protected. This is to prevent the basic amine group accelerating the rate of hydrolysis of the alkoxy silane functional group.

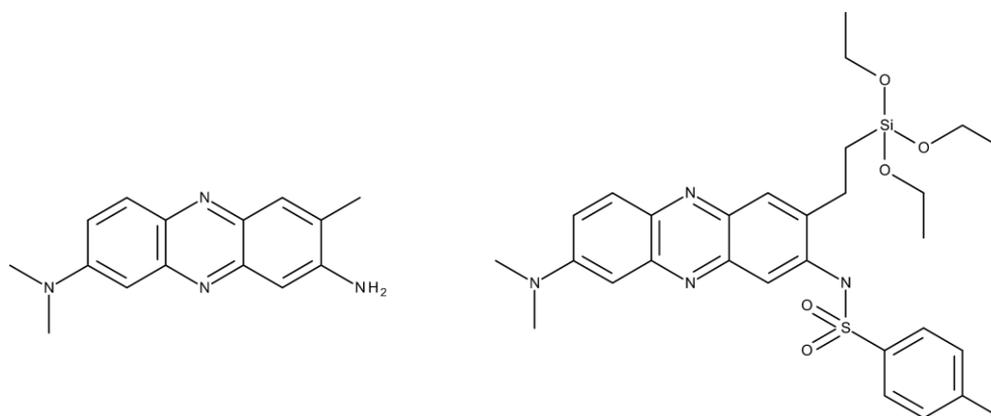


Fig.9.2: (Left) Structure of neutral red and (Right) the structure of the proposed tosyl-protected neutral red silane derivative, (N-[8-(dimethylamino)-3-(2-triethoxysilylethyl)phenazin-2-yl]-4-methyl-benzenesulfonamide).

A multistep synthesis route to the tosyl-protected neutral red silane derivative was proposed, using adaptations of literature procedures⁴⁻¹⁰. The proposed synthesis scheme is shown below in **Fig.9.3**.

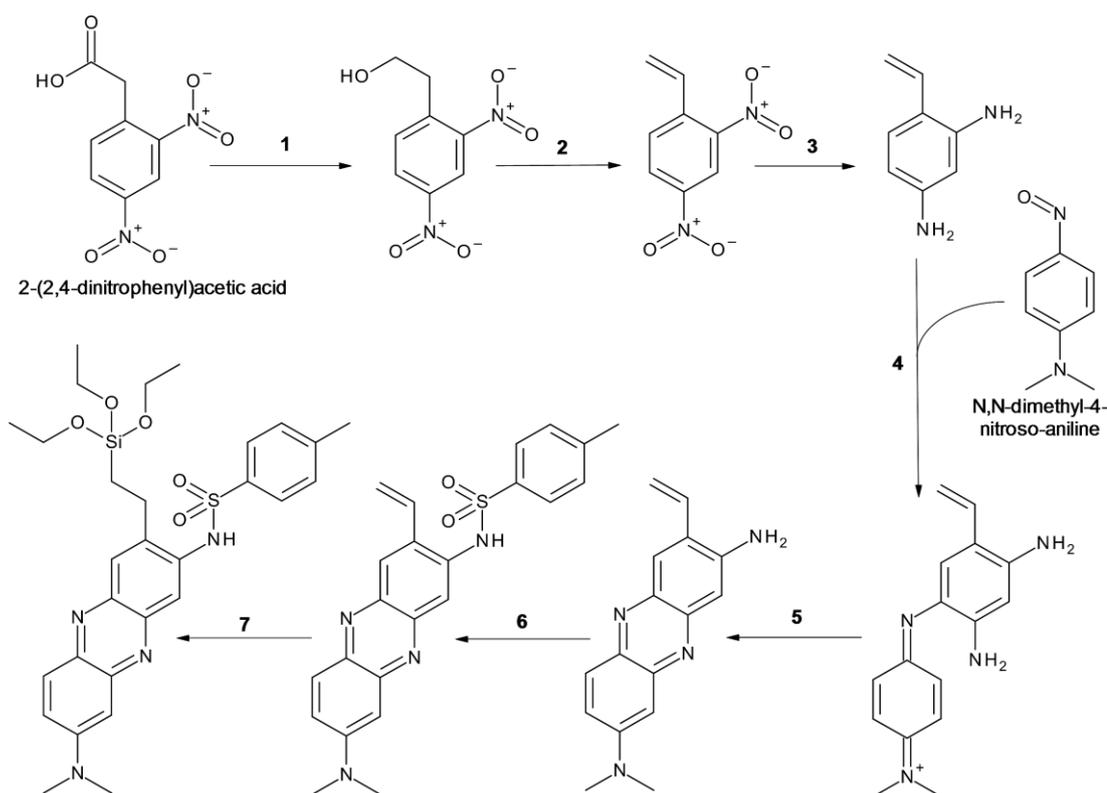


Fig.9.3: Proposed multistep synthetic pathway to achieve the tosyl-protected neutral red silane derivative. Reaction conditions: **1:** (i) BH_3 (THF adduct), THF, 25 °C, 5 hr (ii) H_2O . **2:** (i) nitric acid, urea, -10 °C, 0.5 hr **CARE:** This step produces a potentially explosive nitroester intermediate, (ii) sodium methoxide, MeOH/EtOH, 4 – 6 °C, 2 hr. **3:** (i) potassium carbonate, sodium dithionite, dioctyl viologen, water-DCM two-phase system, N_2 , 8 hr. **4:** N,N -dimethyl-4-nitroso-aniline, water, pH = 4.8, 30 °C, 4 hr. **5:** water, pH = 7.0, 80 °C, 3hr. **6:** 4-toluenesulfonyl chloride, cat. In, MeCN, 12 hr. **7:** i) triethoxysilane, cat. platinum-1,3-divinyldimethylsiloxane, Ar, 0 °C, toluene, ii) Reflux, 50 hr.

Once the derivative is synthesised, a pre-fabricated mesoporous silica sol-gel thin film would be treated with the derivative in mild hydrolysis conditions to facilitate hydrolysis of the trialkoxysilane functional group and subsequent covalent attachment via silicon – oxygen – silicon bond formation as shown in **Fig.9.4** below. The tosyl protecting group, which would have survived the mildly acidic hydrolysis conditions, would then be removed in highly acidic conditions to reveal the neutral red functionalised silica sol-gel thin film.

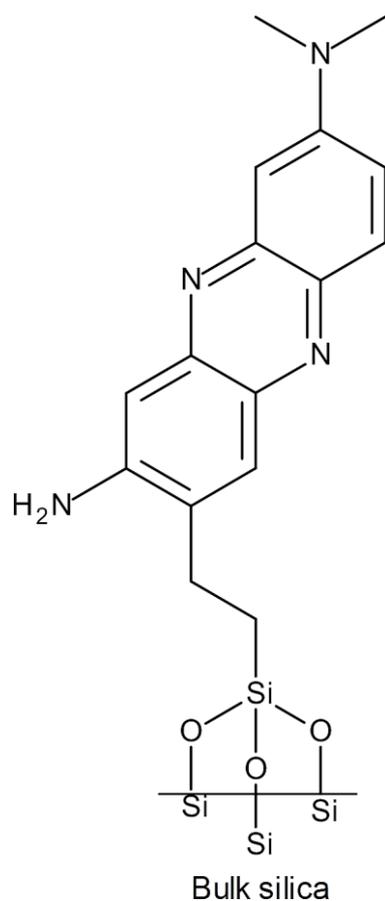


Fig.9.4: The proposed neutral red derivative covalently attached to the surface of the silica sol-gel

9.2.4: Other gas sensing approaches

9.2.4.1: Silica nanoparticles

An alternative approach to increase the interaction volume between the evanescent wave and analyte gas molecules could be by depositing/covalently attaching a monolayer or multiple layers of functionalised silica nanoparticles onto the surface of the sensor. It is expected that the sensitivity of the Bragg device would be increased by orders of magnitude due to a much greater number of analyte species encountered by the evanescent wave compared to a monolayer.

However for this approach to be viable, the size of the tethered particles needs to be considered. The particles must be large enough so a significant increase in surface area, within the region of the evanescent wave, is achieved. However, the particles must also be sufficiently small (smaller than $\sim 1/10$ the wavelength) so as to avoid an increase in optical loss via Rayleigh scattering; at an interrogation wavelength of 1550 nm, the particles must be < 150 nm in diameter.

9.2.4.1: Use of supramolecular and macrocyclic selective gas receptors

Despite the sensitivity and favourable gas sensing characteristics of the sol-gel and polymeric materials utilised in this work, these types of materials offer fewer preparation parameters that can be tailored to achieve selective gas sensing¹¹. In contrast, the control available over the synthesis of supramolecular and macrocyclic gas receptor compounds and subsequent assembly into thin films, makes these types of compounds particularly suitable for selective gas sensing¹¹. The molecular cavities in supramolecular entities such as calixarenes, cyclodextrins and resorcinarenes can be tailored in terms of size and chemical functionality which allows for fine control over selectivity¹¹⁻¹³. The synthetic chemist can also tune the selectivity of macrocyclic compounds, such as transition metal or lanthanide metal phthalocyanines, by changing the metal or appending different peripheral functional groups¹⁴⁻¹⁷. For these reasons, the use of supramolecular and macrocyclic based receptors would be an ideal method to achieve refractometric selective gas sensing with a high degree of control.

9.3 Final comments

In this work planar integrated optical Bragg grating sensors have been demonstrated as suitable platforms for refractometric sensing of gases and vapours. By utilising thin layers of porous or swelling materials, to make full use of the extent of the evanescent waves, high sensitivity to vapours has been demonstrated, in particular water vapour. In addition a proof-of-concept sensor device has been reported that makes use of the relationship between a material changing colour and the resulting change in refractive index. Looking forward, this enables the vast range of stimuli-chromic dye to be used for refractometric gas sensing. Overall the sensors reported herein have been shown to be competitive with other gas sensing techniques. With further advancements, such as achieving selectivity with supramolecular receptors, these planar integrated Bragg grating refractometric gas sensors have potential to be used in real-world gas sensing applications.

9.4 Dissemination of Research

9.4.1 Journal Publications that have arisen from this work

1. D.J. Wales, R.M. Parker, J.C. Gates, M.C. Grossel, P.G.R. Smith, An investigation into relative humidity measurement using an aluminosilicate sol-gel thin film as the active layer in an integrated optical Bragg grating refractometer, *Sensors & Actuators B: Chemical*, 2013, **188**, 857-866

9.4.2 Conference Proceedings that have arisen from this work

1. D.J. Wales, R.M. Parker, J.C. Gates, M.C. Grossel, P.G.R. Smith, Integrated planar Bragg grating oxygen sensor, in *15th European Conference of Integrated Optics (ECIO)*, 7th – 9th April 2010, Cambridge, England
2. D.J. Wales, R.M. Parker, J.C. Gates, P.G.R. Smith, M.C. Grossel, Integrated planar Bragg grating sensors: Towards an oxygen sensor, in *IS:CE-Chem Interreg Symposium*, 7th – 8th December 2010, Ouistreham, France
3. D.J. Wales, R.M. Parker, J.C. Gates, M.C. Grossel, P.G.R. Smith, An integrated Bragg grating oxygen sensor using a hydrophobic sol-gel layer with an organic dye, in *CLEO/Europe-EQEC*, 22nd – 26th May 2011, Munich, Germany
4. D.J. Wales, R.M. Parker, X.R. Bardy, J.C. Gates, P.G.R. Smith, M.C. Grossel, Towards an optoelectronic nose: Metal phthalocyanine modified siloxane polymers as sensing elements for volatile organic compounds, in *The 6th International Symposium on Macrocyclic and Supramolecular Chemistry (6th ISMSC)*, 3rd – 7th July 2011, Brighton, England
5. D.J. Wales, R.M. Parker, J.C. Gates, M.C. Grossel, P.G.R. Smith, Integrated Bragg grating sensors: Achieving chemical sensing in liquid and gas flow systems, in *IONS10 Southampton*, 10th – 12th August, Southampton, England
6. D.J. Wales, R.M. Parker, J.C. Gates, P.G.R. Smith, M.C. Grossel, An integrated ‘opto-electronic’ nose for the detection of gases, in *SET for Britain 2012*, 12th March 2012, House of Commons, Westminster (London), England

7. D.J. Wales, R.M. Parker, C.H. Holmes, J.C. Gates, M.C. Grossel, P.G.R. Smith, Integrated Bragg grating sensors: Achieving chemical sensing in gas flow systems, in *IONS13 Switzerland*, 10th – 12th January 2013, Zurich & Lausanne, Switzerland
8. D.J. Wales, R.M. Parker, C.H. Holmes, J.C. Gates, M.C. Grossel, P.G.R. Smith, Integrated Bragg grating sensors: Achieving chemical sensing in gas flow systems, in *The 56th Gas Analysis and Sensing Group (GASG) Colloquium*, 18th July 2013, National Physical Laboratory (NPL), Teddington, England.

9.4.3 Other journal publications that have arisen from associated work

1. R.M. Parker, J.C. Gates, D.J. Wales, P.G.R. Smith, M.C. Grossel, An investigation into dispersion upon switching between solvents within a microfluidic system using a chemically resistant integrated optical refractive index sensor, *Lab on a Chip*, 2013, **13**, 377-385

1. R. M. Parker, PhD Thesis, University of Southampton, 2010.
2. R. M. Parker, J. C. Gates, M. C. Grossel, and P. G. R. Smith, *Applied Physics Letters*, 2009, **95**, 173306.
3. H. L. Rogers, S. Ambran, C. Holmes, P. G. R. Smith, and J. C. Gates, *Optics letters*, 2010, **35**, 2849–51.
4. T. Bachels, Z. Cherkaoui, J.-F. Eckert, G. Marck, O. Muller, T. Peglow, J. Reichardt, A. Schuster, H. Seiberle, and P. Studer, 2011.
5. P. Kochergin, L. Blinova, G. Karpov, I. Mikhailova, E. Aleksandrova, and O. Korol, *Pharmaceutical Chemistry Journal*, 1999, **33**, 41–44.
6. K. K. Park, C. H. Oh, and W. K. Joung, *Tetrahedron Letters*, 1993, **34**, 7445–7446.
7. M. Philips and B. Cohen, *Biotech. Histochem.*, 1927, **2**, 74–78.

8. J. Fernando, *The Journal of organic chemistry*, 1967, **32**, 1120–1123.
9. J.-G. Kim and D. Jang, *Synlett*, 2007, **2007**, 2501–2504.
10. B. Lebeau, C. Marichal, A. Mirjol, G. J. D. a. a. Soler-Illia, R. Buestrich, M. Popall, L. Mazerolles, and C. Sanchez, *New Journal of Chemistry*, 2003, **27**, 166–171.
11. W. Göpel, *Sensors & Actuators: B. Chemical*, 1995, **24-25**, 17–32.
12. D. Filenko, T. Gotszalk, Z. Kazantseva, O. Rabinovych, I. Koshets, Y. Shirshov, V. Kalchenko, and I. Rangelow, *Sensors and Actuators B: Chemical*, 2005, **111-112**, 264–270.
13. N. S. Venkataramanan, R. Sahara, H. Mizuseki, and Y. Kawazoe, *The Journal of Physical Chemistry C*, 2008, **112**, 19676–19679.
14. A. El-Bosaty, T. El-Brolossy, and S. Abdalla, *Egypt. J. Solids*, 2006, 121–129.
15. F. I. Bohrer, A. Sharoni, C. Colesniuc, J. Park, I. K. Schuller, A. C. Kummel, and W. C. Trogler, *Journal of the American Chemical Society*, 2007, **129**, 5640–6.
16. S. Uttiya, T. Kerdcharoen, S. Vatanayon, and S. Partontep, *Journal of the Korean Physical Society*, 2008, **52**, 1575–1579.
17. N. Preethi, H. Shinohara, and H. Nishide, *Reactive & Functional Polymers*, 2006, **66**, 851–855.

10. Experimental

10.1 Introduction

Within this chapter the chemical and optical experimental procedures performed during this project are described. Firstly details of the synthesis and characterisation of the compounds and materials prepared during this work is presented. All compounds were prepared from commercially available starting materials and characterised by UV-visible spectroscopy, infrared spectroscopy, mass spectrometry, nuclear magnetic resonance (NMR) spectroscopy, melting point determination and elemental analysis where appropriate and compared with known literature data. Where appropriate and relevant, other characterisation techniques were used and these are also detailed within this chapter. In addition, the experimental methodologies used to achieve chemical functionalisation of the optical surfaces and corresponding confirmatory analytical data are presented. After the synthetic chemistry section, the fabrication and interrogation techniques of the optical devices are outlined in addition to full description of the optical gas sensing experiments performed during this study.

Note: The file name of the associated spectra and/or characterisation data is given in the text at appropriate points. The file names given refer to the file names of the spectra/data that are located on the attached spectra CD. The file names are in italic font.

10.2 General Experimental

Commercially available compounds and solvents were obtained from Sigma-Aldrich, Fisher or Acros and were reagent grade or better and used as supplied without further purification, unless explicitly specified below. Tetraethyl orthosilicate (TEOS) and trimethoxy(methyl)silane (MTMS) were of *Acros Seal*

grade. Methanol and ethanol were distilled over $\text{CaSO}_{4(s)}$, collected over 3A molecular sieves and then used immediately. Cetyltrimethylammonium bromide (CTAB) was dried and stored *in vacuo* in a desiccator before use. Lutetium(III) acetate and phthalonitrile were dried in the oven at $\sim 100\text{ }^{\circ}\text{C}$ for 2 hours before use.

Nuclear magnetic resonance (NMR) spectra were obtained using either a Bruker AV300 spectrometer, or a Bruker DPX400 spectrometer; operating at 300 or 400 MHz respectively for ^1H NMR experiments and at 75 MHz or 100 MHz respectively for ^{13}C and Dept-135 NMR experiments. ^{13}C spectra were collected fully decoupled. ^{31}P NMR spectra were collected fully decoupled using a Bruker AV300 spectrometer operating at 121 MHz. ^{29}Si NMR spectra were collected by Dr Neil Wells using a Bruker DPX400 spectrometer operating at 79 MHz with D_2O in an outer tube as a signal lock.

Electrospray (ES) (+ve and -ve) mass spectra were recorded using a Micromass Platform II single quadrupole mass spectrometer.

Melting points (MP) were measured using a Gallenkamp Electrothermal melting point apparatus and are uncorrected.

Combustion analysis (H,C,N) was performed by MEDAC Analytical Services Ltd (Egham, Surrey).

UV/Visible absorbance and transmission spectra were collected using a Shimadzu Recording Spectrophotometer UV-1601 connected to a Windows PC running UVPC version 3.5. The samples were held at an angle 'x' (where $45^{\circ} < x < 90^{\circ}$) to the incident beam to avoid etalon fringe effects.

IR spectra were collected with a Nicolet 380 FT-IR Spectrometer with a SmartOrbit Golden Gate Attenuated Total Reflection (ATR) attachment.

Raman spectra collected using a Perkin-Elmer 2000 FT NIR Raman spectrometer connected to a Windows PC running Raman spectra software. Nd:YAG laser ($\lambda = 1064\text{ nm}$) output power varied (200 mW – 600 mW).

Calcination of templated mesoporous silica sol-gel thin films was performed using a Severn Thermal Solution Tube Furnace (Max. 1200 oC) controlled by a Eurotherm 2408 controller unit and two Eurotherm 2208 slave units.

Surface profile data (Step height and surface roughness, R_a) were recorded using a KLA Tencor P.16 surface profiler running Profiler v7.21.

AFM images were acquired using a AIST-NT Instruments SmartSPM 1000, which was operated in phase imaging mode.

Thin film refractive indices were determined by the prism coupling method using a METRICON Prism Coupler Model 2010/M at 633 nm or 1553 nm.

Thin-film X-ray diffraction studies were performed on both a Siemens D500 powder diffractometer and a Bruker GADDS diffractometer. The Siemens D500 powder diffractometer was run in Bragg-Brentano para-focusing geometry. Cu $K\alpha$ radiation ($\lambda = 1.54056 \text{ \AA}$) from a Ge crystal monochromator was generated at 30 kV, 30 mA. The incident beam passed through a 2 mm divergence slit and the diffracted beam passed through a 2 mm anti-scatter slit and 0.2 mm receiving slit at the focal point of the scintillation counter. The Bruker GADDS diffractometer was run in pseudo-parallel beam geometry. Cu $K\alpha$ radiation ($\lambda = 1.54184 \text{ \AA}$) from a Goebel mirror was generated at 40 kV, 40 mA. The incident beam passed through a 2 mm optics slit and then one 0.5 mm, 15 cm collimator to provide a spot focus on the sample. The system is fitted with a 2D HiStar multi-wire detector which collects a static range of ca $46^\circ 2\theta$. Data was corrected for spatial warping and integrated using GADDS software [GADDS (V 4.1.32) Bruker AXS. Smith, K.L., Jin, Z., Chambers, L., He, B., Preckwinkel, U. & Moran, D.]

Back scattered electron and secondary electron scanning electron micrographs were collected using a ZEISS EVO 50 scanning electron microscope (SEM) in variable pressure mode (40 – 60 Pa) or high vacuum mode controlled by a Windows PC running Zeiss Smart SEM software.

Energy dispersive X-ray spectroscopy (EDX) was performed with an Oxford Instruments INCA X-ray detector (Be window) attachment on the ZEISS EVO 50 (SEM) connected to a computer running INCA EDX software for Windows. The SEM settings for EDX spectra collection were as follows: high vacuum mode; 20 μm aperture; working distance = 9.5 cm; accelerating voltage = 20 kV, gun current ~ 2.45 A, magnification ~ 5000 times.

Spin coating was performed either using a bespoke spin coater (made in-house), or a Speciality Coating Systems Inc. G3P-8SPINCOAT in the Optoelectronics Research Centre (ORC) cleanroom.

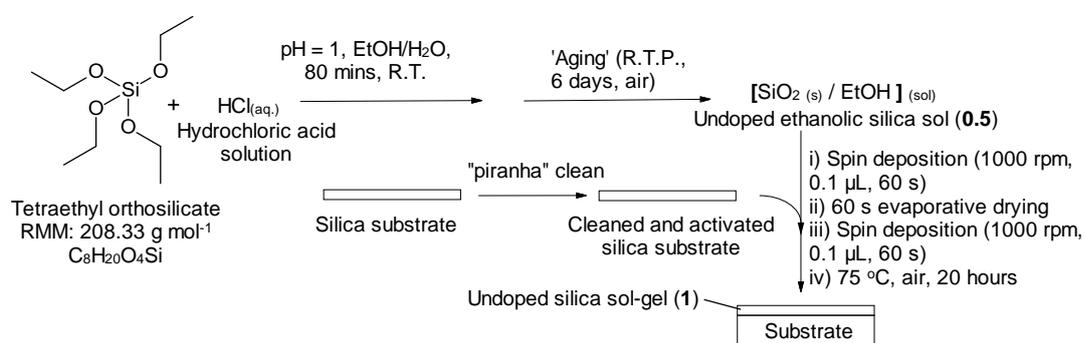
Centrifugation was performed using an Eppendorf Centrifuge 5702 (0 – 4400 rpm) at room temperature.

Direct UV writing of waveguides containing Bragg gratings was performed using a Cambridge Laser Laboratories Lexel 95 SHG UV laser with an Aerotech A3200 air stage.

10.3 Chemical Synthesis

Detailed synthetic procedures and characterisation data for the compounds and materials discussed within this thesis are given below. Where appropriate the characterisation data of the compounds and materials reported herein are compared to reported data in the literature.

10.3.1 Undoped silica sol-gel (1)



Scheme 10.1: Synthetic preparation of (1) via (0.5)

Tetraethyl orthosilicate (TEOS) (2.25 ml, 1.02 x 10⁻² mol) was dissolved in ethanol (2.5 ml) to form a colourless solution which was stirred. After 20 mins an aqueous hydrochloric acid solution (1M, 0.5 ml) was added and the reaction was stirred for 60 mins. Once complete, ethanol (0.5 ml) was added and the resulting colourless sol was left to stir/age for 6 days to form an undoped ethanolic silica sol (0.5). An aliquot of the undoped ethanolic silica sol (0.5) was then characterised. In addition an aliquot of the undoped silica ethanolic sol was evaporated to dryness to form a colourless brittle thin film. This was ground to form a fine white solid which was then characterised.

For spin deposition of a thin film, undoped ethanolic silica sol (**0.5**) (0.2 μL in total) was deposited onto the partially masked top face of a topless silica waveguide by initial dropwise addition of sol (0.1 μL) followed by spin coating at 1000 rpm for 60 s to form a thin layer. Dropwise addition of the final sol aliquot (0.1 μL) onto the previous sol-gel layer followed by spin coating at 1000 rpm for 60 s, formed an uniform layer. This process was carried out at R.T.P in a Class 1000 cleanroom. The sol-gel modified device was then baked at 75 $^{\circ}\text{C}$ for ~20 hours to afford a thin film of the undoped silica sol-gel (**1**) film on the area which had not been masked by polyimide tape during the spin deposition.

Undoped ethanolic silica sol (**0.5**):

UV-Visible (λ_{max} / nm): 201.0

FT-IR (ν / cm^{-1}): 3314 (v.br., - O - H hydrogen bonded, EtOH), 2974 (m, alkyl C - H stretch, EtOH), 2928 (w, alkyl C - H stretch, EtOH), 2892 (w, alkyl C - H stretch, EtOH), 1080 & 1044 (s, Si - O - Si, split band indicative of long siloxane chains), 879 (s, amorphous silica IR absorption) ¹. See: *DJW.6066.Undoped TEOS silica sol (0.5).FT-IR*

¹H NMR (EtOH-d₆, δ / ppm): Only ¹H signals due to ethanol were observed. [5.32 (br. s., CH₃CH₂OH), 3.54 (m, 2H, CH₃CH₂OH), 1.11 (m, 3H, CH₃CH₂OH)]. See: *DJW.6066.Undoped TEOS silica sol (0.5).1H NMR.MA1213DJW1.010.esp*

¹³C NMR (EtOH-d₆, δ / ppm): Only ¹³C signals due to ethanol were observed. [56.72 (s, CH₃CH₂OH), 17.31 (s, CH₃CH₂OH)]. See: *DJW.6066.Undoped TEOS silica sol (0.5).13C NMR.ma1213djw1.011.esp*

Undoped silica sol-gel (**1**):

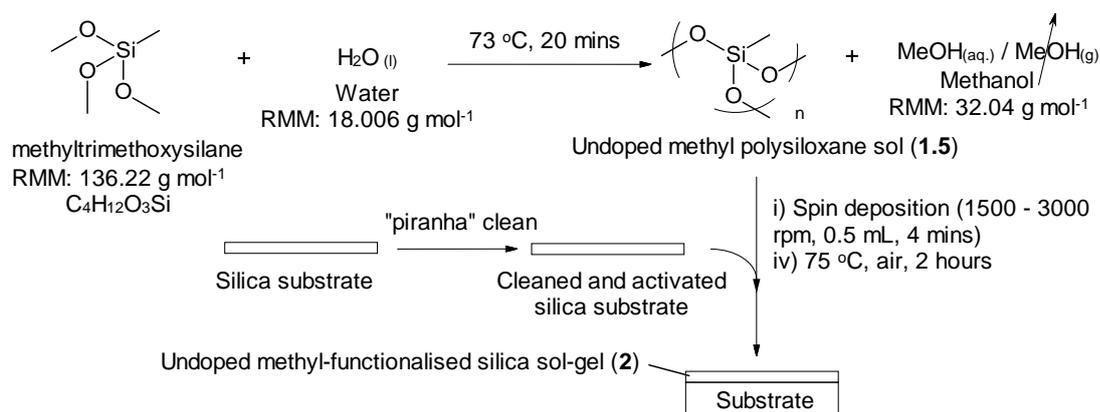
M.P. (uncorrected): > 300 $^{\circ}\text{C}$ (Lit. ²: 1723 $^{\circ}\text{C}$)

FT-IR (ν / cm^{-1}): 3253 (v.br., Si - O - H hydrogen bonded), 1056 (br. & s., Si - O - Si), 942 (br. & s., Si - O - H), 790 (m, characteristic absorption of amorphous silica). See: *DJW.6066.Undoped TEOS silica sol-gel (1).FT-IR*

Raman shifts (1064 nm excitation) / cm^{-1} : 428 (v. br, Si - O - Si bending modes) ³

This is consistent with the reported data ¹⁻³

10.3.2 Undoped methyl-functionalised silica sol-gel (2)



Scheme 10.2: Synthetic preparation of (2) via (1.5)

Deionised water (0.2 ml, 0.01 mol) was added to trimethoxy(methyl)silane (1.05 ml, 7.36×10^{-3} mol) to afford a suspension of water droplets in the colourless trimethoxy(methyl)silane. The reaction mixture was then stirred at 73 °C. After ca. 5 mins condensation of a liquid was observed on the walls of the RBF. After 20 mins, the undoped methyl polysiloxane sol (1.5, 0.5 ml) was applied to the top face of a prepared silica substrate and then spin coated within the range of 1500 – 3000 rpm for 4 mins before being baked at 70 °C for 2 hours to afford colourless and clear silica glass-like films of 2.

Undoped methyltrimethoxysilane sol (1.5):

FT-IR (ν / cm^{-1}): 3405 (br. H – bonded O – H stretch, MeOH or H₂O), 2946 (m, asymmetric C – H stretch, - CH₃ group), 2842 (C – H stretch, Si – O – CH₃), 1268 (s, Si – C bond stretch, Si – CH₃ in H₃C – Si(OR₃) polysiloxane system), 1191 (m, Si – O – CH₃), 1078 (s, Si – O – Si), 792 (s, Si – C bond stretch, Si – CH₃ in H₃C – Si(OR₃) polysiloxane system)¹. See: *DJW.6625.32.MTMS silica sol-gel sol (1.5).FT-IR*

¹H NMR (MeOH-d₄ δ / ppm): 4.89 (br.s., H₂O), 4.47 (v.br.s., -OH, Si – O – H), 3.49-3.46 (m, Si – O – CH₃), 3.31 (br.s., CH₃ – OH), 0.09-0.02 (m, Si – CH₃)⁴. See: *DJW.6625.32.MTMS silica sol (1.5).1H NMR.AP0413DJW1.0.10.esp.*

Unreliable integrals due to overlapping signals and poor signal-to-noise ratios.

^{13}C NMR (MeOH- d_4 δ / ppm): 50.78-49.99 (cluster of six signals, Si – O – CH₃ showing different degrees of hydrolysis), \sim 3.00-7.10 (11 signals, CH₃ – Si –, showing different degrees of hydrolysis) ⁴. See: *DJW.6625.32.MTMS silica sol (1.5).13C NMR.positive ppm.AP0413DJW1.011.esp* AND *DJW.6625.32.MTMS silica sol (1.5).13C NMR.negative ppm.AP0413DJW1.011.esp*.

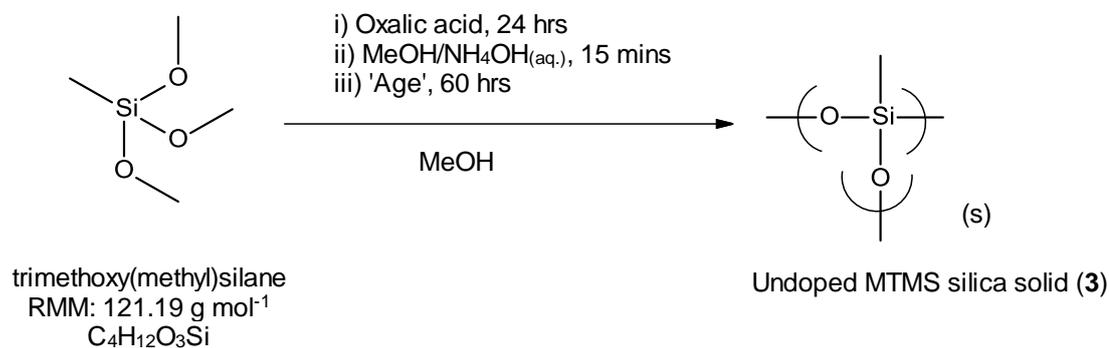
Undoped methyl-functionalised silica sol-gel (2):

M.P. (uncorrected): > 300 °C (Lit. > 257 °C ⁵. decomposition: loss of – CH₃ group)

FT-IR (ν / cm⁻¹): 2969 (w, C – H stretch, - CH₃), 1270 (s, Si – CH₃), 1023 (s. & br., Si – O – Si, broadness indicative of long and branched siloxane chains), 776 (s, Si – CH₃) ¹. See: *DJW.6625.32.MTMS fast sol-gel (2).FT-IR*

This is consistent with the reported data ^{1,4,5}.

10.3.3 Undoped MTMS silica solid (3)



Scheme 10.3: Synthetic preparation of (3)

Trimethoxy(methyl)silane (MTMS) (2.0 ml, 1.40×10^{-2} mol) and methanol (7.8 ml, 1.93×10^{-1} mol) were charged to the reaction vial. To this an aqueous solution of oxalic acid (0.6 ml, 1×10^{-3} M) was added, the reaction vial was sealed and the reaction mixture was left to stir for 24 hours to afford (2.5). After 24 hours aqueous ammonium hydroxide solution (0.8 ml, 11 M) was added to the sol, the vial re-sealed and left to stir for 15 minutes. During this time methanol (0.5 ml) was added with stirring to the sol. After 15 minutes the reaction vial was unsealed and the slightly turbid sol was allowed to ‘age’ without stirring for \sim 60 hours to afford a white sol-gel monolith in the vial. The monolith was mechanically ground into a white

powdery solid (**3**). Varying masses of this solid were suspended in 1.5 ml aliquots of methanol and spin coated with varying parameters (see **Results and Discussion** section above) to afford thin films on glass substrates with different thicknesses. However, all the thin films displayed a powdery appearance.

Undoped MTMS silica sol (2.5)

FT-IR (ν / cm^{-1}): 3405 (br. H – bonded O – H stretch, MeOH or H₂O), 2946 (m, asymmetric C – H stretch, - CH₃ group), 2842 (C – H stretch, Si – O – CH₃), 1268 (s, Si – C bond stretch, Si – CH₃ in H₃C – Si(OR₃) polysiloxane system), 1191 (m, Si – O – CH₃), 1078 (s, Si – O – Si), 792 (s, Si – C bond stretch, Si – CH₃ in H₃C – Si(OR₃) polysiloxane system). See: *DJW.6625.32.MTMS silica sol-gel sol (1.5).FT-IR*

¹H NMR (MeOH-d₄ δ / ppm): 4.87 (br.s., H₂O), 4.57 (br. sh., -OH, Si – O – H), 3.47 (m, -O – CH₃, different degrees of hydrolysis), 3.31 (br.s., CH₃ – OH), 0.07 (m, Si – CH₃, different degrees of hydrolysis)⁴. See: *DJW.6625.32.Fast sol-gel powder sol (2.5).1H NMR.ap1713djw5.010.esp*

Unreliable integrals due to overlapping signals and poor signal-to-noise ratios.

¹³C NMR (MeOH-d₄ δ / ppm): 50.8-50.3 (cluster of signals, Si – O – CH₃ showing different degrees of hydrolysis), -3.50-7.20 (10 signals, CH₃ – Si, showing different degrees of hydrolysis)⁴. See: *DJW.6625.32.MTMS silica sol (1.5).13C NMR.positive ppm.AP0413DJW1.011.esp* AND *DJW.6625.32.MTMS silica sol (1.5).13C NMR.negative ppm.AP0413DJW1.011.esp*.

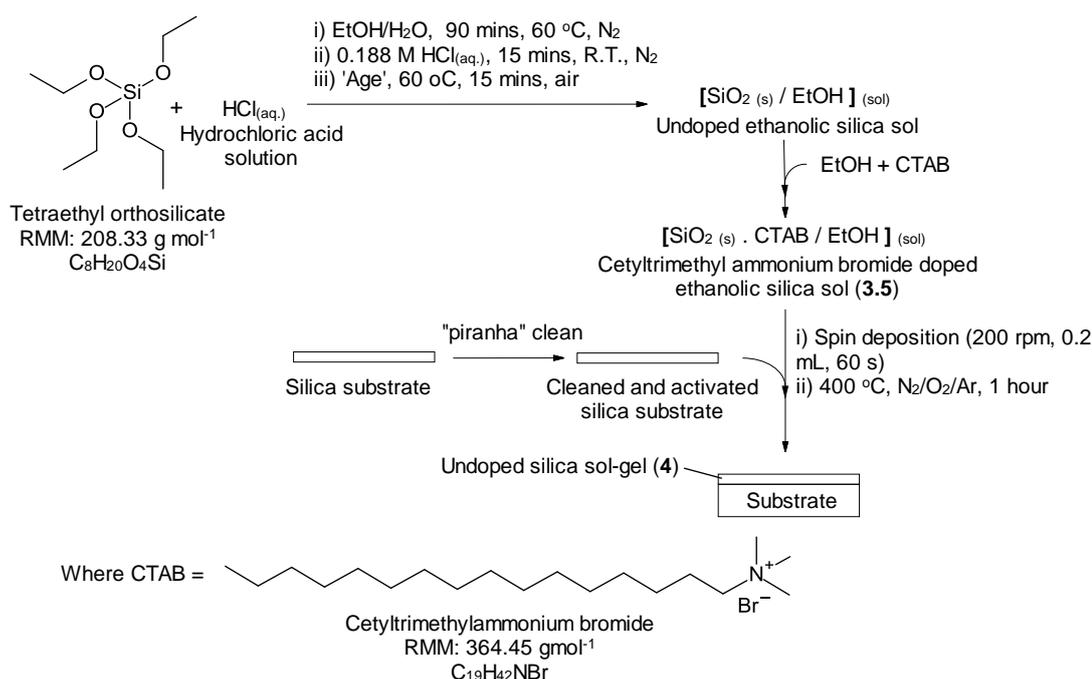
Undoped MTMS silica solid (3):

M.P. (uncorrected): > 300 °C (Lit.⁵: >257 °C (decomposition))

FT-IR (ν / cm^{-1}): 2971 (w, C – H stretch, - CH₃), 1270 (s, Si – CH₃), 1014 (s. & br., Si – O – Si, broadness indicative of long and branched siloxane chains), 762 (s, Si – CH₃)¹. See: *DJW.6625.31.Fast sol-gel MTMS solid (3).FT-IR*

This is consistent with the reported data^{1,4,5}.

10.3.4 Undoped mesoporous silica sol-gel thin film (4)



Scheme 10.4: Synthetic preparation of (4) via (3.5)

Tetraethyl orthosilicate (TEOS) (10 mL, 4.478 × 10⁻² mol), distilled ethanol (7.85 mL, 1.34 × 10⁻¹ mol), de-ionised water (6.432 mL, 3.58 × 10⁻¹ mol) and HCl_(aq.) (0.1 M, 22.4 μL) were added to an RBF with stirring to form a cloudy colourless solution which was heated for 90 mins at reflux under nitrogen. After cooling to room temperature HCl_(aq.) (0.966 mL, 0.188 M) was added to the cloudy reaction mixture and this was then stirred for 15 mins under nitrogen to form a clear and colourless solution. The sol was then 'aged' without stirring in ambient conditions for 15 mins before the addition of distilled ethanol (3 volumes) and cetyltrimethylammonium bromide (2.5518 g, 7.00 × 10⁻³ mol) with stirring in ambient conditions to form a colourless sol. The sol (0.2 mL) was then spin deposited onto a partially masked silica substrate at 2000 rpm for 1 min. The silica substrate had been cleaned in piranha solution for 1 hour, rinsed with de-ionised water and dried under a stream of nitrogen before use. The clear and colourless sol-gel thin films were calcined at 400 °C for 1 hour (heating rate 1.5 °C min⁻¹) in a N₂/O₂/Ar atmosphere before cooling to room temperature.

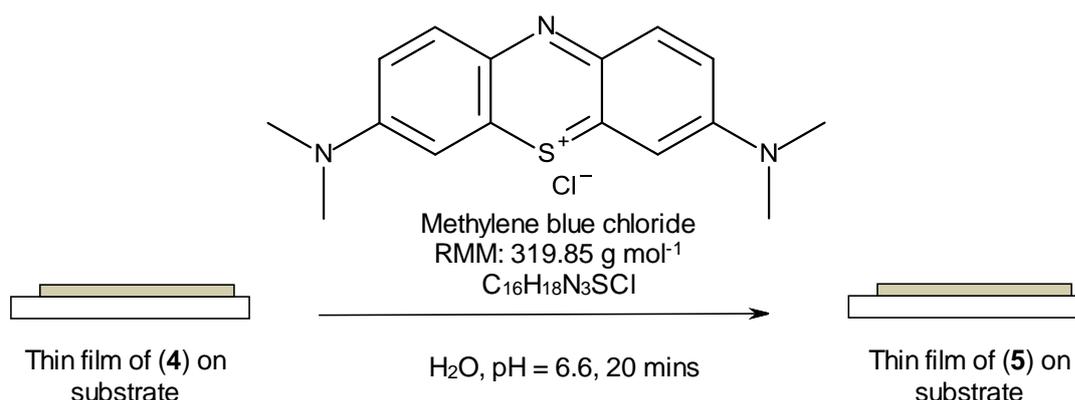
Undoped ethanolic silica sol (3.5)**UV-Visible spectroscopy, neat (λ_{\max} / nm):** 206.0

FT-IR (ν / cm^{-1}): 3334 (br. -O – H hydrogen bonded, EtOH or H₂O), 2973 (s, alkyl C – H stretch, EtOH or CTAB or TEOS), 2926 (m, same as 2973), 2900 (m, same as 2973), 1200 (s, Si – O – Si asymmetric stretch in cyclic structures), 1086 (s, Si – O – Si cyclic structure stretches), 1044 (s, C – O stretch, EtOH or TEOS) ¹. See: *DJW.6066.85.CTAB templated TEOS silica sol (3.5).FT-IR.*

¹H NMR (MeOH-d₄ δ / ppm): Only ¹H signals due to ethanol were observed. No alkoxy signal from TEOS observed. See: *DJW.6066.85.CTAB templated TEOS silica sol (3.5).1H NMR.AP3012DJW1.010.esp*

Undoped mesoporous silica sol-gel (4):**M.P. (uncorrected) / °C:** > 300 °C (Lit. ²: 1723 °C)

FT-IR (ν / cm^{-1}): 3296 (v.br., -O – H stretch, Si – O – H), 1019 (v.br and splitting, Si – O – Si, very broad peak with splitting indicates very long and branched siloxane chains) ¹. See: *DJW.6625.32.CTAB templated TEOS silica sol-gel (4).FT-IR*

This is consistent with the reported data ^{1,2}**10.3.5 Methylene blue doped mesoporous silica sol-gel thin film (5)**

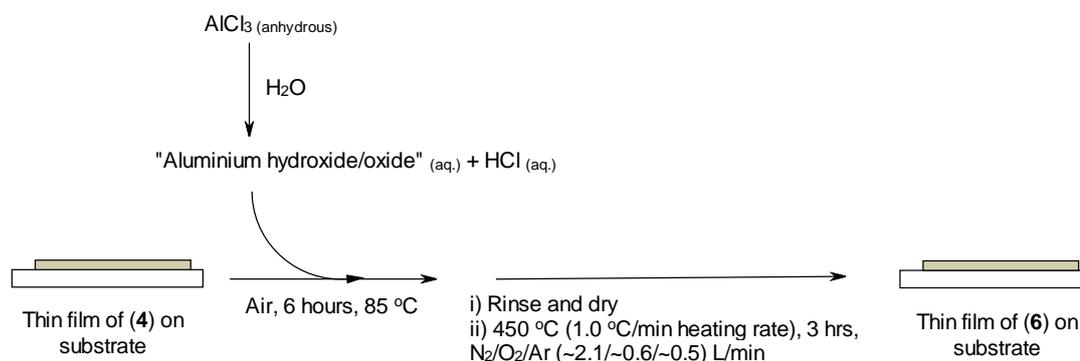
Scheme 10.5: Immersion of a thin film of (4) into an aqueous methylene blue chloride solution to form a blue coloured methylene blue doped thin film, (5).

A thin film sample of (4) (~300 nm) was immersed in an aqueous solution of methylene blue chloride ($1 \times 10^{-4} \text{ mol dm}^{-3}$, pH = 6.6) for 20 mins with stirring. The sample was then removed from the solution, washed copiously with deionised water for 15 secs and then dried for 1 min under a stream of nitrogen gas to afford an intense blue coloured sample of (5).

UV-Visible transmission spectroscopy (solid state, λ_{max} / nm): 600.5⁶

This is consistent with the reported data⁶.

10.3.6 Undoped mesoporous aluminosilicate sol-gel thin film (6)

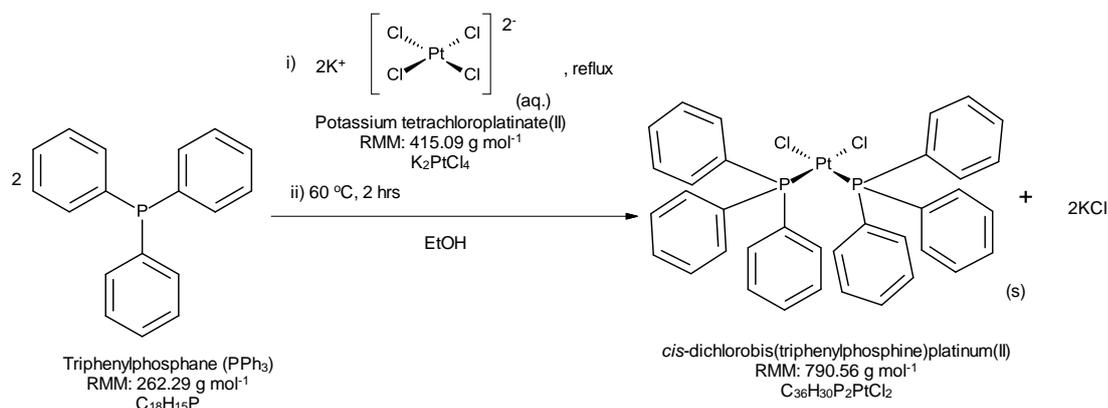


Scheme 10.6: Grafting of aluminium oxide onto a thin film of (4) to form a thin film of (6)

Anhydrous aluminium chloride (~1.6 g) was cautiously added to deionised water (25 mL) with stirring to form a clear and colourless aqueous solution of ‘aluminium hydroxide/oxide’ species. A thin film of (4) was immersed in this solution at 85 °C for 6 hours, rinsed copiously with de-ionised water and dried under a stream of nitrogen gas. The substrate was then calcined at 450 °C for 3 hours (heating rate 1.0 °C/min) in a N₂/O₂/Ar (~2.1 : ~0.7 : ~0.5 L/min) atmosphere to consolidate the aluminium oxide. Mesoporous silica is known to slowly dissolve under these reaction conditions until the protective alumina layer is fully formed. To compensate for this erosion, the thin film of (4) was ~300 nm thick; this was achieved by deposition at a lower spin speed. This film subsequently reduced in thickness during the reaction to 260 ± 24 nm for the aluminium oxide grafted mesoporous thin film. In this way both thin films of (5) and (4) of comparable thickness could be fabricated allowing for direct comparison.

EDX / keV: 1.739 (s, silicon K α emission), 1.486 (w, aluminium K α emission), 0.525 (s, oxygen K α emission), 0.277 (v.s, carbon K α emission, a carbon coating was used to dissipate surface charging) ⁷

10.3.7 *cis*-Dichlorobis(triphenylphosphine)platinum(II) (7)



Scheme 10.7: Synthetic preparation of (7)

Triphenylphosphine (0.367 g, 1.40 mmol) was dissolved in ethanol (4.0 mL) and the solution was heated until reflux. Upon reflux, an orange solution of potassium tetrachloroplatinate(II) (0.266 g, 0.64 mmol) in deionised water (3.33 mL) was added. The reaction was initially orange but with vigorous stirring under reflux several colour changes were observed; orange to clear and colourless then a milky opacity formed. This opacity cleared to yield a colourless solution which turned to yellow before finally an off white viscous suspension formed. Upon formation of the suspension the mixture was then stirred for 2 hours at 60 °C. The solid was collected by filtration and was washed with hot water (10 mL), hot ethanol (15 mL) and finally diethyl ether (10 mL). This afforded the off white clumpy solid of (7), 0.506 g (99%).

MP (uncorrected): 296-300 °C (with decomposition)

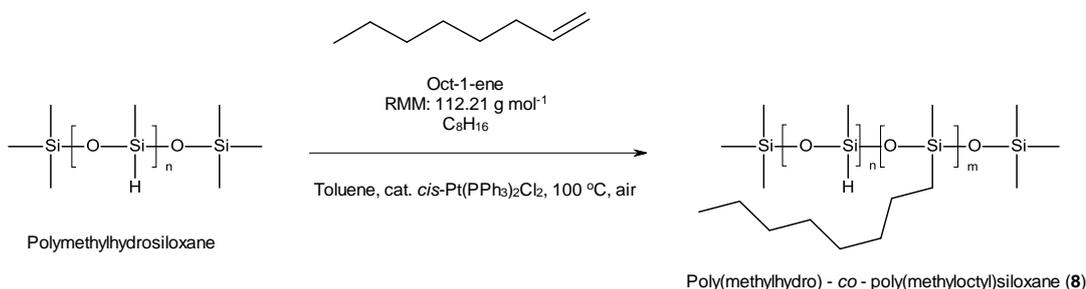
¹H NMR (300 MHz, CDCl₃, δ / ppm): 7.55-7.45 (m, 2H, Ph), 7.38-7.29 (m, 1H, Ph), 7.22-7.13 (m, 2H, Ph). See: *DJW.6674.11.Pt cat. (7).1H NMR.ap0913djw1.010.esp*

$^{13}\text{C}\{^1\text{H}\}$ NMR (75 MHz, CDCl_3 , δ / ppm): 134.89 (C aromatic, PPh_3), 130.74 (C aromatic, PPh_3), 127.94 (C aromatic, PPh_3). See: *DJW.6674.11.Pt cat. (7).13C NMR.ap0913djw1.011.esp*

$^{31}\text{P}\{^1\text{H}\}$ NMR (121 MHz, CDCl_3 , δ / ppm): 15.0 ($^1J_{\text{Pt-P}}$ 3673Hz). See: *DJW.6674.11.Pt cat. (7).31P NMR.ap0913djw1.012.esp*.

FT-IR (ν / cm^{-1}): 3051 (w, C – H stretch, phenyl), 465 (m, Pt – P), 440 (w, Pt – P). See: *DJW.6674.11.Pt cat. (7).FT-IR*

10.3.8 Poly(methylhydro) – co – poly(methyloctyl)siloxane (8)



Scheme 10.8: Reaction scheme for synthesis of (8)

Polymethylhydrosiloxane (5.29 g, clear and colourless viscous oil) was dissolved with stirring in toluene (100 mL) to afford a clear and colourless solution. To this oct-1-ene (0.5 mL, 3.19×10^{-3} mol) was added followed by the catalyst, *cis*-dichlorobis(triphenylphosphine)platinum(II) (240 μg) and both dissolved upon vigorous stirring and heating. Once complete dissolution of the catalyst had been achieved, the reaction mixture was then heated to reflux for either 6 or 24 hours. After the allotted reaction time, the reaction mixture was allowed to cool to room temperature whereupon the catalyst precipitated as a solid and was removed by filtration and ice-cold toluene washes. Toluene and excess oct-1-ene were removed *in vacuo* to afford a clear and colourless viscous oil.

Mass yield: 5.67 g (for 24 hour reaction product)

^1H NMR (300 MHz, Toluene- d_8 , δ / ppm): 5.00 (br. s., Si – H), 1.28 (m., 12H, alkyl methylene protons, $\text{SiCH}_2\text{CH}_2\text{CH}_2\text{CH}_2\text{CH}_2\text{CH}_2\text{CH}_2\text{CH}_3$), 0.90 (m., 3H, alkyl methyl protons, $\text{SiCH}_2\text{CH}_2\text{CH}_2\text{CH}_2\text{CH}_2\text{CH}_2\text{CH}_2\text{CH}_3$), 0.65 (m., 2H, alkyl methylene protons, methylene group bonded to silicon, $\text{SiCH}_2\text{CH}_2\text{CH}_2\text{CH}_2\text{CH}_2\text{CH}_2\text{CH}_2\text{CH}_3$), 0.24-0.15 (br. m., Si-CH₃ in three different environments). See:

DJW.6625.20.poly(methyloctyl)siloxane (8).1H NMR 15percent conversion.ja2313djw1.010.esp

¹³C NMR (75 MHz, Toluene-d₈, δ / ppm): 34.09 (s, CH₂), 33.93 (s, CH₂), 32.77 (s, CH₂), 30.18 (s, CH₂) 23.53 (s, CH₂), 21.74 (s, -CH₂CH₃), 14.72 (s, SiCH₂CH₂-), 2.08 (s, SiCH₂-), 1.79-1.03 (br. m, Si-CH₃ in many different environments). See: *DJW.6625.20.poly(methyloctyl)siloxane (8).13C NMR 15percent conversion.ja2313djw1.011.esp*

²⁹Si NMR [79 MHz, neat (D₂O reference in outer tube), δ / ppm]: 9.30 (-SiMe₃), -34.84 (Si - H). See: *DJW.6625.20.poly(methyloctyl)siloxane (8).29Si NMR.ma0113njwdjw1.001.esp*

FT-IR (ν / cm⁻¹): 2964 (w, C - H, alkyl), 2925 (w, C - H, alkyl), 2857 (w, C - H, alkyl), 2167 (s, Si - H stretch), 1529 (s, Si - C), 1026 (s & br., Si - O - Si, broadness of the peak suggests long siloxane chains), 845 (w, Si - C). See: *DJW.6625.20.poly(methyloctyl)siloxane.FT-IR 15 percent conversion.*

Thin films of **(8)** were fabricated by spin deposition. Poly(methylhydro)-*co*-poly(methyloctyl)siloxane was dissolved in melted *tert*-butyl alcohol to afford a clear and colourless solution (~17.5 % w/w). Spin deposition of the solution (0.1 mL) at 2000 rpm for 5 mins followed by ‘curing’ for 24 hours at 100 °C in air afforded clear and colourless thin films of **(8)**. Measurements of the refractive index of a thin film of **(8)** at 633 nm and 1553 nm were performed with a Metricon prism coupler. Thickness measurements were made by Peter Cooper (PhD student, University of Southampton) using a Zeescope white light interferometer.

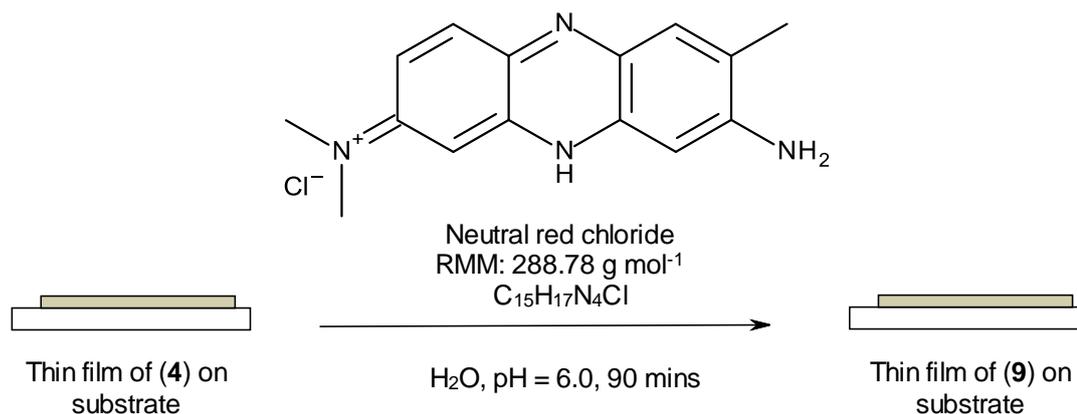
Refractive index @ 663 nm (n₆₃₃ / unitless): 1.4424

Refractive index @ 1553 nm (n₁₅₅₃ / unitless): 1.4397

See: *DJW.6625.20.poly(methyloctyl)siloxane (8).Metricon Prism Coupling Spectrum*

No comparative data found in the literature.

10.3.9 Neutral red-doped mesoporous silica sol-gel thin film (9)

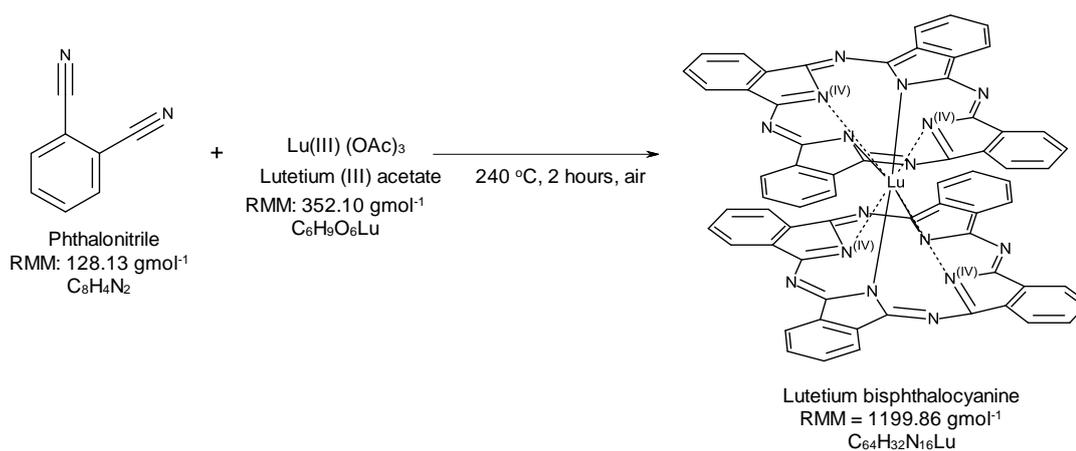


Scheme 10.9: Immersion of a thin film of (4) into an aqueous neutral red solution to form a pink coloured, neutral red doped thin film, (5).

A thin film of (4) was immersed in an aqueous solution of neutral red chloride (1 x 10⁻⁴ mol dm⁻³, pH = 6.0) for 90 mins with stirring. The samples were then removed from the solution, washed copiously with distilled water for 10 secs and then dried for 1 min under a stream of nitrogen gas to afford a bright pink thin film of (9). The samples were stored in ambient conditions before use.

UV-Visible transmission spectroscopy in the solid state (λ_{max} / nm): 514.5

10.3.10 Lutetium(III) bis-phthalocyanine (10)



Scheme 10.10: Immersion of a thin film of (4) into an aqueous neutral red solution to form a pink coloured, neutral red doped thin film, (5).

Phthalonitrile (~2.5 g) and lutetium(III) acetate (~0.6 g) were ground together to form a light brown homogeneous powder. The powder was then heated at 240 °C in

air for 2 hours. During this time sublimation of phthalonitrile was observed within the Vigreux column and the colour of the reaction mixture changed to dark green/blue. The reaction mixture was then transferred to a sublimation set-up and heated at 140 °C for 1 hour whereupon sublimation of a white fluffy solid on the cold finger occurred. The reaction mixture was then dissolved in chloroform (500 mL) using an ultrasonic bath to facilitate complete dissolution. The solution was reduced in volume to ~30 mL and purified by column chromatography on neutral alumina. The fractions containing LuPc₂ were identified by UV-Visible spectroscopy (characteristic absorptions at 658 nm and 320 nm), retained, combined and reduced *in vacuo* to afford a dark green/black solid. This solid was washed thrice with heptane (20 mL) and then dried *in vacuo*. Three vacuum sublimations were then performed to finally afford (**10**) as a fine black powder.

MP (uncorrected): > 300 °C

UV-Visible spectroscopy (λ_{max} / nm): 660.0 ($\epsilon_{660} = 119100 \pm 900 \text{ mol}^{-1} \text{ dm}^3 \text{ cm}^{-1}$)

¹H NMR (300 MHz, CDCl₃, δ / ppm): 9.23 (dd, $J = 8.1, 1.0 \text{ Hz}$, 1H), 7.98 (dd, $J = 7.7, 1.3 \text{ Hz}$, 1H), 7.91 (td, $J = 7.9, 1.5 \text{ Hz}$, 1H), 7.76 (td, $J = 7.6, 1.4 \text{ Hz}$, 1H). See: *DJW.6625.21.LuPc 2 (10).1H NMR.MA1913DJW1.010.ESP*

¹³C NMR (75 MHz, CDCl₃, δ / ppm): No satisfactory spectrum collected despite extended scans.

FT-IR (ν / cm⁻¹): 3076 (w, C – H stretch, aromatic), 3053 (w, C – H stretch, aromatic), 1490 (w, isoindole stretching), 1450 (m, isoindole stretching), 1319 (s, pyrrole stretching), 1114 (s, isoindole breathing mode), 1063 (w, coupling of isoindole deformation and aza stretching), 724 (s, C – H wag, aromatic). See: *DJW.6625.28.LuPc2 (10).FT-IR*

Elemental Analysis (CHN, 2 assays): Formula = C₆₄H₃₂N₁₆Lu. Calculated = C 64.06 %, H 2.69 %, N 18.67 %. Found = C 61.30 % H 2.73 % N 17.32 %. See: *DJW.6625.21.LuPc 2 (10).Elemental Analysis Report*

This result suggests the product consists of 66 % of the bisphthalocyanine and 34 % of the monophthalocyanine side product.

This is consistent with the reported data.

10.4 Optical Experiments

Detailed experimental procedures for all optical experiments described within this thesis and the fabrication and characterisation of the planar integrated Bragg grating sensors are given below.

10.4.1 Fabrication of 6" silica on silicon wafers via the Flame Hydrolysis Deposition (FHD) technique

6" silica on silicon wafers were fabricated either by flame hydrolysis deposition (FHD) at the Centre for Integrated Photonic (CIP, Ipswich) or fabricated within the Optoelectronics Research Centre. FHD involved the deposition of layers of pure or doped silica 'soot' on radially translated planar substrates followed by high-temperature consolidation (~ 1200 °C) to form the glass layers. The soot was produced by combustion of silicon tetrachloride and appropriate amounts of phosphorous, germanium and/or boron volatile species in an oxygen-hydrogen flame. The refractive index of the deposited layers was controlled by varying the amount of each non-silicon dopant species combusted and the thickness of a layer was primarily controlled by varying the radial translation of the platter relative to the burner and the transverse translation of the burner relative to the platter. Further detail on the FHD process can be found in the work of Watts⁸. The fabricated wafers were then diced into practical size integrated photonics chips; typical dimensions of 10 x 20 mm or 10 x 40 mm.

10.4.2 Hydrogen loading to increase photosensitivity

After fabrication by FHD and dicing, the wafer segment underwent hydrogen loading to enhance the photosensitivity to the frequency doubled Ar-ion laser operating at 244 nm (UV) used for the direct writing technique. This was achieved by transferring the wafer segment into a ≥ 120 bar hydrogen (H_2) atmosphere for at least three days. The wafer segment was removed from the H_2 atmosphere and stored in liquid nitrogen for no-more than 2-3 days before direct UV-writing.

10.4.3 Simultaneous Direct UV-writing of waveguides and Bragg gratings

The wafer sample was stored in liquid nitrogen to prevent out diffusion until the UV writing process. Direct UV writing of waveguides containing Bragg gratings was performed using a Cambridge Laser Laboratories Loxel 95 SHG UV laser with an Aerotech A3200 air stage. The UV power applied was determined by the maximum

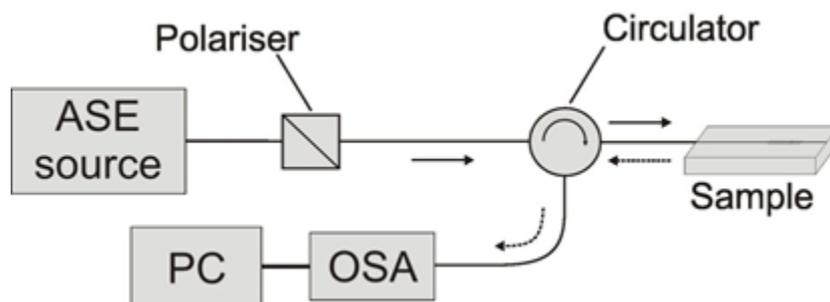
stable laser power output that could be achieved (~20 mW). The required fluence was then controlled by altering the sample translation speed. A linear waveguide containing eight apodised Bragg gratings was then written into the germanium doped silica core layer of a “topless” Bragg grating device using automated patterning and pulsing of the crossed UV lasers that was determined by the prewritten ‘g-code’.

10.4.4 Pigtailling

Before “pigtailling” the end facets of the Bragg sensor devices were manually wiped clean with isopropanol and acetone soaked cleaning buds. The device was then held on a vacuum chuck and the “pigtail” was brought into contact with one of the end facets. HeNe laser (633 nm) was guided through the pigtail into the device and the output light from the other end facet of the device was focussed onto a beam stop with a 4x magnification lens. The Bragg device was manipulated in the x, y and z axes until the output light pattern was a horizontal red line containing dots which shows the presence of waveguides. Once a waveguide was found in this way the source was switched to the ASE 1550 nm source and Bragg peaks were observed on the OSA. AT this stage the “pigtail” was carefully removed from the device in the x axis and UV curing glue (Dymax OP-4-20641) was applied the end facet of the pigtail before intimate reintroduction with the device. Bragg device was manipulated in the x, y and z axes to obtain maximum amplitude of Bragg peaks observed on the OSA. The glue was then cured with a UV light source and left to cure further overnight.

10.4.5 Characterisation of a Bragg grating device

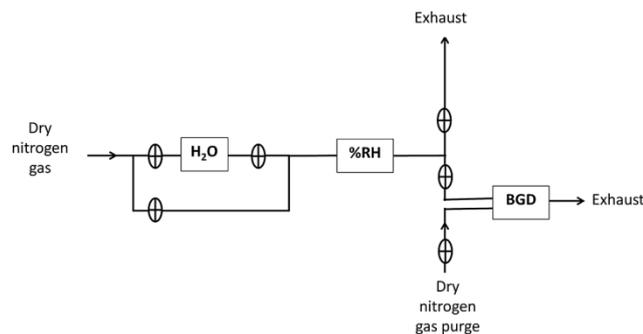
Bragg wavelength shift characterisation was achieved via the following optical set – up:



OSA = Optical Spectrum Analyser, ASE Source = Amplified Stimulated Emission Source, Sample = the Bragg grating sensor device

The broadband ASE source was connected to the polariser which was connected to the circulator via a polarisation maintaining (PM) fibre. PM fibre was used to prevent change in the polarisation of the propagating light due to movement/bending of the fibre. This is important as the peak wavelength of the transverse electric and magnetic mode, TE and TM respectively, are different in a topless Bragg grating device and any switch between the two or ratio of the two modes excited could result in anomalous peak wavelength shifts. The circulator directs the back reflected signal from the Bragg grating to the optical spectrum analyser (OSA). The OSA was connected to and remotely controlled by a Windows PC running Labview software. TE mode was used because it was measured to be more sensitive to changes in refractive index (used calibrated refractive index oils) compared to the TM mode. The optical fibre was “pigtailed” to the waveguide to fabricate the Bragg device as detailed above.

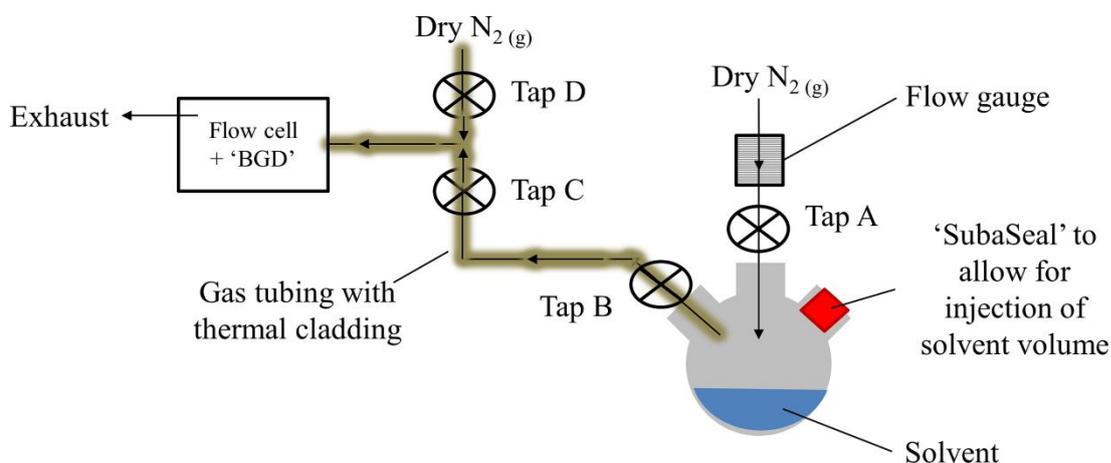
10.4.6 Water vapour sensing in a gas flow system



The gas delivery apparatus for optical water vapour sensing experiments was set-up as shown above. The integrated optical Bragg grating device ('BGD') was mounted within a flow cell and interrogated whilst exposed to a flow of nitrogen gas. The temperature within the flow cell was monitored via a thermocouple. The water vapour in the nitrogen carrier gas was introduced by bubbling dry nitrogen gas (typical flow rate $\sim 3.5 \text{ L min}^{-1}$) through a reservoir of deionised water ('H₂O'). By altering the temperature of water the concentration of water vapour in the nitrogen carrier gas was controlled. The temperature of the reservoir was incrementally changed using an external water bath, the temperature of which was raised or lowered via heating with a hotplate or addition of ice to the external water bath respectively. To return the integrated Bragg grating hygrometer device to its initial state after exposure to water vapour, 'H₂O' was bypassed allowing the cell to be

purged with dry nitrogen gas ($> 5 \text{ L min}^{-1}$). In addition, before a humidity measurement was recorded, a stable %RH value for the moist nitrogen gas flow was first achieved by altering the water bath temperature and referenced against an in-line electronic commercial Testo 625 hygrometer ('%RH'). Once a constant %RH value was achieved, the moist nitrogen gas was introduced into the cell containing 'BGD'. It should be noted that while the vapour flow was stabilising, the sensor device was kept under a secondary dry nitrogen flow to avoid contamination. The full spectrum of the reflected peaks of the Bragg gratings was sampled every 20 – 25 seconds via the OSA. The average shift in Bragg wavelengths upon exposure of the sensor device to changes in humidity were calculated by subtraction of an average over at least 5 mins of the Bragg wavelength measured during the exposure to water vapour from the average of the stable background, measured under dry nitrogen before and after, allowing thermal effects to be minimised.

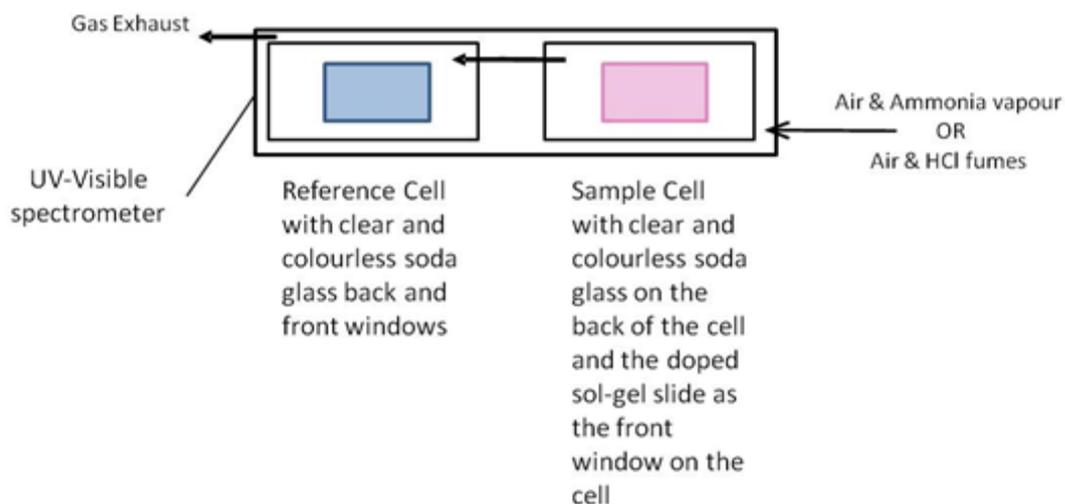
10.4.7 Sensing of organic solvent vapour in a flow system at 1550 nm using a Bragg grating device modified with a film of (8)



The experimental was set-up as shown above. A Bragg grating sensor device 'BGD' was modified with a thin film of (8) as per the procedure above. The 'BGD' was then placed in a flow cell; the temperature within the flow cell was monitored throughout the experiment with a thermocouple. During the experiment the 'BGD' was continuously exposed to a flow of dry nitrogen gas ($> 5 \text{ L min}^{-1}$) to prevent contamination, unless the 'BGD' was exposed to a flow of organic solvent vapour in dry nitrogen carrier gas for a sensing event. The three neck flask (used as the reservoir for the liquid solvent analytes) was preheated to a temperature $> 20 \text{ }^\circ\text{C}$ higher than the boiling point of the chosen analyte solvent for at least 20-30 mins,

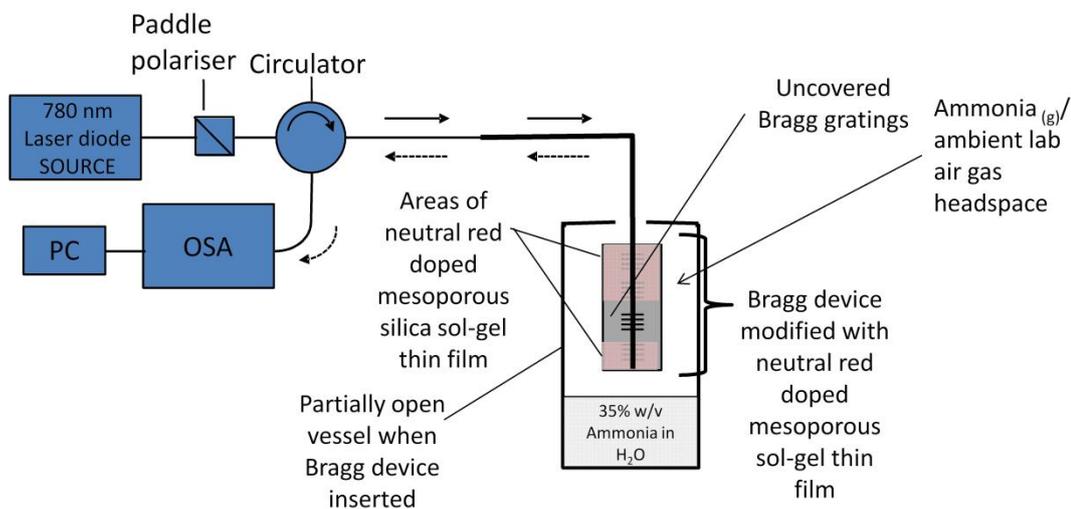
e.g. for dichloromethane (boiling point ~ 40 °C) the three neck flask was heated to ~ 60 - 65 °C. NOTE: Extra care was taken, when carbon disulphide (CS_2) was used as the analyte solvent, that the temperature of the flask did not exceed the flash point temperature of CS_2 . When at the appropriate temperature, analyte solvent (3 mL) was injected into the three neck flask via the 'Suba Seal'. Within a few seconds the liquid solvent began bubbling and condensation of liquid was seen at the top of the flask. At this point the dry nitrogen gas flow over the 'BGD' was removed and Tap D was shut. Taps B, C and then A were then opened in that order in quick succession immediately followed by application of a flow of dry nitrogen carrier gas (~ 1.5 L min^{-1}) over the volume of the analyte solvent as shown in the diagram above. Evaporation of the analyte solvent was observed indirectly by noting that the volume of liquid solvent within the flask decreased with continued application of the dry nitrogen carrier gas flow. The flow of dry nitrogen carrier gas through the three neck flask reservoir was maintained for at least 5 mins after it was first observed that all the liquid solvent had evaporated. Tap C was then shut, the flow of dry nitrogen carrier gas through the flask was ceased, Tap D was opened and a flow of dry nitrogen gas (> 5 L min^{-1}) was reintroduced to the flow cell before finally Tap A and Tap B were shut. This procedure was repeated for every sensing event. NOTE: A sufficient period (usually 10-15 mins) of dry nitrogen gas was allowed between sensing events to ensure Bragg wavelength shift values had returned to baseline levels.

10.4.8 UV-Visible spectrometric measurement of the absorbance changes of (9) when exposed to acidic and basic gases



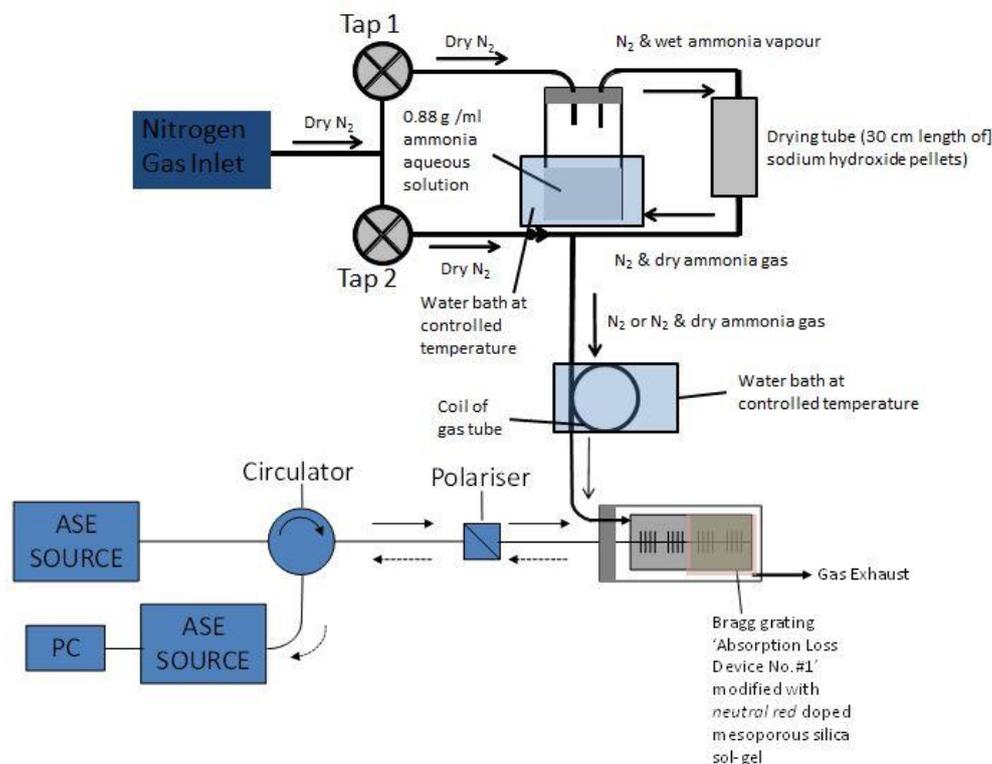
The experiment was set-up as shown in the diagram above. (9) was fabricated as per the procedure given above. The reference and sample cells were set-up in the UV-Visible spectrometer at an angle 'x' (where $45^\circ < x < 90^\circ$) to the incident beam to avoid etalon fringe effects. The reference and sample cells were periodically filled simultaneously with ambient air, air and ammonia gas or air and HCl vapour. UV-Visible spectra were recorded in the 1000 – 300 nm wavelength region or absorbance values at 535 nm, 515 nm and 455 nm (these wavelengths are the values at which the λ_{max} of three colour states, blue, pink and yellow are respectively) were recorded via a Windows PC running *UVPC* software.

10.4.9 Experimental investigation of refractometric sensing at 1550 nm of ammonia gas in a static ‘dunk’ system using a 1550 nm Bragg grating sensor device modified with (9)



The experiment was set-up as shown in the diagram. A thin film of (4) was synthesised as detailed above and spin deposited onto a 1550 nm planar Bragg grating sensor device. The thin film of (4) was spin deposited onto the Bragg grating in such a manner that the four Bragg gratings in the middle of the Bragg grating device were uncovered and the all of the remaining gratings were covered by the thin film ~250 nm. This thin film of (4) on the Bragg grating device was then loaded with the neutral red pH indicator as described in the procedure above to yield a thin film of (9). The Bragg grating device was interrogated at 1550 nm throughout the experiment. The Bragg wavelength data from the experiment was collected using an OSA that was connected to a PC running *Labview*. During the experiment the device was exposed to either ambient lab air or ammonia gas in the headspace above a 35% w/v aqueous ammonia solution (vapour pressure at 21 °C ~ 87 kPa) for varying durations, 10s through to 10 mins.

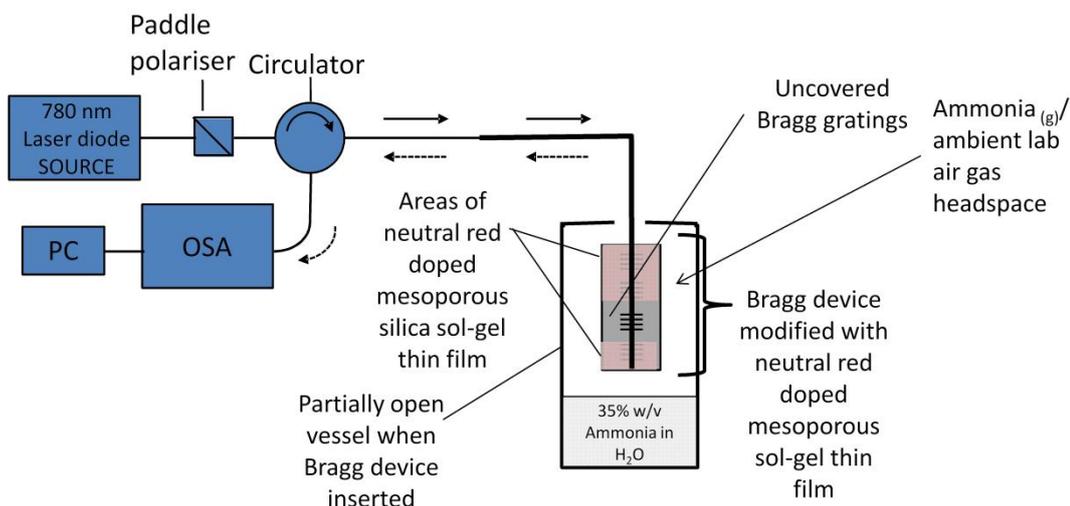
10.4.10 Experimental investigation of refractometric sensing at 1550 nm of ammonia gas in a flow system using a 1550 nm Bragg grating sensor device modified with (9)



The experiment was set-up as shown in the diagram. A thin film of (4) was synthesised as detailed above and spin deposited onto a 1550 nm planar Bragg grating sensor device. The thin film of (4) was spin deposited onto the Bragg grating in such a manner that the four Bragg gratings in the middle of the Bragg grating device were uncovered and the all of the remaining gratings were covered by the thin film. This thin film of (4) on the Bragg grating device was then loaded with the neutral red pH indicator as described in the procedure above to yield a thin film of (9). The Bragg grating device was interrogated at 1550 nm throughout the experiment. The Bragg wavelength data from the experiment was collected using an OSA that was connected to a PC running *Labview*. During the experiment the Bragg grating device was exposed to cycles of either dry nitrogen gas (0.0 % relative humidity controlled to be at ~25 °C) or a dry mixture of ammonia gas in nitrogen gas (relative humidity < 0.5 %, controlled to be at ~25 °C) for varying durations between 10 mins and 30 mins. The dry mixture of ammonia gas in nitrogen was obtained by passing dry nitrogen gas over concentrated aqueous ammonia solution to form a ‘wet’ gas mixture (ammonia gas and water vapour in nitrogen gas). This ‘wet’

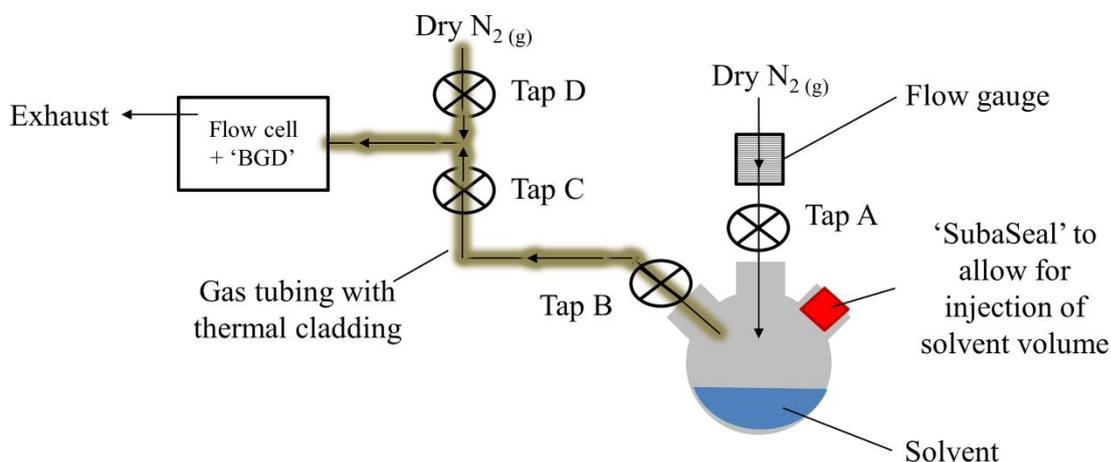
mixture was dried by passage through a 30 cm column of closely packed sodium hydroxide pellets; the resulting relative humidity of the dry mixture $< 0.5\%$.

10.4.11 Experimental investigation of refractometric sensing at 780 nm of either ammonia gas or hydrogen chloride (HCl) vapour in a static ‘dunk’ system using a 1550 nm Bragg grating sensor device modified with (9)



The experiment was set-up as shown in the diagram. A thin film of (4) was synthesised as detailed above and spin deposited onto a 1550 nm planar Bragg grating sensor device. The thin film of (4) was spin deposited onto the Bragg grating in such a manner that the four Bragg gratings in the middle of the Bragg grating device were uncovered and the all of the remaining gratings were covered by the thin film. This thin film of (4) on the Bragg grating device was then loaded with the neutral red pH indicator as described in the procedure above to yield a thin film of (9). The Bragg grating device was interrogated at 1550 nm throughout the experiment. The Bragg wavelength data from the experiment was collected using an OSA that was connected to a PC running *Labview*. During the experiment the device was exposed to either ambient lab air, ammonia gas in the headspace above a 35% w/v aqueous ammonia solution (vapour pressure at 21 °C ~ 80 kPa⁹) or hydrogen chloride vapour in the headspace above a 37% w/v hydrochloric acid aqueous solution (hydrogen chloride vapour pressure at 21 °C ~ 4.0 MPa¹⁰) for varying durations, 10s through to 10 mins. This experiment was performed after the device had been equilibrated in ambient humidity conditions for ~ 5 days and had just been removed from a neutral red aqueous solution (briefly dried under a stream of compressed dry air for ~ 20 s upon removal and then used immediately).

10.4.12 Sensing of organic solvent vapour in a flow system at 1550 nm using a Bragg grating device modified with a thin film of (10)



The experimental set-up diagram above is identical to the experimental set-up diagram for 9.4.7; the same experimental set-up was used. In addition the experimental procedure was identical for both experiments however a full description of the procedure is given below again for completeness.

The experimental was set-up as shown above. A Bragg grating sensor device 'BGD' was modified with a thin film of (10) as per the procedure above. The 'BGD' was then placed in a flow cell; the temperature within the flow cell was monitored throughout the experiment with a thermocouple. During the experiment the 'BGD' was continuously exposed to a flow of dry nitrogen gas ($> 5 \text{ L min}^{-1}$) to prevent contamination, unless the 'BGD' was exposed to a flow of organic solvent vapour in dry nitrogen carrier gas for a sensing event. The three neck flask (used as the reservoir for the liquid solvent analytes) was preheated to a temperature $> 20 \text{ }^\circ\text{C}$ higher than the boiling point of the chosen analyte solvent for at least 20-30 mins, e.g. for dichloromethane (boiling point $\sim 40 \text{ }^\circ\text{C}$) the three neck flask was heated to $\sim 60\text{-}65 \text{ }^\circ\text{C}$. When at the appropriate temperature, analyte solvent (3 mL) was injected into the three neck flask via the 'Suba Seal'. Within a few seconds the liquid solvent began bubbling and condensation of liquid was seen at the top of the flask. At this point the dry nitrogen gas flow over the 'BGD' was removed and Tap D was shut. Taps B, C and then A were then opened in that order in quick succession immediately followed by application of a flow of dry nitrogen carrier gas ($\sim 1.5 \text{ L min}^{-1}$) over the volume of the analyte solvent as shown in the diagram above. Evaporation of the analyte solvent was observed indirectly by noting that the volume

of liquid solvent within the flask decreased with continued application of the dry nitrogen carrier gas flow. The flow of dry nitrogen carrier gas through the three neck flask reservoir was maintained for at least 5 mins after it was first observed that all the liquid solvent had evaporated. Tap C was then shut, the flow of dry nitrogen carrier gas through the flask was ceased, Tap D was opened and a flow of dry nitrogen gas ($> 5 \text{ L min}^{-1}$) was reintroduced to the flow cell before finally Tap A and Tap B were shut. This procedure was repeated for every sensing event. NOTE: A sufficient period (usually 10-15 mins) of dry nitrogen gas was allowed between sensing events to ensure Bragg wavelength shift values had returned to baseline levels.

1. P. J. Launer, in *Silicone Compounds Register and Review*, ed. B. Arkles, Petrarch Systems, Inc., 1987, p. 323.
2. C. M. Carney, T. a. Parthasarathy, and M. K. Cinibulk, *Journal of the American Ceramic Society*, 2011, **94**, 2600–2607.
3. A. Bertoluzza, C. Fagnano, M. A. Morelli, V. Gottardi, and M. Guglielmi, *Journal of Non-Crystalline Solids*, 1982, **48**, 117–128.
4. J. Liu and S. D. Kim, *Journal of Polymer Science Part B: Polymer Physics*, 1996, **34**, 131–140.
5. A. V. Rao, S. D. Bhagat, H. Hirashima, and G. M. Pajonk, *Journal of Colloid and Interface Science*, 2006, **300**, 279–85.
6. T. Levchenko, Y. Plyuto, and N. Kovtyukhova, *Journal of Sol-Gel Science and Technology*, 2007, **43**, 269–274.
7. JEOL, 1.
8. S. P. Watts, PhD Thesis, University of Southampton, 2001.
9. Air Liquide, 2013.
10. Air Liquide, 2013.

Appendix 1: Utilising the relation between absorption & refraction to sense gases

A1.1 Introduction

Light can interact with matter in a variety of ways such as propagation through a material followed by subsequent transmission from the material, reflection from the interface of a material, scattering, refraction (as described in **Chapter 2**) and also absorption ¹. The absorption and refraction of a material can be described by a quantity known as the complex refractive index, \tilde{n} , which is comprised of a real and imaginary parts. The normal part of the complex refractive index is the normal refractive index, n , as defined by in **Chapter 2** and the imaginary part is the extinction coefficient, κ . In this chapter it is shown how n and κ are linked through the complex relative dielectric constant of the material and then a method for achieving refractometric gas sensing by exploiting the relationship between n and κ is proposed. The theory for this approach has been taken from the text of Fox ¹.

A1.2 The complex relative dielectric constant ¹

As stated above, the refraction and absorption of a material can be described by the complex refractive index, \tilde{n} . Before the complex refractive index is defined the phenomenon of refraction and absorption will be introduced.

A1.2.1 Refraction

The refraction of a material results in propagating light waves to propagate at a smaller velocity relative to the velocity of light in a vacuum. Refraction is described

by the refractive index, n , as defined in **Chapter 2**. However, for completeness n will be redefined here as the ratio of the velocity of the propagating light in vacuum, c , to the propagation velocity of the light in the material, v , as given by:

$$n = \frac{c}{v}$$

Eqn.A1.1

The refractive index is dependent on the frequency of the propagating light beam; this is known as dispersion.

A1.2.2 Absorption¹

The absorption of a material describes the attenuation of certain frequencies of light when propagating through the material. If the frequency of the propagating light is resonant with the transition frequencies of the atoms in the material, then absorption occurs and the beam of light is attenuated¹. Absorption at particular frequencies is responsible for the colour of many optical materials; blue sapphires absorb red and green light, but not blue light. The absorption of light by an optical material can be quantified by the absorption coefficient, α , of the material. The absorption coefficient is defined as the amount of optical power absorbed in a unit length of the material, for a particular frequency of light. If the absorption coefficient, at a particular frequency, is known for a material, the intensity of the propagating light at a certain point along the propagation path of the light through the material can be calculated as follows.

A1.2.2.1 Beer's Law¹

If a light beam is propagating in the x direction and the intensity of the light beam, I (defined as the optical power per unit area), at position x is $I(x)$, then the decrease in the intensity, in an incremental slice of the material, dx , is given by the differential equation:

$$dI = -\alpha dx \times I(x)$$

Eqn.A1.2

By rearrangement to make $I(x)$ a function of x gives,

$$\frac{1}{I(x)} dI = -\alpha dx$$

Eqn.A1.3

Subsequent integration then gives,

$$\ln[I(x)] = -\alpha x + C$$

Eqn.A1.4

For a non-infinitesimal thick slice of the material of thickness, l , the difference of intensity is I_0 at $x = 0$, and I_l at $x = l$. By using **Eqn.A1.4**, the difference in intensity can be written as,

$$\ln(I_l) - \ln(I_0) = (-\alpha l + C) - (-\alpha 0 + C)$$

$$\ln(I_l) - \ln(I_0) = -\alpha l$$

$$\ln\left(\frac{I_l}{I_0}\right) = -\alpha l$$

Eqn.A1.5

By taking the exponential of both sides of **Eqn.8.5** and rearrangement in terms of I_l yields:

$$I_l = I_0 e^{-\alpha l}$$

Eqn.A1.6

Then, by rewriting **Eqn.A1.6** in the general case for any thickness, x , gives the final equation:

$$I_x = I_0 e^{-\alpha x}$$

Eqn.A1.7

This equation is known as Beer's Law and can be used to determine the attenuation of a propagating light beam in a material, if the absorption coefficient of that material is known.

A1.2.3 Complex refractive index ¹

The complex refractive index, \tilde{n} , is defined by the following equation:

$$\tilde{n} = n + i\kappa$$

Eqn.A1.8

The real part of the equation is the normal refractive index of the material, n , as defined above in **Eqn.A1.1** and the imaginary part of the equation, κ , is defined as the extinction coefficient, which is directly related to the absorption coefficient, α . This equation is important as it demonstrates that the absorption and the refractive index of a material can be described through one parameter.

The relationship between α and κ is an integral part of the relationship between the absorption and the refractive index of a material. Therefore, the relationship between α and κ is described below.

A1.2.3.1 Relationship between α and κ ¹

The following description involves equations that are obtained upon analysis of Maxwell's Equations. For the aim of this chapter, which is to show that the absorption and refractive index of a material are intrinsically linked and how this can be used to achieve gas sensing, the derivation of these equations from Maxwell's Equations was deemed unnecessary. However, these equations are marked with an asterisk. For the interested reader, derivation of these equations and Maxwell's Equations can be found in texts by Fox ¹, Fleisch ² and Hecht ³.

Firstly, consider electromagnetic plane waves propagating through a medium with a complex refractive index. If a wave is propagating in the x direction, the time, t , and spatial dependence of the electric field of the propagating wave is given by:

$$\varepsilon(x, t) = \varepsilon_0 e^{i(kx - \omega t)}$$

Eqn.A1.9*

where k is the wave vector of the light wave and ω is the angular frequency (both defined in **Chapter 2**) and $|\varepsilon_0|$ is the amplitude at $x = 0$ ¹. If the light is of a particular frequency that does not undergo absorption in the material, and the material has a refractive index of n , then the wavelength of the light is reduced by a factor of n compared to the free-space wavelength of the light, λ . Therefore it can be shown that k and ω are related by the following relationship:

$$k = \frac{2\pi}{(\lambda/n)} = \frac{n\omega}{c}$$

Eqn.A1.10

However, if the material is absorbing at the frequency of the light, then by allowing the refractive index to be complex and using **Eqn.A1.10**, the following relationship is revealed:

$$k = \tilde{n} \frac{\omega}{c} = (n + i\kappa) \frac{\omega}{c}$$

Eqn.A1.11

By substitution of **Eqn.A1.11** into **Eqn.A1.9**, the following result is obtained.

$$\varepsilon(x, t) = \varepsilon_0 e^{i\left(\frac{\omega \tilde{n} x}{c - \omega t}\right)}$$

$$\varepsilon(x, t) = \varepsilon_0 e^{\left(\frac{-\kappa \omega x}{c}\right)} e^{i\left(\frac{\omega n x}{c - \omega t}\right)}$$

Eqn.A1.12

From **Eqn.A1.12** it is clear to see that a non-zero value of the extinction coefficient, κ , gives rise to an exponential decay of the propagating wave in the material. In addition, the real part of \tilde{n} determines the phase velocity of the wave front.

Taking the following proportionality, that arises from analysis of Maxwell's Equations,

$$I \propto \varepsilon^2$$

Eqn.A1.13*

which implies the intensity of the light is proportional to the square of the amplitude of the electric field, it can be deduced from **Eqn.A1.12** that the intensity of the light in the material decays exponentially with a decay constant equal to $2 \times (\kappa\omega/c)$ ¹. Upon comparison to **Eqn.A1.7** (Beer's Law), it can be concluded that:

$$\alpha = \frac{2\kappa\omega}{c} = \frac{4\pi\kappa}{\lambda}$$

Eqn.A1.14

where λ is the wavelength of the light in free space. Therefore from **Eqn. A1.14** it is shown that the extinction coefficient κ is directly proportional to the absorption coefficient α .

A1.2.3.2 Relationship between refractive index and the relative dielectric constant¹

Another crucial relationship to define is the relationship between the normal refractive index of a material and the relative dielectric constant of a material. To demonstrate the relationship between the absorption and refractive index of material near a significant optical absorption then the real and imaginary parts of the refractive index and the relative dielectric constant must be known.

The relative dielectric constant of a material is defined as the ratio of the capacitance of a capacitor with the material as a dielectric between the plates, C , to the capacitance of a capacitor with free space as the dielectric, C_0 ⁴, as shown in **Eqn.A1.15** below:

$$\varepsilon_r = \frac{C}{C_0}$$

Eqn.A1.15

Knowing that at the frequencies of visible light $\mu_r \sim 1$, then the refractive index can be defined as shown below in **Eqn.A1.16**:

$$n = \sqrt{\varepsilon_r}$$

Eqn.A1.16*

Therefore if n is complex then it follows that ε_r must also be complex. Thus, the complex relative dielectric constant $\tilde{\varepsilon}_r$ can be defined by:

$$\tilde{\varepsilon}_r = \varepsilon_1 + i\varepsilon_2$$

Eqn.A1.17

Analogous to **Eqn.A1.16**, it follows that,

$$\tilde{n}^2 = \tilde{\varepsilon}_r$$

Eqn.A1.18

which demonstrates that \tilde{n} & $\tilde{\varepsilon}_r$ are related. The relationships between the real and imaginary parts of both \tilde{n} & $\tilde{\varepsilon}_r$ can be determined by combining **Eqn.A1.8**,

Eqn.A1.17 and **Eqn.A1.18** together, as demonstrated by Fox ¹. These are as follows:

$$\varepsilon_1 = n^2 - \kappa^2$$

Eqn.A1.19

$$\varepsilon_2 = 2n\kappa$$

Eqn.A1.20

And

$$n = \frac{1}{\sqrt{2}} \sqrt{\left(\varepsilon_1 + \sqrt{(\varepsilon_1^2 + \varepsilon_2^2)} \right)}$$

Eqn.A1.21

$$\kappa = \frac{1}{\sqrt{2}} \sqrt{\left(-\varepsilon_1 + \sqrt{(\varepsilon_1^2 + \varepsilon_2^2)}\right)}$$

Eqn.A1.22

This analysis by Fox, shows that \tilde{n} & $\tilde{\varepsilon}_r$ are not independent variables; if ε_1 & ε_2 are known for a material, then n and κ can be calculated. The *vice versa* argument also holds true. At a particular optical frequency, where the material is weakly absorbing, then it can be assumed that κ is very small. Thus, **Eqn.A1.21** and **Eqn.A1.22** both simplify to,

$$n = \sqrt{\varepsilon_1}$$

Eqn.A1.23

and

$$\kappa = \frac{\varepsilon_2}{2n}$$

Eqn.A1.24

respectively.

These equations demonstrate that the normal refractive index is determined by the real part of the dielectric constant and the absorption of the material at a particular frequency is mostly determined by the imaginary part. These last two equations are only valid at optical frequencies at which the material does not have a very large absorption coefficient. This is the reason why data tables for optical materials that are transparent at visible frequencies generally only list the real parts of the refractive index and the dielectric constant.

A1.2.4 Microscopic classical dipole oscillator model ¹

Now that the quantities of \tilde{n} , α , κ and $\tilde{\varepsilon}_r$ have been defined, a classical dipole oscillator model will be described to enable definition of the frequency dependence of n , α and $\tilde{\varepsilon}_r$ near to, and on, a resonance and explain the physical causes of these optical properties. Despite real material being more complicated than simple atomic

oscillators the following model is sufficient to describe the relationship between the refractive index of a material and the absorption of a material through the complex relative dielectric constant.

A classical model of the propagation of light in an optical material was developed after Maxwell's theory of electromagnetic waves and the concept of the dipole oscillator concept had been proposed¹. The main assumption in the model is that there are several different types of oscillator in the optical material and each have has a characteristic resonant frequency¹. At the frequencies of light in the visible region of the electromagnetic spectrum the most significant contribution to the model is from the oscillation of bound electrons within the atoms; atomic oscillators. At infrared frequencies, vibrational oscillators are the significant contribution. However, to achieve the first aim of this chapter, which is to highlight the relationship between the absorption and refraction of a material, only the explanation of an atomic oscillator is required.

A1.2.4.1 Atomic oscillators¹

Atomic oscillators were first proposed by Lorentz as a model, in the terms of Maxwell's electromagnetic theories, to describe the observation that atoms emitted and absorbed at discrete frequencies¹. The oscillator model of the atom, as proposed by Lorentz, assumes that a negative point charge is held in a stable orbit around a positive centre by a spring; the spring represents the restoring force for small displacements away from the equilibrium state. Each negative point charge and the positively charged centre form an individual electric dipole with magnitudes dependent on the distance between the charges. This is shown in **Fig.A1.1** below.

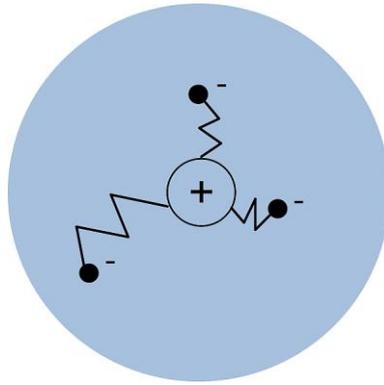


Fig.A1.1: Pictorial representation of the classical atomic oscillator dipole model proposed by Lorentz in 1878. The blue circle represents the extent of the atom, the circle containing a '+' in the middle of the atom represents the fixed position positive charge, the 'zigzag' lines represent the restoring force 'springs' and \bullet^- represents the negative point charges.

Lorentz proposed the atomic oscillator dipole model in 1878, 19 years before the discovery of electrons by Thompson and 33 years before the discovery of nuclei by Rutherford, hence the negative point charges were not called electrons and the positive charge at the centre of the atom was not called the nucleus ¹. However, since the discovery of electrons and nuclei, the classical atomic oscillator model was adapted so that positive charge in the middle of the atom was the nucleus and the negative point charge were the orbiting electrons.

The natural resonant frequency, ω_0 , of the atomic dipoles is defined as follows:

$$\omega_0 = \sqrt{\left(\frac{K_s}{\mu}\right)}$$

Eqn.A1.25

Where, K_s is the spring constant of the restoring force and μ is the reduced mass as given by:

$$\frac{1}{\mu} = \frac{1}{m_e} + \frac{1}{m_N}$$

Eqn.A1.26

However, as $m_N \gg m_e$ then it may be assumed that $\mu \approx m_e$. Therefore **Eqn.A1.25** can be rewritten as:

$$\omega_0 \approx \sqrt{\left(\frac{K_s}{m_e}\right)}$$

Eqn.A1.27

As stated above, it is defined that there are several dipoles within every atom to account for the experimental fact that an atom has many transition frequencies as evident in the experimental absorption and emission spectra in the UV, visible and infrared frequency ranges ¹. The link between the atomic oscillating dipoles and the emission spectrum can be understood qualitatively as demonstrated below.

By taking an electric dipole in the Lorentz classical atomic oscillator model in isolation, i.e. no other interacting electric dipoles or other atoms are present, it can be said the dipole consists of a positive charge, $+q$, at position \mathbf{r}_+ and a negative charge, $-q$, at position \mathbf{r}_- . The overall electric dipole, \mathbf{p} , can be defined as:

$$\mathbf{p} = q(\mathbf{r}_+ - \mathbf{r}_-)$$

Eqn.A1.28

Hence the magnitude of the dipole that arises between the positively charged nucleus and the negatively charged electron is equal to $e|\mathbf{r}_N - \mathbf{r}_e|$ ¹. During oscillations of the atomic dipole over time, it is assumed that the nucleus remains stationary due $m_N \gg m_e$, whilst the electron oscillates forwards and backwards at the frequency of ω_0 , as defined in **Eqn.A1.27** above. Thus the oscillations produce a dipole which varies with time, in addition to any permanent dipole the system may have. The magnitude of this time-varying dipole, $p(t)$, can be given by,

$$p(t) = -ex(t)$$

Eqn.A1.29

where e is the charge of the electron ($e = 1.60217657 \times 10^{-19}$ coulombs) and $x(t)$ is the change in displacement of the electron over time relative to the equilibrium position of the electron. This is represented pictorially in **Fig.A1.2** below.

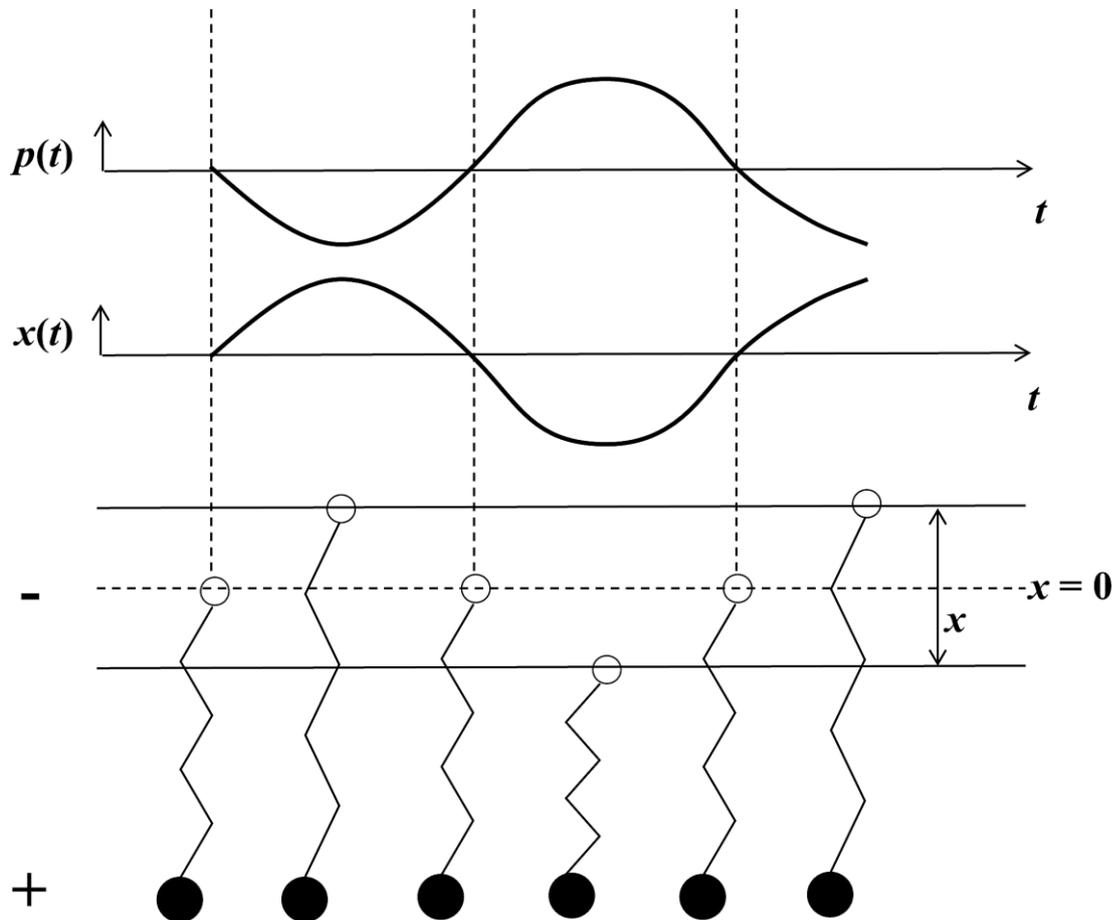


Fig.A1.2: The oscillations of a Lorentzian classical atomic dipole oscillator consisting of a massive nucleus (large solid black circle) which has a positive charge, +, and a relatively small mass electron (small black circle) which has a negative charge, -. In this model the nucleus and the electron are held together with a 'spring' which represents the restoring force. $x(t)$ is the displacement of the electron from its equilibrium position, $x = 0$, over time. The vibrations of the dipole about the equilibrium point produce at the frequency ω_0 produces a time dependent dipole moment $p(t)$. Adapted from the text by Fox ¹.

In accordance with the theory of oscillating classical Hertzian dipoles, the oscillating dipole will emit electromagnetic waves at frequency ω_0 ⁵. Therefore, it can be expected that the atom in this system will emit light at its resonant frequency whenever sufficient energy, at the correct frequency, is imparted to it to excite the oscillations.

However, in practise there are other electric dipoles and atoms present in the system therefore the oscillations of the atomic dipole oscillator will be affected accordingly. For example the oscillating dipoles can lose energy through collisional processes. Therefore to model the atomic dipole oscillator quantitatively, the following differential equation of motion for the displacement, x , of the electron, which includes a damping term to account for energy loss through collisional processes, is given below in **Eqn.A1.30**. Again the assumption $m_N \gg m_e$ is invoked, therefore the reduced mass, $m_0 = m_e$, where m_e is the mass of the electron.

$$m_e \frac{d^2x}{dt^2} + m_e \gamma \frac{dx}{dt} + m_e \omega_0^2 x = -e\varepsilon$$

Eqn.A1.30

Where m_e is the mass of the electron, γ is the damping rate, e is the magnitude of charge of the electron ($e = 1.60217657 \times 10^{-19}$ coulombs), ω_0 is the resonant frequency of the oscillator and ε is the magnitude of the electric field. In **Eqn.A1.30**, the second order differential describes the acceleration of the electron in x , the first order differential describes the damping of the system and the last term on the left-hand side of the equation describes the restoring force. The term on the right-hand side of **Eqn.A1.30** describes the driving force due to the AC electric field of the incident light wave.

Now considering the interaction of the atomic oscillating dipole with the incident monochromatic light wave, of frequency $= \omega$, over time, the electric field can be described as a function of time as follows:

$$\varepsilon(t) = \varepsilon_0 \cos(\omega t + \Phi) = \varepsilon_0 \Re_{\varepsilon}(\exp(-i\omega t - \Phi))$$

Eqn.A1.31

where ε_0 is the amplitude of the incident light wave, Φ is the phase of the incident light wave and \Re_{ε} represents the real part of the complex equation. Note the exponential function has been written as \exp so as to avoid confusion with e which is the magnitude of the charge of the electron. If the frequency of the incident light

wave is ω , then the alternating electric field (AC field) drives the oscillations of the atomic dipole oscillator system at a frequency of ω . Therefore, by substitution of **Eqn.A1.31** into **Eqn.A1.30**, solutions of the following type will describe the oscillations:

$$x(t) = X_0 \underline{\mathcal{A}}_{\underline{\epsilon}}(\exp(-i\omega t - \Phi')),$$

Eqn.A1.32

where X_0 is the amplitude of the oscillation and Φ' is the phase of the oscillation.

It is important to note that the phase factors for the light and the forced oscillations are not equivalent, $\Phi \neq \Phi'$; the phase of the electrons tend to lag behind the phase of the driving light wave. This is typical for forced oscillations systems; the oscillations are at the same frequency of the driving force but lag due to damping. The damping in this model can be explained by collisions between the oscillating atomic dipoles and the other atoms in the system¹. Despite the phase lag, all the atoms re-radiate instantaneously, but the phase lag does accumulate along the propagation path of the light and results in retardation of the wave front. This retardation of the propagating wave front suggests that the wave velocity is lower in the material than in free space; this is the physical origin of the refractive index. This retardation of the wave front can also be physically interpreted as repeated scattering processes where the each atom acts as a Huygens point source; the scattering is coherent and elastic. By constructive interference of the scattered light waves in the direction of the propagating beam and destructive interference in all other directions, the beam direction is unchanged, but the repeated scattering processes take time to occur; this results in the phase lag¹. These phase factors, in **Eqn.A1.31** & **Eqn.A1.32**, can be incorporated into the amplitudes by allowing ϵ_0 and X_0 to be complex numbers. This is achieved by defining $\underline{\epsilon}(t) = \epsilon_0 e^{-i\omega t}$ and substituting this into **Eqn.A1.30**. Then, if solutions of the form $x(t) = X_0 e^{-i\omega t}$ are sought, then this gives:

$$-m_0 \omega^2 X_0 e^{-i\omega t} - im_0 \gamma \omega X_0 e^{-i\omega t} + m_0 \omega_0^2 X_0 e^{-i\omega t} = -e \epsilon_0 e^{-i\omega t}$$

Eqn.A1.33

Therefore this implies that X_0 is given by,

$$X_0 = \frac{\left(\frac{-e\epsilon_0}{m_0}\right)}{\omega_0^2 - \omega^2 - i\gamma\omega}$$

Eqn.A1.34

As demonstrated in Fig.A1.2 above, the displacement of the electrons from equilibrium position results in a dipole moment that varies with time, $p(t)$ and the magnitude of dipole moment is given by **Eqn.A1.29**. This individual dipole moment contributes a resonant contribution to the overall polarisation of the material. Thus, if N is defined as the number of atom per unit volume, in the material, the resonant polarization (the dipole moment per unit volume) $P_{resonant}$ is given by:

$$P_{resonant} = Np$$

$$P_{resonant} = -Nex$$

$$P_{resonant} = \frac{Ne^2}{m_0} \frac{1}{(\omega_0^2 - \omega^2 - i\gamma\omega)} \epsilon$$

Eqn.A1.35

As is obvious from **Eqn.A1.35**, if ω is vastly different in magnitude to ω_0 then $P_{resonant}$ is small. This is another typical property of forced oscillator systems; the oscillations are small in magnitude unless the driving frequency is close to resonance with the natural resonant frequency of the system.

Now the resonant polarization of the material has been defined, the complex relative dielectric constant can now be obtained; this will elucidate the connection between the absorption and refraction of an optical material.

The electric displacement of the optical material, \mathbf{D} , is related to the electric field ϵ and the polarization \mathbf{P} through:

$$\mathbf{D} = \varepsilon_0 \boldsymbol{\epsilon} + \mathbf{P}$$

Eqn.A1.36

where \mathbf{D} , $\boldsymbol{\epsilon}$ & \mathbf{P} are vectors.

In a real optical material the overall resonant polarization is a sum of all the resonant contributions. However, in this model only the resonant polarization due to the optically driven oscillation is of interest. Therefore, this optically driven oscillation is labelled as $\mathbf{P}_{\text{resonant}}$ and the other contributing polarization elements are labelled collectively as $\mathbf{P}_{\text{background}}$, as shown in **Eqn.A1.37** below:

$$\mathbf{D} = \varepsilon_0 \boldsymbol{\epsilon} + \mathbf{P}_{\text{background}} + \mathbf{P}_{\text{resonant}}$$

$$\mathbf{D} = \varepsilon_0 \boldsymbol{\epsilon} + \varepsilon_0 \chi \boldsymbol{\epsilon} + \mathbf{P}_{\text{resonant}}$$

Eqn.A1.37

where χ is a scalar quantity, known as the electric susceptibility, to describe the background polarisation contributions.

Further simplification of the problem can be achieved by assuming the material is isotropic. Therefore the relative dielectric constant can be defined as:

$$D = \varepsilon_0 \varepsilon_r \boldsymbol{\epsilon}$$

Eqn.A1.38

By combination of **EqnsA1.35 – A1.38** (inclusive) the following equation is obtained:

$$\varepsilon_r(\omega) = 1 + \chi + \frac{Ne^2}{\varepsilon_0 m_0} \frac{1}{(\omega_0^2 - \omega^2 - i\gamma\omega)}$$

Eqn.A1.39

By using **Eqn.A1.17**, $\varepsilon_r(\omega)$ can be split into the constituent real and imaginary parts, which gives,

$$\varepsilon_1(\omega) = 1 + \chi + \frac{Ne^2}{\varepsilon_0 m_0} \frac{(\omega_0^2 - \omega^2)}{(\omega_0^2 - \omega^2)^2 + (\gamma\omega)^2}$$

Eqn.A1.40

and

$$\varepsilon_2(\omega) = \frac{Ne^2}{\varepsilon_0 m_0} \frac{\gamma\omega}{(\omega_0^2 - \omega^2)^2 + (\gamma\omega)^2}$$

Eqn.A1.41

respectively.

As the system of interest is being driven at a frequency close to resonance, where $\omega \approx \omega_0$ and $\omega \gg \gamma$, then the term $(\omega_0^2 - \omega^2)$ can be approximated by $2\omega_0\Delta\omega$, where $\Delta\omega = (\omega - \omega_0)$ i.e. the detuning difference between the driving frequency and the resonant frequency. Thus this gives the low and high frequency limits of $\varepsilon_r(\omega)$ as,

$$\varepsilon_r(0) \equiv \varepsilon_{st} = 1 + \chi + \frac{Ne^2}{\varepsilon_0 m_0 \omega_0^2}$$

Eqn.A1.42

and

$$\varepsilon_r(\infty) \equiv \varepsilon_\infty = 1 + \chi$$

Eqn.A1.43

respectively, where ε_{st} represents the dielectric response to external static electric fields. It can now be written that:

$$(\varepsilon_{st} - \varepsilon_\infty) = \frac{Ne^2}{\varepsilon_0 m_0 \omega_0^2}$$

Eqn.A1.44

Finally, the following equations become evident, upon rewriting of **EqnsA1.40** & **A1.41** which holds for frequencies close to the resonant frequency:

$$\varepsilon_1(\Delta\omega) = \varepsilon_\infty - (\varepsilon_{st} - \varepsilon_\infty) \frac{2\omega_0\Delta\omega}{4(\Delta\omega)^2 + \gamma^2}$$

Eqn.A1.45

and

$$\varepsilon_2(\Delta\omega) = (\varepsilon_{st} - \varepsilon_\infty) \frac{\gamma\omega_0}{4(\Delta\omega)^2 + \gamma^2}$$

Eqn.A1.46

Where $\varepsilon_1(\Delta\omega)$ is the real part of the complex relative dielectric constant and $\varepsilon_2(\Delta\omega)$ is the imaginary part of the complex relative dielectric constant.

Substituting in some values of $\omega_0 = 1 \times 10^{15}$ rad s⁻¹, $\gamma = 5 \times 10^{12}$ s⁻¹, $\varepsilon_{st} = 15$ and $\varepsilon_\infty = 11$ the following curves can be generated (on next page):

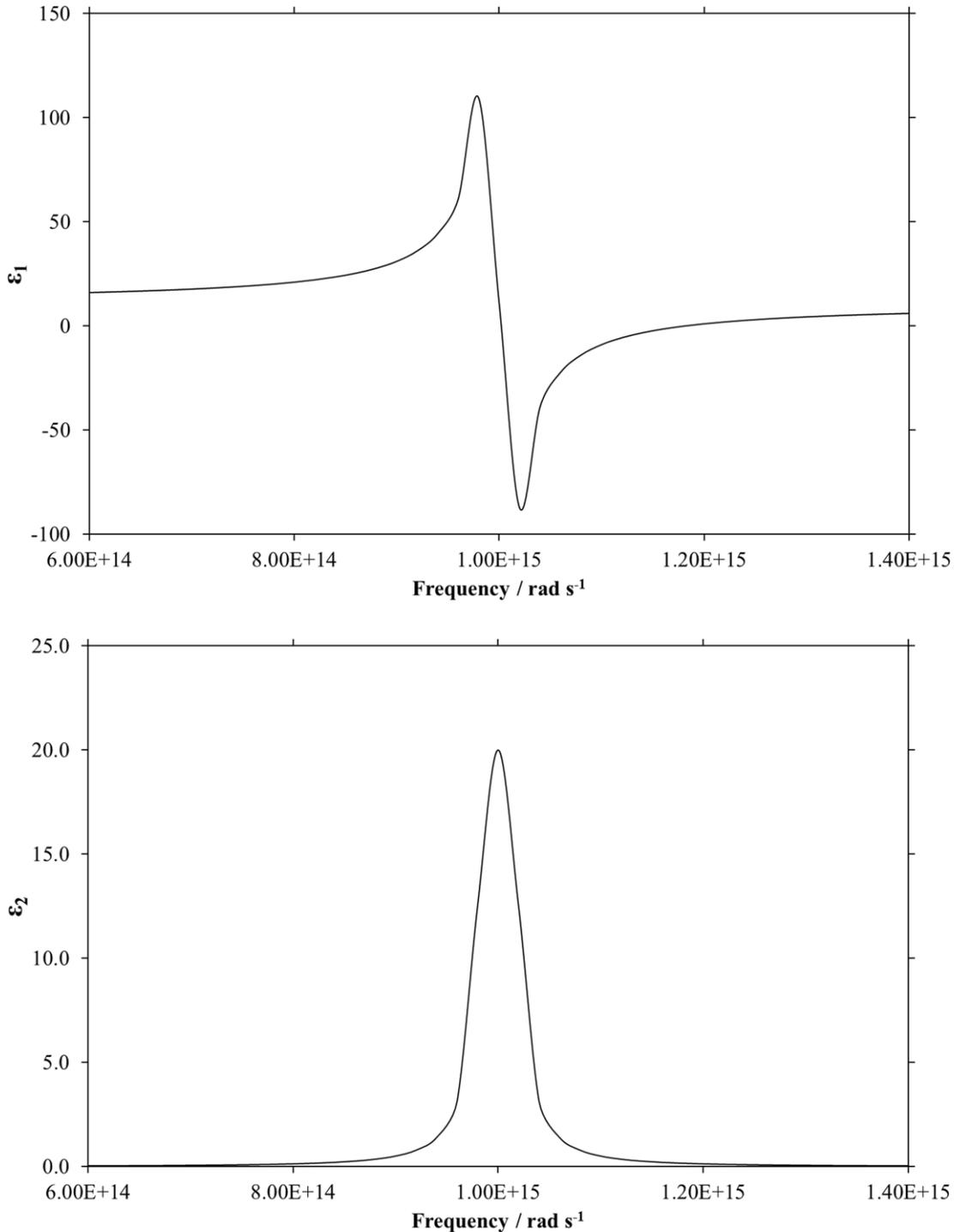


Fig.A1.3: The predicted response of ϵ_1 and ϵ_2 near to a resonance for $\omega_0 = 1 \times 10^{15}$ rad s⁻¹,

$$\gamma = 5 \times 10^{12} \text{ s}^{-1}, \epsilon_{st} = 15 \text{ and } \epsilon_{\infty} = 11$$

As can be seen in **Fig.A1.3** the shape of the curves for both ϵ_1 and ϵ_2 are identical to the shape of a typical curve showing the change in refractive index of a material near to a resonance feature and the shape of an absorption spectrum respectively. This is

because the refractive index n and the extinction coefficient κ are intimately linked to the real and imaginary parts of the complex relative dielectric constant respectively. Indeed, the n vs. ω and κ vs. ω curves can be generated through **Eqn.A1.21** and **Eqn.A1.22** respectively.

A1.3 The Kramers-Kronig Relations

The Kramers-Kronig relations relate the real and imaginary parts of a generic frequency-dependent linear response function $f(\omega)$ ⁶:

$$\text{Re}[f(\omega)] = \frac{1}{\pi} \mathbf{P} \int d\omega' \frac{\text{Im}[f(\omega')]}{\omega' - \omega}$$

Eqn.A1.47

$$\text{Im}[f(\omega)] = -\frac{1}{\pi} \mathbf{P} \int d\omega' \frac{\text{Re}[f(\omega')]}{\omega' - \omega}$$

Eqn.A1.48

where \mathbf{P} means the principal part of the integral. These functions were derived by Kramers and Kronig in the 1920's ⁷. These equations can be applied to the real and the imaginary parts of the complex refractive index, as it is dependent on frequency, and with causality invoked and with complex number analysis the following equations are revealed ¹:

$$n(\omega) = 1 + \frac{1}{\pi} \mathbf{P} \int_{-\infty}^{\infty} d\omega' \frac{\kappa(\omega')}{\omega' - \omega}$$

Eqn.A1.49

$$\kappa(\omega) = -\frac{1}{\pi} \mathbf{P} \int_{-\infty}^{\infty} d\omega' \frac{n(\omega') - 1}{\omega' - \omega}$$

Eqn.A1.50

where again, \mathbf{P} means the principal part of the integral. The Kramers-Kronig relationships allow for the calculation of κ from n and *vice versa* ¹.

A1.4 Utilising the relationship between n and κ to sense gases

In the previous sections the relationship between the refractive index, n , and the extinction coefficient, κ has been established. It was then shown that n and the κ are related through the complex relative dielectric constant, which is dependent on the resonant frequency of the absorption feature. Therefore, it is proposed that by changing the position of the resonant frequency, the value of n at a particular wavelength, at which the system is being interrogated, will change. If the system was interrogated at 1550 nm then the change in refractive index at 1550 nm, due to the change to the resonant absorption frequency would cause a measurable Bragg wavelength shift.

To achieve this it was proposed that a sol-gel thin film, on top of the waveguide layer of the Bragg grating sensor, would be doped with an organic dye. The choice of organic dye would be influenced by the ability of the organic dye to undergo a reversible chemical reaction with an analyte gas and, by doing so, change in colour. The change in colour of the organic dye is due to a change in the resonant frequency of the main absorption resonance of the dye. Thus, through the relationship revealed in the sections above, the refractive index of the dye will change and a Bragg wavelength shift at the interrogation wavelength will occur; refractometric gas sensing achieved by utilisation of the relationship between the absorption and the refraction of a material.

1. M. Fox, *Optical Properties of Solids*, Oxford University Press Inc., New York, 1st edn., 2001.
2. D. Fleisch, *A Student's Guide to Maxwell's Equations*, Cambridge University Press, 1st edn., 2008.
3. E. Hecht, *Optics*, Addison-Wesley, 4th edn., 2001.
4. Training Technical Teachers Institute, *Electrical Engineering Materials*, Tata McGraw-Hill Education, New Delhi, 1989.
5. H. Hertz, *Ann. der Phys. und Chemie*, 1888, **270**, 155–170.
6. B. Y.-K. Hu, *Am. J. Phys.*, 1989, **57**, 821.
7. C. F. Bohren, *Eur. J. Phys.*, 2010, **31**, 573–577.

